University of Massachusetts Amherst

ScholarWorks@UMass Amherst

November 2015

Polymer and Fullerene Zwitterions: From Synthesis to Solar Cells

Zachariah A. Page
University of Massachusetts - Amherst

Recommended Citation

POLYMER AND FULLERENE ZWITTERIONS:
FROM SYNTHESIS TO SOLAR CELLS

A Dissertation Presented

By

ZACHARIAH ALLEN PAGE

Submitted to the Graduate School of the
University of Massachusetts Amherst in partial fulfillment
of the requirements for the degree of

DOCTOR OF PHILOSOPHY

September 2015

Polymer Science and Engineering

**POLYMER AND FULLERENE ZWITTERIONS:
FROM SYNTHESIS TO SOLAR CELLS**

A Dissertation Presented

By

ZACHARIAH ALLEN PAGE

Approved as to style and content by:

_____
Todd Emrick, Chair

_____
Thomas Russell, Member

_____
Alejandro Briseno, Member

_____
Paul Lahti, Member

_____
David Hoagland, Department Head
Polymer Science and Engineering

ABSTRACT

POLYMER AND FULLERENE ZWITTERIONS:
FROM SYNTHESIS TO SOLAR CELLS

September 2015

ZACHARIAH ALLEN PAGE, B.S., JUNIATA COLLEGE

M.S., UNIVERSITY OF MASSACHUSETTS AMHERST

PH.D., UNIVERSITY OF MASSACHUSETTS AMHERST

Directed by: Professor Todd Emrick

This thesis describes the synthesis and applications of hydrophilic conjugated polymers and fullerenes containing dipole-inducing pendent groups. The pendent groups include tertiary amines, sulfobetaine (SB) zwitterions, quaternary ammoniums, and sulfonates, providing solubility in polar solvents. Particular emphasis is placed on zwitterions functalized structures. Suzuki-Miyaura (SM) and Horner-Wadsworth-Emmons (HWE) coupling reactions proved valuable for the preparation of the hydrophilic conjugated polymers, while the Prato reaction afforded the functional fulleropyrrolidines. Ultraviolet photoelectron spectroscopy (UPS) probed the interactions between the hydrophilic conjugated polymers and conductive metal substrates. In particular, UPS revealed that conjugated polymer zwitterions (CPZs) substantially reduce work function (Φ) of metals, represented by a negative interfacial dipole (Δ). Their solubility properties and interactions with metals make CPZs attractive for integration into solar cells, specifically at the interface between a photoactive layer and high Φ metal cathode. This thesis thus provides routes to improve polymer-based solar cell (PSC) technology through the implementation of novel hydrophilic semiconductors.

Initial syntheses focused on the preparation of polythiophene with pendent SB groups, producing CPZs that were incorporated into PSCs as cathode modification layers. Tuning the electronic properties of CPZs with different polymer backbones further enhanced their effectiveness as interlayers in PSCs. Diketopyrrolopyrrole (DPP), *iso*-indigo (*i*In) and naphthalene diimide (NDI) were functionalized with SB, followed by SM polymerization to provide the corresponding CPZs. Unprecedented power conversion efficiency (PCE) values (> 10%) were achieved for devices containing the NDI CPZs, and improved electron transport of the interlayers was found central to this efficiency enhancement.

Fulleropyrrolidines functionalized with tertiary amines and SB groups represent an alternative, non-polymeric, class of materials studied as interfacial modifiers in PSCs. The intrinsic n-type properties of fullerene provide an ideal platform for such interlayers, and led to state-of-the-art devices with record PCE values, irrespective of the selection of conductive cathode (Al, Ag, Cu and Au), while eliminating the need for precise control over interlayer thickness.

Finally, HWE coupling was investigated as a new approach to hydrophilic CPZs. The methodology presented afforded room temperature production of a variety of hydrophilic poly(arylene vinylene)s (PAVs) from water, including zwitterionic, cationic and anionic derivatives. The scope and limitations of the HWE reaction in water is discussed, along with the utility of the resulting PAVs in sensing and PSCs.

TABLE OF CONTENTS

LIST OF TABLES

LIST OF FIGURES

LIST OF SCHEMES

CHAPTER 1

ORGANIC PHOTOVOLTAICS AND POLAR SEMICONDUCTORS

1.1 Introduction

World-wide dependence on non-renewable energy sources such as fossil fuels have met societal demands to date, however as these materials are depleted and their harmful emissions accumulate there grows a need for renewable and clean energy sources. Current research focuses on new ways to harness renewable energy associated with Earth's numerous physical processes such as wind, geothermal gradients, moving water and sunlight. Solar energy conversion has outstanding potential to provide a sustainable future given that sunlight reaching earth's surface amounts to 6,000 times the current rate of energy consumption.[1] Over the past decade the amount of solar research has increased dramatically, yet the current technology suffers from major drawbacks preventing large-scale production and integration into modern society, including high cost of device fabrication and low sunlight-to-electricity conversion efficiency, known as power conversion efficiency (PCE). Since the discovery of photoactive materials there have been significant improvements in the understanding and design of solar cells, with advancements continuing today.

1.2 Photovoltaic technology: history and operation

The first crystalline silicon solar cell was fabricated in Bell Laboratories in 1954,[2] followed by the first organic photovoltaic (PV) device in 1959,[3] using an anthracene single crystal. It was not until 1982 when the first polymer-based solar cell (PSC) was developed, where polyacetylene was utilized as the photoactive material.[4] The organic

homojunction/single junction solar cells all resulted in low efficiencies ($< 0.1\%$) (**Figure 1.1A**). The poor performances were attributed to the formation of bound charge carriers (electron-hole pairs, commonly known as excitons) upon absorption of light. The energy from the mobile excited state can only be harnessed by separating the electron and hole, giving free charge carriers that must be extracted to the cathode and anode respectively.[5] In 1986, Tang discovered that a heterojunction between an electron donor and electron acceptor can provide the necessary driving force to dissociate the bound charges,[6] provided that the difference in potential energy (offset between lowest unoccumpied molecular orbital, LUMO, energy levels) is greater than the exciton binding energy. The first heterojunction devices were bilayers reaching efficiencies around 1% (**Figure 1.1B**).[5] In order to increase interfacial area between the donor and acceptor the dispersive/bulk heterojunction (BHJ) concept was developed in the 1990s. In 1995 Yu and coworkers fabricated the first fully organic BHJ, which contained poly(phenylene vinylene) as the donor and fullerene as the acceptor (**Figure 1.1C**).[7] The BHJ concept was quickly adopted by many and has become the most highly utilized morphology in PSCs to-date.
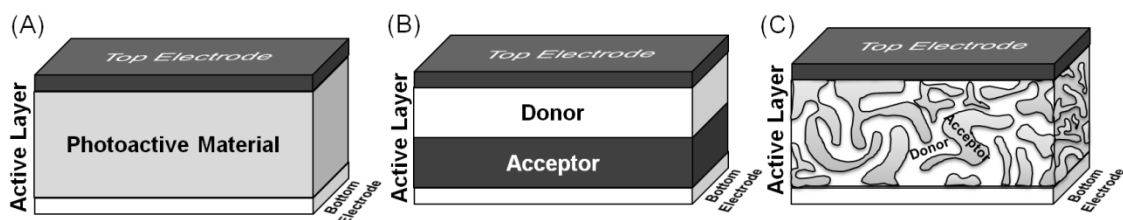
Figure 1.1 Photovoltaic device architectures: (A) single-junction; (B) bilayer; (C) bulk-heterojunction.

The photovoltaic devices depicted in **Figure 1.1** have commonalities, despite obvious differences of the active layer architecture. In all cases, the semiconducting active layer is sandwiched between two metals with different work functions, driving an

internal electric field, which draws electrons toward the cathode and holes toward the anode. Following a classical metal-insulator-metal (MIM) concept, the open-circuit voltage (V_{OC}) is directly related to the difference in electrode work function (**Figure 1.2**);[5] this only holds true if the Fermi levels of the electrodes are within the bandgap of the insulator, or rather, in this case, the semiconductor.[5] Ohmic contacts occur when the negative electrode matches the LUMO energy of the acceptor and positive electrode matches the highest occupied molecular orbital (HOMO) energy of the donor (**Figure 1.2**).[5]
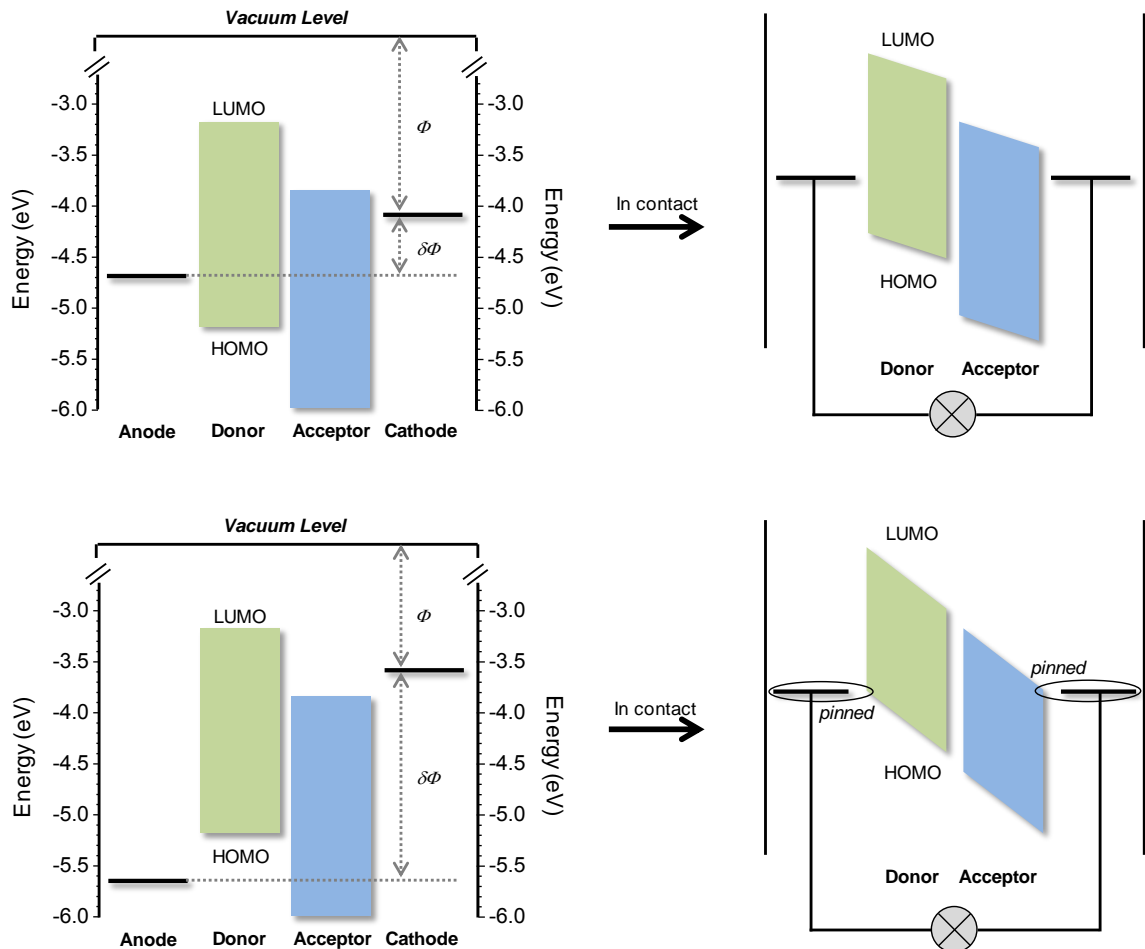
Figure 1.2 Metal – donor/acceptor – metal device: Top – non-ohmic contact; Bottom – ohmic contact.

3

In the case of Ohmic contacts the Fermi levels of the electrodes become "pinned" to the LUMO/HOMO levels of the semiconductor, and the V_{OC} is dictated by the offset of these orbitals (equation 1.1) where e is elementary charge, E is energy level, and 0.3 eV is the empirical value for charge separation.[11]

$$V_{OC} = e^{-1} \times \left(\left| E_{HOMO}^{donor} \right| - \left| E_{LUMO}^{acceptor} \right| - 0.3 \, eV \right) \qquad 1.1$$

V_{OC} is one of three factors that directly affect the overall PCE (η) of a solar cell device. The other two are short-circuit current density (J_{SC}) and fill factor (FF) (equation 1.2). Specifically, V_{OC} is the maximum voltage obtainable at the load under open-circuit conditions, J_{SC} is the maximum current through the load under short-circuit conditions and FF refers to the ratio of the maximum power divided by J_{SC} and V_{OC} displayed among the light current density voltage (J-V) characteristics. J_{SC} can be increased by enhancing photon absorption and balancing charge mobilities, but increasing FF has proven to be more complex since it is affected by many features (*e.g.* charge carrier mobility/balance, recombination, film morphology, series and shunt resistances, etc.).[10]

$$PCE \, (\eta) = V_{OC} \times J_{SC} \times FF \qquad 1.2$$

Semiconducting organic small molecules and polymers are excellent platforms for solar cells due to their ease of chemical modification through synthetic tailoring, providing a wide range of tunable properties; *e.g.* electronic (energy levels) to physical (wettability, mixing, solubility, etc.). Inexpensive production of large-area PSCs can be applied to flexible, light-weight and robust substrates, made possible through the availability of a number of wet-processing techniques (spin-casting, dip-coating, ink-jet printing, spray coating, roll-to-roll printing, paint brush application, screen printing, etc.).[8,9] The process is also made scalable by a naturally wide abundance of organic

materials used to synthesize semiconducting polymers. In addition, due to their typically high attenuation coefficients ($\varepsilon > 10^5$ cm^{-1}), thin films of conjugated polymers can be used to absorb a large percentage of the solar spectrum, which reduces material consumption (~300 nm thick film leads to complete photon absorption at the maximum wavelength of absorption).[10] Current drawbacks to standard BHJ organic photovoltaics (OPVs) are their low efficiencies ($\leq 11\%$) and poor stability, requiring protection from ambient conditions (air and moisture) to support device longevity.[11] Inorganic silicon PV devices have higher efficiencies ($> 20\%$), but suffer from expensive manufacturing. In order to have solar energy as an economically viable route to a renewable future, the PV devices must be both efficient and inexpensive.[12]

Significant research efforts on BHJ OPVs have focused on understanding device physics, especially with regards to the movement of charges. Conjugated organic compounds have a quantized energy gap (E_g), and due to their delocalized π electron system they act as semiconductors where the electrons in the HOMO can be energized given a perturbation, such as through the absorption of a photon.[13] The photo-excitation results in an electronic transition from the HOMO level to the LUMO level (**Scheme 1.1**).[13] For organic semiconductors the excited electron is Coulombically bound to the hole and following thermalization of the primary excitation, a singlet exciton (electron/hole pair) is formed.[13] The intermolecular forces localizing excitons are largely due to the low dielectric constants inherent to typical organic semiconductors (dielectric constant $\approx 2 - 4$ compared to ~10 for inorganic semiconductors).[15] Following formation, the exciton diffuses and if it comes in contact with a donor(p-type)/acceptor(n-type) (D/A) interface prior to bimolecular/geminate recombination then charge or energy

transfer may occur. Following transfer, charge separation will transpire given sufficient

energy to overcome the Coulombically bound pair also known as the exciton binding

energy ($E_b \approx 0.4 - 0.5$ eV);[14] Recently, it has been suggested that dissociation of charges

at the interface may occur prior to full thermalization/exciton formation, but this is the

main discrepancy with the well accepted charge mechanism and will not be discussed in

further detail here.[13] Once free charge carriers (electrons and holes) are formed, they

travel to the electrodes (cathode and anode respectively), guided by an internal electric

field (**Scheme 1.1**).[13] This process is possible because charge separation at an interface is

much faster (< 100 fs) than competing processes such as photoluminescence (ns time

scale) and charge recombination (μs time scale).[15]
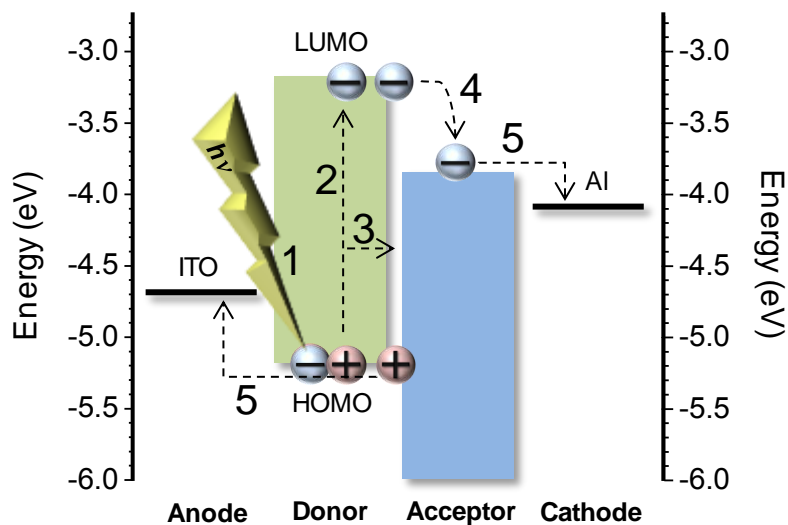
Scheme 1.1 General mechanism for charges in OPV BHJs: 1) Photon absorption; 2) Exciton formation; 3) Exciton diffusion to interface; 4) Charge transfer; 5) Exciton dissociation/charge transport to electrodes.

In order for charges to reach the D/A interface, light absorption must take place

within the exciton diffusion length (5 – 20 nm).[16,17] Ensuring that D/A interfaces are

within reach of photo-generated excitons, while also maintaining a bicontinuous network

of p- and n-type material, is critical for an efficient device and relies heavily on the morphology of the blend. The methods currently utilized to alter the morphology of blends include choice of solvent and concentration of solute, initial D/A ratio, casting method (*e.g.* spin, dip, spray, etc), processing temperature/annealing and chemical composition (mixing parameter) of the blend components.[18] Optimizing these factors have allowed for bicontinuous networks with domains on the order of the exciton diffusion length to be produced in a BHJ photovoltaic active layer, resulting in some of the highest efficiencies to date.[19]

Another facet of PSCs that has attracted recent attention is the ability to tune the HOMO and LUMO energy levels through chemical modification. This has proven vital since the maximum irradiance of the standard solar spectrum (AM 1.5G) is ~500 nm with peak photon flux at ~670 nm, and initial PSCs that contained alkylated poly(phenylene vinylene) (**1**) (PPV) and poly(3-alkyl thiophene) (**2**) (P3AT) as the p-type material did not efficiently absorb light in these regions (with bandgaps exceeding 1.8 eV, the solar absorption was ≤ 30%) (**Figure 1.3**).[11] The development of "push-pull"/donor-acceptor copolymers provided new semiconductros with reduced bandgaps due to orbital hybridization, which led to improved light absorption. Additionally, stabilization of the quinoid mesomeric structure increases planarity and maximizes conjugation length to further reduce the energy gap (E_g) of "push-pull" copolymers.[10] As a consequence, the reduction of E_g often lowers V_{OC} (given ohmic contacts). Spectral engineering continues to be a developing field of research, with the desire to produce novel materials with tailored energy levels to maximize V_{OC} and minimize E_g.[5]
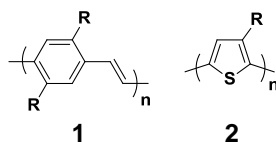
Figure 1.3 Poly(phenylene vinylene) (**1**), and poly(thiophene) (**2**).

Some of the common motifs in donor-acceptor polymers include benzothiadiazole (BT) (**3**), diketopyrrolopyrrole (DPP) (**4**), *iso*indigo (*i*In) (**5**), naphthalene diimide (NDI) (**6**) and benzodithiophene (BDT) (**7**) in combination with thiophene (**8**), fluorene (**9**), carbazole (**10**), cyclopentadithiophene (CPDT) (**11**) and thienothiophene (**12**) derivatives (**Figure 1.4**).[18,20] The synthetic efforts to create new n-type materials have not been as extensive as those to create p-type, but functionalization of fullerene has recently proven an effective method to produce soluble acceptors with desirable electronic properties for solar cell applications (*e.g.* strong electronegativity and high electron mobility).[21] In 1995 Wudl and coworkers synthesized a methanofullerene derivative, phenyl-C_{60} butyric acid methylester ($PC_{61}BM$), which has become the benchmark acceptor, along with the more recent fullerene-C_{70} derivative ($PC_{71}BM$).[10] The utilization of these PCBM derivatives has led to number of single junction photovoltaic devices that exceed PCEs of 9%, but the devices suffer from poor lifetimes and inefficient syntheses of active layer components, which will be necessary hurdles to overcome for practical commercialization.[22-37] The use of multijunction (tandem and triple junction) solar cell technology has resulted in the highest reported PCEs to date (> 10 %) , but come at the cost of more complex device fabrication.[38-43]
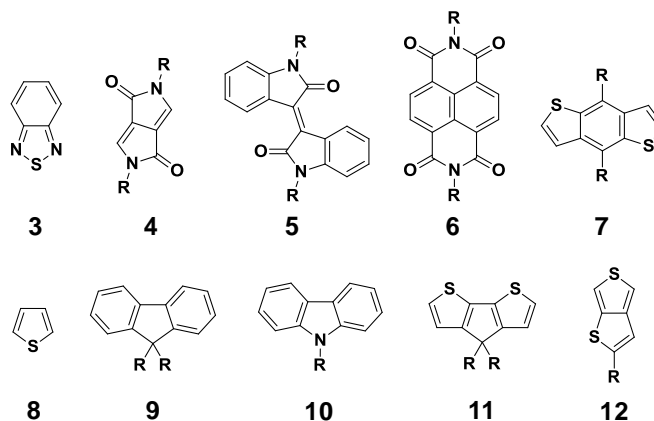
Figure 1.4 Common repeat units seen in donor-acceptor copolymers: From left to right – benzothiadiazole (BT, **3**), diketopyrrolopyrrole (DPP, **4**), *iso*indigo (*i*In, **5**), naphthalene diimide (NDI, **6**) and benzodithiophene (BDT, **7**) in combination with thiophene (**8**), fluorene (**9**), carbazole (**10**), cyclopentadithiophene (CPDT, **11**) and thieonthiophene (TT, **12**).

1.3 Interlayers in organic photovolatics

Thin interlayers placed between organic active layers and metal electrodes in organic electronic and optoelectronic devices offer routes to improved device performance. In organic light-emitting diodes (OLEDs) and field-effect transistors (OFETs), interlayers give higher injection current densities.[44,45] In organic photovoltaics (OPVs), a significant increase of open circuit voltage and short circuit current is achieved, with interlayers in conventional,[46] inverted,[47] and tandem[48] device architectures. More recently, organic and polymeric interlayer materials were developed, since they allow synthetic tailoring of functionality and integration into devices through simple fabrication procedures. Interlayer materials under investigation include self-assembled monolayers (SAMs),[45,49-51] neutral small molecules[52] and polymers,[53] ionic surfactants,[54] conjugated polymers with solubilizing pendent groups[55] and conjugated polyelectrolytes (CPE).[56-59] Such materials are either functionalized to bind to the electrode surface,[45,49] segregate on the surface,[50] or possess orthogonal solubility with the active layer, which enables sequential deposition of films.[52,54,56,57,60]

9

The operation of organic electronic and optoelectronic devices relies on the electronic characteristics between the organic active layer and electrode. A number of inorganic interlayers (i.e. LiF, ZnO and TiO_2) have been integrated into device architectures to improve performance.[61] In recent years CPEs have emerged as organic interlayers.[61] CPEs are charged hydrophilic semiconductors that improve polymer light-emitting diodes (PLEDs),[56] dye-sensitized solar cells (DSSCs),[62,63] organic thin-film transistors (OTFTs),[64] light emitting field-effect transistors (LEFETs)[65,66] and bulk heterojunction (BHJ) solar cells.[67-69] CPE interlayers assist charge injection, generally from the cathode to the active layer, and their aqueous solubility enables deposition with little disruption of the underlying layer.[57,60] In PLEDs, CPE electron injection layers allow the use of stable metal cathodes (i.e. silver and gold), and give devices with reduced turn-on-voltage and several orders-of-magnitude higher efficiency relative to those without an interlayer.[70] For OTFTs, reduced contact resistance (R_c) and higher drain to source currents (I_{DS}) were obtained with a cationic polyfluorene layer between the source/drain electrodes and active layers.[98] In BHJ solar cells, a CPE layer between the active layer and cathode enhanced the open circuit voltage (V_{OC}) by 50%, and improved short-circuit current density (J_{SC}) and fill factor (FF) to give a two-fold increase in power conversion efficiency (PCE).[68]

The mechanisms invoked to explain the role of interlayers range from improved surface wettability and adhesion to morphological optimization and electronic structure modifications.[89] The effects from CPE interlayers are proposed to arise from: 1) ion-motion that redistributes the electric field within a device,[71] and 2) a modification of the work function at the organic/metal interface arising from dipole alignment.[72,73] An

10

interfacial dipole (Δ) at a metal-organic interface may arise from a compression of the metal electron density tail.[74-77] Recently, Kemerink and coworkers conducted an in-depth study on the origin of work function modification for CPE- and amine-based interlayers to elucidate between four proposed mechanisms on the formation of an Δ: 1) electric double layer formation upon interlayer doping, 2) charge transfer between electrode and interlayer, 3) spontaneous dipole orientation within the interlayer and 4) spontaneous dipole orientation at the interface only.[78-83] They suggest that the formation of an interfacial dipole arises from one mechanism, spontaneous dipole orientation at the interface due to the formation of an image charge in the conductor, for both CPE- and amine-based interlayers.[78] The electrode work function modification of PSCs containing interlayers, due to the formation of an interfacial dipole, has been identified as one of the primary factors that improves device performance.[84,85] In PSCs a change in the work function of the electrodes directly influences V_{OC}, given non-ohmic contacts. For photovoltaic devices this change in V_{OC} occurs under the principle that two conducting electrodes connected in a circuit will have an alignment of their E_F levels. The E_F alignment is what drives the internal electric field, which guides the electrons and holes to their respective electrodes, where the Fermi energy offset ($\delta\Phi$) at the organic-metal interface dictates the strength of this field (**Figure 1.5**). Introducing an Δ at the electrode modifies work function ($\delta\Phi^m$), enhancing the internal electric field, increasing V_{OC} and ultimately PCE (specifically for a $+\Delta$ at the anode, increased work function, and $-\Delta$ at the cathode, decreased work function). In addition to the formation of an Δ, interlayers have recently been shown to improve solar cell devices by protecting the active layer from hot

atoms upon thermal evaporation of the electrode and suppression of surface states that increases the rate of charge extraction and reduces bimolecular recombination.[86,87]
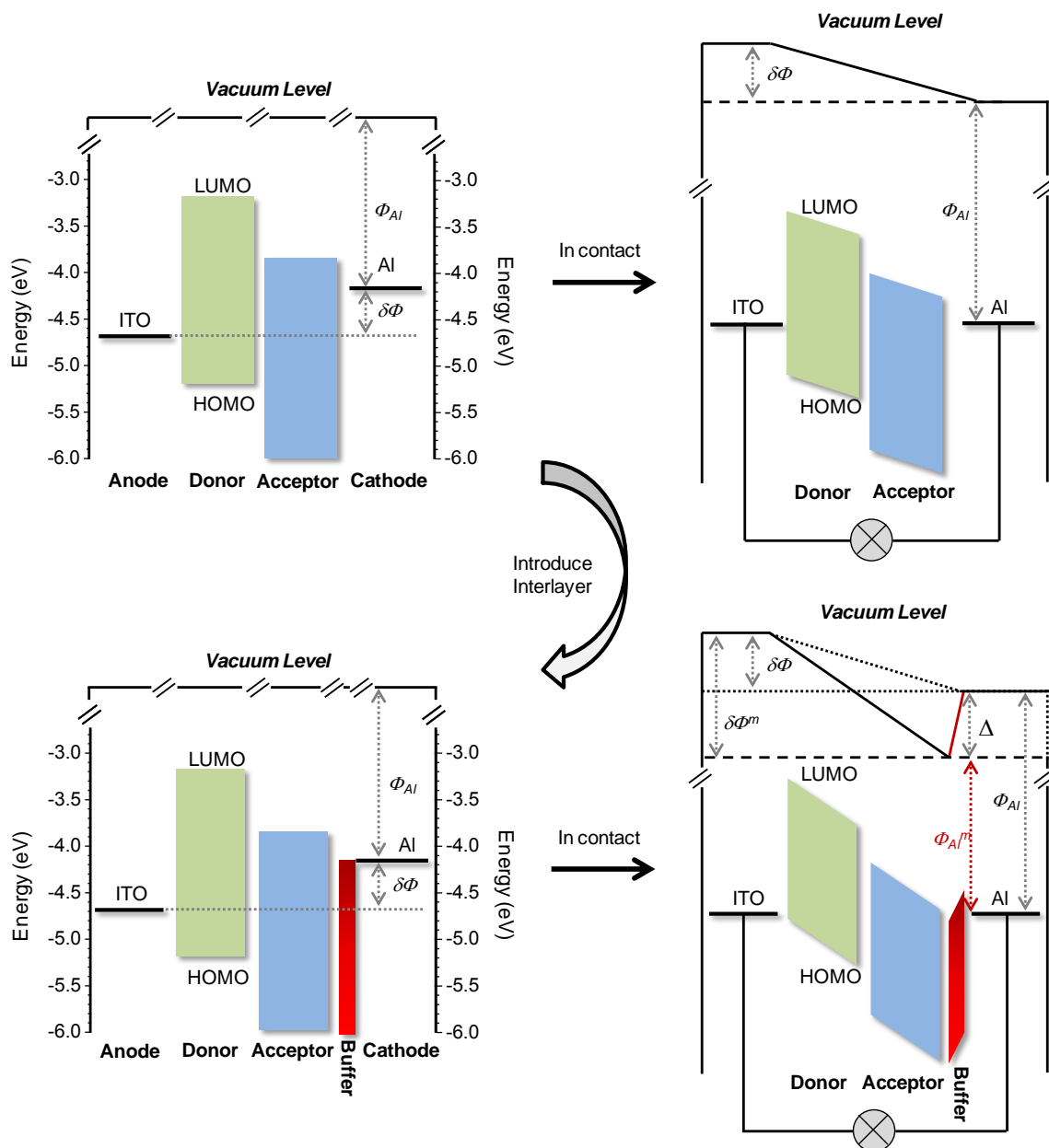
Figure 1.5 Formation of an internal electric field and the effect of a buffer layer on the strength of the field, represented by the gradient of HOMO, LUMO and vacuum energy levels. Left – Energy levels of individual components (common vacuum level); Right – Metals brought in contact to create a circuit leading to the introduction of an interfacial dipole. The energy scale is removed from the circuit figures (right) since the exact energy levels post E_F alignment is unknown.

1.4 Conjugated polymer zwitterions (CPZs)

The ability to fabricate OPV's through a layer-by-layer, solution-based, approach provides an avenue towards inexpensive mass production. As such, a surge of recent research efforts to prepare new electronically active materials that possess unique solubility has taken place, with particular emphasis on polymer-based materials given their unrivaled ability to form thin uniform films. Orthogonality of solute miscibility plays a key role in preparing efficient OPVs, since it allows for discrete layers to be obtained with little interruption of the underlying material. Because active layer components are typically non-polar, thus soluble in relatively apolar solvents (*eg* toluene, chloroform, chlorobenzene, etc.), the layers above and below (often described as interlayers) should be soluble in polar solvents (giving orthogonal solubility). The development of hydrophilic semiconducting polymers has played a major role in furthering OPV technology, specifically through interfacial engineering. This section introduces a new class of hydrophilic semiconducting polymers, called conjugated polymer zwitterions (CPZs), which are central to this thesis.

While polyelectrolytes, such as CPEs, contain either cationic or anionic moieties that are associated with transient counterions, polymer zwitterions contain both cationic and anionic groups and thus do not have counterions.[88] Although polymer zwitterions encompass both polyampholytes (charged groups located on different monomer units) and polybetaines (charged groups located on the same monomer unit) the term zwitterion will only be used in this thesis to describe polybetaines. The first example of a zwitterionic, albeit non-polymeric, interlayer in optoelectronic devices was presented by Bazan and coworkers, where alkylated imidazolium borate zwitterions was used to

enhance electron injection from high work function electrodes.[89] The development of CPZs soon followed, bringing neutral and hydrophilic zwitterionic side-chains, to electronically active polymer backbones. CPZs are attractive for achieving the beneficial properties of CPEs (water solubility; pendent dipoles) without the complications of counter ions (*e.g.*, long turn-on times for LEDs).[90] To-date only a few examples of CPZs have been reported (apart from pH sensitive derivatives such as amino acid substituted structures[91-93]). Synthetic routes besides this work utilize post-polymerization reactions to convert polymer precursors to CPZs.[90,94,95] For example, Huck and coworkers synthesized an alternating copolymer of di-*n*-octylfluorene and a sulfobetaine (SB) substituted fluorene,[90] while Huang and coworkers prepared homopolymers of a SB-substituted fluorene.[94] These CPZs were characterized as electron-injection materials in PLEDs, reducing response times to less than 10 μs, and improving brightness/efficiency two-fold relative to calcium-based devices.[90,94]

1.5 Thesis outline

The development of new electronically active materials has led to dramatic improvements in polymer solar cell technology in the last decade, yet many aspects of current devices fall short of what is required for wide-spread implementation. Although recent devices exceeding 10% PCE have been obtained (a benchmark standard for acceptable commercialization) they have come at the cost of expensive and complex syntheses and device fabrication techniques, while often setting aside issues related to module stability and scalability. The utility of interfacial modification layers in PSCs placed between the electrode and active has recently been identified as a promising solution to the residual issues. Polar semiconducting molecules, such as CPEs and CPZs,

have orthogonal solubility to typical active-layer materials, enabling multi-layer solution processing. Incorporation of CPEs and CPZs into optoelectronic devices as electrode modification layers has led to improved performance. The purpose of this thesis was to develop methods towards novel zwitterionic semiconductors, while shedding light on how their utility as interlayers in PSCs could advance state-of-the-art solar technology.

Chapter 2 describes the initial design and synthesis of novel thiophene-based CPZs using Suzuki-Miyaura (SM) coupling, in which the zwitterion is present on the monomer from the outset.[96] Further optimization led to the use of ionic liquids (ILs) for rapid air-stable Suzuki polymerization, which precluded the need for volatile organic solvents, phosphine ligands and phase transfer catalysts.[97] The final part of chapter 1 discusses the incorporation of thiophene-based CPZs as cathode modification layers in PSCs along with optoelectronic characterization that provides insight regarding observed variations in PSC performance.[98]

Chapter 3 describes the synthesis and characterization of diketopyrrolopyrrole- (DPP), *iso*-indigo- (*i*In), and naphthalene diimide- (NDI) based narrow energy gap CPZs and their integration as buffer layers in PSCs.[99,100] The disparity in backbone composition provides key structure-property relationships as they relate to device efficiency. Chapter 4 describes the extension of the CPZ work to n-type zwitterionic fulleropyrrolidines.[101] Chapter 5 describes a new platform from which polar arylene-vinylne polymers, including zwitterion-substituted derivatives, can be synthesized in basic water through the Horner-Wadsworth-Emmons (HWE) reaction as an alternative approach to SM coupling, precluding organic solvents and transition metal catalysts.[102]

1.6 References

1.   Grätzel, M. *Acc. Chem. Res.* **2009**, *42*, 1788-1798.

2.   Chapin, D. M.; Fuller, C. S.; Pearson, G. L. *J. Appl. Phys.* **1954**, *25*, 676.

3.   Kallmann, H.; Pope, M. *J. Chem. Phys.* **1959**, *30*, 585-586 .

4.   Weinberger, B. R.; Akhtar, M.; Gau, S. C. *Synth. Met.* **1982**, *4*, 187-197.

5.   Blom, P. W. M.; Mihailetchi, V. D.; Koster, L. J. A.; Markov, D. E. *Adv. Mater.* **2007**, *19*, 1551-1566.

6.   Tang, C. W. *Appl. Phys. Lett.* **2012**, *183*, 5-8.

7.   Yu, G.; Gao, J.; Hummelen, J. C.; Wudl, F.; Heeger, A. J. *Science* **1995**, *270*, 1789-1791.

8.   Yang, Y.; Wudl, F. *Adv. Mater.* **2009**, *21*, 1401-1403.

9.   Cowan, S. R.; Banerji, N.; Leong, W. L.; Heeger, A. J. *Adv. Funct. Mater.* **2012**, *22*, 1116-1128.

10.   Li, G.; Zhu, R.; Yang, Y. *Nat. Photonics.* **2012**, *6*, 153-161.

11.   Gunes, S.; Neugebauer, H.; Sariciftci, N. S. *Chem. Rev.* **2007**, *107*, 1324-1338.

12.   Coakley, K. M.; McGehee, M. D. *Chem. Mater.* **2004**, *16*, 4533-4542.

13.   Cowan, S. R.; Banerji, N.; Leong, W. L.; Heeger, A. J. *Adv. Funct. Mater.* **2012**, *22*, 1116-1128.

14.   Zhu, X.-Y.; Yang, Q.; Muntwiler, M. *Acc. Chem. Res.* **2009**, *42*, 1779-1787.

15.   Cai, W.; Gong, X.; Cao, Y. *Sol. Energ. Mat. Sol. Cells* **2010**, *94*, 114-127.

16.   Theander, M.; Yartsev, A.; Zigmantas, D.; Sundstrom, V.; Mammo, W.; Andersson, M. R.; Inganas, O. *Phys. Rev. B* **2000**, *61*, 957-963.

17.   Haugeneder, A.; Neges, M.; Kallinger, C.; Spirkl, W.; Lemmer, U.; Feldmann, J.; Scherf, U.; Harth, E.; Gügel, A.; Müllen, K. *Phys. Rev. B* **1999**, *59*, 15346–15351.

18.   Boudreault, P.-L. T.; Najari, A.; Leclerc, M. *Chem. Mater.* **2011**, *23*, 456-469.

19.   Jackson, N. E.; Savoie, B. M.; Marks, T. J.; Chen, L. X.; Ratner, M. a. *J. Phys. Chem. Lett.* **2015**, *6* (1), 77.

20.   Po, R.; Bianchi, G.; Carbonera, C.; Pellegrino, A. *Macromolecules* **2015**, *48*, 453.

21. Li, C.-Z.; Yip, H.-L.; Jen, A. K.-Y. *J. Mater. Chem.* **2012**, *22* (10), 4161-4177.

22. He, Z.; Zhong, C.; Su, S.; Xu, M.; Wu, H.; Cao, Y. *Nat. Photonics* **2012**, *6*, 591-597.

23. Yao, K.; Salvador, M.; Chueh, C.; Xin, X.; Xu, Y.; Dane, W.; Hu, T.; Chen, Y.; Ginger, D. S.; Jen, A. K. *Adv. Energy Mater.* **2014**, *4*, 1400206.

24. Zhang, W.; Wu, Y.; Bao, Q.; Gao, F.; Fang, J. *Adv. Energy Mater.* **2014**, *4*, 1400359.

25. Guo, X.; Zhang, M.; Ma, W.; Ye, L.; Zhang, S.; Liu, S.; Ade, H.; Huang, F.; Hou, J. *Adv. Mater.* **2014**, *26*, 4043-4049.

26. Li, C.-Z.; Chang, C.-Y.; Zang, Y.; Ju, H.-X.; Chueh, C.-C.; Liang, P.-W.; Cho, N.; Ginger, D. S.; Jen, A. K.-Y. *Adv. Mater.* **2014**, *26* (36), 6262-6267.

27. He, Z.; Xiao, B.; Liu, F.; Wu, H.; Yang, Y.; Xiao, S.; Wang, C.; Russell, T. P.; Cao, Y. *Nat. Photonics* **2015**, *9* (3), 174-179.

28. Chen, J.-D.; Cui, C.; Li, Y.-Q.; Zhou, L.; Ou, Q.-D.; Li, C.; Li, Y.; Tang, J.-X. *Adv. Mater.* **2015**, *27*, 1035.

29. Zhang, Q.; Kan, B.; Liu, F.; Long, G.; Wan, X.; Chen, X.; Zuo, Y.; Ni, W.; Zhang, H.; Li, M.; Hu, Z.; Huang, F.; Cao, Y.; Liang, Z.; Zhang, M.; Russell, T. P.; Chen, Y. *Nat. Photonics* **2014**, *9* (1), 35-41.

30. Lim, D. C.; Seo, B. Y.; Nho, S.; Kim, D. H.; Hong, E. M.; Lee, J. Y.; Park, S.; Lee, C.; Kim, Y. D.; Cho, S. *Adv. Energy Mater.* **2015**, 1500393.

31. Zhang, K.; Zhong, C.; Liu, S.; Mu, C.; Li, Z.; Yan, H.; Huang, F.; Cao, Y. *ACS Appl. Mater. Interfaces* **2014**, *6*, 10429-10435.

32. Nguyen, T. L.; Choi, H.; Ko, S.-J.; Uddin, M. a.; Walker, B.; Yum, S.; Jeong, J.-E.; Yun, M. H.; Shin, T. J.; Hwang, S.; Kim, J. Y.; Woo, H. Y. *Energy Environ. Sci.* **2014**, *7* (9), 3040-3051.

33. Ye, L.; Zhang, S.; Zhao, W.; Yao, H.; Hou, J. *Chem. Mater.* **2014**, *26*, 3603-3605.

34. Liu, C.; Yi, C.; Wang, K.; Yang, Y.; Bhatta, R. S.; Tsige, M.; Xiao, S.; Gong, X. *ACS Appl. Mater. Interfaces* **2015**, *7* (8), 4928.

35. Jagadamma, L. K.; Al-Senani, M.; El-Labban, A.; Gereige, I.; Ngongang Ndjawa, G. O.; Faria, J. C. D.; Kim, T.; Zhao, K.; Cruciani, F.; Anjum, D. H.; McLachlan, M. a.; Beaujuge, P. M.; Amassian, A. *Adv. Energy Mater.* **2015**, 1500204.

36. Zhang, S.; Ye, L.; Zhao, W.; Yang, B.; Wang, Q.; Hou, J. *Sci. China. Chem.* **2015**, *58* (2), 248-256.

37. Liao, S.-H.; Jhuo, H.-J.; Yeh, P.-N.; Cheng, Y.-S.; Li, Y.-L.; Lee, Y.-H.; Sharma, S.; Chen, S.-A. *Sci. Rep.* **2014**, *4*, 6813.

38. You, J.; Chen, C.-C.; Hong, Z.; Yoshimura, K.; Ohya, K.; Xu, R.; Ye, S.; Gao, J.; Li, G.; Yang, Y. *Adv. Mater.* **2013**, *25* (29), 3973.

39. You, J.; Dou, L.; Yoshimura, K.; Kato, T.; Ohya, K.; Moriarty, T.; Emery, K.; Chen, C.-C.; Gao, J.; Li, G.; Yang, Y. *Nat. Commun.* **2013**, *4*, 1410-1446.

40. Chen, C.-C.; Chang, W.-H.; Yoshimura, K.; Ohya, K.; You, J.; Gao, J.; Hong, Z.; Yang, Y. *Adv. Mater.* **2014**, *26*, 5670.

41. Zheng, Z.; Zhang, S.; Zhang, M.; Zhao, K.; Ye, L.; Chen, Y.; Yang, B.; Hou, J. *Adv. Mater.* **2015**, *27* (7), 1189-1194.

42. Zhou, H.; Zhang, Y.; Mai, C.-K.; Collins, S. D.; Bazan, G. C.; Nguyen, T.-Q.; Heeger, A. J. *Adv. Mater.* **2015**, *27*, 1767-1773.

43. Mohd Yusoff, A. R. Bin; Kim, D.; Kim, H. P.; Shneider, F. K.; da Silva, W. J.; Jang, J. *Energy Environ. Sci.* **2015**, *8*, 303-316.

44. Tang C.W.; VanSlyke, S.A. *Appl. Phys. Lett.* **1987**, 51, 913-915.

45. DiBenedetto, S.A.; Facchetti, A.; Ratner, M.A.; Marks, T. *Adv. Mater.* **2009**, 21, 1407-1433.

46. Brabec, C.J.; Shaheen, S.E.; Winder, C.; Sariciftci, N.S.; Denk, P. *Appl. Phys. Lett.* **2002**, 80, 1288-1290.

47. Li, G.; Chu, C.W.; Shrotriya, V.; Huang, J.; Yang, Y. *Appl. Phys. Lett.* **2006**, 88, 253503.

48. Kim J.Y.; Lee, K.; Coates, N.E.; Moses, D.; Nguyen, T.Q.; Dante, M.; Heeger, A.J. *Science* **2007**, 317, 222-225.

49. Campbell, I.H.; Kress, J.D.; Martin, R.L.; Smith, D.L.; Barashkov, N.N.; Ferraris, J.P. *Appl. Phys. Lett.* **1997**, 71, 3528-3530.

50. Boer, B. de; Hadipour, A. Mandoc, M. M. Woudenbergh, T. V.; Blom, P. W. M. *Adv. Mater.* **2005**, *17*, 621-625.

51. Yip, B. H.-lap; Hau, S. K. Baek, N. S. Ma, H.; Jen, A. K. *Adv. Mater.* **2008**, *20*, 2376-2382.

52. Wei, Q.; Nishizawa, T.; Tajima, K.; and Hashimoto, K. *Adv. Mater.* **2008**, 20, 2211-2216.

53. Zhou, Y.; Fuentes-Hernandez, C.; Shim, J.; Meyer, J.; Giordano, A. J.; Li, H.; Winget, P.; Papadopoulos, T.; Cheun, H.; Kim, J.; Fenoll, M.; Dindar, A.; Haske,

W.; Najafabadi, E.; Khan, T. M.; Sojoudi, H.; Barlow, S.; Graham, S.; Brédas, J.-L.; Marder, S. R.; Kahn, A.; Kippelen, B. *Science* **2012**, *336*, 327-332.

54. O'Malley, K. M.; Li, C.-Z.; Yip, H.-L.; and Jen, A. K.-Y. *Adv. Energy Mater.* **2012**, 2, 82-86.

55. Ma, H.; Yip, H.-L.; Huang, F.; and Jen, A. K.-Y. *Adv. Funct. Mater.* **2010**, 20, 1371-1388.

56. Wu, H.; Huang, F.; Mo, Y.; Yang, W.; Wang, D.; Peng, J.; and Cao, Y. *Adv. Mater.* **2004**, 16, 1826-1830.

57. Ma, W.; Iyer, P. K.; Gong, X.; Liu, B.; Moses, D.; Bazan, G. C.; Heeger, A. J. *Adv. Mater.* **200**5, 17(3), 274-277.

58. Duarte, A.; Pu, K.-Y.; Liu, B.; Bazan, G. C. *Chem. Mater.*, **2011**, 23(3), 501-515.

59. Hou, L.; Huang, F.; Peng, J.; Wu, H.; Wen, S.; Mo, Y.; Cao, Y. *Thin Solid Films* **2006**, 515, 2632-2634.

60. Steuerman, D. W.; Garcia, A.; Dante, M.; Yang, R.; Löfvander, J. P.; Nguyen, T.-Q. *Adv. Mater.* **2008**, *20*(3), 528-534.

61. Dou, L. You, J. Yang, J. Chen, C.-C. He, Y. Murase, S. Moriarty, T. Emery, K. Li, G.; Yang, Y. *Nat. Photonics* **2012**, *6*, 180–185.

62. Liu, X.; Zhu, R.; Zhang, Y.; Liu, B.; Ramakrishna, S. *Chem. Commun.* **2008**, 3789-3791.

63. Mwaura, J. K.; Zhao, X.; Jiang, H.; Schanze, K. S.; Reynolds, J. R. *Chem. Mater.* **2006**, *18*(26), 6109-6111.

64. Seo, J. H.; Gutacker, A.; Walker, B.; Cho, S.; Garcia, A.; Yang, R.; Nguyen, T.-Q.; Heeger, A. J.; Bazan, G. C. *J. Am. Chem. Soc*. **2009**, *131*, 18220-18221.

65. Seo, J. H.; Namdas, E. B.; Gutacker, A.; Heeger, A. J.; Bazan, G. C. *Appl. Phys. Lett*. **2010**, *97*(4), 043303.

66. Seo, J. H.; Namdas, E. B.; Gutacker, A.; Heeger, A. J.; Bazan, G. C. *Adv. Funct. Mater.* **2011**, *21*, 3667-3672.

67. Seo, J. H. Gutacker, A. Sun, Y. Wu, H. Huang, F. Cao, Y. Scherf, U. Heeger, A. J.; Bazan, G. C. *J. Am. Chem. Soc.* **2011**, *133*, 8416-8419.

68. Luo, J.; Wu, H.; He, C.; Li, A.; Yang, W.; Cao, Y. *Appl. Phys. Lett*. **2009**, *95*(4), 043301.

69.   Rider, B. D. A.; Worfolk, B. J.; Harris, K. D.; Lalany, A.; Shahbazi, K.; Fleischauer, M. D.; Brett, M. J.; Buriak, J. M. *Adv. Funct. Mater.* **2010**, *20*, 2404-2415.

70.   Hoven, C. V.; Yang, R.; Garcia, A.; Crockett, V.; Heeger, A. J.; Bazan, G. C.; Nguyen, T.-Q. *Proc. Natl. Acad. Sci. U. S. A.* **2008**, *105*(35), 12730-12735.

71.   Slinker, J. D.; DeFranco, J. A.; Jaquith, M. J.; Silveira, W. R.; Zhong, Y.-W.; Moran-Mirabal, J. M.; Craighead, H. G.; Abruña, H. D.; Marohn, J. A.; Malliaras, G. G. *Nat. Mater.* **2007**, *6*(11), 894-899.

72.   Ishii, B. H.; Sugiyama, K.; Ito, E.; Seki, K. *Adv. Mater.* **1999**, *11*(8), 605-625.

73.   Seo, J. H.; Yang, R.; Brzezinski, J. Z.; Walker, B.; Bazan, G. C.; Nguyen, T.-Q. *Adv. Mater.* **2009**, *21*(9), 1006-1011.

74.   Crispin, X. Geskin, V. Crispin, A. Cornil, J. Lazzaroni, R. Salaneck, W. R.; Brédas, J.-L. *J. Am. Chem. Soc.* **2002**, *124*, 8131-8141.

75.   Gao, Y. *Mater. Sci. Eng., R.* **2010**, *68*, 39-87.

76.   Koch, N. *J. Phys.: Condens. Matter.* **2008**, *184008*.

77.   Osikowicz, W.; Jong, M. P.; Braun, S.; Tengstedt, C.; Fahlman, M.; Salaneck, W. R. *Appl. Phys. Lett.* **2006**, *88*, 193504.

78.   Reenen, S. van; Kouijzer, S.; Janssen, R. A. J.; Wienk, M. M.; Kemerink, M. *Adv. Mater. Interfaces* **2014**, *1*, 1400189.

79.   Braun, B. S.; Salaneck, W. R.; Fahlman, M. *Adv. Mater.* **2009**, *21*, 1450-1472.

80.   Vázquez, H.; Flores, F.; Kahn, A. *Org. Electron.* **2007**, *8* (2-3), 241-248.

81.   Kahn, A.; Koch, N.; Gao, W. *J. Polym. Sci., Part B Polym. Phys.* **2003**, *41*, 2529.

82.   Xia, R.; Leem, D.-S.; Kirchartz, T.; Spencer, S.; Murphy, C.; He, Z.; Wu, H.; Su, S.; Cao, Y.; Kim, J. S.; DeMello, J. C.; Bradley, D. D. C.; Nelson, J. *Adv. Energy Mater.* **2013**, *3* (6), 718-723.

83.   Li, C.; Chueh, C.; Ding, F.; Yip, H.; Liang, P.; Li, X.; Jen, A. K. *Adv. Mater.* **2013**, *25*, 4425-4430.

84.   Worfolk, B.J.; Hauger, T.C.; Harris, K.D.; Rider, D.A.; Fordyce, J.A.M.; Beaupre, S.; Leclerc, M.; and Buriak, J.M. *Adv. Energy Mater.* **2012**, 2, 361-368.

85.   He, Z.; Zhong, C.; Huang, X.; Wong, W.-Y.; Wu, H.; Chen, L.; Su, S.; and Cao, Y. *Adv. Mater.* **2011**, 23, 4636-4643.

86. Kumar, A.; Lakhwani, G.; Elmalem, E.; Huck, W. T. S.; Rao, A.; Greenham, N. C.; Friend, R. H. *Energy Environ. Sci.* **2014**, *7*, 2227-2231.

87. Qi, B.; Zhang, Z.-G.; Wang, J. *Sci. Rep.* **2015**, *5*, 7803.

88. Lowe, A. B.; McCormick, C. L. *Chem. Rev.* **2002**, *102* (11), 4177-4189.

89. Li, H.; Xu, Y.; Hoven, C. V; Li, C.; Seo, J. H.; Bazan, G. C. *J. Am. Chem. Soc.* **2009**, *131*, 8903-8912.

90. Fang, J.; Wallikewitz, B. H.; Gao, F.; Tu, G.; Muller, C.; Pace, G.; Friend, R. H.; Huck, W. T. S. *J. Am. Chem. Soc*. **2011**, *133*, 683-685.

91. Nilsson, K. P. R.; Inganäs, O. *Nat. Mater*. **2003**, *2*, 419-424.

92. Karlsson, K. F. Asberg, P. Nilsson, K. P. R.; Inganas, O. *Chem. Mater.* **2005**, *17*, 4204-4211.

93. Andersson, M. Ekeblad, P. O. Hjertberg, T.; Wennerstrom, O. *Polym. Commun.* **1991**, *32*, 546–548.

94. Duan, C.; Wang, L.; Zhang, K.; Guan, X.; Huang, F. *Adv. Mater*. **2011**, *23*, 1665-1669.

95. Duan, C.; Zhang, K.; Guan, X.; Zhong, C.; Xie, H.; Huang, F.; Chen, J.; Peng, J.; Cao, Y. *Chem. Sci.* **2013**, *4* (3), 1298-1307.

96. Page, Z. A.; Duzhko, V. V.; Emrick, T. *Macromolecules* 2013, **46**, 344-351.

97. Page, Z. A.; Liu, F.; Russell, T. P.; Emrick, T. *Chem. Sci.* **2014**, *5*, 2368-2373.

98. Liu, F.; Page, Z. A.; Duzhko, V. V.; Russell, T. P.; Emrick, T. *Adv. Mater.* **2013**, *25*, 6868-6873.

99. Page, Z. A.; Liu, F.; Russell, T. P.; Emrick, T. *J. Polym. Sci., Part A Polym. Chem.* **2015**, *53* (2), 327-336.

100. Liu, Y.; Page, Z. A.; Russell, T. P.; Emrick, T. *Submitted*, **2015**.

101. Page, Z. A.; Liu, Y.; Duzhko, V. V.; Russell, T. P.; Emrick, T. *Science* **2014**, *346*, 441-444.

102. Page, Z. A.; Liu, Y.; Puodziukynaite, E.; Russell, T. P.; Emrick, T. *In preparaiton*, **2015**.

CHAPTER 2

THIOPHENE-BASED CONJUGATED POLYMER ZWITTERIONS

2.1 Introduction

Ultra-thin interlayers, placed between the active layer and conductive electrodes, have been shown to significantly improve the performance of organic photovoltaic devices (OPVs).[1-5] Often such interlayers are multifunctional materials that act as selective charge blocking layers,[1] or modify the work functions of electrodes to produce larger internal electric fields.[2,3] Inorganic materials, such as LiF, ZnO, TiO$_2$ and MoO$_x$, have been used extensively as interlayers, however organic/polymeric interlayers[6-9] offer better compatibility in device fabrication steps with facile room-temperature processing from solution, while allowing for synthetic tailoring of the materials. Additionally, organic/polymeric interlayers have been integrated into all-organic (flexible) devices [10] and permitted the use of high work function metals, such as Ag,[11,12] Au and Cu, which can benefit device stability.[13]

Conjugated polymer zwitterions (CPZs) comprise a class of organic polymer materials that combine neutral and hydrophilic side chains with electronically active backbones. They are attractive for achieving the beneficial properties of CPEs (water solubility; pendent dipoles) without the complications of counter ions (*e.g.* long turn-on times for LEDs).[14] However, only a few examples of CPZs have been reported (apart from pH sensitive derivatives such as amino acid substituted structures[15-17]). Synthetic routes reported to-date involve an organometallic catalyzed polymerization (*e.g.,* Suzuki or Stille coupling) in organic solvents, followed by post-polymerization modification to

introduce the pendent zwitterionic moieties.[14,18] As such, pendent group density along the polymer backbone depends on the efficiency of post-polymerization modification.

Polymer solubility in either the aqueous or organic phase of a polymerization reaction lends towards high molecular weight, and higher molecular weight polymers can improve film formation and charge mobility;[19] for example, higher molecular weight cathode buffer layers in OPVs afforded higher PCE values.[20] Providing a methodology for the synthesis of reasonably high molecular weight (> 10 kDa), polar conjugated polymers may prove beneficial for the production of new electronically active interlayer materials.

ILs are organic salts, typically considered as room temperature liquids or having melting points < 100 °C.[21] IL properties, such as high thermal stability, negligible vapor pressure, and the ability to solvate a wide variety of small molecules and polymers, make them "green" alternatives to volatile organic liquids.[22] ILs have been utilized as solvents for numerous reactions including organometallic-catalyzed couplings (where ILs have good compatibility with transition metal catalysts),[23,24] and polymerizations, such as,[25] free radical,[26,27] ring-opening[28] and cationic and anionic mechanisms.[29,30] Palladium catalyzed carbon-carbon bond forming reactions, such as Suzuki-Miyaura (SM) coupling, has been studied in the presence of ILs, specifically taking advantage of imidazolium salts[31] that serve as ligands following *N*-heterocyclic carbene formation, which resulted in improved catalytic activity.[32-37] A report by Zhang and coworkers utilized imidazolium ILs as solvents for the phosphine-free SM coupling to give biaryls (adding water to improve reactivity).[31] Thiophene,[38,39] pyrrole[39] and aniline[40-42] have been polymerized by oxidative or electrochemical methods in ILs, typically giving insoluble films or fibrils,

yet there is no prior report on SM polymerization in an IL medium. To this end, we chose to investigate ILs as solvents for SM polymerization of zwitterion substituted dihalides, to determine whether the polarity of ILs could enhance the polymerizations and produce higher molecular weight polymers to act as interlayers in OPVs and improve device performance.

Interlayers improve numerous metrics of OPVs, including open circuit voltage (V_{OC}), short circuit current density (J_{SC}), and fill factor (FF).[43] In BHJ OPVs, the value of V_{OC} equals the energy difference between the donor HOMO and acceptor LUMO;[44,45] minus the energy required for the formation of a charge transfer complex (CTC) state.[46] However, the difference in work function between the anode and cathode ($\delta\Phi_{AC}$) will dictate V_{OC} if it is smaller than this HOMO/LUMO energy difference in the active layer.[47,48] This difference also determines the strength of the internal electric field that affects charge extraction efficiency and associated losses from recombination and, as a result, J_{SC} and FF.[49]

The mechanisms invoked to explain the role of interlayers range from improved surface wettability and adhesion to morphological optimization and electronic structure modifications.[7] Specifically, formation of an interfacial dipole (Δ) at the interface of an organic active layer and metal electrode causes electrode work function modification, and has been identified as an integral feature of interlayers that leads to enhanced device performance.[13,43,50-52] Such electronic properties of interlayer materials are probed by ultraviolet photoelectron spectroscopy (UPS).[53,54] Vacuum level alignment at an organic-organic interface is likely to occur for an interfacial dipole moment induced by an organic interlayer (such as a CPE), resulting in a decreased injection barrier into the active

layer.[53,55] Thus, UPS probes the electronic properties of thin films on a metal substrate[53] to determine work function (*WF*), ionization potential (*I$_P$*) and vacuum energy (*E$_{vac}$*).[56] For example, Nguyen and coworkers used UPS to characterize anionic and cationic CPEs on gold, suggesting that the presence of an Δ leads to enhanced charge injection.[54,57]

This chapter describes the design and synthesis of novel thiophene-based CPZs with sulfobetaine (SB) pendant groups, in which the zwitterion is present on the monomer from the outset.[58] As such, the conditions described allow reliable polymerization of zwitterionic monomers that do not hinge on post-polymerization modification. Both homopolymers and copolymers were prepared, having shorter (methylene) and longer (tetramethylene) tethers between the polymer backbone and SB groups. In addition, an improved SM procedure to produce thiophene-based CPZs that takes advantage of ILs as reaction media is also detailed.[59] These novel synthetic polymers were characterized by solution and solid-state UV-Vis absorption spectroscopy, and by UPS as thin films on Ag and Au substrates. The integration of CPZs as interfacial modification layers into OPVs is also described, finding improved PCE of devices using Al as the cathode, and greatly improved devices when using more stable (higher work function) Ag as the cathode.[60] A systematic correlation was found between Δ and PCE, as a result of larger *V$_{OC}$*, *J$_{SC}$* and *FF* in the fabricated devices. Near edge x-ray absorption fine structure (NEXAFS) of the CPZs on the active layer revealed the orientation of the backbone and pendant dipoles at the active layer and air interface respectively. Moreover, a model of electrostatic self-alignment of dipoles at the metal surface is proposed to account for the interfacial dipoles observed.

2.2 Synthesis of thiophene-based CPZs

The novel CPZs shown in **Figure 2.1A** are composed of SB-substituted polythiophene (**PTSB-1**, **13**, and **PTSB-2**, **14**), and alternating thiophene-benzothiadiazole (**PTBTSB-1**, **15**, and **PTBTSB-2**, **16**) backbones, where **PTBTSB-1** and **PTBTSB-2** have $(CH_2)_x$ tether lengths of x = 1 and 4, respectively. The SB zwitterion was chosen for its pH insensitivity, and proved effective for solubilizing the conjugated polymers when placed on every second aromatic unit in the backbone. For comparison, alkyl-substituted analogues **POT-a-T** (**17**) and **POT-a-BT** (**18**) were also prepared (**Figure 2.1B**).
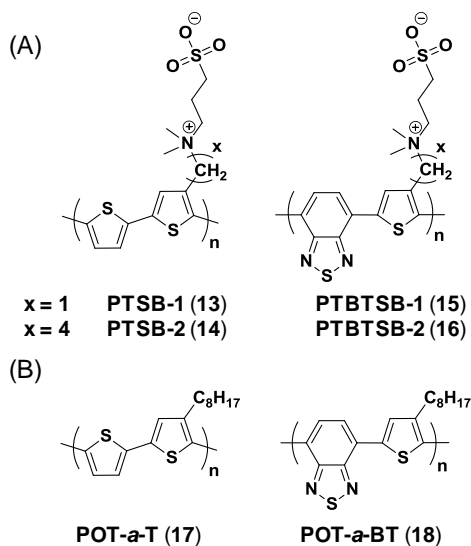
Figure 2.1 Structures of novel SB-substituted polymers: (A) polythiophene (PTSB) and poly(thiophene-benzothiadiazole) (PTBTSB) CPZs; and (B) alkyl-substituted analogues. Reproduced from reference 58.

The monomer syntheses, shown in **Scheme 2.1**, began with the ring-opening of 1,3-propanesultone[61] with dimethylaminothiophene **20** (prepared from tribromide **19** and dimethylamine under phase-transfer conditions in 82% yield). This gave monomer **21** as a white powder (HRFAB-MS: (m/z) [M+H]$^+$ calculated: 421.8918, found: 421.8898). A tetramethylene spacer was introduced by reacting alkyl-bromide **22** with dimethylamine

to give **23**, followed by ring-opening of 1,3-propanesultone in acetonitrile. Precipitation gave sulfobetaine-thiophene monomer **24** in 92% yield as a white crystalline solid (HRFAB-MS: (m/z) [M+H]$^+$ calculated: 461.9408, found: 461.9408).
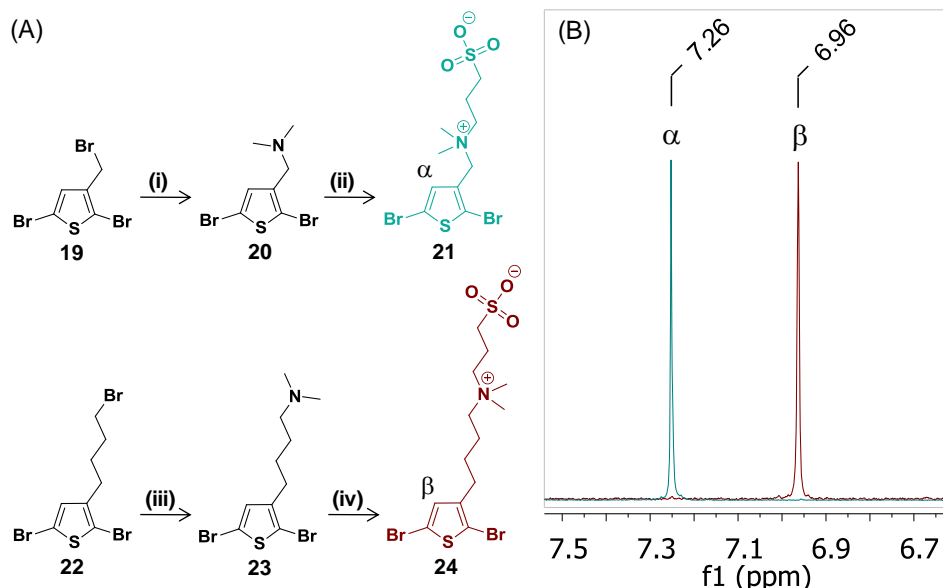
Scheme 2.1 (A) Synthesis of SB-substituted thiophene monomers **21** and **24**. Reagents and conditions: (i) Me$_2$NH, Bu$_4$NBr, CHCl$_3$:H$_2$O; (ii) 1,3-propanesultone, CH$_3$CN; (iii) Me$_2$NH, THF; (iv) 1,3-propanesultone, CH$_3$CN. (B) Partial ^{1}H-NMR spectra in D$_2$O showing thiophene protons (α in **21** and β in **24**). Reproduced from reference 58.

^{1}H NMR spectroscopy of monomers **21** and **24** in D$_2$O showed the influence of the proximity of the zwitterions to the thiophene ring. The 0.3 ppm downfield shift of the thiophene proton on **21** (7.26 ppm) relative to **24** (6.96 ppm) (**Scheme 2.1**) indicates an electron withdrawing effect of the SB group. As Grignard metathesis (GRIM) polymerization conditions are unsuitable for dibromothiophenes **21** and **24**, alternative polymerization methodologies were examined. Attempts to polymerize **21** by Yamamoto dehalogenative polycondensation with dicyclooctadiene nickel(0) in DMF afforded only oligomers. Thus, to accommodate the limited organic solubility of these zwitterionic monomers, we examined SM coupling of **21** with diboronic ester-thiophene **25** in a biphasic solvent system (**Scheme 2.2**). Dichloro[bis(triphenylphosphine)] palladium(II)

[Pd(PPh$_3$)$_2$Cl$_2$] successfully produced polymers with reasonably high molecular weights (ranging from 6 to 80 kDa) in ~24 hours, while other catalysts (e.g. tetrakis(triphenylphosphino) palladium(0) [Pd(PPh$_3$)$_4$], bis(tri-*o*-tolylphosphine) palladium(0) [Pd(P(*o*-tol)$_3$)$_2$] and palladium(II) acetate [Pd(OAc)$_2$]) were less effective. Addition of NaBr to the aqueous phase of the SM polycondensation was crucial for producing PTSB and PTBTSB, giving these polymers in greater than 70% isolated yield; the presence of salt in the reaction mixture enhances solubility of the growing polymers. The CPZs were purified thoroughly using sequential Soxhlet extraction with tetrahydrofuran, acetone, methanol (MeOH), and trifluoroethanol (TFE), followed by dialysis against pure water. MeOH extraction removed oligomers (< 3 kDa), and during the dialysis step the polymers precipitated, since their solubility in pure water is low (< 0.5 mg/mL at 22°C).
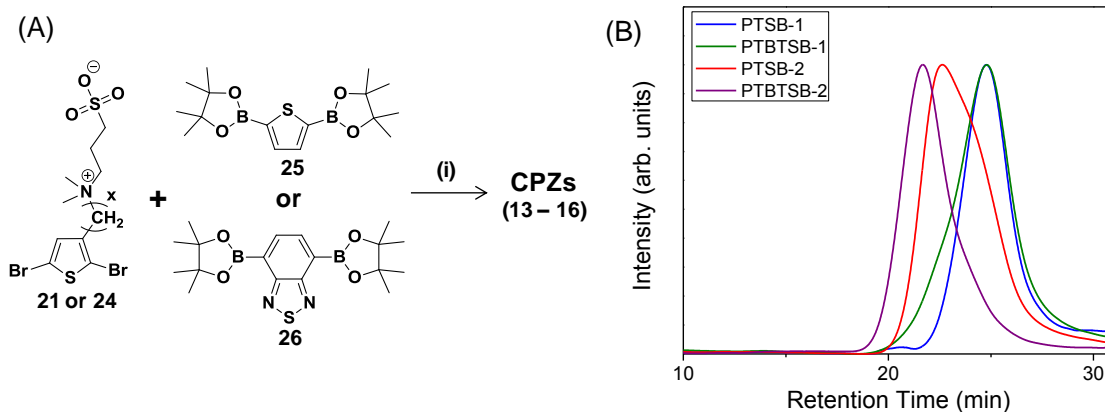
Scheme 2.2 (A) SM polycondensation of monomers **21**, **24**, **25** and **26**, yielding thiophene-based CPZs **13**, **14**, **15** and **16**. Reagents and conditions: (i) K$_2$CO$_3$, AQ336, Pd(PPh$_3$)$_2$Cl$_2$, toluene, water. (B) Representative GPC traces of CPZs to determine polymer molecular weight and Đ using water as eluent and poly(ethylene oxide) as standards.

PTSB-1 and **PTBTSB-1** obtained by SM polycondensation exhibited poor solubility in water, but excellent solubility in water containing small amounts of salt (~10 mg/mL in 0.5 M NaBr$_{aq}$). Such a pronounced effect of salt on polymer solubility is

known for other SB-containing polymers, such as poly(sulfobetaine methacrylate);[62] salt interrupts dipole-dipole pairing, an "anti-polyelectrolyte" characteristic.[63,64] The CPZs were soluble in a few organic solvents, in particular trifluoroethanol (TFE) and hexafluoroisopropanol (HFIP) (>20 mg/mL). Deuterated TFE was used for NMR characterization, noting broad signals centered at ~3 ppm and ~7 ppm representing methylene and methyl groups of the SB side chains and aromatic protons of the backbone respectively. Polymer molecular weights were estimated by aqueous size exclusion chromatography (SEC) relative to poly(ethylene oxide) (PEO) standards, to give values ranging from 6-15 kDa for **PTSB-1** and 7-10 kDa for **PTBTSB-1**. **PTSB-2** and **PTBTSB-2** were synthesized under similar SM conditions, with GPC estimated molecular weights of 6-22 and 47-80 kDa respectively, and disperisty (Đ) values of 1.7-2.6. The longer tether CPZs (**PTSB-2** and **PTBTSB-2**) were also subjected to SEC eluting in TFE (with 0.02 M silver trifluoroacetate, against PMMA calibration standards), which typically resulted in lower estimated molecular weights, ranging from ~10 to 40 kDa, which is likely due to enhanced solubility, reducing aggregation of CPZs in TFE relative to water.

2.3 Ionic liquids as polymerization media

The synthesis of **PTSB-1** (**Figure 2.2**) was chosen as a test case for polymerizations in ILs since the previously discussed methodology resulted in low molecular weight polymer (6-15 kDa).[58,60] **PTSB-1** was previously prepared from dibromide **21** with diboronic-ester **25** in a biphasic, toluene/water (2M NaBr, 2M K_2CO_3) reaction mixture, under an inert atmosphere with [Pd(PPh$_3$)$_2$Cl$_2$] as the catalyst and Aliquat 336 as the phase transfer catalyst (**Figure 2.2**).[58,60] The reaction terminated upon

precipitation of an orange polymer product at only 5 − 10 kDa (estimated by aqueous SEC).
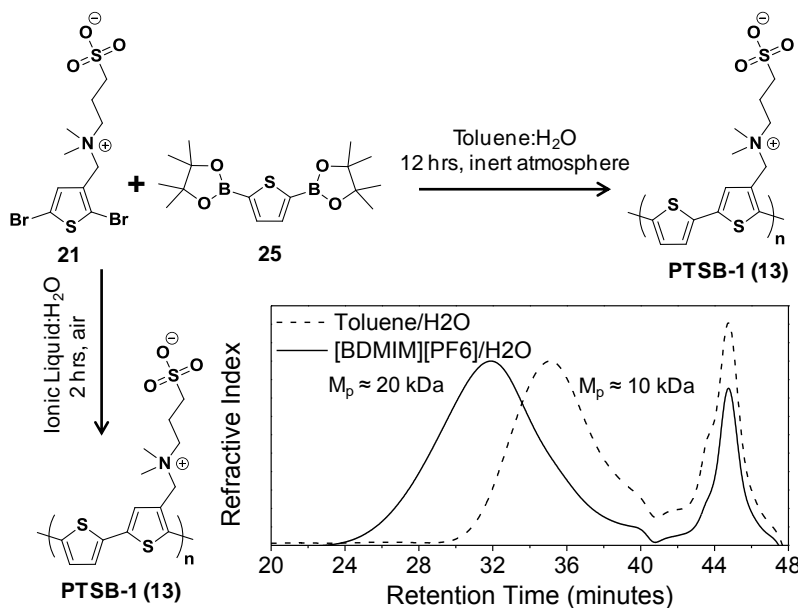
Figure 2.2 Synthesis of **PTSB-1** using SM polycondensation, and representative size exclusion chromatograms of polymers resulting from polymerization in ([BDMIM][PF$_6$])/H$_2$O and toluene/H$_2$O. Reproduced from reference 59.

Attempts to increase the molecular weight of **PTSB-1** by adjusting the oil-to-water ratio, temperature and concentration were unsuccessful. While TFE is an excellent solvent for zwitterioinc polymers, addition of TFE to any mixture containing palladium catalyst led to catalyst decomposition (immediate appearance of a black solution) and low monomer conversion (indicated by blue-green solution fluorescence). A broad-based solubility study of **PTSB-1** and selected CPZs revealed their solubility in a number of commercially available imidazolium salts. 1,2,3-Substituted imidazolium, pyridinium and pyrrolidinium ILs (**Figure 2.3**), were tested as solvents in the preparation of **PTSB-1** and **PTBTSB-2** (**Figure 2.1**). Selected counterions included hexafluorophosphate [PF$_6$], tetrafluoroborate [BF$_4$], triflate [OTf] and bis(trifluoromethansulfonamide) [NTf$_2$].

30
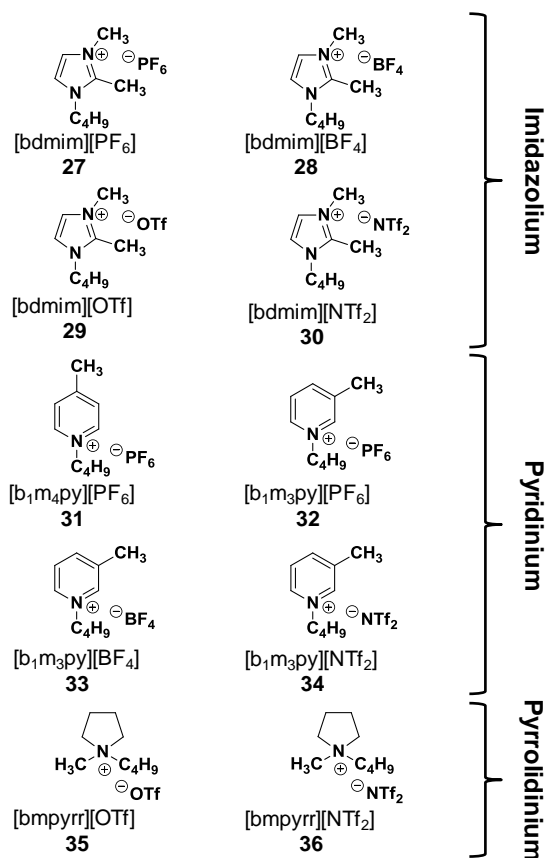
Figure 2.3 Chemical structure of ILs tested as co-solvents for SM polymerization. Reproduced from reference 59.

The reaction conditions were kept constant, using a 2.5:1 weight ratio of IL to 2M NaBr (aq) and 3 mole% Pd(OAc)$_2$ loading, stirring at 100 °C for 2 hours. Conveniently, using ILs precluded the need for inert conditions typically used in such metal-mediated polymerizations. All reactions in ILs were performed in air. However, some ILs proved unsuitable for polymerization of zwitterionic monomers. For example, reactions in 1-butyl-3-methylimidazolium hexafluorophosphate [bmim][PF$_6$] led to low conversion, likely due to deprotonation at the *2*-position of the ring, forming an *N*-heterocyclic carbene that can coordinate to palladium.[35,65]

In a typical polymerization, following two hours of stirring at 100 °C in the IL, the polymers were isolated by precipitation into MeOH, and purified by centrifugation

and trituration with MeOH. SEC, eluting in water (0.1 M NaNO$_3$, 0.02 wt % NaN$_3$) at 45

°C, provided an estimation of polymer molecular weight and Đ. Average polymer

molecular weights and molecular weight distributions resulting from the ILs tested are

given in **Table 2.1**.

Table 2.1 Average polymer molecular weights (kDa) and Đ's of **PTSB-1** determined
with aqueous SEC relative to PEO standards for polymerizations conducted in toluene
and ILs at 100 °C for two hours in air. Values represent averages from three
polymerizations. *Polymerizations in toluene were run for 12 hours in a nitrogen
atmosphere. Reproduced from reference 59.

		Imidazolium IL				Pyridinium IL				Pyrrolidinium IL	
	Toluene*	27	28	29	30	31	32	33	34	35	36
M$_n$	6.5	8.0	6.4	8.0	8.6	5.0	11.4	9.1	9.9	13.7	11.8
M$_p$	10.0	13.1	10.7	12.6	14.3	8.0	17.5	14.4	15.1	19.7	18.4
Đ	1.5	1.7	1.5	1.5	1.7	1.7	1.9	1.7	1.8	1.6	1.9

Purification by Soxhlet extraction using MeOH led to complete removal of

residual IL, confirmed by the lack of a signal by ^{19}F NMR (**Figure 2.4**). The polymers

were obtained as orange powders in 70-85% yield.
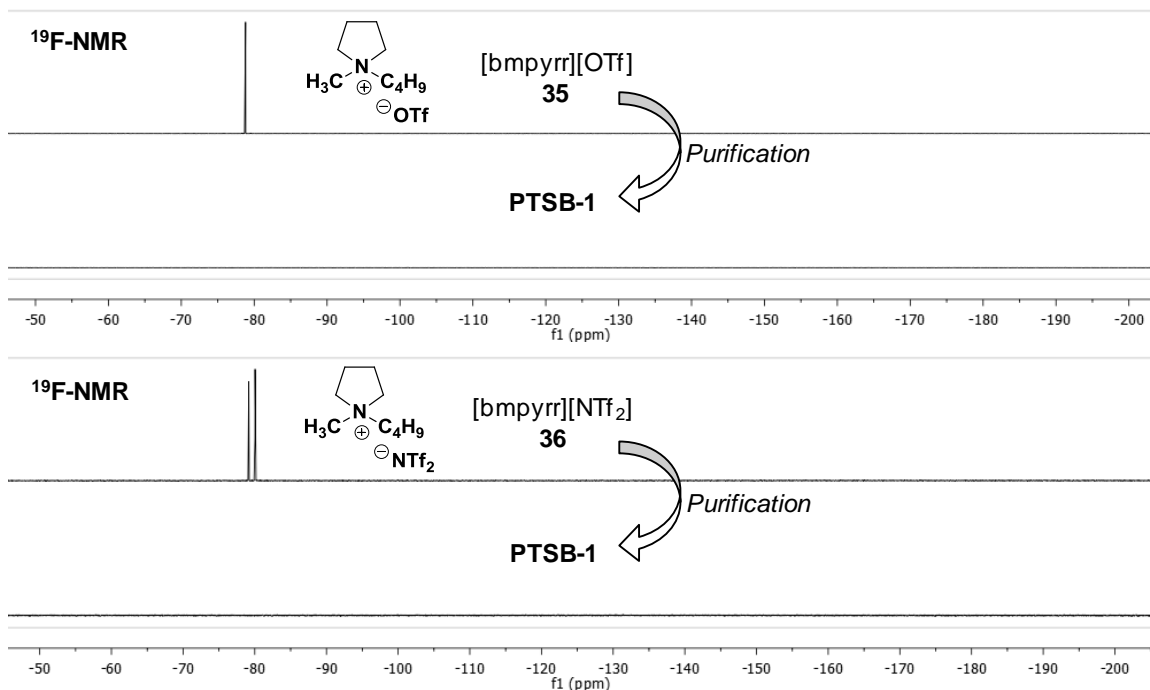
Figure 2.4 Representative ^{19}F-NMR spectra of ILs (top spectra) and of the polymers (corresponding bottom spectra) in D$_2$O containing 0.2 M NaCl. The absence of fluorine signal confirms IL removal following purification. Reproduced from reference 59.

The ILs discussed here containing either [PF$_6$] or [NTf$_2$] anions are not readily miscible with salt water (0.2 M NaCl), but do fully mix when heated (~40 °C), which was noticed when preparing ILs **27**, **30**, **31**, **32**, **34**, **36** for NMR analysis in D$_2$O (0.2 M NaCl). ILs containing [BF$_4$] and [OTf] (**28**, **29**, **33** and **35**) are fully miscible with salt water (0.2 M NaCl). **PTSB-1** has the greatest solubility in ILs containing [OTf] (**33** and **35**), as shown in the fluorescence images in **Figure 2.5**, where a substantial red-shift and attenuation (typical of aggregated semiconducting polymers) was noted for all the ILs except **29** and **35**. The high solubility of **PTSB-1** in **35** may have contributed to the higher molecular weight obtained when using it as a cosolvent compared to the other ILs. Higher molecular weight polymers typically form more uniform thin films, an important factor for consideration when using these materials as interlayers in optoelectronic applications.

33
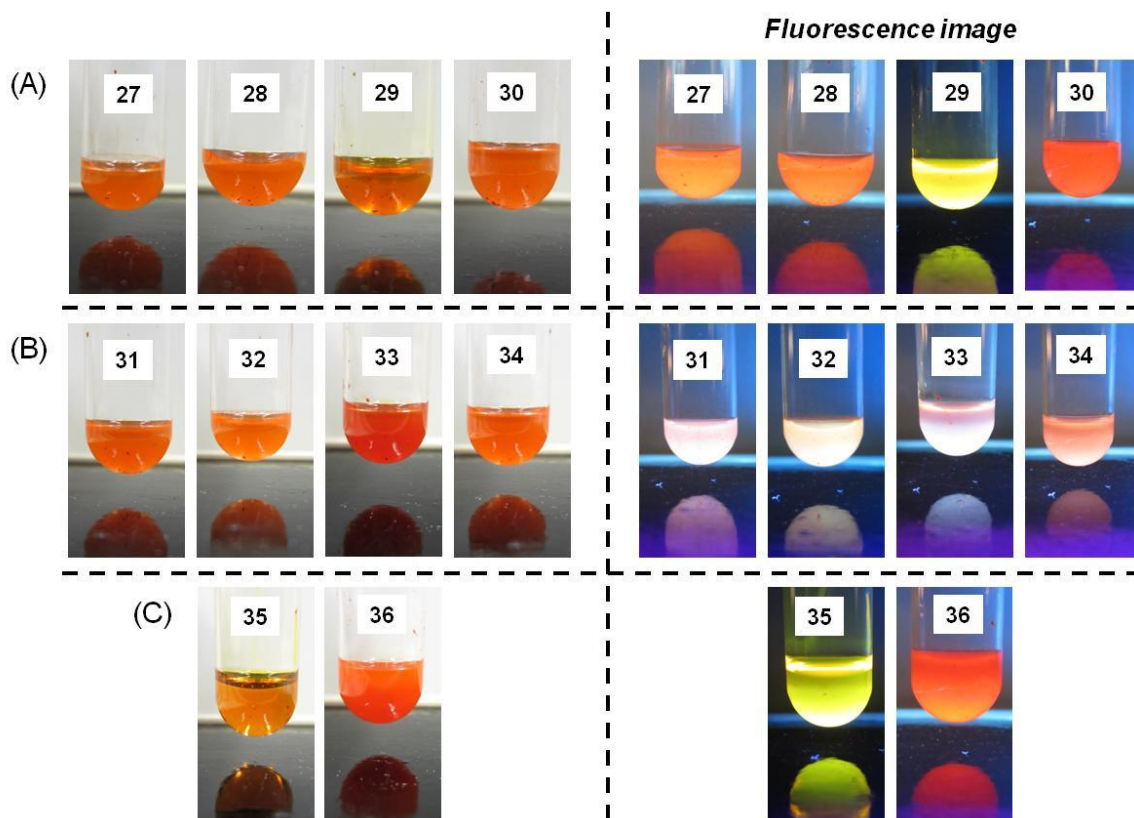
Figure 2.5 Non-UV-irradiated (left) and UV-irradiated (fluorescent) (right) images of a common, average molecular weight (~15 kDa) **PTSB-1** sample dissolved in the ten different ionic liquids; (A) Imidizolium; (B) pyridinium*; (C) pyrrolidinium. The polymer/IL mixture was heated at 100°C for 5 minutes prior to taking the pictures. *The fluorescent images of the pyrrolidinium's appear different from the imidizolium and pyrrolidinium due to the ILs weak blue fluorescence. Reproduced from reference 59.

CPZ formation in ILs was rapid; after only two hours, polymers were obtained with molecular weights on the order of, or higher than, those obtained using organic solvents at longer reaction times (12 hours). Allowing the reactions to proceed for a longer time (12 hours vs. 2 hours) in IL **27** resulted in higher molecular weight polymers, having twice the apex molecular weight ($M_p \approx 20$ kDa) relative to those typically obtained using toluene/H$_2$O mixtures ($M_p \approx 10$ kDa) (**Figure 2.2**) (M_P was chosen to remove variability associated with start and end retention times, or uneven baselines in the chromatograms). The increase in Ð, from 1.5 to 2.0, in going from toluene as solvent to IL as solvent, suggests that polymerization in the IL leads to full conversion, which

agrees with the higher yields typically obtained when using ILs (75-85% in ILs; 55-70% in toluene/H_2O).

M_p values greater than 10 kDa were obtained in all cases with the exception of IL **31** (**Figure 2.6**). We expect that both IL polarity and viscosity influence polymerization kinetics; however other factors such as IL-catalyst interactions should be considered. We note that IL polarity typically follows the trend (most polar to least polar) OTf > BF_4 > PF_6 > NTf_2 for the anions used and viscosity (most viscous to least viscous) PF_6 > BF_4 > OTf > NTf_2.[66-70] While a clear trend in IL properties vs. polymer molecular weight did not emerge, the solubility of CPZs increased with IL polarity, with the greatest solubility in ILs **29** and **35** (OTf anions) (**Figure 2.5**). However, we consistently found that the highest average molecular weight was obtained with **35**, [bmpyrr][OTf] (M_p = 19.7 kDa), which may be attributed to its low viscosity and high polarity relative to many of the other ILs.
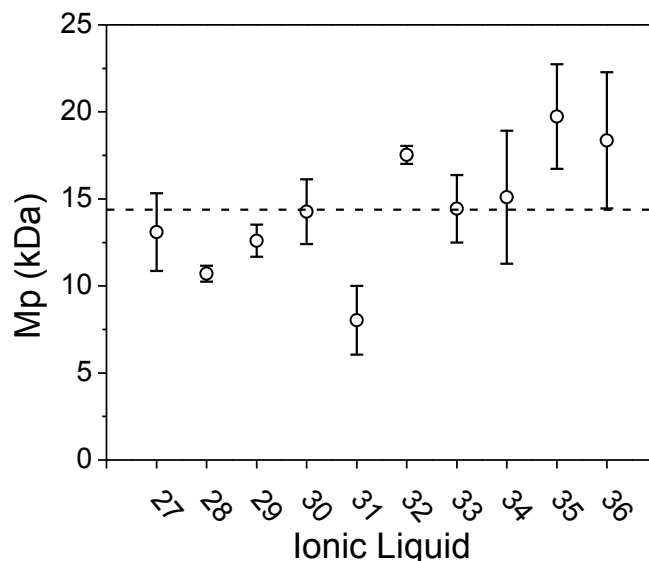
Figure 2.6 Peak-average molecular weight values of **PTSB-1** obtained from polymerizations conducted in different ILs (three reactions per IL) at 100 °C for two hours. Error bars represent ± standard deviation. Reproduced from reference 59.

A second CPZ, a benzothiadiazole-co-thiophene polymer, **PTBTSB-2** (**Scheme 2.2**), was synthesized to test the versatility of this SM polymerization in ILs to afford higher molecular weight, polar semiconducting polymers. The reaction mixtures were heated at 100 °C for 12 hours, where in both polymerizations containing either toluene or IL **35** led to polymer precipitation. The precipitate was washed with MeOH, and size exclusion chromatography in TFE (0.02 M sodium trifluoroacetate) revealed a peak average molecular weight of greater than 40 kDa for **PTBTSB-2** synthesized using IL **35**, while 28 kDa was the maximum molecular weight obtainable using toluene as the organic phase. Indeed, the polymerization kinetics of **PTBTSB-2** are very rapid, yielding polymer with molecular weight >20 kDa in minutes (**Figure 2.7**) and a steady increase in molecular weight up to two hours, beyond which the polymer does not appear to grow further. The kinetics clearly does not match typical step-growth polymerization. This may be expected given a change in reactivity of the active coupling site (aryl bromide and boronic ester) as the conjugation length changes during the course of polymerization of a semiconducting polymer. Additional factors, such as viscosity and rate of initial heating from room temperature to 100 °C are expected to play a vital role in the rate of polymerization.
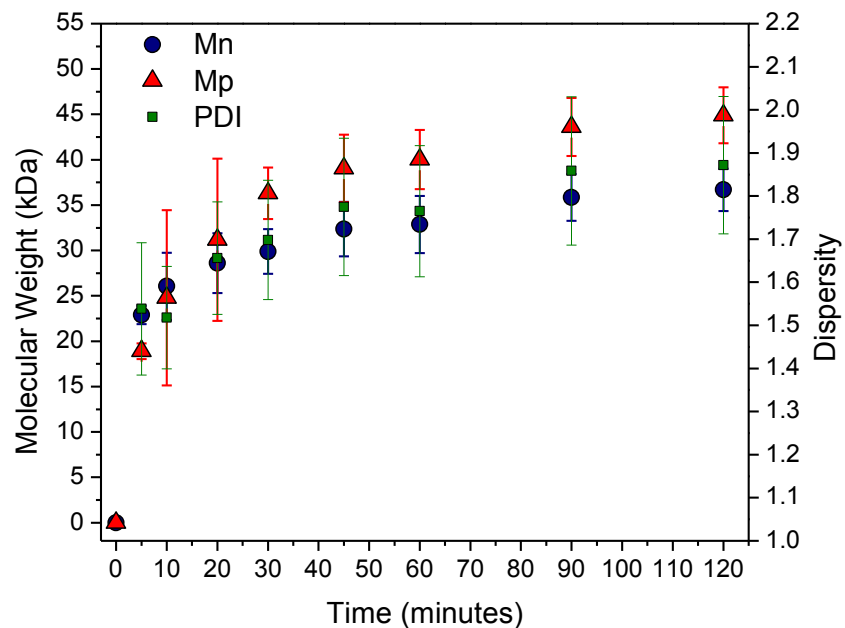
Figure 2.7 Polymerization of **PTBTSB-2** in IL **35**. Averages of the three reactions are given with error bars representing ± 1 standard deviation. Reproduced from reference 59.

2.4 Optoelectronic characterization

UV-Vis absorption spectroscopy was performed on the thiophene-based CPZs and compared with the analogous alkylated thiophene-based polymers, in solution and as thin films, as shown in **Figure 2.8**.
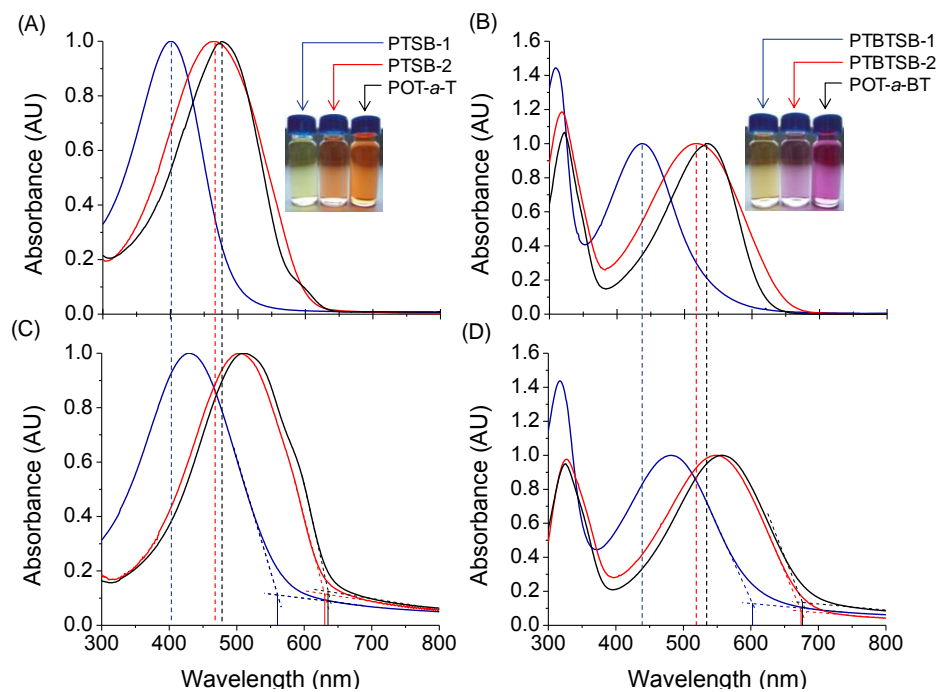
Figure 2.8 Comparison of solution (A,C) and solid state (B,D) absorption of CPZs and alkyl-substituted analogues. Spectra are normalized at (longer wavelength) absorption maxima. Insets: photograph of polymers in dilute solution (0.025 mg / mL in TFE for CPZs and in *o*DCB for alkylated counterparts). Reproduced from reference 58.

The UV-Vis absorption spectra of **Figure 2.8** illustrate the influence of the zwitterions on the polymer electronic properties. **PTSB-1** and **PTBTSB-1**, with short (methylene) spacers are blue shifted compared to **PTSB-2** and **PTBTSB-2**, which have the longer (tetramethylene) backbone-to-SB spacing. This is due to an electron withdrawing effect of the zwitterions that widens the polymer band gap.[71,72] Notably, the alkylated versions have similar absorption spectra to the long-tethered SB polymers. The polymer samples used to record these absorption spectra are all above their maximum conjugation length, such that the shifts seen are influenced solely by the pendent SB groups (**Figure 2.9**).
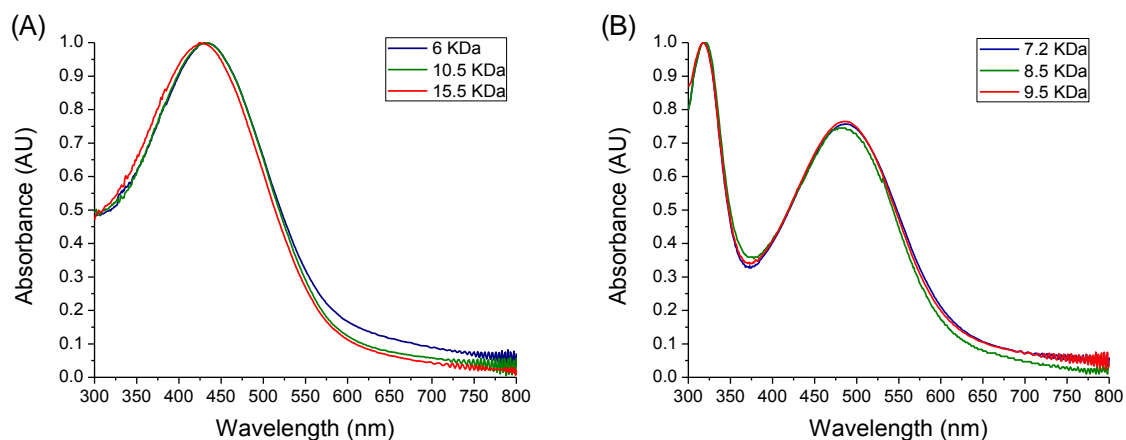
Figure 2.9 Thin film absorption of CPZs with three different number average molecular weights. (A) **PTSB-1**; (B) **PTBTSB-1**. Reproduced from reference 58.

For the alternating polymers, a leveling in the intensity of the two absorption bands, attributed to an intermediate band (**Figure 2.10**),[73] demonstrates color tunability based on SB-placement in the conjugated backbone.[74,75]
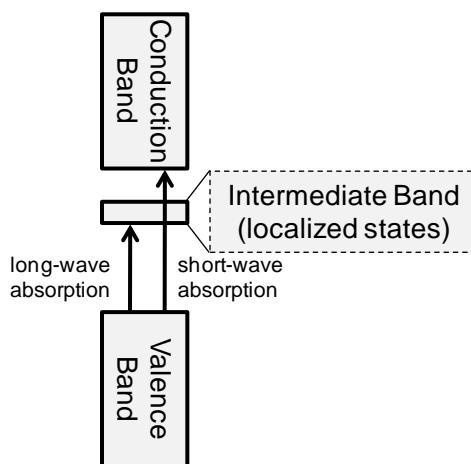
Figure 2.10 Depiction of energy bands giving rise to two peak absorption for donor-acceptor polymers **PTBTSB-1** and **PTBTSB-2**. Reproduced from reference 58.

The band gap energies (E_g) of the CPZs and their alkylated analogues (**Table 2.2**) were determined from the long-wavelength onset of absorption using the tangential lines indicated in **Figures 2.8B** and **D**. The nearly identical E_g values of **PTSB-2** and **POT-*a*-T** (1.96 and 1.94 eV respectively) and **PTBTSB-2** and **POT-*a*-BT** (1.83 and 1.82 eV

respectively) indicated that the effect of the zwitterions is removed upon separation from the backbone with a tetramethylene tether.

UPS was utilized to characterize the intrinsic electronic characteristics in thin films of the polymers and polymer-metal interfaces. **Figure 2.11A** shows representative UPS spectra of **PTBTSB-1** on a Au surface (upper left pane) and of Au itself (lower left pane).[76] The onset at higher binding energy - a secondary electron cutoff (E_{SEC}) - corresponds to a photoexcitation of electrons energy of 21.2 eV from the deep occupied electronic states to the vacuum level (E_{vac}), where both the binding and kinetic energies of electrons are zero on an absolute energy scale. The position of E_{vac} for a given material (relative to the energy scale of the instrument) is determined from the UPS spectrum using equation 2.1.

$$E_{vac} = E_{SEC} - 21.2 \ eV \qquad\qquad 2.1$$

The lower binding energy onset corresponds to a Fermi level (E_F) for metals and a HOMO energy level for semiconductors, and their separation from the vacuum level is equal to the work function (WF) of a metal or to the ionization potential (I_P) of a semiconductor respectively (equation 2.2).

$$I_P = h\nu - (E_{SEC} - HOMO) \qquad\qquad 2.2$$

Combining I_P and E_g gives the electron affinity (E_A) and thus LUMO energy. The offset of vacuum levels at the semiconductor/metal interface is the interfacial dipole energy (Δ),[77,78] calculated as the difference in measured E_{SEC} values of the coated and uncoated metals (Δ = -1.29 eV as shown in **Figure 2.11A**). **Figure 2.11B** shows the energy band diagram of a metal-semiconductor interface, and summarizes the energy characteristics that describe the interface, as determined by UPS and UV-Vis. The energy

barriers for electron and hole injection from the metal electrode into a semiconductor LUMO and HOMO are denoted $\Phi_{electron}$ and Φ_{hole} respectively.
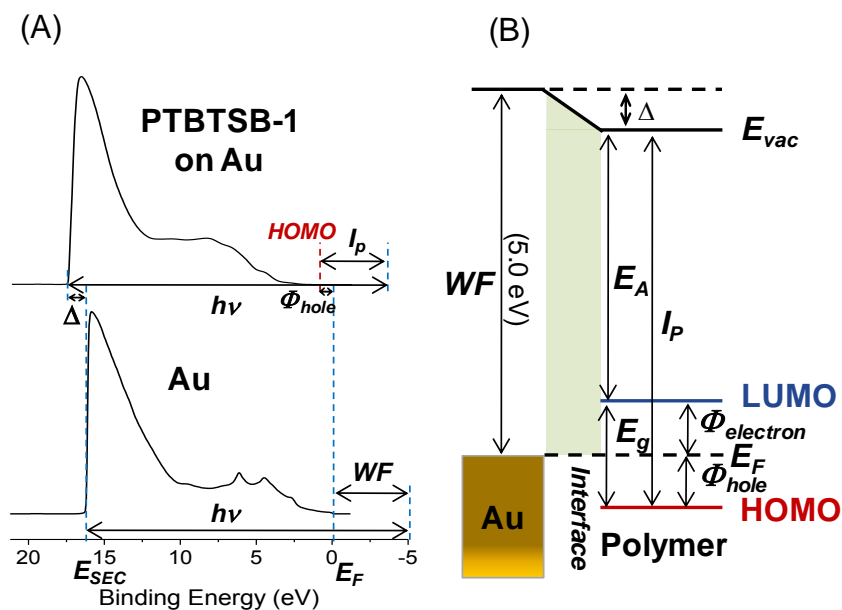
Figure 2.11 Schematic representation of electronic energy levels at the polymer-metal interface characterized by UPS: (A) Overlay of UPS spectra of **PTBTSB-1** on gold (top) and bare gold (bottom); (B) Diagram showing the effect of interfacial dipole, Δ, on vacuum and other energy level alignment. The values of E_g (E_A and LUMO) were determined by UV-Vis spectroscopy. Reproduced from reference 58.

Representative UPS spectra of CPZs on Au and Ag substrates are shown in **Figure 2.12**. The intrinsic properties of organic materials and metal substrates, I_P and E_F respectively, as well as the characteristics of an interfacial energy level alignment, Δ and Φ_{hole}, were extracted from these spectra. Additionally, using the E_g values, E_A and $\Phi_{electron}$ were calculated. These are summarized in **Table 2.2**.

41
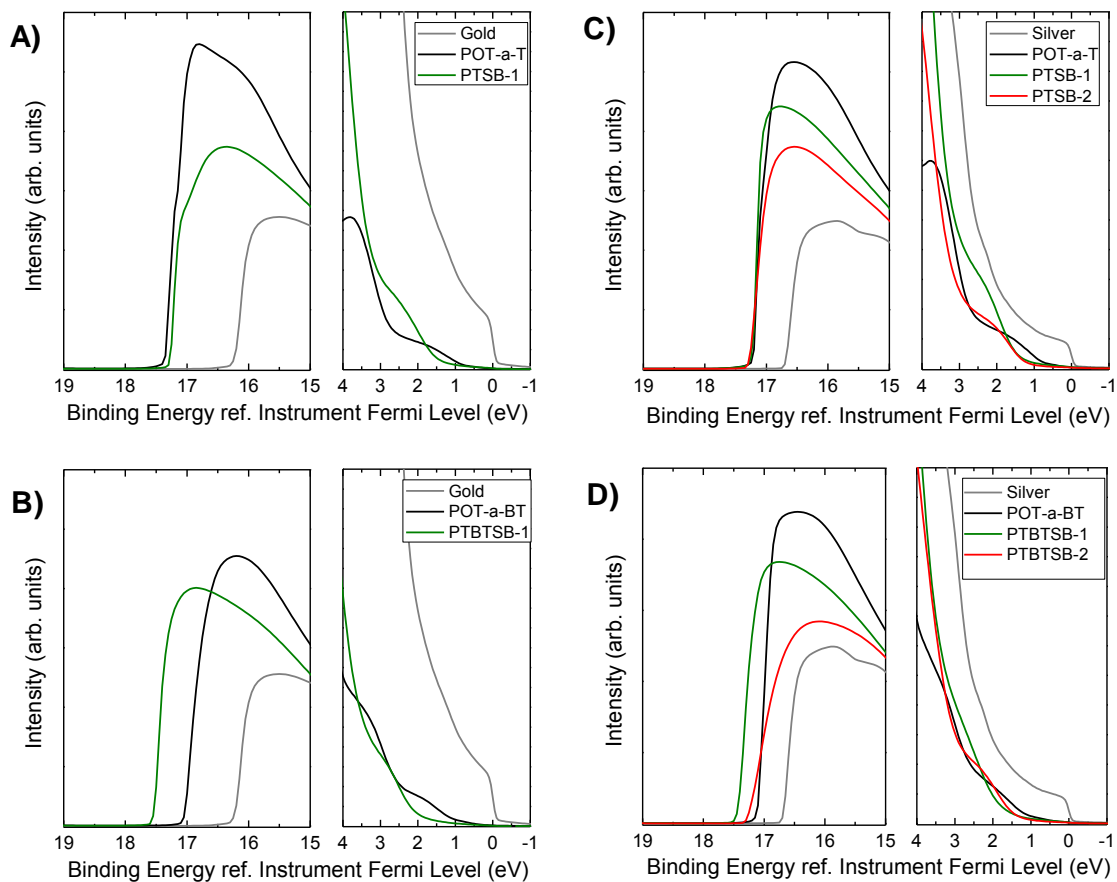
Figure 2.12 Representative UPS spectra. (A) **POT-*a*-T** and **PTSB-1** on Au; (B) **POT-*a*-BT** and **PTBTSB-1** on Au; (C) **POT-*a*-T**, **PTSB-1** and **PTSB-2** on Ag; (D) **POT-*a*-BT**, **PTBTSB-1** and **PTBTSB-2** on Ag. Left and right panes of each figure show the energy range near the E_{SEC} and Fermi/HOMO energy level, respectively. Reproduced from reference 58.

Table 2.2 Summary of electronic energy levels of CPZs and alkylated analogues and their interfaces with Au and Ag determined by UPS and UV-Vis absorption. Electron and hole injection barriers are $\Phi_{electron}$ and Φ_{hole} respectively, I_P denotes ionization potential and E_A denotes electron affinity. All values are given in eV. Reproduced from reference 58.

Substrate	Polymer	E_g	Φ_{hole}	$\Phi_{electron}$	I_P	E_A	Δ
Gold	**POT-*a*-T**	1.94	0.65	1.29	4.59	2.65	-1.02 ± 0.10
	PTSB-1	2.19	1.41	0.78	5.46	3.27	-0.96 ± 0.11
	POT-*a*-BT	1.82	0.84	0.98	5.03	3.21	-0.78 ± 0.07
	PTBTSB-1	2.04	1.95	0.09	5.69	3.65	-1.29 ± 0.04
Silver	**POT-*a*-T**	1.94	0.59	1.35	4.63	2.69	-0.48 ± 0.07
	PTSB-1	2.19	1.55	0.64	5.46	3.27	-0.61 ± 0.03
	PTSB-2	1.96	1.36	0.60	5.09	3.13	-0.79 ± 0.02
	POT-a-BT	1.82	0.92	0.90	5.08	3.26	-0.37 ± 0.08
	PTBTSB-1	2.04	2.01	0.03	5.69	3.65	-0.84 ± 0.09
	PTBTSB-2	1.83	1.68	0.15	5.24	3.41	-0.96 ± 0.05

The difference in E_g between the CPZs and alkyl-counterparts are attributed to the proximity of the quaternary ammonium to the polymer backbone, withdrawing electron density and increasing I_P by lowering the HOMO level. UV-Vis absorption and UPS measurements of **PTSB-2** and **PTBTSB-2** on Ag probe this further. CPZs with SB chains separated by one methylene group had a larger I_P than CPZs with SB chains separated by four methylene groups, as shown in **Figure 2.13**. In addition, the band gaps of **PTSB-1** and **PTBTSB-1** are larger than **PTSB-2** and **PTBTSB-2**, respectively, due to their deeper HOMO levels consistent with electron withdrawal by the SB side-chains. It is uncertain why both E_A and I_P are significantly larger for the CPZs than their alkyl-substituted analogues. We speculate that this originates from inserting the conjugated backbones into a medium with a larger dielectric constant, *i.e.* a network of dipolar side chains.
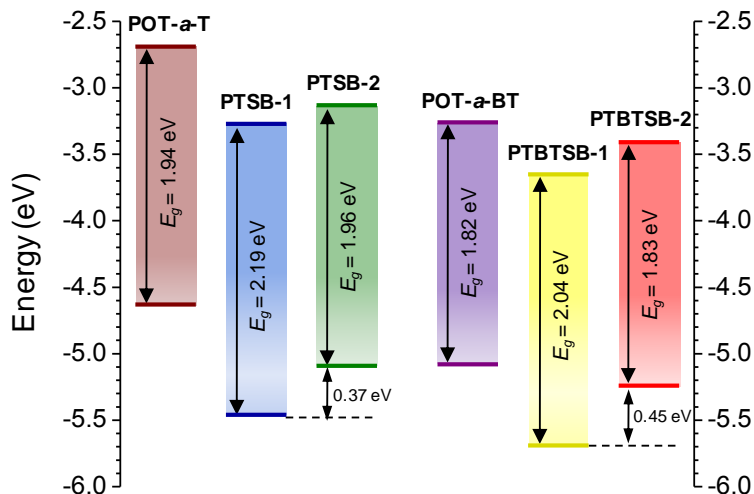
Figure 2.13 I_p (bottom bands), E_A (top bands) and E_g values of CPZs and alkylated polymers, plotted with reference to a common vacuum level.

Figure 2.14 shows the energy band diagrams of CPZs and their alkyl-substituted counterparts on gold and silver surfaces. Notably, the alkyl-substituted polymers were found to have significant interfacial dipoles: 1.02 eV and 0.48 eV for **POT-a-T** on Au and Ag, respectively; and 0.78 eV and 0.37 eV for **POT-a-BT** on Au and Ag,

respectively. The values for **POT-a-T** are similar to those reported for P3HT, which induces larger dipoles than other conjugated polymers.[79,80] Although UV-Vis spectra in solution and solid-state are quite similar for alkylated polymers **POT-*a*-T** and **POT-*a*-BT**, and zwitterionic **PTSB-2** and **PTBTSB-2**, UPS characterization reveals significant electronic differences, as **PTSB-2** and **PTBTSB-2** on Ag have larger interface dipoles (0.79 eV and 0.96 eV, respectively), relative to **POT-*a*-T** (0.48 eV) and **POT-*a*-BT** (0.37 eV). We suggest that this increase arises from a preferential macroscopic alignment of dipolar side chains, with negative charges directed towards the metal surface.

For applications where a conjugated polymer serves as the active layer at the interface with a metal cathode, a small $\Phi_{electron}$ is favorable for efficient device performance. **Figure 2.14** shows all the metal-CPZ interfaces to be characterized by significantly reduced $\Phi_{electron}$, relative to their alkylated analogues. Most notably was a decrease from 0.90 eV for **POT-*a*-BT** to 0.03 eV for **PTBTSB-1** on Ag. This effect comes partially from the increased dipole moments and partially from the increased ionization potentials (except for **PTSB-1** and **PTSB-2** on Ag where only the latter effect applies). For applications of CPZs as interlayers, the magnitude of injection barriers between the metal electrodes and the active layers are important. The Δ introduced by CPZ interlayers is expected to reduce the $\Phi_{electron}$ between the cathode and an additional organic active layer in a device.[53,55]

44
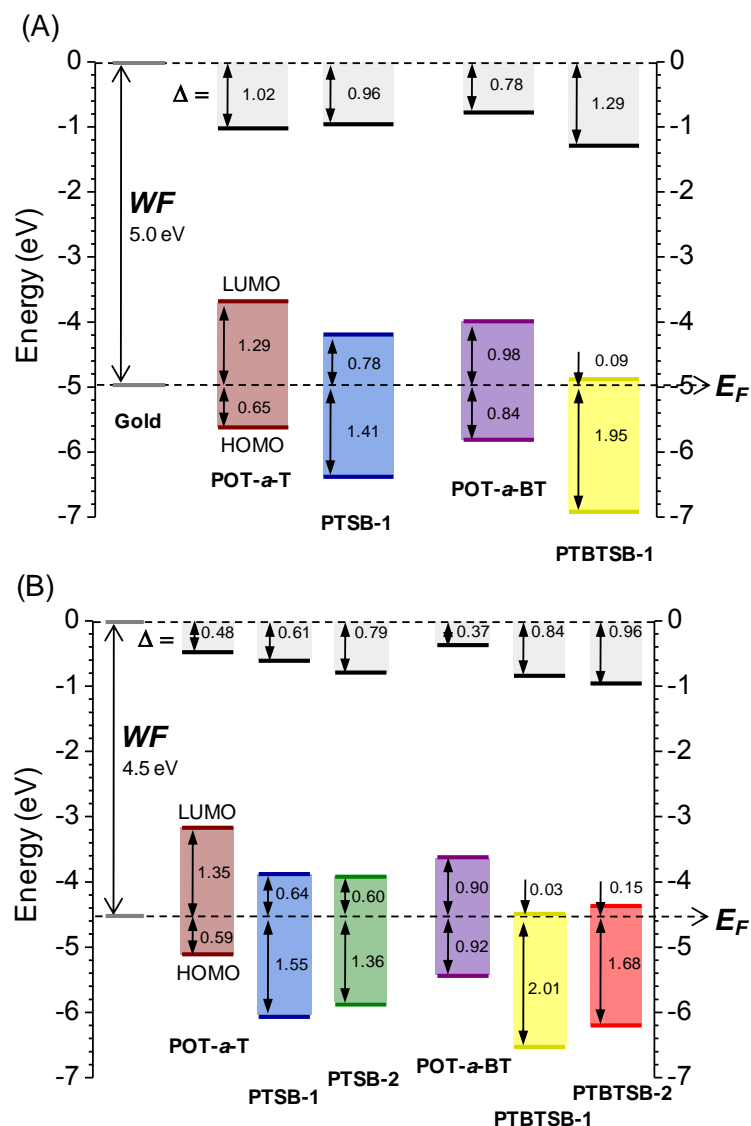
Figure 2.14 Energy band diagrams of CPZ-coated Au (A) and Ag (B). All materials share a common Fermi level (E_F). The interfacial dipole (Δ), electron ($\Phi_{electron}$) and hole (Φ_{hole}) injection barriers are specified.

2.5 Solar cell device integration

The chemical structures of the organic compounds that were used in PSC device fabrication, both thiophene-based CPZs as interlayers and PTB7 (**37**) and PC$_{71}$BM (**38**) as an active layer blend, are shown in **Figure 2.15**. While the solubility properties of CPZs are interesting (low solubility in pure water, high solubility in salt water), the key to solar cell fabrication is their orthogonal solubility with the active layer. The CPZs were

deposited from TFE,[62] enabling a simple deposition on the active layer (which is insoluble in TFE). The low solubility of CPZs in pure water relative to more hydrophilic interlayers stands to reduce problems connected to absorbing ambient moisture, a potential advantage since water uptake is prominent among device degradation problems facing OPVs.[81]
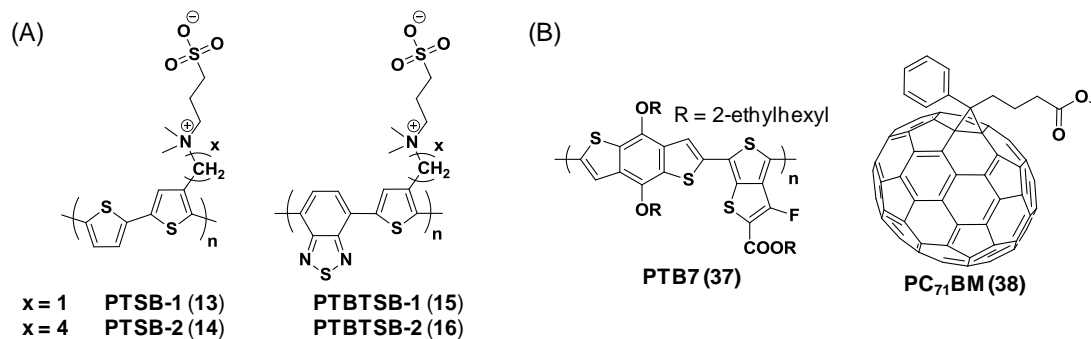
Figure 2.15 Chemical structures of (A) CPZ used as interlayers in solar cell fabrication; (B) the active layer components employed: electron donor **37** (PTB7) and acceptor **38** (PC$_{71}$BM) materials. Reproduced from reference 60.

Figure 2.16 shows the PSC device architecture and resulting effects of CPZ interlayers (5-nm thick film of **PTSB-1**, **PTSB-2**, **PTBTSB-1**, or **PTBTSB-2**) that were placed between the PTB7:PC$_{71}$BM active layer and Ag cathode. As compared to OPVs with a bare Ag cathode, all of the CPZs significantly improved device performance, with the largest effect observed with **PTBTSB-2**. A strong dependence of device performance on interlayer thickness was observed as shown for the **PTBTSB-2** interlayer in **Figure 2.16C. PTBTSB-2** also improves the performance of devices with Al cathodes (**Figure 2.16D**). However, this improvement is modest, since Al-cathode devices can achieve relatively high efficiency without an interlayer.
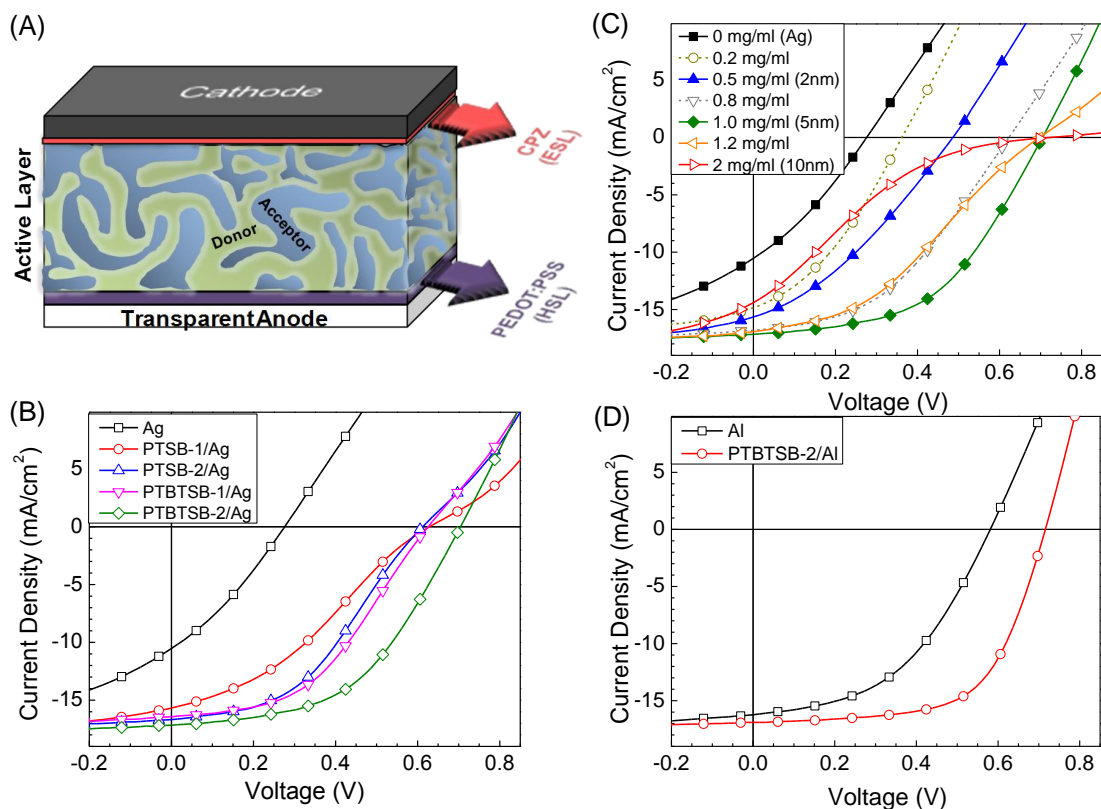
Figure 2.16 (A) Device architecture, with CPZ as the electron selective layer (ESL) and PEDOT:PSS as the hole selective layer (HSL). (B) J-V characteristics of OPVs with a bare Ag cathode and with 5 nm-thick interlayers (**PTSB-1**, **PTSB-2**, **PTBTSB-1** or **PTBTSB-2**) between the PTB7:PC$_{71}$BM active layer and Ag cathode; (C) Representative J-V curves showing the effect of CPZ coating concentration and resulting thicknesses using **PTBTSB-2**. (D) J-V characteristics of the devices with Al cathode: with and without the 5 nm-thick **PTBTSB-2** interlayer. Reproduced from reference 60.

An advantage of the CPZ design is their ability to produce large interfacial dipoles with metal electrodes.[58] We rationalized that CPZs would improve the performance of OPVs having a Ag cathode, an attractive design given the relative stability of Ag and its availability as an easily processed paste.[11,12] As the PTB7:PC$_{71}$BM active layer achieves high levels of efficiency with a modified Al cathode,[82] we examined the performance of CPZ interlayers with Al cathode. **Figure 2.17** shows the performance of a series of devices, testing four CPZ interlayers on Ag (**Figure 2.17**, left panels), **PTBTSB-2** interlayers on Al (**Figure 2.17**, right panels), and control devices with no

interlayer. Relative to devices with Ag and no interlayer (**Figure 2.17A**, left panel), devices with interlayers displayed higher V_{OC} values (increasing from 0.3 V to 0.7 V). J_{SC} (**Figure 2.17B**, left panel) and *FF* (**Figure 2.17C**, left panel) depend strongly on the choice of interlayer CPZ: CPZs with longer alkyl spacers (**PTSB-2** and **PTBTSB-2**) outperformed those with the shorter spacers (**PTSB-1** and **PTBTSB-1**). Moreover, the alternating thiophene-benzothiadiazole polymers (**PTBTSB-1** and **PTBTSB-2**) gave higher PCEs higher than the thiophene versions (**PTSB-1** and **PTSB-2**) following the order **PTSB-1** < **PTSB-2** < **PTBTSB-1** < **PTBTSB-2**. The best performing interlayer, **PTBTSB-2** on Ag, enhanced the PCE from 0.92 % to 5.78 %. This result was not simply due to effects from the solvent alone.[83-86] Control devices prepared by spin-coating of TFE (no CPZ) onto the active layer prior to Ag deposition gave little enhancement in PCE (0.92 % to 1.23 %).
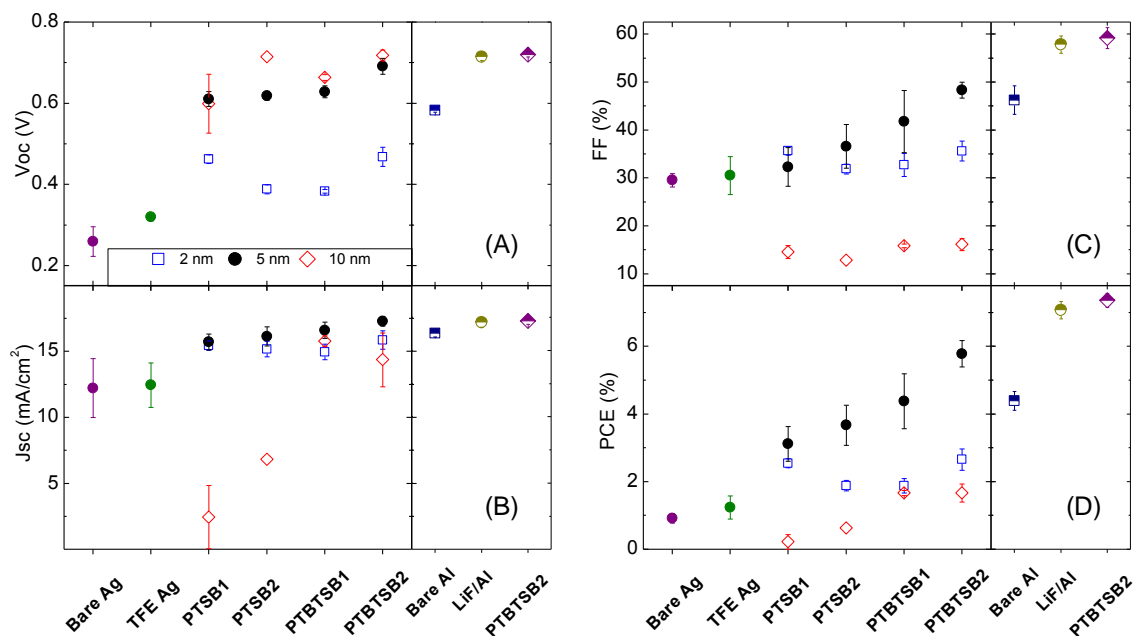
Figure 2.17 Summary of device performance with Ag- (left panels) and Al- (right panels) cathodes, with or without 2 nm, 5 nm or 10 nm thick CPZ interlayers: (A) open-circuit voltage (V_{OC}); (B) short-circuit current density (J_{SC}); (C) fill factor (*FF*); and (D) power conversion efficiency (PCE). The LiF/Al cathode is shown for reference. Reproduced from reference 60.

The thickness of these CPZ interlayers is critical for devices having a Ag cathode (**Figure 2.16B** and **Figure 2.17**, left panels), with ~5 nm thick films producing the largest PCEs (**Figure 2.17D**) in all cases, with the highest PCE of 6.36 % being obtained for **PTBTSB-2**/Ag) (**Figure 2.18**).
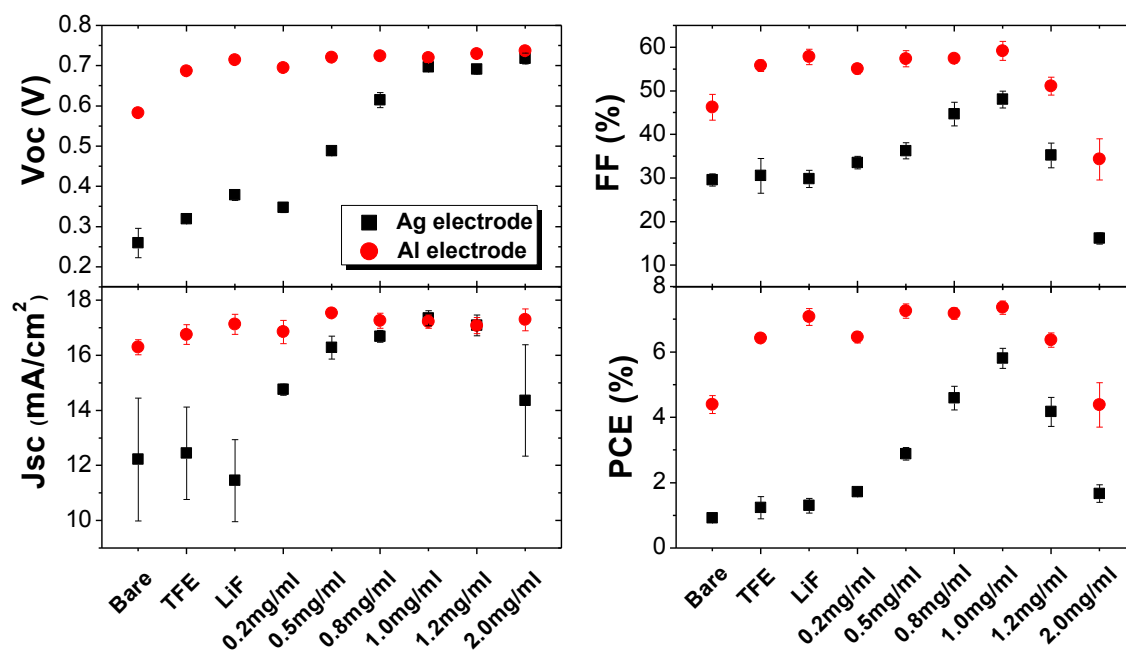
Figure 2.18 Device characteristics as a function of **PTBTSB-2** interlayer thickness for Ag and Al cathodes. The device performance peaks at 5 nm thickness for Ag cathode devices, and saturates for Al cathode devices. Reproduced from reference 60.

With thinner CPZ interlayers (~2 nm), no significant increase of V_{OC} was found, remaining near the level of bare Ag. This might arise from a non-uniform coverage of CPZ on the active layer, as evidenced by atomic force microscopy (AFM) and water contact angle measurements (**Figure 2.19**), which would expose the BHJ to the cathode.
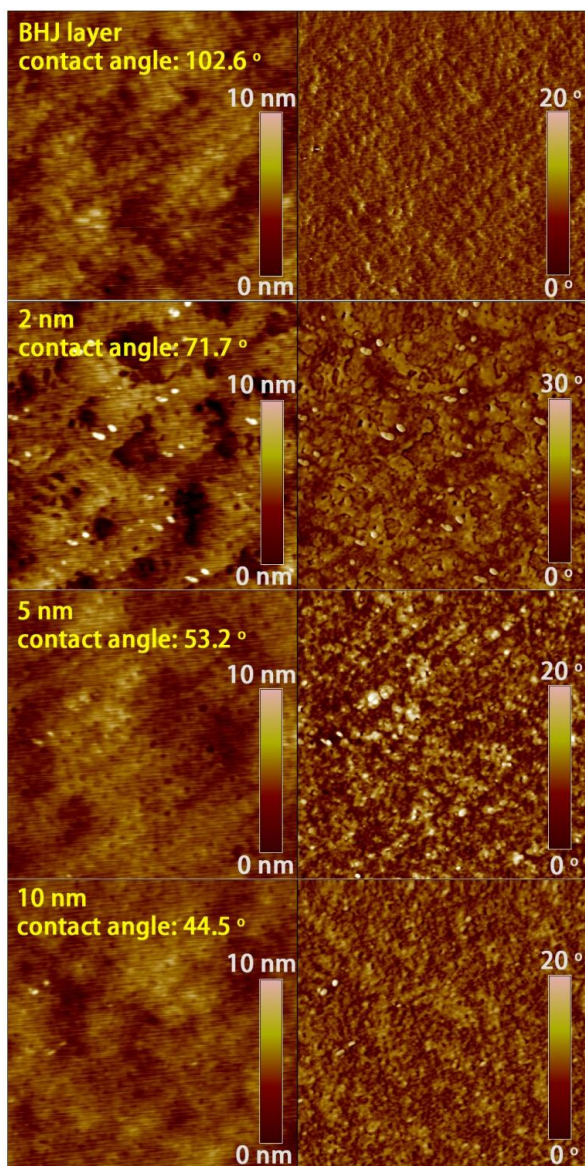
Figure 2.19 A comparison of AFM images, 2 μm x 2 μm images, (left column: height-image; right-column: phase-image) of PTB7:PC71BM active layer and a 2, 5, 10 nm-thick CPZ interlayer spin-coated onto the active layer, showing a discontinuous coverage of the CPZ interlayer for 2 nm thick films. The contact angle measurement, indicated in the AFM image, also confirms the coverage trend. Reproduced from reference 60.

With thicker CPZ interlayers (~10 nm), *FF* was reduced by 15% or more, due to the "S-shape" of the resultant J-V curve (**Figure 2.16B**). This may arise from a charge extraction imbalance, due to unbalanced mobilities between the donor and acceptor components,[87] inefficient surface recombination at the electrode,[88] or poor charge

transport[89] properties of the CPZ. The Al-cathode devices were more efficient than those with Ag-cathodes (**Figure 2.17**, right panels), yielding an average PCE of 4.49% (without an interlayer). This is in agreement with the importance of a larger $\delta\Phi_{AC}$ for different cathode materials ($\Phi_{Al} \approx 4.25$ eV vs. $\Phi_{Ag} \approx 4.5$ eV with reference to $\Phi_{PEDOT:PSS} \approx 5.4$ eV) to improve device characteristics. In this case, simply treating the active layer with TFE (no dissolved CPZ) resulted in further improvement of PCE up to 6.42%, while devices having a LiF interlayer yielded a PCE of 7.07%. In comparison to LiF, any CPZ interlayer led to comparable or slightly better device performance, with the best performing **PTBTSB-2** interlayer, at 5 nm thickness, giving an average PCE of 7.36% (best PCE of 7.74%) (**Figure 2.17**, right panels and **Figure 2.18**). The Ag-based devices depended systematically on choice of CPZ, whereas the CPZ interlayers in Al-containing solar cells affected little change in device performance, consistent with the lower Φ_{Al} (*i.e.* requiring a smaller Δ for efficient device operation).

UPS was used to determine the I_P of PTB7 and PC$_{71}$BM individually as thin films (~20 − 30 nm) on PEDOT:PSS cast onto clean ITO-coated glass substrates. For PTB7, the LUMO energy was calculated from a combination of the optical E_g, determined from the UV-Vis absorption onset, and I_P from UPS (**Figure 2.20A and B**). The LUMO energy of PC$_{71}$BM was directly measured by cyclic voltammetery (CV) (**Figure 2.20C**), taking the reduction onset relative to ferrocene oxidation onset, and the E_g was calculated from the difference between LUMO and HOMO (calculated from I_P).
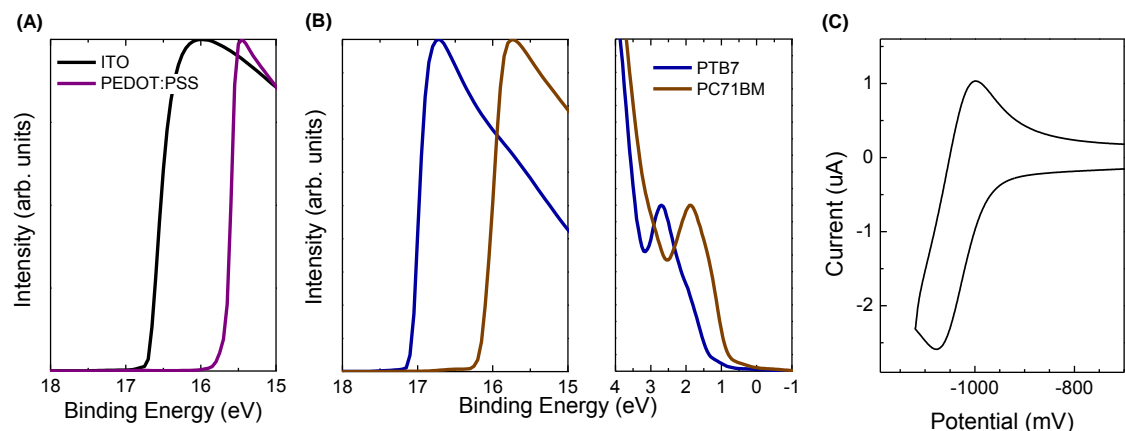
Figure 2.20 Energy level determination of various device components. (A) Normalized UPS spectrum showing the high binding energy region for ITO and PEDOT:PSS, where E_{SEC} was used to determine E_F of ITO and PEDOT:PSS (4.55 eV and 5.42 eV respectively) and Δ between them (0.87 eV). (B) Normalized high and low binding energy regions of UPS spectra used to determine HOMO levels for PTB7 and PC$_{71}$BM (5.33 eV and 5.87 eV respectively). (C) CV of PC$_{71}$BM, corrected against a ferrocene standard. Reduction onset used to determine LUMO level of PC$_{71}$BM (-3.83 eV). Reproduced from reference 60.

The magnitude of Δ, measured by UPS for the CPZs in contact with Ag, provided a direct correlation to device performance (**Figure 2.21**), where **PTSB-1** had the smallest Δ value (-0.61 eV) and lowest PCE (3.12 ± 0.51%) and **PTBTSB-2** had the largest Δ value (-0.96 eV) and highest PCE (5.78 ± 0.39%).
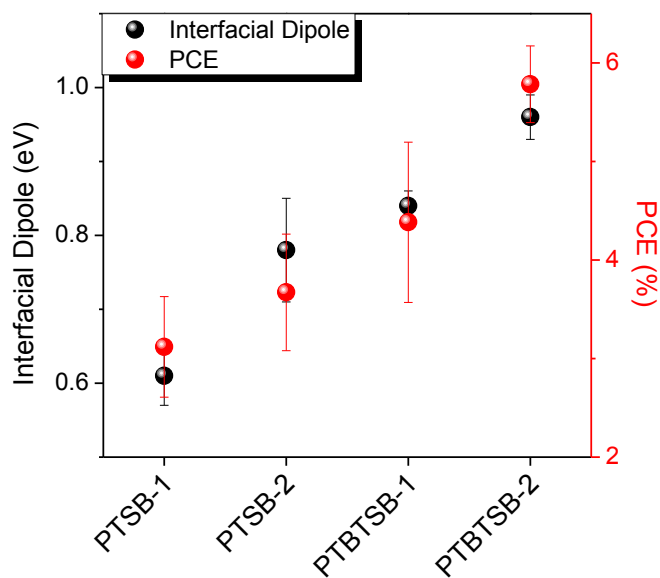
Figure 2.21 Correlation between Δ and PCE for the four CPZs in contact with Ag.

The observed relationship between Δ and PCE can be rationalized by an increased built in device potential. The difference in work function ($\delta\Phi_{AC}$) between the anode (PEDOT:PSS) and cathode (Ag or Al) induces a potential gradient across the active layer (**Figure 2.22A**). An interlayer that reduces the work function (negative Δ) at the cathode interface increases $\delta\Phi_{AC}$ and thus increases V_{OC}. The stronger built in potential gradient arising from larger $\delta\Phi_{AC}$ should improve the charge extraction efficiency and reduce recombination losses, leading to an increase of J_{SC} and FF.
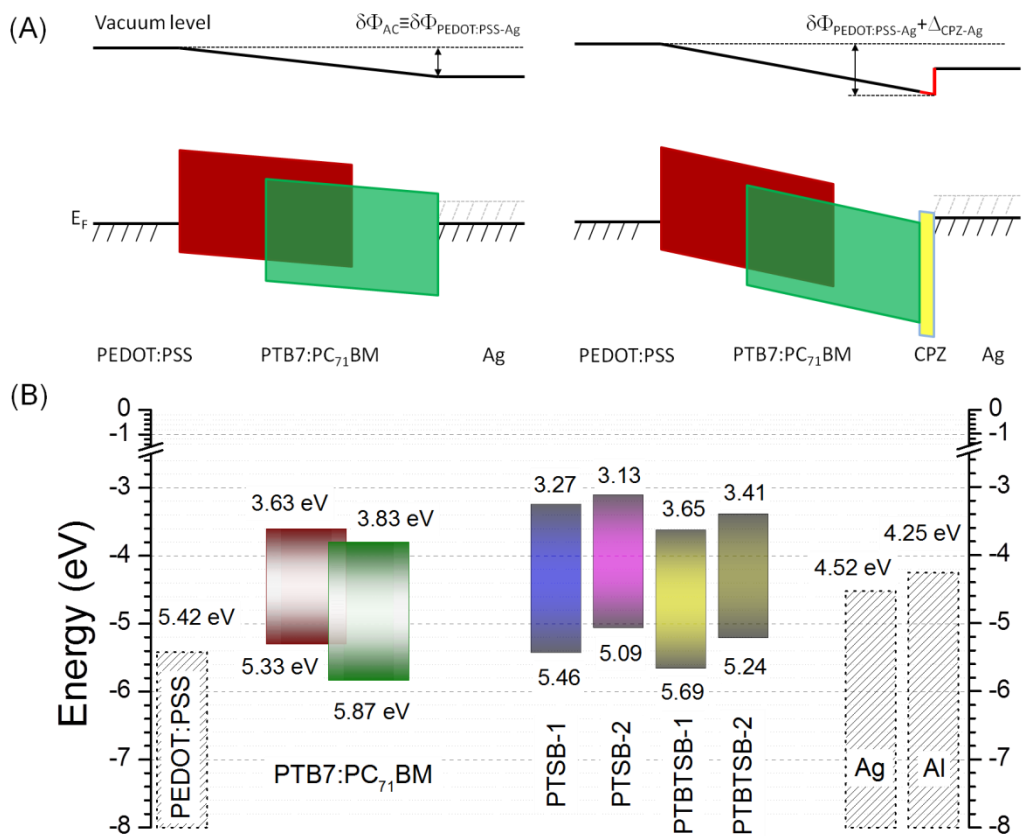
Figure 2.22 (A) Schematic illustration of the built-in potential difference in the photovoltaic devices without (left) and with (right) a CPZ interlayer, given for a common Fermi level (E_F) alignment (zero bias). (B) A summary of UPS measurements of electronic energy levels of the materials comprising the solar cells under investigation, given on the energy scale with a common vacuum level (materials are not in contact). *The LUMO energies for all materials, except of $PC_{71}BM$, were measured by UV-vis absorbance spectroscopy (optical band gaps), **The LUMO of $PC_{71}BM$ was determined from cyclic voltammetry. Reproduced from reference 60.

We note that there was no difference in Δ for CPZ-on-Ag at film thickness values of 2, 5 and 10 nm (**Figure 2.23**), suggesting that reduced device performance observed when deviating from the optimal 5 nm thick interlayer was not a result of changes in Δ.
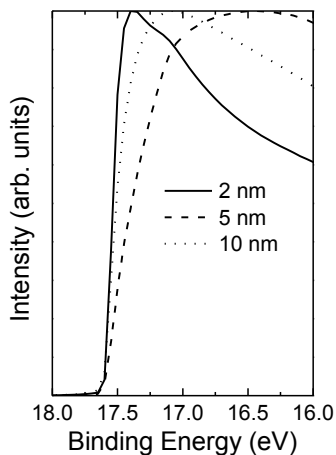
Figure 2.23 High binding energy UPS spectrum for **PTBTSB-2** on Ag with varied thickness, showing no change in E_{SEC} (*eg* no change of interfacial dipole). Reproduced from reference 60.

While the larger work function difference between the electrodes can be considered a dominant mechanism for the device improvement, several other factors must be considered while using a semiconducting interlayer material, such as CPZs, that hold the potential to directly contribute to the photocurrent within the device (**Figures 2.24**-**2.26**). The CPZ-coated active layer has a slightly stronger absorption around 550 nm as compared to the absorption of the active layer alone, which is consistent with the absorption peak for **PTBTSB-2** at this wavelength (**Figure 2.24** and see **Figure 2.8D** for absorption profile of **PTBTSB-2**). The contribution of the interlayer absorption to the total absorption in the partially-completed device geometry is minor.
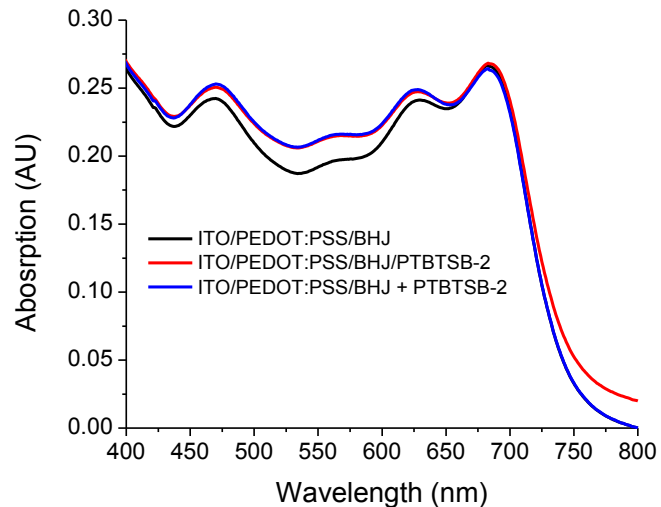
Figure 2.24 Absorption spectra of partially-completed devices, glass/ITO/PEDOT:PSS/BHJ/ with (red) or without (black) CPZ layer (5 nm-thick **PTBTSB-2**) as well as the sum of absorptions of the device without the interlayer and of the interlayer itself (blue). Reproduced from reference 60.

Figure 2.25 compares the IPCE spectra of the device with bare Ag cathode (black) and with **PTBTSB-2**/Ag cathode (red) as well as shows the difference between the two spectra (blue) obtained by subtraction. The enhancement of IPCE peaks at 680 nm is primarily in the spectral range of PTB7 absorption, and is observed in a much broader spectral range than where the **PTBTSB-2** interlayer absorbs efficiently (around 550 nm). The broad spectral range of IPCE enhancement is consistent with the increased electric field in the device with the **PTBTSB-2** interlayer due to a larger work function offset between the anode and cathode. The photogenerated charge carriers can be extracted quicker by the larger built-in electric field which prevents their recombination. Also, the quantum yield of free carrier generation can be increased due to larger built-in electric field, leading to the overall increase in the short circuit current. The fact that the IPCE improvement occurs in the spectral range of PTB7 absorption indicates that the aforementioned effects occur primarily in the PTB7. On the other hand, a redistribution

of an optical field, an "optical spacer" effect, by the **PTBTSB-2** interlayer may lead to more efficient absorption by PTB7 and as such this effect cannot be ruled out.[90,91]
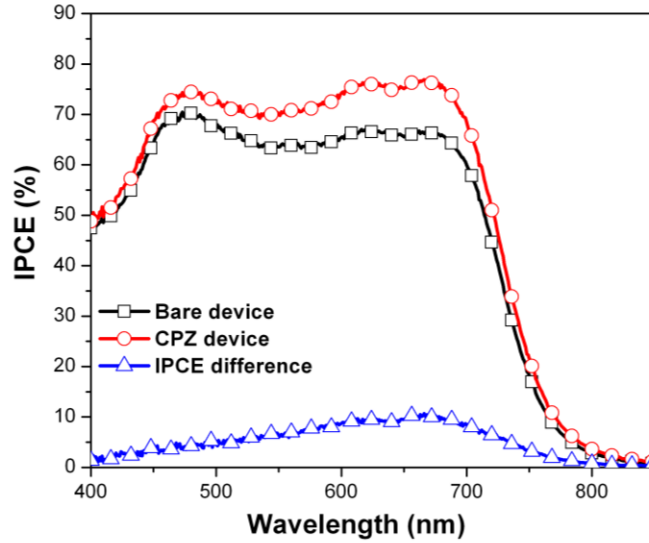
Figure 2.25 IPCE spectra of devices with (red) and without (black) 5 nm-thick PTBTSB-2 interlayer, and the difference of the two spectra (blue). Reproduced from reference 60.

The overall improvement of IPCE due to a **PTBTSB-2** interlayer is relatively small, peaking at 12%. The ratio between the two spectra with and without the interlayer that are integrated over the entire spectral region is consistent with the ratio of short circuit current densities of the respective devices. A very marginal improvement of J_{SC} of the devices with Ag cathodes with and without the 5-nm **PTBTSB-2** interlayer was observed, 16.5 mA/cm^2 and 17.6 mA/cm^2, respectively. At the same time, since the 5-fold increase of the overall device PCE improvement was achieved, at the expense of larger V_{OC} and better *FF*, the contribution of the aforementioned effects is not expected to be significant. **Figure 2.26** shows the performance of "partial" devices under AM1.5G illumination. No photovoltaic performance of such devices was observed. This indicates that exciton dissociation and free carrier generation are not efficient at the

PC$_{71}$BM/**PTBTSB-2** interface. Therefore, this effect is not expected to contribute to the improved performance of the devices with a **PTBTSB-2** interlayer.
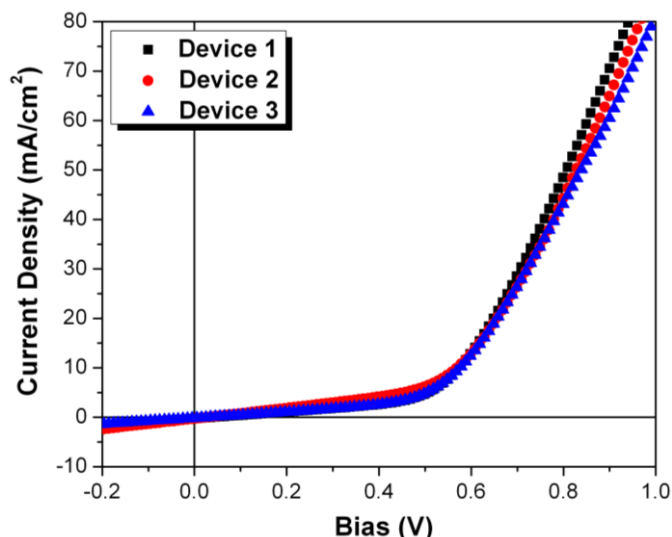
Figure 2.26 Photocurrent density – voltage characteristics of "partial" devices in ITO/PEDOT:PSS/PC$_{71}$BM (70 nm)/**PTBTSB-2** (5 nm)/Ag geometry. Reproduced from reference 60.

To determine the effect of CPZ interlayer molecular weight on device performance, solar cells were fabricated using **PTBTSB-2** at an optimal thickness of 3 – 5 nm and having molecular weights of 22 and 35 kDa (for those prepared with and without IL respectively) (**Figure 2.27**). Solar cells containing a bare Ag cathode (no CPZ interlayer), fabricated as controls, showed poor device performance (PCE 1.61%) as a result of a weak built in device potential. Adding a thin layer of **PTBTSB-2** dramatically improved V_{OC}, J_{SC} and *FF*, resulting in PCE > 5%. The 22 and 35 kDa **PTBTSB-2** interlayers led to average PCE values of 5.68 ± 0.23% and 7.36 ± 0.17% respectively (with the best devices having a PCE of 6.00% and 7.57% respectively) (**Figure 2.27**).
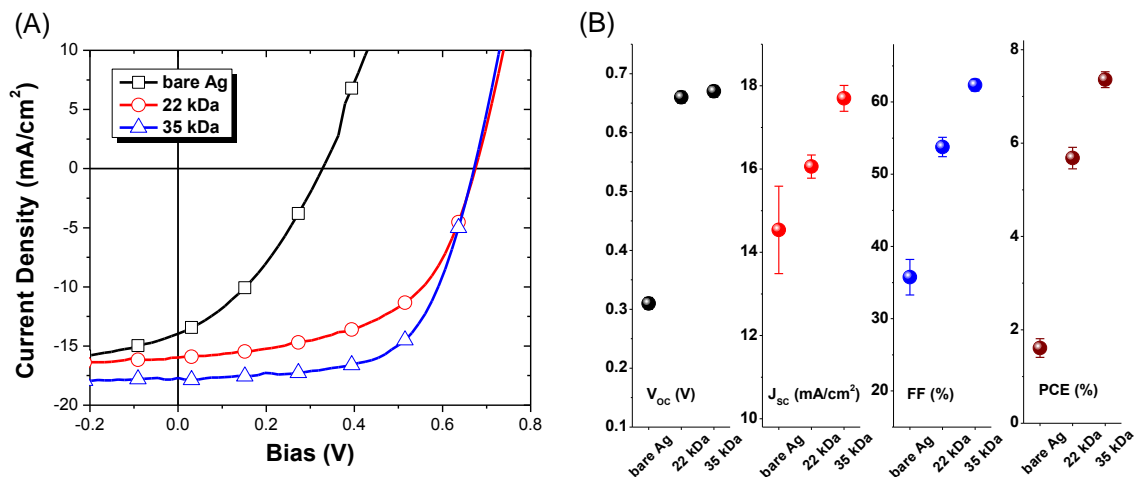
Figure 2.27 (A) Representative J-V curve of solar cells containing a ~5 nm thick layer of **PTBTSB-2**, between the active layer (PTB7:PC$_{71}$BM) and Ag cathode; (B) Overall device metrics averaged over 18 devices, with error bars representing ± 1 standard deviation. Reproduced from reference 59.

The improvement in PCE correlated with higher J_{sc} and *FF*, with little to-no change in V_{OC}. A $V_{OC} \approx 0.7$ V suggests that **PTBTSB-2** results in an Ohmic contact with Ag, where the *Voc* is dictated not by the anode-cathode work function offset, but rather the PTB7-HOMO/PC$_{71}$BM-LUMO offset.[92] UPS showed that the 22 kDa and 35 kDa **PTBTSB-2** samples have equivalent Δ values as thin layers on Ag, which correlates with the minor change of V_{OC} (**Figure 2.28**). A reduction in charge build-up / recombination at the interface would lead to an increase in both J_{SC} and *FF*, which may occur as a result of using higher molecular weight polymer interlayers. Thus, we speculate that the higher molecular weight polymers provide better interfacial contact with the Ag electrode and / or enhanced electron mobility, relative to films fabricated from lower molecular weight polymers.
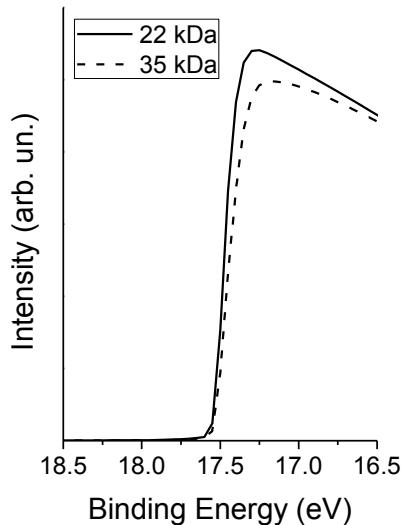
Figure 2.28 High binding energy region of the UPS spectra for **PTBTSB-2** on Ag showing no significant difference of Δ; 22 kDa (solid line); 35 kDa (dashed line). Reproduced from reference 59.

An interlayer can work as an "optical spacer", changing the redistribution of an optical field in the active layer, as well as a barrier that reduces interfacial recombination as compared to bare metal electrode. However, these effects are not significant because they would primarily lead to improvements in J_{SC}, where-as in our devices the enhancement can be largely attributed to an increase in V_{OC} and *FF*. For thicker CPZ interlayers (>5 nm), diminished OPV performance can be rationalized by considering the position of CPZ energy levels relative to PTB7 and PC$_{71}$BM (**Figure 2.22B**). **PTBTSB-1** and **PTBTSB-2** have deeper LUMO levels than **PTSB-1** and **PTSB-2** (on a common vacuum level scale) and larger interfacial dipoles with Ag, leading to a reduced potential barrier for electrons to overcome upon their collection at the cathode. Relative to the thiophene-benzothiadiazole CPZs, the higher LUMO levels of the all-thiophene CPZs may result in charge accumulation at the active layer/interlayer interface, leading to "S-shaped" J-V curves, and thus poorer device performance. However, since the shape of J-V curves strongly depends on the interlayer thickness for all CPZs, possible inefficiency

59

of charge transport through the CPZ materials should also be considered.

The orientation of the chemical constitutents of CPZs on the surface of the active layer was determined by near edge x-ray absorption fine structure (NEXAFS).[93] Carbon K-edge total electron yield (TEY, ~10 nm) and Auger electron yield (AEY, ~1 nm) NEXAFS spectra were used to access orientation at different average depths. The NEXAFS spectrum of the CPZs on PTB7:PC$_{71}$BM is dominated by signals arising from transitions from the 1s core level to unfilled π^* and σ^* orbitals. In **Figure 2.29A** (NEXAFS TEY), the peak at 285.5 eV is characteristic of the thiophene C=C π^*, and the signal at 284.5 eV represents benzothiadiazole C=C π^* orbitals. The broad features at higher energies are transitions to σ^* orbitals. The orientation of the π^* orbitals was determined by measuring the spectra of the linearly polarized soft X-rays at different angles of incidence, where an increased angle of incidence (*i.e.,* increasing the in-plane component of polarization of the incident x-rays) weakens the peak intensity, indicating that the CPZs assume a face-on orientation with respect to the underlying active layer. By measuring the NEXAFS spectra arising from the AEY, information characterizing only the surface is obtained, showing a smaller intensity ratio for the σ^*-to-π^* transitions in the AEY spectra compared to TEY, indicating that the aliphatic chains are not oriented normal to the film surface. An illustration of CPZ orientation is given in **Figure 2.29D**.

An electrostatic model was developed to describe the interaction of the zwitterionic CPZ pendent groups with a metal surface. The electrostatic dipole moment p_o near a metal surface induces surface polarization (**Figure 2.29B**).

60
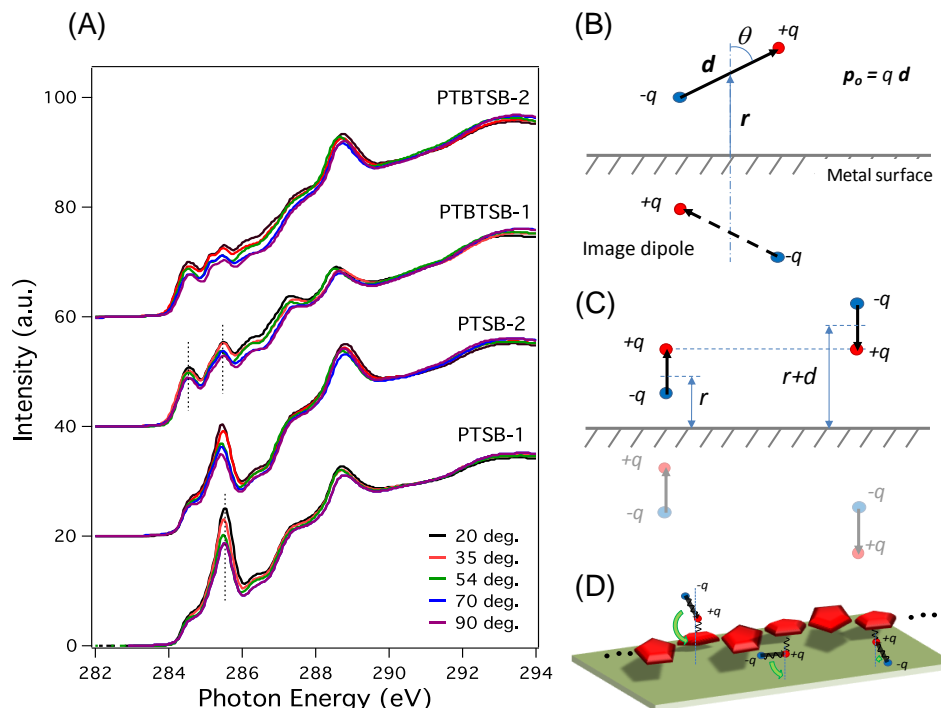
Figure 2.29 (A) NEXAFS TEY spectroscopy of CPZs on the active layer (PTB7:PC71BM); (B) illustration of an "image" dipole where $p_o = qd$ (q is the elementary charge and d is a vector pointing from a negative charge, $-q$, to a positive charge, $+q$, which is equal to the separation distance between the charges) located a distance r from a metal surface; (C) two possible orientations of an electrostatic dipole fixed rigidly at the point of positive charge, where an upward orientation (left side) is a state with lower energy; (D) alignment of dipolar side chains of a zwitterionic polymer on a metal surface. Reproduced from reference 60.

The electrostatic problem of a dipole-metal surface interaction can be described in terms of an "image" dipole – an imaginary dipole of two charges imaged across the metal surface plane (**Figure 2.29B**).[94] Due to the interaction between the original dipole, p_o, and its image, p_i, the torque on the original dipole is given by equation 2.3.

$$\tau = \left[p_0 \times E_{dip-dip}\right] = \frac{1}{4\pi\varepsilon_0}\left[p_0 \times \left(\frac{3(p_i \cdot r)\cdot r}{r^5} - \frac{p_i}{r^3}\right)\right] \qquad 2.3$$

Fixing the dipole at its center of mass causes the torque to rotate the dipole, align it normal to the surface, and reduce to zero at either $\theta = 0$ or $\theta = \pi$ (**Figure 2.29C**). The zwitterionic side chains of CPZs can be considered as dipoles fixed rigidly to the conjugated backbone. The two dipole orientations, pointing away from or towards the

61

surface, have different potential energies since the distance to the surface differs by d (**Figure 2.29C**). The potential interaction energy between the original dipole p_o and its image p_i is given by equation 2.4.

$$U_{dip-dip} = \frac{1}{8\pi\varepsilon_0}\left(\frac{p_o \cdot p_i}{r^3} - \frac{3(p_o \cdot r)(p_i \cdot r)}{r^5}\right)$$
2.4

The upward orientation (**Figure 2.29C**, left side) has a smaller distance, making it more energetically favorable than the downward orientation (**Figure 2.29C**, right side) (r vs. $r + d$). In the vicinity of a metal surface (**Figure 2.29D**), the self-induced torque of dipolar side chains, and energy minimization, directs the negative charges towards the surface. Such charge re-distribution is expected to reduce the work function of the metal. The strong distance dependence for potential interaction energies (equation 2.4) leads to minimal impact beyond the first monolayer.

The model discussed here is similar to the physical adsorption of dipolar organic molecules onto metal surfaces, where the interaction energies and work function modifications were estimated using the classical electrostatic model[95] or density functional theory calculations.[96] However, in our case the re-orientation of side chains along the surface normal is restricted by the allowed conformations of chemical bonds. The greater flexibility of longer side chains might explain why **PTSB-2** and **PTBTSB-2** reduce the work function of Ag more than **PTSB-1** and **PTBTSB-1**.

2.6 Summary and future outlook

In summary, four novel conjugated polymers with sulfobetaine side-chains were prepared from the corresponding zwitterionic monomers by SM polycondensation. The use of ionic liquids as solvent further increases molecular weight due to improved zwitterion solubility, providing CPZs rapidly (~2 hours) in the presence of air, which

precluded the necessity for volatile organic solvents, inert atmosphere, toxic phosphine ligands and phase transfer catalysts. Using UV-Vis absorption and UPS structure-property relationships between energy levels and the proximity of the zwitterioinc side-chain to the polymer backbone were identified. The thiophene-based CPZs were shown to be effective materials for improving the PCE of bulk heterojunction OPVs through interfacial modification. For devices with Ag cathodes, a dramatic improvement in device performance was achieved relative to devices with no interlayers (PCE ≈ 1% for bare Ag cathodes and 6% for deivces containing a **PTBTSB-2** interlayer). PCE values were further increased from 6% to greater than 7.5% using higher molecular weight CPZs obtained using ILs as the solvent. A direct correlation between interfacial dipole and device performance was found, where the largest interfacial dipole value (-0.96 eV) for the **PTBTSB-2**/Ag interface yielded the highest PCE. Finally a model detailing the origin of work function modification by the CPZs is proposed, where electrostatic realignment of the dipolar zwitterionic side chains in the vicinity of a metal surface is hypothesized to cause the observed negative Δ. This chapter provided a platform for the development of new hydrophilic conjugated polymers using SM coupling, while simultaneously showing their practical and effective use as interfacial layers in PSCs.

2.7 References

1. Peumans, P.; Yakimov, A.; Forrest, S.R. *J. Appl. Phys.* **2003**, 93, 3693-3723.

2. Schlaf, R.; Parkinson, B.A.; Lee, P.A.; Nebesny, K.W.; Jabbour, G.; Kippelen, B.; Peyghambarian, N.; Armstrong, N.R. *J. Appl. Phys.* **1998**, 84, 6729-6736. 6729-6736.

3. White, M.S.; Olson, D.C.; Shaheen, S.E.; Kopidakis, N.; Ginley, D.S. *Appl. Phys. Lett.* **2006**, 89, 143517.

4. Dou, L. You, J. Yang, J. Chen, C.-C. He, Y. Murase, S. Moriarty, T. Emery, K. Li, G.; Yang, Y. *Nat. Photonics* **2012**, *6*, 180-185.

5. Kim, J.Y.; Kim, S.H.; Lee, H.-H.; Lee, K.; Ma, W.; gong, X.; Heeger, A.J. *Adv. Mater.* **2006**, 18, 572-576.

6. Wu, H.; Huang, F.; Mo, Y.; Yang, W.; Wang, D.; Peng, J.; and Cao, Y. *Adv. Mater.* **2004**, 16, 1826-1830.

7. Ma, H.; Yip, H.-L.; Huang, F.; and Jen, A. K.-Y. *Adv. Funct. Mater.* **2010**, 20, 1371-1388.

8. Li, C.; Chueh, C.; Yip, H.; Malley, K. M. O.; Chen, W.; Jen, A. K. *J. Mater. Chem.* **2012**, *22*, 8574-8578.

9. Duarte, A.; Pu, K.-Y.; Liu, B.; Bazan, G. C. *Chem. Mater.*, **2011**, 23, 501-515.

10. Zhou, Y.; Fuentes-Hernandez, C.; Shim, J.; Meyer, J.; Giordano, A.J.; Li, H.; Winget, P.; Papadopoulos, T.; Cheun, H.; Kim, J.; Fenoll, M; Dindar, A.; Haske, W.; Najafabadi, E.; Khan, T. M.; Sojoudi, H.; Barlow, S.; Graham, S.; Brédas, J.-L.; Marder, S.R.; Kahn, A.; Kippelen, B.; *Science* **2012**, 336, 327-332.

11. Krebs, F. C. *Sol. Energ. Mat. Sol. Cells* **2009**, *93*, 465-475.

12. Krebs, F. C.; Gevorgyan, S. A.; Alstrup, J. *J. Mater. Chem.* **2009**, *19*, 5442-5451.

13. O'Malley, K. M.; Li, C.-Z.; Yip, H.-L.; and Jen, A. K.-Y. *Adv. Energy Mater.* **2012**, 2, 82-86.

14. Fang, J.; Wallikewitz, B. H.; Gao, F.; Tu, G.; Muller, C.; Pace, G.; Friend, R. H.; Huck, W. T. S. *J. Am. Chem. Soc*. **2011**, *133*, 683-685.

15. Nilsson, K. P. R.; Inganäs, O. *Nat. Mater*. **2003**, *2*, 419-424.

16. Karlsson, K. F. Asberg, P. Nilsson, K. P. R.; Inganas, O. *Chem. Mater.* **2005**, *17*, 4204-4211.

17. Andersson, M. Ekeblad, P. O. Hjertberg, T.; Wennerstrom, O. *Polym. Commun.* **1991**, *32*, 546-548.

18. Duan, C.; Wang, L.; Zhang, K.; Guan, X.; Huang, F. *Adv. Mater.* **2011**, *23*, 1665-1669.

19. Kline, R. J.; McGehee, M. D. *J. Macromol. Sci., Polym. Rev.* **2006**, *46*, 27-45.

20. Kesters, J.; Ghoos, T.; Penxten, H.; Drijkoningen, J.; Vangerven, T.; Lyons, D. M.; Verreet, B.; Aernouts, T.; Lutsen, L.; Vanderzande, D.; Manca, J.; Maes, W. *Adv. Energy Mater.* **2013**, *3*, 1180-1185.

21. Lu, J.; Yan, F.; Texter, J. *Prog. Polym. Sci.* **2009**, *34*, 431-448.

22. Hallett, J. P.; Welton, T. *Chem. Rev.* **2011**, *111*, 3508-3576.

23.   Sheldon, R. *Chem. Commun.* **2001**, 2399-2407.

24.   Wasserscheid, P.; Keim, W. *Angew. Chem. Int. Ed. Engl.* **2000**, *39*, 3772-3789.

25.   Vygodskii, Y. S.; Lozinskaya, E. I.; Shaplov, A. S.; Lyssenko, K. A.; Antipin, M. Y.; Urman, Y. G. *Polymer* **2004**, *45*, 5031-5045.

26.   Chen, X.; McRae, S.; Samanta, D.; Emrick, T. *Macromolecules* **2010**, *43*, 6261-6263.

27.   Johnston-Hall, G.; Harjani, J. R.; Scammells, P. J.; Monteiro, M. J. *Macromolecules* **2009**, *42*, 1604-1609.

28.   Vygodskii, Y. S.; Shaplov, A. S.; Lozinskaya, E. I.; Filippov, O. a.; Shubina, E. S.; Bandari, R.; Buchmeiser, M. R. *Macromolecules* **2006**, *39*, 7821-7830.

29.   Kubisa, P. *Prog. Polym. Sci.* **2009**, *34*, 1333-1347.

30.   Olivier-Bourbigou, H.; Magna, L.; Morvan, D. *Appl. Catal., A* **2010**, *373*, 1-56.

31.   Xin, B.; Zhang, Y.; Liu, L.; Wang, Y. *Synlett* **2005**, 3083-3086.

32.   Mathews, C. J.; Smith, P. J.; Welton, T. *Chem. Commun.* **2000**, 1249-1250.

33.   Yang, X.; Fei, Z.; Geldbach, T. J.; Phillips, A. D.; Hartinger, C. G.; Li, Y.; Dyson, P. J. *Organometallics* **2008**, *27*, 3971-3977.

34.   McLachlan, F.; Mathews, C. J.; Smith, P. J.; Welton, T. *Organometallics* **2003**, *22*, 5350-5357.

35.   Jin, C.; Twamley, B.; Shreeve, J. M. *Organometallics* **2005**, 3020-3023.

36.   Zou, G.; Wang, Z.; Zhu, J.; Tang, J.; He, M. Y. *J. Mol. Catal. A: Chem.* **2003**, *206*, 193-198.

37.   Yan, N.; Yang, X.; Fei, Z.; Li, Y.; Kou, Y.; Dyson, P. J. *Organometallics* **2009**, *28*, 937-939.

38.   Pang, Y.; Li, X.; Ding, H.; Shi, G.; Jin, L. *Electrochim. Acta* **2007**, *52*, 6172-6177.

39.   Pringle, J. M.; Ngamna, O.; Lynam, C.; Wallace, G. G.; Forsyth, M.; MacFarlane, D. R. *Macromolecules* **2007**, *40*, 2702-2711.

40.   Haldorai, Y.; Zong, T.; Shim, J.-J. *Mater. Chem. Phys.* **2011**, *127*, 385-390.

41.   Yuan, C.; Hou, L.; Shen, L.; Zhang, X. *J. Electrochem. Soc.* **2012**, *159*, A1323-A1328.

42. Margaretta, E.; Olmeda, C.; Yu, L. *J. Appl. Polym. Sci.* **2013**, *127*, 2453-2457.

43. He, Z.; Zhong, C.; Huang, X.; Wong, W.-Y.; Wu, H.; Chen, L.; Su, S.; and Cao, Y. *Adv. Mater.* **2011**, 23, 4636-4643.

44. Gadisa, A.; Svensson, M.; Andersson, M.R.; Inganas O. *Appl. Phys. Lett.* **2004**, 84, 1609-1611.

45. Scharber, M.C.; Muehlbacher, D.; Koppe, M.; Denk, P.; Waldauf, C.; Heeger, A.J.; and Brabec C.J. *Adv. Mat.* **2006**, 18, 789-794.

46. Vandewal, K.; Tvingstedt, K.; Gadisa, A.; Inganas, O.; Manca, J.V. *Nat. Mater.* **2009**, 8, 904-909.

47. Mihailetchi, V. D.; Koster, L. J. A.; Blom, P. W. M. *Appl. Phys. Lett.* **2004**, *85*, 970-972.

48. Mihailetchi, V. D.; Blom, P. W. M.; Hummelen, J. C.; Rispens, M. T. *J. Appl. Phys.* **2003**, *94*, 6849-6854.

49. Deibel, C.; Dyakonov, V. *Rep. Prog. Phys.* **2010**, 73, 096401.

50. Wei, Q.; Nishizawa, T.; Tajima, K.; and Hashimoto, K. *Adv. Mater.* **2008**, 20, 2211-2216.

51. Worfolk, B.J.; Hauger, T.C.; Harris, K.D.; Rider, D.A.; Fordyce, J.A.M.; Beaupre, S.; Leclerc, M.; and Buriak, J.M. *Adv. Energy Mater.* **2012**, 2, 361-368.

52. Reenen, S. van; Kouijzer, S.; Janssen, R. A. J.; Wienk, M. M.; Kemerink, M. *Adv. Mater. Interfaces* **2014**, *1*, 1400189.

53. Ishii, B. H.; Sugiyama, K.; Ito, E.; Seki, K. *Adv. Mater.* **1999**, *11*(8), 605-625.

54. Seo, J. H.; Nguyen, T.-Q. *J. Am. Chem. Soc.* **2008**, 130, 10042-10043.

55. Hill, I.G.; Milliron, D.; Schwartz, J.; Kahn, A.; *Appl. Surf. Sci.*, **2000**, 166, 354-362.

56. Tengstedt, C. Osikowicz, W. Salaneck, W. R. Parker, I. D. Hsu, C.-h; Parker, I. D. *Appl. Phys. Lett.* **2006**, *88*, 053502.

57. Seo, J. H.; Yang, R.; Brzezinski, J. Z.; Walker, B.; Bazan, G. C.; Nguyen, T.-Q. *Adv. Mater.* **2009**, *21*(9), 1006-1011.

58. Page, Z. A.; Duzhko, V. V.; Emrick, T. *Macromolecules* **2013**, *46*, 344-351.

59. Page, Z. A.; Liu, F.; Russell, T. P.; Emrick, T. *Chem. Sci.* **2014**, *5*, 2368-2373.

60. Liu, F.; Page, Z. A.; Duzhko, V. V.; Russell, T. P.; Emrick, T. *Adv. Mater.* **2013**, *25*, 6868-6873.

61. Sonnenschein, L.; Seubert, A. *Tetrahedron Lett.* **2011**, *52*, 1101-1104.

62. Huglin, M. B.; Radwan, M. A. *Makromol. Chem.* **1991**, *192*, 2433 -2445.

63. Georgiev, G. S. Kamenska, E. B. Vassileva, E. D. Kamenova, I. P. Georgieva, V. T. Iliev, S. B.; Ivanov, I. A. *Biomacromolecules*. **2006**, *7*, 1329-1334.

64. Mary, P.; Bendejacq, D. D.; Labeau, M.; Dupuis, P. *J. Phys. Chem. B.* **2007**, *111*, 7767-7777.

65. Herrmann, W. A.; Kocher, C. *Angew. Chem. Int. Ed. Engl.* **1997**, *36*, 2162-2187.

66. Zhang, S.; Sun, N.; He, X.; Lu, X.; Zhang, X. *J. Phys. Chem. Ref. Data* **2006**, *35*, 1475-1517.

67. Reichardt, C. *Green Chem.* **2005**, *7*, 339-351.

68. Weingärtner, H. *Angew. Chem. Int. Ed.* **2008**, *47*, 654-670.

69. Yu, G.; Zhao, D.; Wen, L.; Yang, S.; Chen, X. *AIChE J.* **2012**, *58*, 49-53.

70. Crowhurst, L.; Mawdsley, P. R.; Perez-Arlandis, J. M.; Salter, P. a.; Welton, T. *Phys. Chem. Chem. Phys.* **2003**, *5*, 2790-2794.

71. Shi, C. Yao, Y. Yang, Y.; Pei, Q. *J. Am. Chem. Soc.* **2006**, *128*, 8980-8986.

72. Huo, L. Zhou, Y.; Li, Y. *Macromol. Rapid Commun.* **2009**, *30*, 925-931.

73. Salzner, U.; Kose, M. E. *J. Phys. Chem. B.* **2002**, *106*, 9221-9226.

74. Beaujuge, P. M.; Ellinger, S.; Reynolds, J. R. *Nat. Mater.* **2008**, *7*, 795-799.

75. Beaujuge, P. M.; Amb, C. M.; Reynolds, J. R. *Acc. Chem. Res.* **2010**, *43*, 1396-1407.

76. Seo, J. H.; Namdas, E. B.; Gutacker, A.; Heeger, A. J.; Bazan, G. C. *Appl. Phys. Lett.* **2010**, *97*(4), 043303.

77. Salaneck, W.R.; Loegdlund, M.; Fahlman, M.; Greczynski, G.; Kugler, Th. *Mat. Sci. Eng. R* **2001**, 34, 121-146.

78. Hwang, J.; Wan A.; Kahn, A. *Mat. Sci. Eng. R* **2009**, 64, 1-31.

79. Osikowicz, W.; Jong, M. P.; Braun, S.; Tengstedt, C.; Fahlman, M.; Salaneck, W. R. *Appl. Phys. Lett.* **2006**, *88*, 193504.

80. Lyon, J. E. Cascio, A. J. Beerbom, M. M. Schlaf, R. Zhu, Y.; Jenekhe, S. A. *Appl. Phys. Lett.* **2006**, *88*, 222109.

81. Jørgensen, M.; Norrman, K.; Krebs, F. C. *Sol. Energ. Mat. Sol. Cells* **2008**, *92*, 686-714.

82. Liang Y.Y.; Xu, Z.; Xia, J.B.; Tsai, S.T.; Wu, Y.; Li, G.; Ray, C.; Yu, L.P. *Adv. Mat.* **2010**, 22, E135-E138.

83. Li, H.; Tang, H.; Li, L.; Xu, W.; Zhao, X.; Yang, X. *J. Mater. Chem.* **2011**, *21*, 6563-6568.

84. Liu, X.; Wen, W.; Bazan, G. C. *Adv. Mater.* **2012**, *24*, 4505-4510.

85. Nam, S.; Jang, J.; Cha, H.; Hwang, J.; An, T. K.; Park, S.; Park, C. E. *J. Mater. Chem.* **2012**, *22*, 5543-5549.

86. Zhou, H.; Zhang, Y.; Seifter, J.; Collins, S. D.; Luo, C.; Bazan, G. C.; Nguyen, T.-Q.; Heeger, A. J. *Adv. Mater.* **2013**, *25*, 1646-1652.

87. Tress, W.; Petrich, A.; Hummert, M.; Hein, M.; Leo, K.; Riede, M. *Appl. Phys. Lett.* **2011**, *98*, 063301.

88. Wagenpfahl, A.; Rauh, D.; Binder, M.; Deibel, C.; Dyakonov, V. *Phys. Rev. B* **2010**, *82*, 115306.

89. Zhang, M.; Wang, H.; Tang, C. W. *Appl. Phys. Lett.* **2011**, *99*, 213506.

90. He, Z.; Zhong, C.; Su, S.; Xu, M.; Wu, H.; Cao, Y. *Nat. Photon.* **2012**, *6*, 593-597.

91. Park, S. H.; Roy, A.; Beaupr e, S.; Cho, S.; Coates, N.; Moon, J. S.; Moses, D.; Leclerc, M.; Lee, K.; Heeger, A. J. *Nat. Photon.* **2009**, *3*, 297-302.

92. He, Z.; Wu, H.; Cao, Y. *Adv. Mater.* **2014**, *26* (7), 1006-1024.

93. Brown, H. R.; Russell, T. P. *Macromolecules* **1996**, *9297*, 8334 − 8342.

94. Landau, L.D.; Lifshitz, E.M. Course of Theoretical Physics: Electrodynamics of continuous media; Nauka, Moscow, **1981**.

95. Maschhoff, B.L.; Cowin, J.P. *J. Chem. Phys.* **1994**, 101, 8138 − 8151.

96. Fernandez-Torre, D.; Kupiainen, O.; Pyykkoe, P.; Halonen, L. *Chem. Phys. Lett.* **2009**, 471, 239 − 243.

CHAPTER 3

NARROW ENERGY GAP CONJUGATED POLYMER ZWITTERIONS

3.1 Introduction

Interest in narrow band gap conjugated polymers for optoelectronic applications, including solar cells, has increased due to synthetic advances that improve solar absorption and favorable charge injection into metal electrodes.[1,2] Most polymer-based solar cells (PSCs) use conjugated polymers with alkyl substituents that afford desirable solubility. Bazan and coworkers reported hydrophilic conjugated polymers, such as narrow band gap conjugated polyelectrolytes (NBGCPEs), having cationic pyridinium functionalized side-chains.[3] CPZs differ from CPEs in that their pendent chains possess no net charge nor transient counterion, yet preserve a polar, hydrophilic character. The orthogonal polarity of CPZs relative to typical active layer materials allows for facile layer-by-layer solution deposition, with little disruption of the underlying material. This is important for PSCs given that they are are typically composed of multiple layers, where electronic communication at each interface is crucial for improving the selectivity of charge transport and minimizing series resistance (R_s) to maximize power conversion efficiency (PCE).[4-10] The synthesis of new, rationally designed polar conjugated polymers is critically important to address this issue of interfacial engineering for PSCs.

Placing ultra-thin films of polar polymers between the active layer and conductive electrode has been shown to substantially improve OPV device efficiency, owing to an interfacial dipole (Δ) generated at the electrode-polymer interface.[11-16] Δ modifies the electrode work-function (Φ), useful for OPVs, since a reduction in cathode Φ increases

the built-in electrostatic potential difference across the device, and increases charge extraction efficiency.[17,18] Benefits derived from surface modification of the electrode include improvement of numerous PSC metrics, such as open circuit voltage (V_{OC}), fill factor (FF) and short circuit current density (J_{SC}).[19] As Δ is an intrinsic surface property, the bulk characteristics of the metal electrode (including Φ) are preserved, allowing for stable high Φ metals, such as Ag, to be used in PSCs and prolong device lifetime.[20-22]

Poly(ethylenedioxythiophene):poly(styrene sulfonate) (PEDOT:PSS) functions as a solution processible hole-selective anode modification layer that has proven generally useful for PSCs. Recent efforts have been devoted to developing new cathode modification layers to enhance electron extraction efficiency. Small molecule organic interlayers integrated into PSCs afford noteworthy device improvement, including functional fullerenes,[7,22-30] perylene-diimides,[31] and oligomeric fluorenes.[8] Polymer interlayers provide advantages of both facile solution processing and robust film formation, precluding the necessity for evaporative deposition,[32] offering an avenue towards all-solution processed PSCs.[33] In addition, functionlization of polymers with various substituents makes it easy to fine-tune electronic properties of the components with which they interface.[34-36] Two recently reported examples of effective polymer-based cathode modification layers includes poly(ethyleneimine) (PEI)[33,37] and tertiary-amine substituted polyfluorene (PFN),[6,38] but these materials suffer from inefficient electron transport, constraining their optimal film thickness range to an extremely narrow window of < 5 nm. To circumvent this, new interlayers with appreciable electron transport properties are needed to reduce the deleterious impact of charge build-up and surface recombination in devices.

In chapter 2 the incorporation of thiophene-based CPZs as cathode-modification layers in OPVs was discussed.[16,39,40] It was shown that CPZs generate large Δ values, as measured by ultraviolet photoelectron spectroscopy (UPS), and on high Φ metals, like Ag, are seen to provide several-fold improvement of PCE values.[16] The thiophene-based CPZs are mid-to-wide energy gap (E_g) materials ($E_g > 1.8$ eV) and it has been proposed that wide energy gap interlayers are required for solar cell devices to confine excitons to the active layer.[4] However, narrow E_g interfacial layers have not been extensively studied, in-part due to a lack of suitable narrow band gap hydrophilic materials.

This chapter describes the design and synthesis of novel CPZs having two pendant sulfobetaine (SB) zwitterions per repeat unit.[41,42] Section 3.2 discusses the utility of six narrow energy gap CPZs, containing either diketopyrrolopyrrole (DPP) or *iso*indigo (*i*In) repeat units in the back-bone and SB groups in the side-chains, as cathode modification layers in PSCs.[41] All six novel narrow E_g CPZs led to substantial improvements in device PCE, obtaining values in the range of 6.7-7.7%, rivaling the champion CPZ described in chapter 2, **PTBTSB-2**, that led to PCE values in the range of 5.7-7.4% (depending on molecular weight).[16,40] This chapter clearly demonstrates that wide-energy gap interlayers are not a prerequisite to efficient sunlight-to-electricity conversion. In particular, one DPP-benzothiadiazole example, the narrowest E_g CPZ (~1.2 eV), stood out for its ability to be used as an effective interlayer at thicknesses exceeding 5 nm. This work led to the development of a naphthalene diimide (NDI) based CPZ, which is described in section 3.3.[42] The NDI polymers overcome a general shortcoming in most cathode modification layers (i.e., having aliphatic or p-type backbones), namely inefficient electron transport that requires the interlayer to be very

71

thin (~5 nm or less). A strucuture-property-relationship between interlayer electron transport and PSC efficiency is described, with the demonstration of PCE values that exceed 10% for devices containing NDI-based CPZs.

3.2 Diketopyrrolopyrrole and *iso*indigo: synthesis and solar cells

The chemical structures of the new, low bandgap, CPZ polymers prepared are shown in **Figure 3.1**. Six derivatives were synthesized, specifically composed of SB-substituted terthiophene-DPP (**PT₃DPPSB**) (**39**), bisthiophenebenzothiadiazole-DPP (**PT₂BTDPPSB**) (**40**), tetrathiophene-DPP (**PT₄DPPSB**) (**41**) thiophene-*i*In (**PT*i*InSB**) (**42**), benzothiadiazole-*i*In (**PBT*i*InSB**) (**43**) and bisthiophene-*i*In (**PT₂*i*InSB**) (**44**). The SB zwitterions were placed pendent to the conjugated backbone through *n*-hexyl spacers. Branched alkyl analogues (2-octyldodecyl) were also prepared for comparison (chemical structures given in **Figure 3.2**).
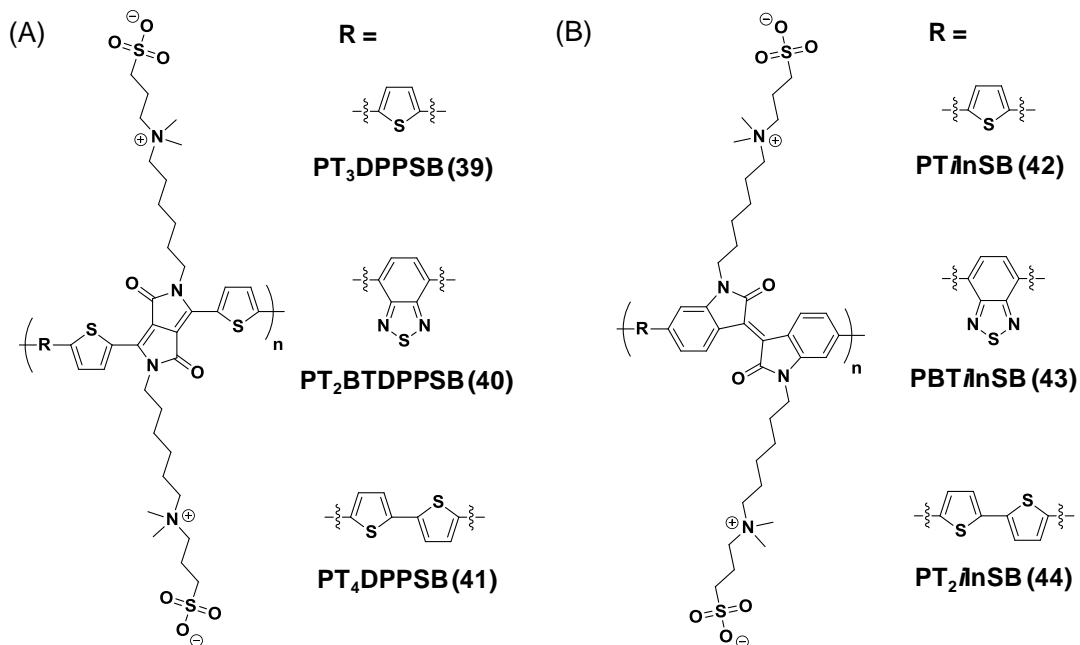
Figure 3.1 Chemical structures of narrow energy-gap CPZs. (A) DPP CPZs; **PT₃DPPSB** (**39**) **PT₂BTDPPSB** (**40**), **PT₄DPPSB** (**41**) and (B) *i*In CPZs; **PT*i*InSB** (**42**), **PBT*i*InSB** (**43**), **PT₂*i*InSB** (**44**). Reproduced from reference 41.
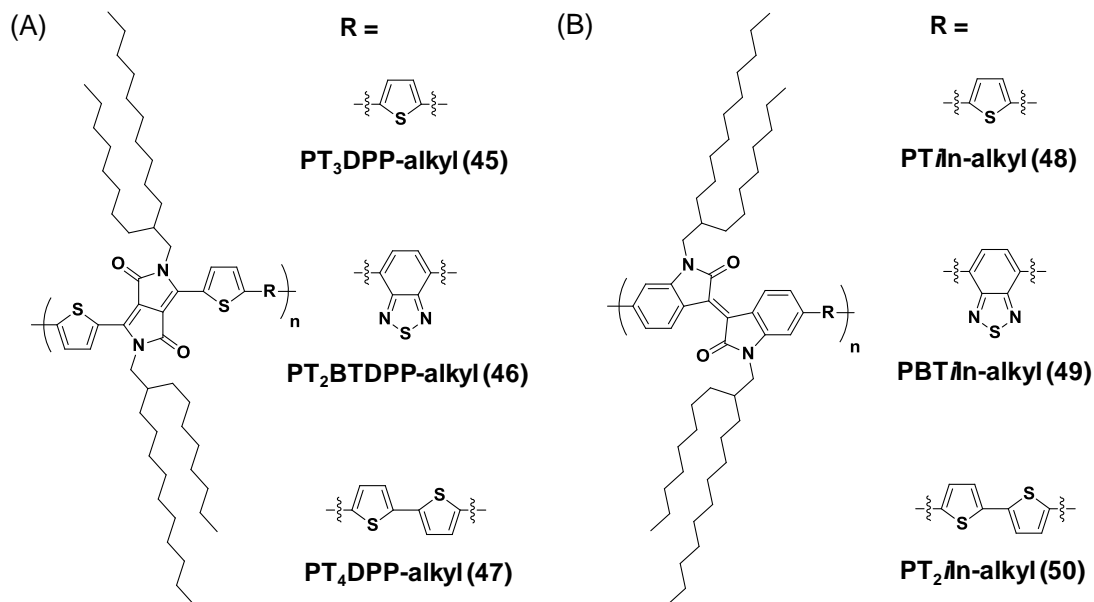
Figure 3.2 Chemical structures of narrow energy-gap alkyl-analogs. (A) DPP CPZs; **PT$_3$DPP-alkyl** (**45**) **PT$_2$BTDPP-alkyl** (**46**), **PT$_4$DPP-alkyl** (**47**) and (B) *i*In CPZs; **PT*i*In-alkyl** (**48**), **PBT*i*In-alkyl** (**49**), **PT$_2$*i*In-alkyl** (**50**). Reproduced from reference 41.

The monomer syntheses yielding DPP-SB **55** and *i*In-SB **59** are outlined in **Scheme 3.1**. Both syntheses began with nucleophilic substitution of diiodohexane on the respective starting materials, **51** and **56**, giving alkylated derivatives **52** and **57** (using excess alkyl-halide to prevent disubstitution). In the synthesis of DPP **52** and alkylated analog **60**, an unavoidable imidate (imino ether) isomer, **61**, (**Figure 3.3**) was obtained and identified by ^{1}H NMR spectroscopy from the chemical shift of the methylene protons α to the imidate (4.59 ppm) relative to the methylene protons α to the amide (3.99 ppm).[13]
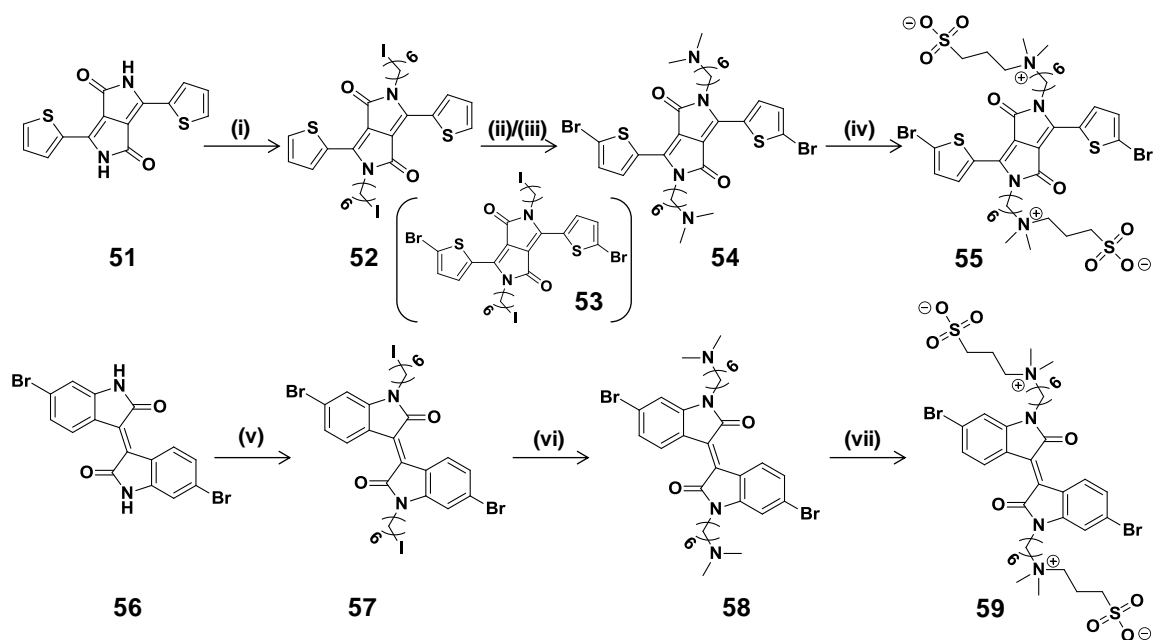
Scheme 3.1 Synthesis of DPP-SB and *i*In-SB monomers, **55** and **59** respectively. Reagents and conditions: (i) 1,6-diiodohexane, cesium carbonate, NMP, 48%; (ii) NBS, CHCl$_3$, 70%; (iii) (CH$_3$)$_2$NH, THF, 76%; (iv) 1,3-propanesultone, THF, 92%; (v) diiodohexane, cesium carbonate, NMP, 37%; (vi) (CH$_3$)$_2$NH, THF, 89%; (vii) 1,3-propanesultone, THF, 98%. Reproduced from reference 41.
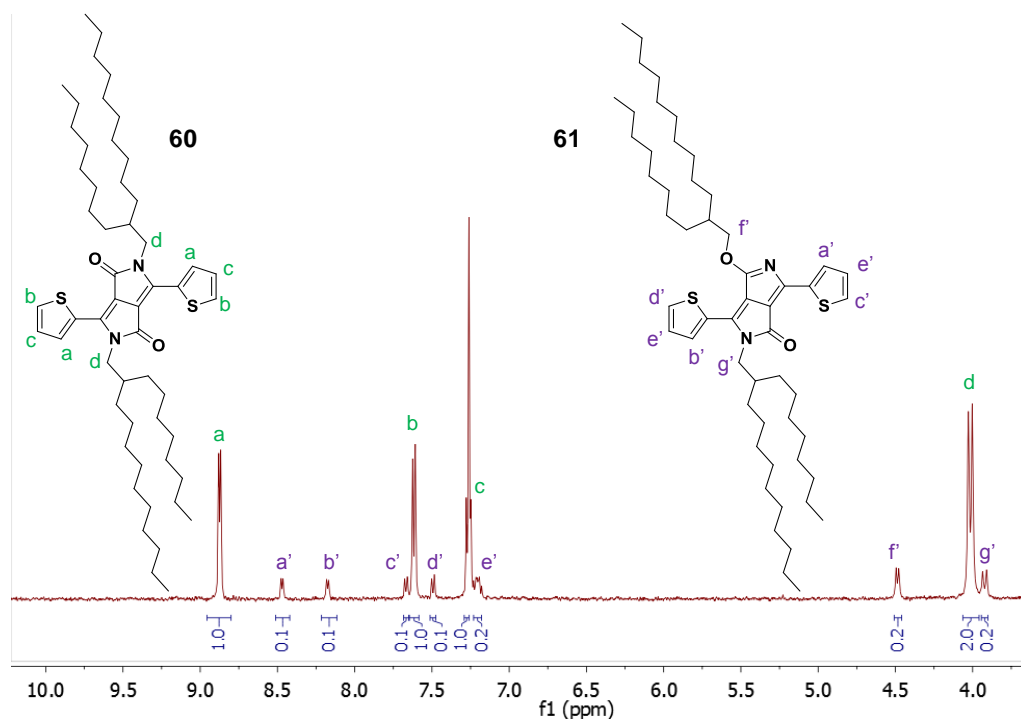
Figure 3.3 Representative ^{1}H-NMR spectrum and peak assignments of the crude reaction products, **60** and **61**, resulting from attempted *N*-substitution of dithieno-diketopyrrolopyrrole showing the presence of an imino-ether isomer. Reproduced from reference 41.

74

Removal of the imidate isomer by column chromatography gave **52** in 48% yield.

Compound **52** was fully brominated using an excess of *N*-bromosuccinimide (NBS) in

CHCl$_3$ to give **53**, which was coincident with a small amount of bromide-for-iodide

exchange at the alkyl chain-ends, giving byproduct **62** as confirmed by mass

spectroscopy (**Figure 3.4**). ^{1}H NMR spectroscopy in CD$_2$Cl$_2$ wass also used to identify

the side-product, specifically looking at the resonance of the methylene protons α to the

bromide at 3.42 ppm relative to those α to the iodide at 3.20 ppm.
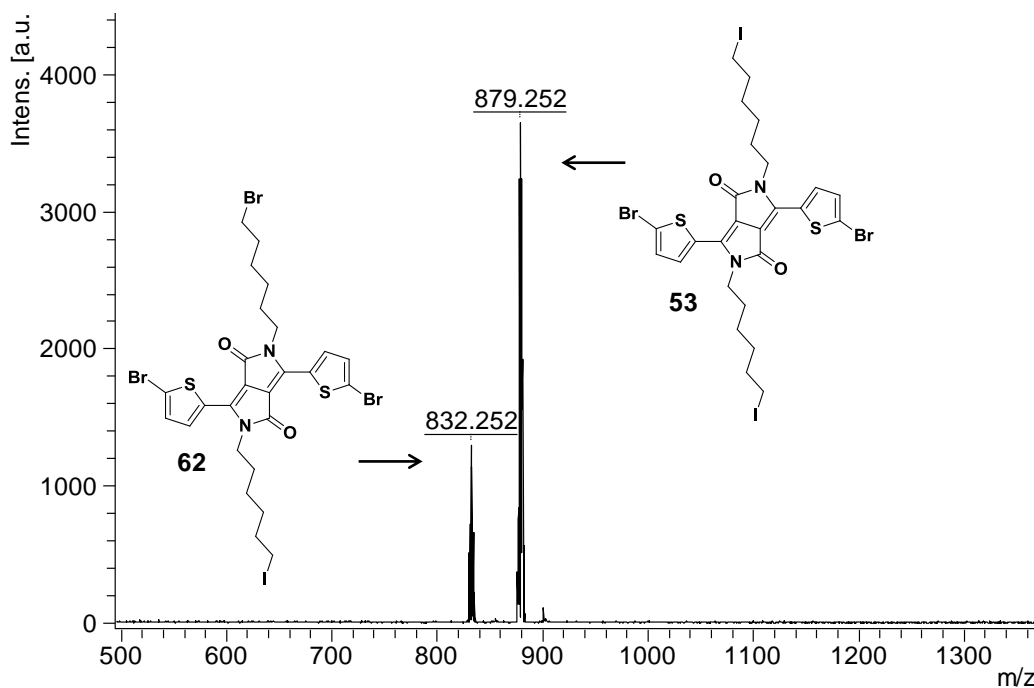
Figure 3.4 Matrix assisted laser desorption ionization time of flight (MALDI-TOF) mass spectrum of dibrominated-bis(iodohexyl)DPP (**53**) (m/z = 879.252) and dibrominated-(iodo-hexyl)-(bromo-hexyl) side-product (**62**) (m/z = 832.252). Reproduced from reference 41.

After isolating **53**, it was reacted with 2M dimethylamine in THF to give

dibrominated-bis(dimethylaminohexyl)DPP **54**. Dibromide **56** was subjected to similar

alkylation and amination to give **58**. Ring-opening of 1,3-propanesultone with the amines

of **54** and **58** in THF gave the desired A$_2$ zwitterionic DPP and *i*In monomers **55** and **59**,

respectively. Compounds **55** and **59** were observed to precipitate as deeply colored solids, and were isolated easily by filtration and washing with THF to remove excess 1,3-propanesultone. Mass spectroscopy confirmed the identity of both **55** ([M+H]$^+$ found 957.31) and **59** ([M+H]$^+$ found 919.04) (**Figure 3.5**). ^{1}H NMR of **55** and **59** were obtained as solutions in 2,2,2,-trifluoroethanol-d_3, identifying signatures of the pendant SB-zwitterions (multiplet at 3.4 ppm for the 4 protons α to the sulfonates; singlet at 3.0 ppm for the 12 methyl protons of the ammoniums).
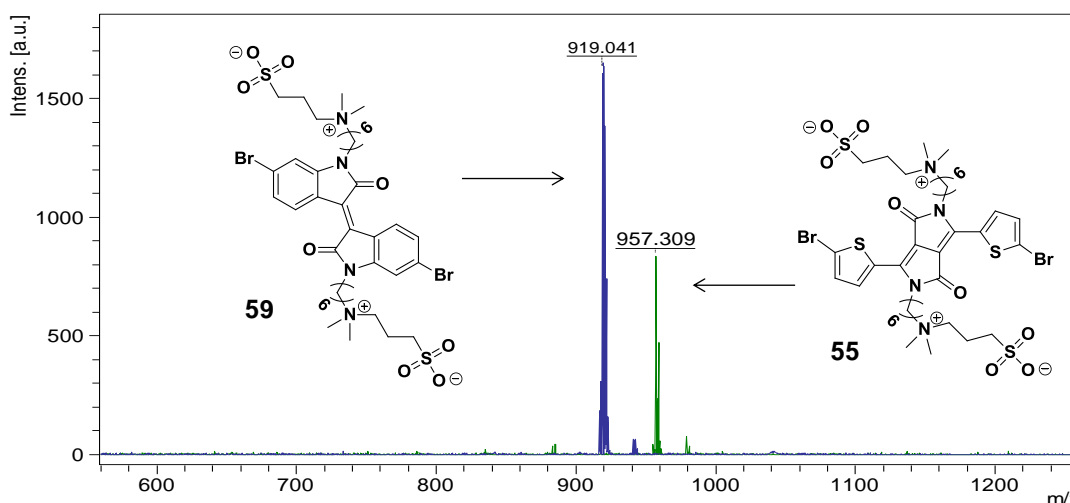
Figure 3.5 Overlay of MALDI-TOF mass spectra of DPPSB monomer **55** and *i*InSB monomer **59**. Reproduced from reference 41.

As shown in **Figure 3.6**, monomers **55** and **59** were polymerized with aromatic diboronic esters **25**, **26**, and **63** to afford the desired CPZs. Specifically, Suzuki-Miyaura (SM) polymerization with diboronic ester-thiophene **25** gave **PT₃DPPSB** (**39**) and **PT*i*InSB** (**42**); with diboronic ester-benzothiadiazole **26** gave **PT₂BTDPPSB** (**40**) and **PBT*i*InSB** (**43**); and with diboronic ester-bithiophene, **63** gave **PT₃DPPSB** (**41**) and **PT₂*i*InSB** (**44**), respectively (**Figure 3.6**). Polymerizations were run at 110 °C in the absence of light for 24 hours for the DPP-based CPZs, and at 90 °C for 10 hours for *i*In-based CPZs. Important among reaction conditions was the selection of base, noting that

potassium carbonate led to degradation of the *iso*indgo materials, probably a result of hydrolysis that affords brominated isatin and oxindole derivatives.[43,44] Tetra-n-butylammonium fluoride (TBAF) was found effective as an alternative,[45] providing enhanced solubility of the reaction mixture compared to the aqueous and ionic liquid conditions we described previously.[39,40] The enhanced solubility in TBAF solution led to rapid coupling and higher molecular weights ($\approx$20 kDa DPP polymers obtained using TBAF; $\approx$5 kDa using $K_2CO_{3(aq)}$). CPZs obtained in this fashion were purified by sequential Soxhlet extraction with tetrahydrofuran, acetone, MeOH, and trifluoroethanol (TFE), followed by dialysis against pure water. MeOH extraction removed oligomers, and the polymers precipitated during dialysis against pure water. Lyophilization gave the CPZs as fluffy powders, and molecular weight was estimated by size exclusion chromatography (SEC) (**Figure 3.6C**), giving values in the range of 10-20 kDa (eluting in TFE with 0.02 M silver trifluoroacetate). These CPZs displayed excellent solubility (> 20 mg/mL) in fluorinated alcohols (TFE and hexafluoroisopropanol (HFIP)), good solubility in salt-water ($\approx$10 mg/mL) and poor solubility in pure (salt-free) water.
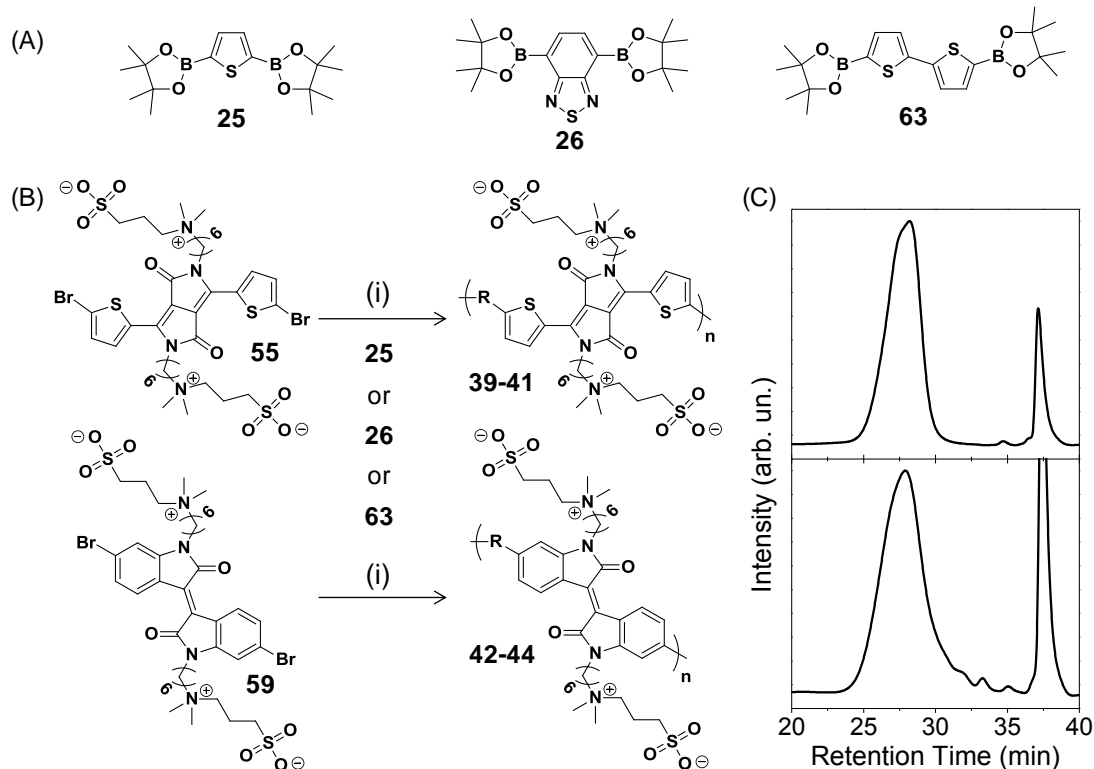
Figure 3.6 (A) Chemical structures of bis(boronic ester) B_2 monomers (**25**, **26** and **63**) used in SM polymerization; (B) SM polymerization of dibromides **55** and **59** with boronic-ester monomers **25**, **26** and **63** to give corresponding thiophene (**PT₃DPPSB** and **PT*i*InSB**), benzothiadiazole (**PT₂BTDPPSB** and **PBT*i*InSB**) and bithiophene polymers (**PT₄DPPSB** and **PT₂*i*InSB**). Reagents and conditions: (i) **25**, **26** or **63**, Pd₂(dba)₃, XPhos, Toluene, TBAF₍ₐq₎. (C) Representative SEC traces of **PT₃DPPSB** (M_n = 17 kDa) and **PT*i*InSB** (M_n = 17 kDa). Reproduced from reference 41.

The electronic properties of the CPZs prepared were examined by UV-Vis absorption spectroscopy (**Figures 3.7** and **3.8**, **Table 3.1**). Optical E_g were determined from the absorption onset of polymers in the solid state, giving values of 1.2-1.7 eV, similar to their alkyl counterparts (**Table 3.1**). Thus, in these CPZs, the hydrocarbon spacer between the zwitterions and the backbone precludes substantive impact on the E_g.[39] Optical attenuation coefficients (α) were determined on CPZ films cast onto glass with film thickness measured by profilometry: the DPP CPZs structures had α_{max} in the range of 84,000-95,000 cm⁻¹ and the *i*In CPZ structures from 35,000-45,000 cm⁻¹ (**Figure 3.7**).
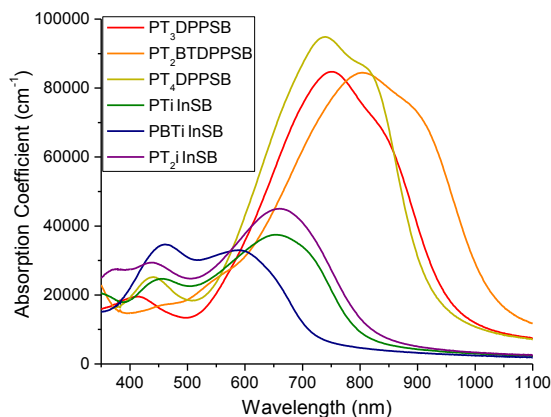
Figure 3.7 UV-Vis absorption of narrow energy gap CPZ films. Optical energy gaps were determined from the absorption onset (1.2 to 1.7 eV). Reproduced from reference 41.

For thin films, the thickness was estimated by UV-Vis absorption spectroscopy using the Beer-Lambert law with the pre-determined α and measured absorption intensity (*A*). The UV-Vis spectra of the branched-alkyl analogues contained more intense vibronic peaks/shoulders relative to the CPZs, attributed to their greater propensity to π-stack in the solid state (**Figure 3.8**).
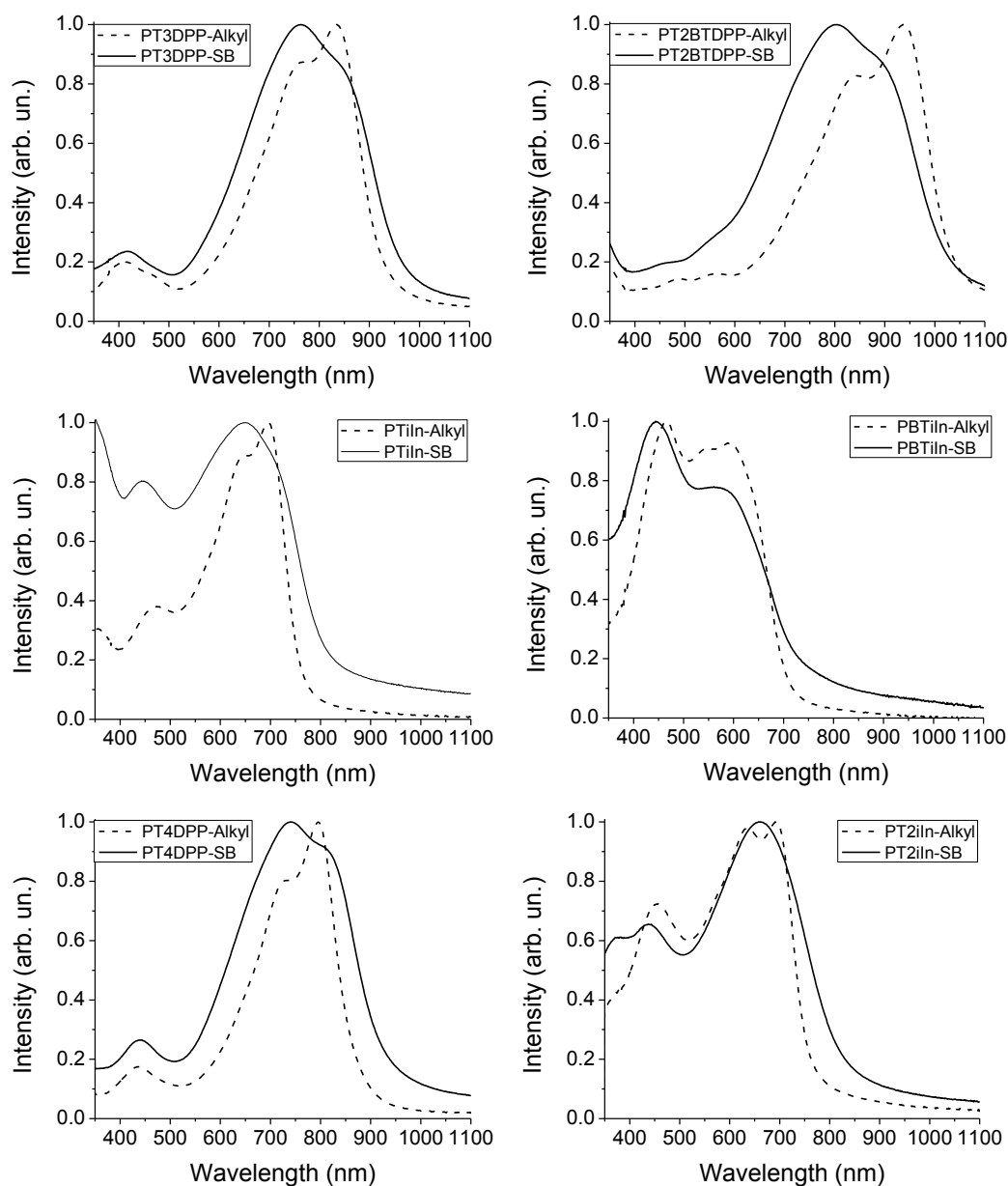
Figure 3.8 UV-Vis absorption of polymer films for CPZs (solid lines) and the branched alkyl analogues (dashed lines). Reproduced from reference 41.

The DPP and *i*In CPZs were cast as thin films (≈5 nm) on freshly prepared Ag substrates, and UPS was used to determine ionization potential (I_P) (low binding energy onset) and Δ (high binding energy secondary electron cutoff, E_{SEC}) (**Figure 3.9**). Taken together with the optical E_g determined using UV-Vis absorption spectroscopy, electron affinity (E_A) was calculated (**Table 3.1**). The E_A values for the DPPs (3.48 – 3.26 eV) are

80

substantially smaller than the *i*Ins (4.15 – 4.05 eV) and may act as a barrier to electron extraction in devices that contain an acceptor with higher E_A (PC$_{71}$BM = 3.83 eV). The Δ values were 0.3 – 0.6 eV larger for the CPZ polymers containing zwitterionic sulfobetaine side-chains compared to the analogous polymers containing branched alkyl side-chains. All of the SB-containing polymers had Δ values of approximately -0.9 eV, modifying the work function of Ag (Φ_{Ag}^m) from 4.5 eV to 3.6 eV at the CPZ/Ag interface, which allows Ag to be used as an effective cathode in PSCs by providing an ample built-in electrostatic potential across the device. The larger Δ values for the CPZs must result from interactions of the pendant zwitterions with the metal substrate, since the zwitterions are too far removed from the polymer backbone to influence its electronic characteristics directly.

Table 3.1 Summary of electronic energy levels of narrow E_g CPZs and their alkylated analogues, and their measured Δ values on Ag. Values determined by UPS and UV-Vis absorption spectroscopy. Reproduced from reference 41.

Polymer	E_g (eV)	I_P (eV)	E_A (eV)	Δ (eV)
PT$_3$DPPSB (**39**)	1.29	4.68	3.39	-0.89 ± 0.02
PT$_3$DPP-alkyl (**45**)	1.34	4.89	3.55	-0.34 ± 0.08
PT$_2$BTDPPSB (**40**)	1.22	4.70	3.48	-0.84 ± 0.01
PT$_2$BTDPP-alkyl (**46**)	1.21	4.97	3.76	-0.54 ± 0.04
PT$_4$DPPSB (**41**)	1.35	4.61	3.26	-0.89 ± 0.02
PT$_4$DPP-alkyl (**47**)	1.43	4.72	3.29	-0.30 ± 0.04
PT*i*InSB (**42**)	1.54	5.69	4.15	-0.87 ± 0.02
PT*i*In-alkyl (**48**)	1.63	5.84	4.20	-0.36 ± 0.05
PBT*i*InSB (**43**)	1.69	5.76	4.07	-0.87 ± 0.01
PBT*i*In-alkyl (**49**)	1.74	5.78	4.00	-0.36 ± 0.07
PT$_2$*i*InSB (**44**)	1.50	5.55	4.05	-0.89 ± 0.02
PT$_2$*i*In-alkyl (**50**)	1.63	5.96	4.33	-0.32 ± 0.01

Bulk heterojunction (BHJ) photovoltaic devices were fabricated with the following architecture: ITO/PEDOT:PSS/(PTB7:PC$_{71}$BM)/**CPZ**/Ag (**Figure 3.9A**). The PTB7:PC$_{71}$BM active layer was cast from 1,2-dichlorobenzene (*o*DCB), and the CPZ

layers from 2,2,2-trifluoroethanol (TFE). The active layer is insoluble in TFE, allowing for effective layer-by-layer deposition without disrupting the underlying BHJ.
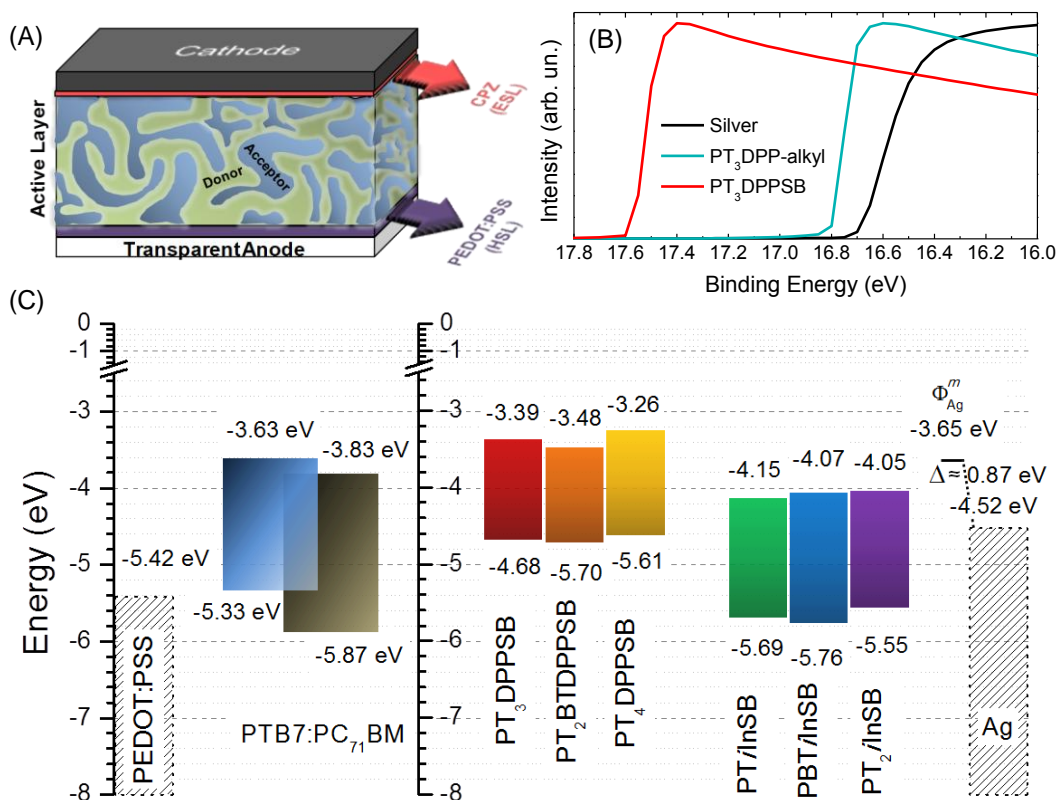
Figure 3.9 (A) Illustration of device architecture using CPZs as the cathode modification layer; (B) Representative UPS spectra showing the E_{SEC} onset used to determine Δ for narrow E_g **PT₃DPPSB** zwitterion vs **PT₃DPP-alkyl** on Ag; (C) Summary of UPS and UV-Vis absorption measurements, giving electronic energy levels of the materials comprising the solar cells, with a common vacuum level energy scale. Φ_{Ag}^m represents the average work function at the modified Ag/CPZ interface, given an $\Delta = 0.87$ eV. *The E_A energies for all materials, except PC₇₁BM, were calculated from $I_P - E_g$; **The E_A energy of PC₇₁BM was determined by cyclic voltammetry (CV). Reproduced from reference 41.

Reference OPV devices fabricated without a CPZ interlayer (bare Ag cathode, **Figure 3.10**) had low efficiencies (PCE = 1.55 ± 0.01 %) due to a low V_{OC} (0.29 V) and the high work function (Φ) intrinsic to Ag. This results in a small built-in electrostatic potential difference and low J_{SC} (15.2 mA/cm^2) and FF (36 %). Thin ($\approx$1.5 nm) LiF interlayers at the cathode did not significantly enhance device performance.[16] However, thin layers (4-10 nm) of the CPZs led to very significant improvements in PCE, reaching

over 7% in most cases, one of the highest reported PCE values at the time for a single-junction PSC with a Ag cathode, noting a report of a 3.5 nm layer of bathocuproine that gave 7.7% PCE.[46] Specifically, optimized interlayer thickness (4-10 nm) resulted in the following PCE values for the respective CPZs: 6.81 ± 0.13% for **PT$_3$DPPSB**, 7.65 ± 0.11% for **PT$_2$BTDPPSB**, 6.73 ± 0.20% for **PT$_4$DPPSB**, 7.73 ± 0.20% for **PTiInSB**, 7.42 ± 0.10% for **PBTiInSB**, and 7.28 ± 0.10% for **PT$_2$$i$InSB**. The enhancement in PCE relative to OPVs containing a bare Ag cathode is attributed directly to a doubling of V_{OC} ($\approx$ 0.67 V) and *FF* ($\approx$ 61 %) and an increase of J_{SC} ($\approx$ 18.0 mA/cm^2) (**Figure 3.10**). This demonstrates that buffer layers need not possess a wide E_g to afford efficient OPVs. Wide E_g interlayers might be expected to perform as more effective interlayers due a better confinement of excitons to the active layer. However, it has been suggested that photoactive interlayers, such as the ones described in this section, provide an avenue for charge formation given their capability to absorb solar radiation and provide a new interface where exciton separation may occur.[47,48] For the CPZs described here, the best solar cells fabricated (PCE 7.65%) contained the narrowest E_g CPZ, **PT$_2$BTDPPSB** (1.22 eV). Thus, the effectiveness of a conjugated polymer interlayer cannot be predicted based solely on the position of its energy levels, and narrow E_g materials prove effective as candidates in novel interlayer design and synthesis.
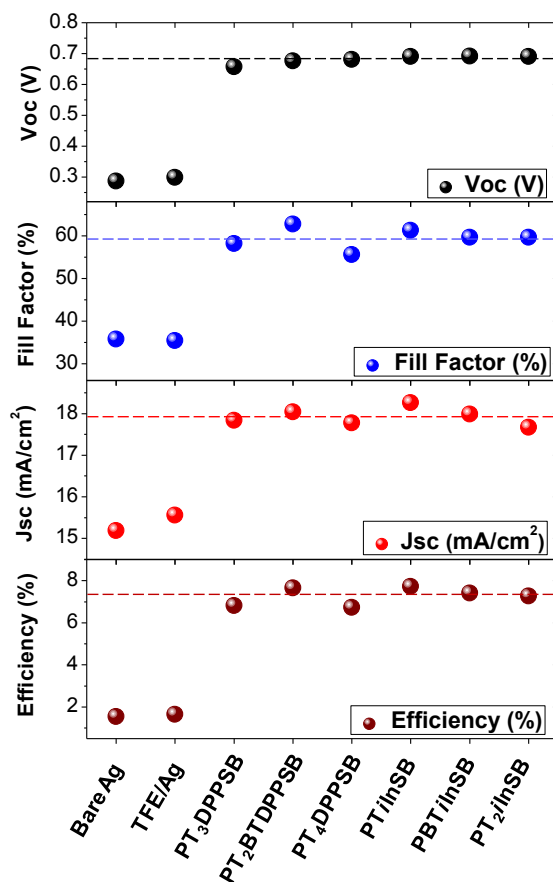
Figure 3.10 Device metrics of solar cells containing a thin CPZ layer between the active layer (PTB7:PC$_{71}$BM) and Ag cathode. Dashed line represents the average of each metric for the six interlayers. Reproduced from reference 41.

Thiophene-based CPZs require precise control over interlayer thickness to achieve the desired high PCE values of solar cells containing these interlayers. For example, for **PTBTSB-2**, increasing interlayer thickness from 5.2 to 9.3 nm led to an "S-shaped" J-V curve and reduced *FF* (48% for 5.2 nm to 16% for 9.3 nm) and PCE (5.81% for 5.2 nm and 1.67% for 9.3 nm) (**Figure 3.11A**).[16] The "S-shaped" J-V curve for the device having the thicker interlayer can be attributed to charge accumulation at the BHJ/electrode interface that would result from inefficient surface recombination at the electrode or insufficient charge transport properties of the CPZs.[16] For the narrow E_g

CPZs, optimal OPV device performance was obtained with 5 ± 1 nm interlayers, with the exception of **PT₂BTDPPSB**, which had an optimal thickness of ~9 nm.
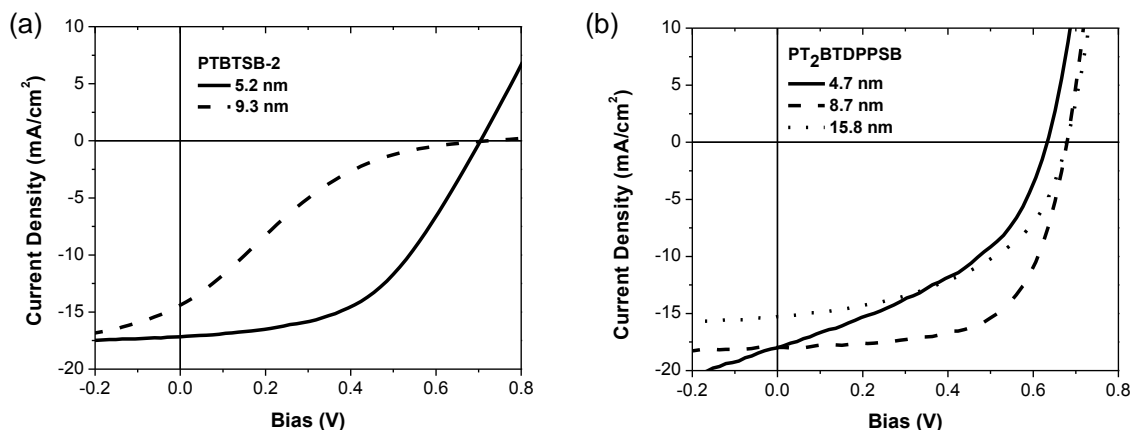
Figure 3.11 J-V characteristics of OPVs with two different CPZ interlayer thicknesses given the following device architecture; ITO/PEDOT:PSS/PTB7:PC$_{71}$BM/CPZ/Ag. Showing the effect of film thickness on OPV device performance for (A) **PTBTSB-2**[16] (B) **PT₂BTDPPSB**. Reproduced from reference 41.

OPVs prepared with low band gap CPZ interlayers did not produce the "S-shaped" J-V curves seen for devices containing the thiophene-based CPZs (PTSB/PTBTSB series).[16] For the case of **PT₂BTDPPSB**, interlayers of 4.7, 8.7 and 15.8 nm thickness led to PCE values of 4.9, 7.65 and 5.0% respectively, with no "S-shaped" curves (**Figure 3.12B**). If the presence of an "S-shaped" curve is attributed to charge build-up at the BHJ/cathode interface, then we speculate that an enhanced electron mobility of the narrow E_g CPZs relative to those previously reported (PTSB/PTBTSB),[16] allows for more efficient electron transport through the CPZ interlayer. This may be expected given the high charge mobilities measured for numerous DPP and *i*In-based conjugated polymers,[44,49].

3.3 Naphthalene diimide: synthesis and solar cells

The synthesis of SB-functionalized thiophene, DPP and NDI monomers hinged on incorporating tertiary amines into the aromatic monomer precursors for ring-opening

of 1,3-propanesultone (**Scheme 3.2**). Specifically, NDISB (**66**) monomer synthesis began by reacting dibromo-naphthalenetetracarboxylic dianhydride (**64**) with dimethylaminohexylamine in acetic acid to afford the tertiary amine functionaized diimide (**65**), followed by SB formation. As shown in **Scheme 3.2,** CPZs were obtained by SM coupling/polymerization of dibrominated SB-monomers with diboronic ester bithiophene (**63**) to give poly(bithiophene naphthalene diimide sulfobetaine) (**PT$_2$NDISB**) (**67**) and poly(trithiophene sulfobetaine) (**PT$_3$SB**) (**68**), as well as with diboronic-ester benzothiadiazole to afford poly(bithiophene-benzothiadiazole diketopyrrolopyrrole-sulfobetaine) (**PT$_2$BTDPPSB**) (**40**) (**Figure 3.12**).
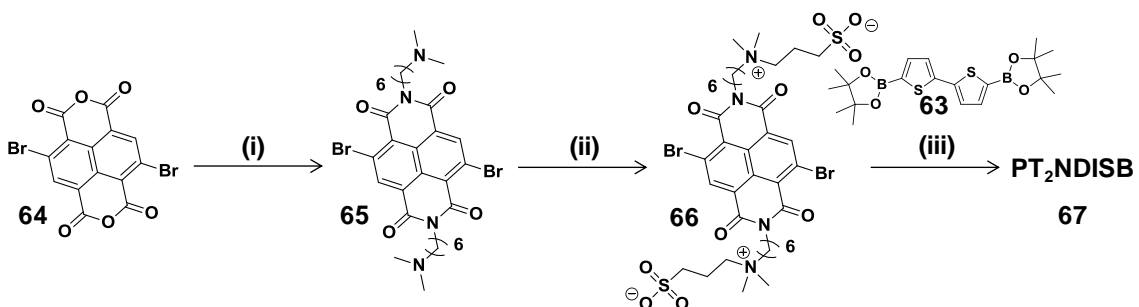
Scheme 3.2 Synthesis of zwitterionic NDI polymer, **PT$_2$NDISB** (**67**). Reagents and conditions: (i) 6-(dimethylaminohexyl)amine, CH$_3$COOH, 18%; (ii) 1,3-propanesultone, THF, 90%; (iii) **63**, Pd$_2$(dba)$_3$, XPhos, Toluene, TBAF$_{(aq)}$, 92%.

Aqueous TBAF, selected as base and solvent, proved crucial for maintaining solubility during the course of the polymerization. Estimated number-average molecular weight (M_n) values of the resulting polymers were 20-40 kDa (determined by SEC in TFE relative to PMMA standards).[41] CPZs in this molecular weight range gave uniform films (average roughness of ~1 nm, according to atomic force microscopy (AFM) analysis following spin-casting onto the BHJ active layer, **Figure 3.13**).
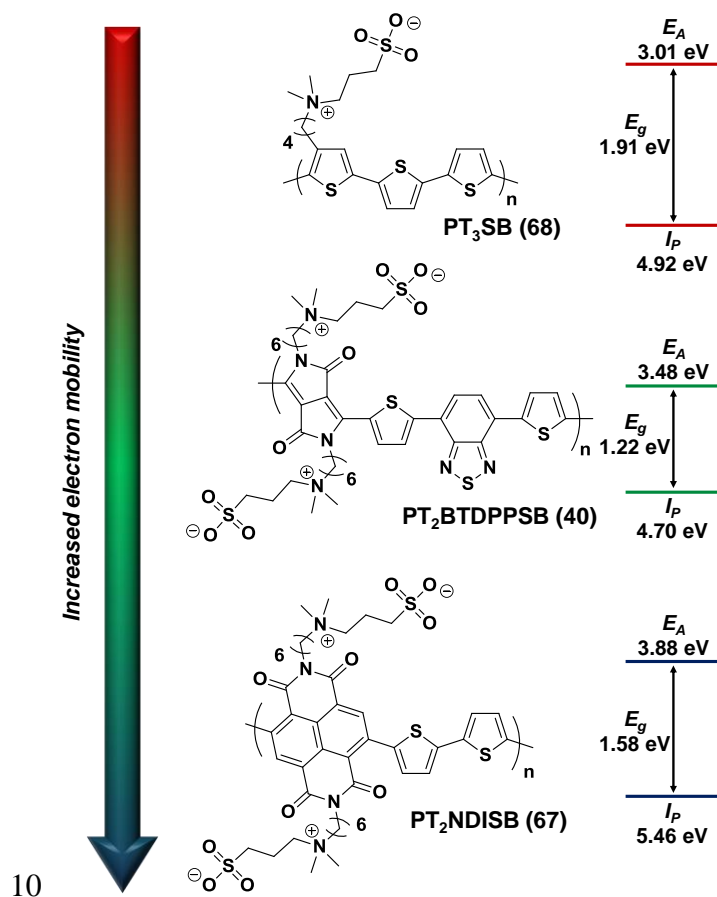
Figure 3.12 Chemical structures and experimentally determined energy levels for **PT$_3$SB** (**68**), **PT$_2$BTDPPSB** (**40**) and **PT$_2$NDISB** (**67**).

The resulting novel **PT$_3$SB** was designed to contain a similar density of SB side chains to that of **PT$_2$BTDPPSB** and **PT$_2$NDISB**, in an attempt to impart comparable CPZ-metal interactions for electrode Φ modification across the different samples studied, while maintaining good solution processability. The DPP interlayer was chosen as a bench-mark, given its excellent performance as a cathode modification layer in PSCs relative to prior CPZs tested.[16,41] The novel **PT$_2$NDISB** was synthesized and incorporated into PSCs for comparison with the thiophene and DPP cases, potentially benefiting from the distinct n-type electronic properties identified in alkyl-substituted NDI polymers.[50,51]
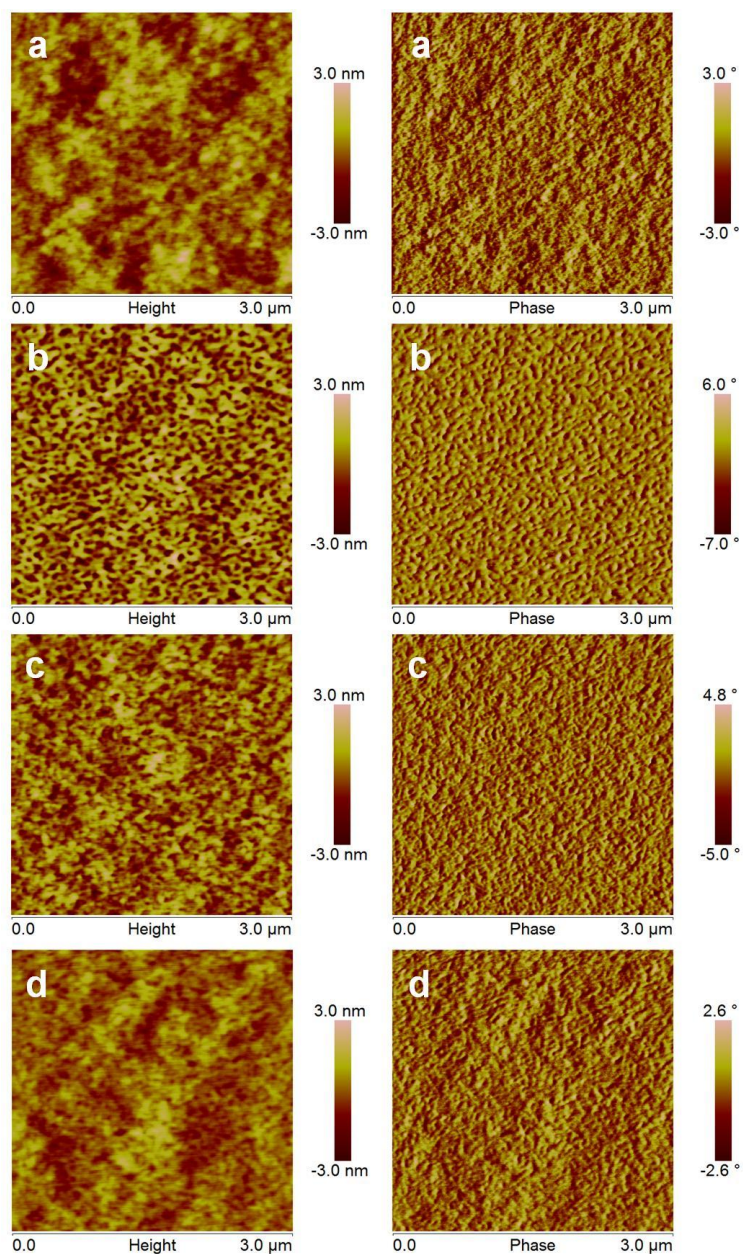
Figure 3.13 Atomic force microscopy images of CPZs on the photoactive layer, giving average roughness values of ~1 nm. (a) No interlayer (BHJ surface); (b) **PT₃SB** (4.3 nm thick film); (c) **PT₂BTDPPSB** (7.7 nm thick film); (d) **PT₂NDISB** (7.7 nm thick film).

Optical E_g values were determined on thin CPZ films from their absorption onset (**Figure 3.14**), noting that **PT₃SB** had the largest E_g (1.91 eV, red), **PT₂BTDPPSB** the smallest E_g (1.22 eV, green) and **PT₂NDISB** was intermediate between (E_g = 1.58 eV, blue) (**Figure 3.12**).
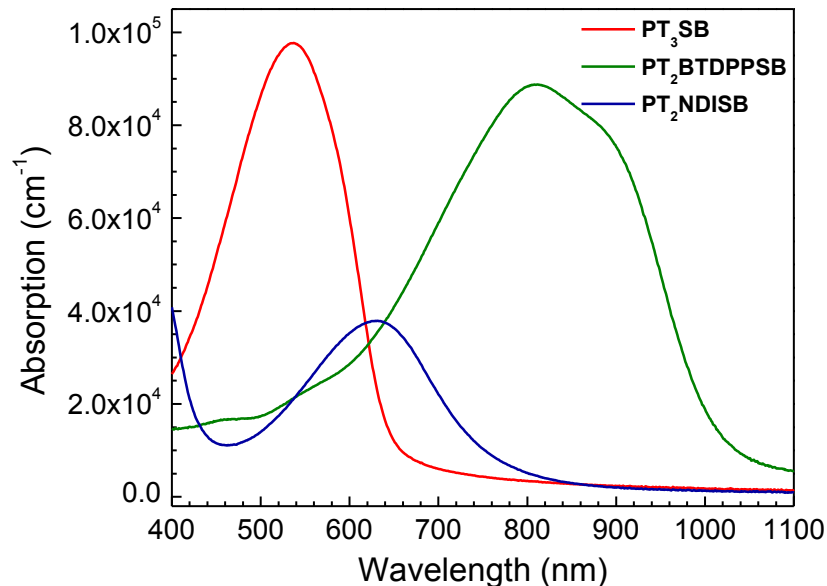
Figure 3.14 UV-Vis absorption spectra of CPZ films. Onset of absorption was used to determine E_g values (1.91 eV for **PT₃SB**, 1.22 eV for **PT₂BTDPPSB** and 1.58 eV for **PT₂NDISB**).

I_P values were determined by UPS, with E_A taken as the difference between I_P and E_g. The higher I_P (5.46 eV) and E_A (3.88 eV) values for **PT₂NDISB** suggest hole-blocking and electron extracting capabilities, respectively, relative to **PT₃SB** and **PT₂BTDPPSB**. For an interlayer that bridges the active layer and cathode, a large E_A minimizes the barrier to electron transport from the active layer to the interlayer, which in turn minimizes R_s.

OPV devices were fabricated in a BHJ device architecture, using the narrow E_g donor polymer, poly(benzodithiophene-*a*-thieno[3,4-*b*]thiophene) with 2-(ethylhexyl)thienyl side chains (PBDTT-TT) (**69**), purchased from 1-Material Inc., and [6,6]-phenyl C₇₁-butyric acid methyl ester (PC₇₁BM) (**38**) as the acceptor (**Figure 3.15**).
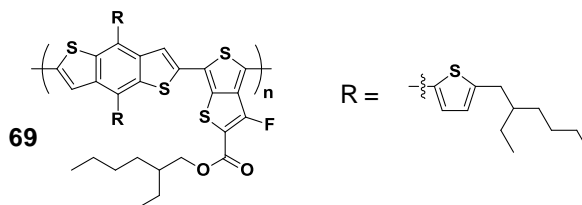
Figure 3.15 Chemical structure of donor polymer **69** (PBDTT-TT) used in this study.

An ITO/PEDOT:PSS/PBDTT-TT:$PC_{71}BM$/CPZ/Ag architecture was utilized for all fabricated PSCs. The CPZ was placed between the active layer and top reflective Ag cathode, selecting Ag in place of more commonly used Al to highlight the utility of stable high Φ metal electrodes in conjunction with CPZ interlayers. **Figure 3.16A** shows *J-V* curves for OPV devices containing no interlayer (bare Ag control) and **PT₃SB** (~5 nm), **PT₂BTDPPSB** (~8 nm) and **PT₂NDISB** (~5 nm) interlayers of optimal thickness. The bare Ag devices gave a maximum PCE of 3.17%, while incorporation of **PT₃SB**, **PT₂BTDPPSB** and **PT₂NDISB** interlayers improved PCE to *average/maximum* values of 5.08/5.09%, 9.39/9.49% and 9.94/10.19% respectively, where averages were calculated over six device measurements (**Tables 3.2-3.4**). This markedly improved device performance stems from the substantial increase in V_{OC} (~0.44 to 0.75 V) and *FF* (~42 to 70%), as well as J_{SC} (~17.5 to 19 mA/cm^2) and reduced R_s (~9.5 to 3.5 $\Omega \cdot$cm^2) for **PT₂NDISB** relative to bare Ag control devices. The effect of CPZ interlayer thickness on device performance was investigated by varying CPZ concentration for spin coating, yielding thicknesses from nominally 1 nm up to >20 nm (**Figure 3.16B** and **Tables 3.2-3.4**).
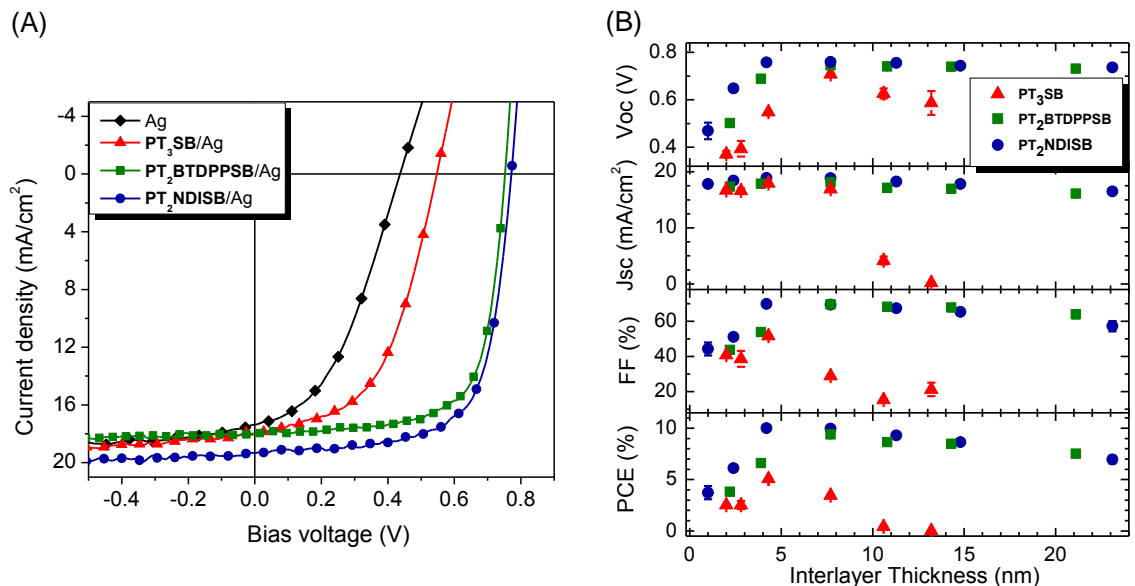
Figure 3.16 Solar cell performance of OPV devices with the architecture and composition of ITO/PEDOT:PSS/PBDTT-TT:PC$_{71}$BM/(**CPZ**)/Ag. (A) *J-V* curves for OPV devices containing no interlayer (bare Ag) and **PT$_3$SB**, **PT$_2$BTDPPSB** and **PT$_2$NDISB** interlayers; (B) OPV device metrics as a function of interlayer thickness (± 1 standard deviation for each point was obtained from more than six devices).

Table 3.2 Summarized photovoltaic performance of devices with architectures of ITO/PEDOT:PSS/PBDTT-TT:PC$_{71}$BM/**PT$_3$SB**/Ag. PCE error represents $\pm$ 1 standard deviation for averages obtained over six devices; PCE$_{max}$ is given parenthetically.

Thickness (nm)	V_{OC} (V)	J_{SC} (mA/cm^2)	FF (%)	PCE (%)	R_s ($\Omega \cdot$cm^2)
2.0	0.37	16.7	40.8	2.53 ± 0.12 (2.67)	10.8
2.8	0.39	16.6	38.6	2.53 ± 0.40 (3.03)	13.3
4.3	0.55	17.9	51.6	5.08 ± 0.01 (5.09)	9.5
7.7	0.71	16.9	28.9	3.46 ± 0.06 (3.54)	80.4
10.6	0.63	4.2	15.4	0.40 ± 0.07 (0.49)	402.3
13.2	0.59	0.2	21.3	0.02 ± 0.02 (0.04)	5497.7

Table 3.3 Summarized photovoltaic performance of devices with architectures of ITO/PEDOT:PSS/PBDTT-TT:PC$_{71}$BM/**PT$_2$BTDPPSB**/Ag. PCE error represents $\pm$ 1 standard deviation for averages obtained over six devices; PCE$_{max}$ is given parenthetically.

Thickness (nm)	V_{OC} (V)	J_{SC} (mA/cm^2)	FF (%)	PCE (%)	R_s ($\Omega \cdot$cm^2)
2.2	0.50	17.3	43.7	3.80 ± 0.19 (4.05)	9.5
3.9	0.69	17.9	53.7	6.60 ± 0.22 (7.00)	6.9
7.7	0.75	18.1	69.6	9.39 ± 0.11 (9.49)	3.5
10.8	0.74	17.2	68.1	8.65 ± 0.06 (8.73)	4.0
14.3	0.74	16.9	67.7	8.49 ± 0.06 (8.59)	4.1
21.1	0.73	16.1	63.9	7.52 ± 0.32 (7.87)	5.1

91

Table 3.4 Summarized photovoltaic performance of devices with architectures of ITO/PEDOT:PSS/PBDTT-TT:PC$_{71}$BM/**PT$_2$NDISB**/Ag. PCE error represents ± 1 standard deviation for averages obtained over six devices; PCE$_{max}$ is given parenthetically.

Thickness (nm)	V_{OC} (V)	J_{SC} (mA/cm^2)	FF (%)	PCE (%)	R_s (Ω·cm^2)
2.4	0.65	18.4	51.0	6.10 ± 0.28 (6.56)	7.5
4.2	0.76	18.9	69.7	9.99 ± 0.15 (10.17)	3.9
7.7	0.76	18.8	69.5	9.94 ± 0.27 (10.19)	3.7
11.3	0.76	18.3	67.3	9.29 ± 0.09 (9.43)	4.8
14.8	0.74	17.8	65.4	8.65 ± 0.12 (8.83)	6.0
23.1	0.74	16.5	57.2	6.95 ± 0.37 (7.63)	12.3

To determine thickness, UV-Vis absorption traces for **PT$_2$NDISB** cast from different concentrations at 4000 rpm onto clean glass substrates were gathered and the thicknesses were determined by taking an average over the wavelength region of 720-520 nm, given pre-determined attenuation coefficients (cm^{-1}) (**Figure 3.17**).
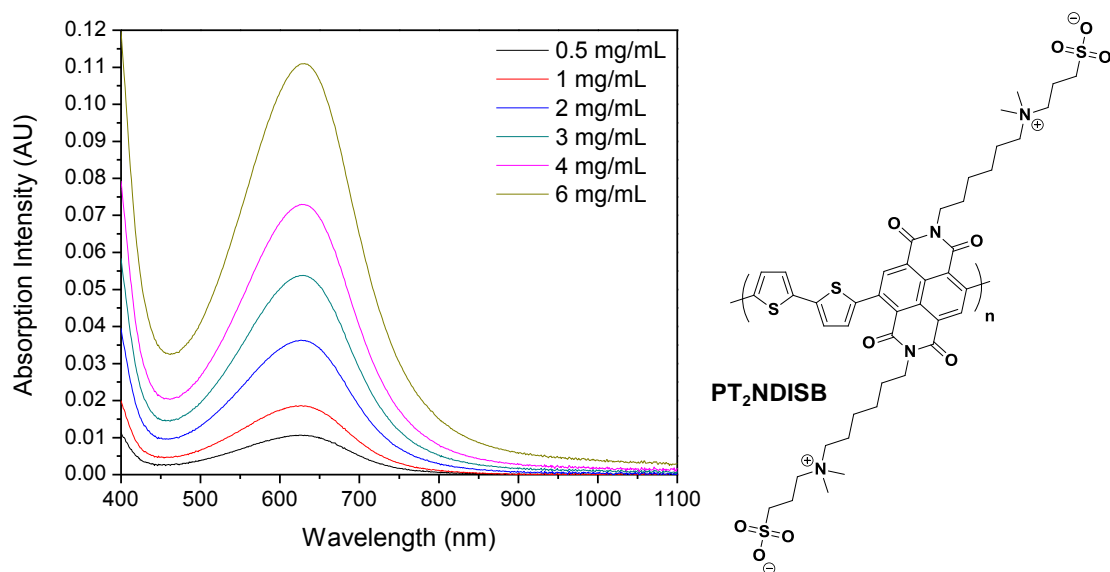
	Average thickness determined over 720 - 520 nm wavelengths					
PT$_2$NDISB	0.5 mg/mL	1 mg/mL	2 mg/mL	3 mg/mL	4 mg/mL	6 mg/mL
Thickness (nm)	2.7	4.8	9.4	14.0	19.0	29.3

Figure 3.17 UV-Vis absorption traces for **PT$_2$NDISB** cast from different concentrations at 4000 rpm onto clean glass substrates.

The performance of OPVs containing **PT$_3$SB** was sensitive to interlayer thickness, with appreciable reduction in PCE noted for layers exceeding 5 nm, due to a large decrease in *FF* and *J$_{SC}$* and increased *R$_s$* (**Table 3.2**). In contrast, both **PT$_2$DPPSB** (**Table 3.3**) and **PT$_2$NDISB** (**Table 3.4**) proved more tolerant to variation in interlayer thickness, with *V$_{OC}$* (~0.75 V), *FF* (~70%) and *R$_s$* (~ 3.5 Ω·cm^2) plateauing at 5-10 nm thickness, but maintaining near maximum values at > 20 nm thickness. In addition, *J$_{SC}$* was not significantly influenced by CPZ interlayer thickness, with values exceeding 16 mA/cm^2 across the entire thickness range investigated for **PT$_2$DPPSB** and **PT$_2$NDISB**.

The electronics of CPZ films were studied by UPS to determine their interaction with Ag (**Figure 3.18A**), and by space charge limited current (SCLC) measurements to estimate electron mobility (**Figure 3.18B**). By UPS, the *E$_{SEC}$* in the high binding energy region probes the effect of CPZs on the work function of Ag, where the difference in *E$_{SEC}$* for bare Ag and CPZ-coated Ag yields Δ values. Ultra-thin (<2 nm) CPZ layers led to an Δ ≈ -0.5 to -0.6 eV, corresponding to a reduction in work function from 4.45 eV (native Ag) to 3.9 eV. Increasing the CPZ layer thickness led to further work function reduction to 3.8 eV for **PT$_2$NDISB** and 3.6 eV for **PT$_3$SB** and **PT$_2$BTDPPSB** (**Figure 3.18A**), a finding attributed to better film uniformity and fewer pinholes.[16] Interlayer thickness tracked closely with *V$_{OC}$* values in the PSCs, with peak performance at ~8 nm interlayer thickness that remained nearly constant with increasing thickness.
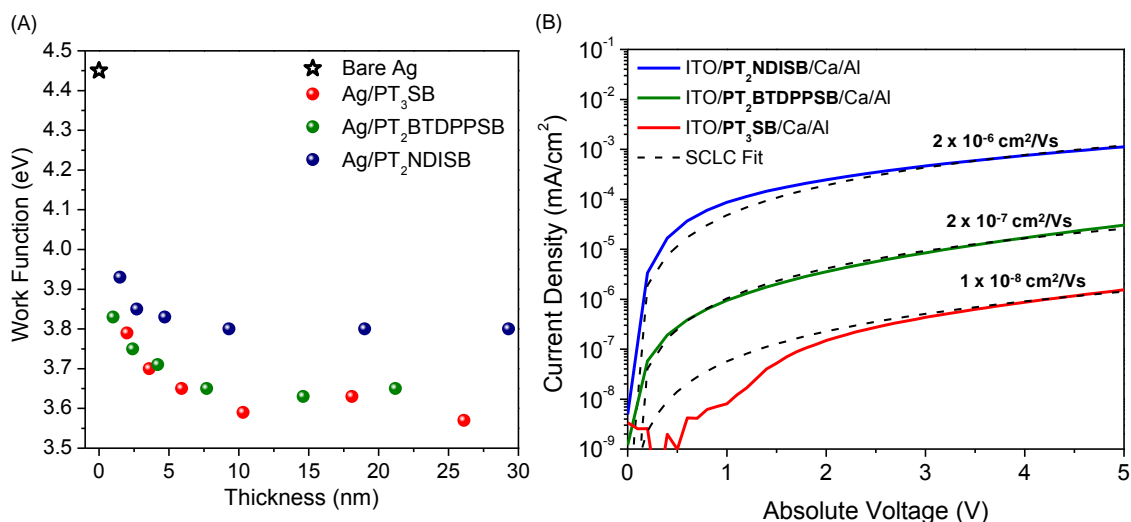
Figure 3.18 Electronic characterization of CPZ films. (A) Effect of CPZ thickness on the Φ of Ag; (B) Relative electron mobilities of CPZs estimated using the Mott-Gurney law in the SCLC regime for device architecture of ITO/CPZ/Ca/Al.

To better understand these findings, electron only devices with an architecture of ITO/CPZ/Ca/Al were fabricated to estimate electron mobility using SCLC and fitting with the Mott-Gurney law, finding 1×10^{-8} cm^2/Vs for **PT$_3$SB**, 2×10^{-7} cm^2/Vs for **PT$_2$BTDPPSB** and 2×10^{-6} cm^2/Vs for **PT$_2$NDISB** (**Figure 3.18B**). These values were obtained using dielectric constants (ε) of ~5, determined separately by impedance spectroscopy (**Figure 3.19**).
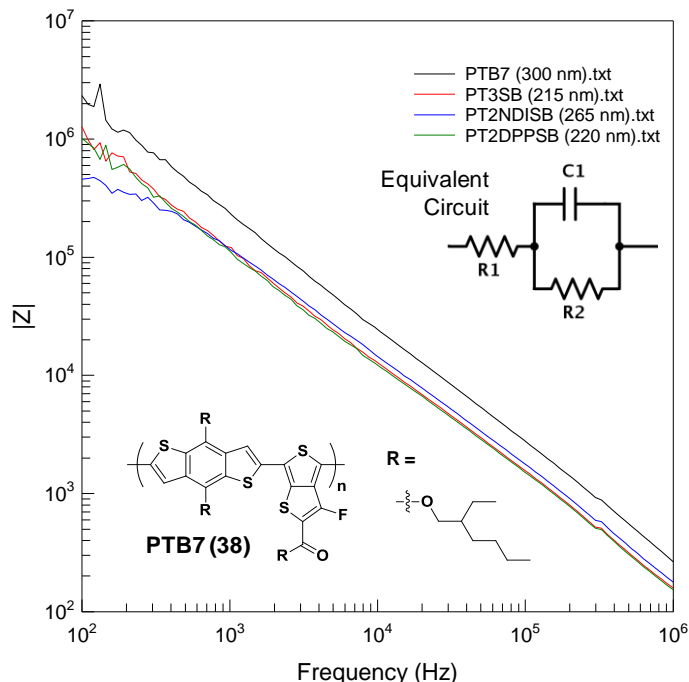
Figure 3.19 Representative impedance spectra utilized to determine capacitance values by fitting to the equivalent circuit model given as an inset.

The higher electron mobility of **PT$_2$BTDPPSB** and **PT$_2$NDISB** explain their superior performance with increasing interlayer thickness, as these interlayers are less prone to charge accumulation at the active-layer/CPZ interface which would lead to increased R_s and reduced *FF* and J_{SC} (**Figure 3.16B**). The small E_A for **PT$_3$SB** may contribute to its inferior performance relative to the other polymers. For **PT$_2$BTDPPSB** and **PT$_2$NDISB**, the relatively constant *FF* for devices with interlayer thickness exceeding 5 nm suggests that electron transport is not significantly impeded through these thicker layers, irrespective of their difference in electron mobility.

Optical characterization of the PSCs distinguished interlayer and active layer absorption, providing insight as to the origin of J_{SC} enhancement. Reflectance spectroscopy performed on OPV devices containing a 4-8 nm CPZ interlayer were compared to devices with no interlayer. This revealed a 4% decrease in reflectance from

~650-700 nm, corresponding to enhanced absorption over those wavelengths for devices containing CPZ interlayers (**Figure 3.20** and **3.21**).
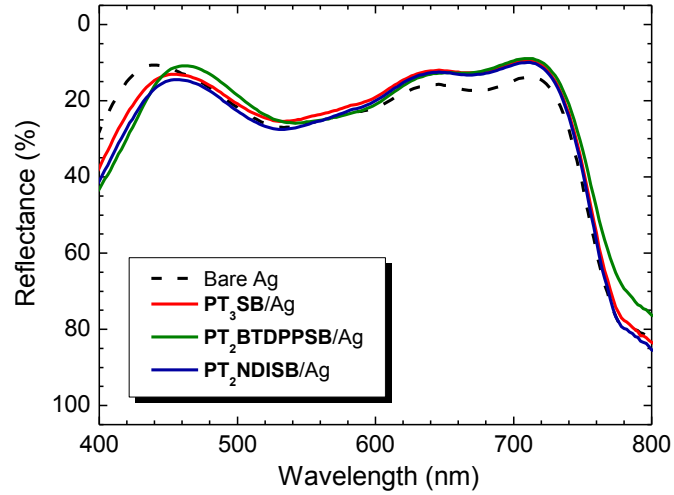
Figure 3.20 Representative reflectance spectra of optimized devices with CPZ interlayers and control device with no interlayer.
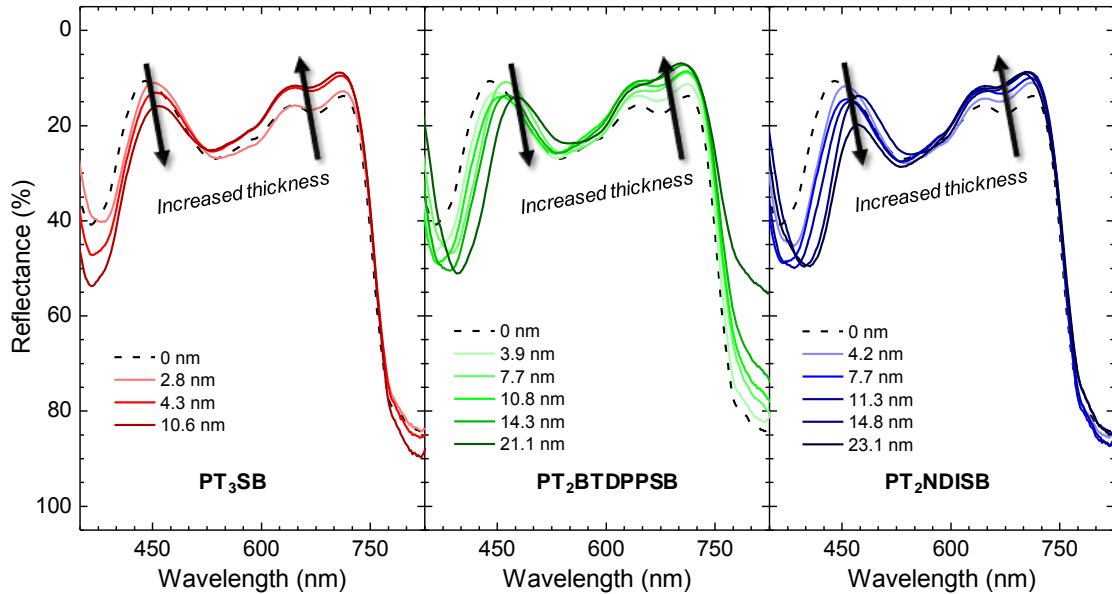
Figure 3.21 UV-Vis reflectance spectroscopy of OPV devices containing no interlayer (control) or **PT₃SB** (left), **PT₂BTDPPSB** (middle), and **PT₂NDISB** of varying thicknesses. Reflectance measured through the ITO substrate at 5° with respect to the surface normal.

External quantum efficiency (EQE) measurements show larger photocurrent collection in the active layer absorption regime (600-740 nm) for devices containing CPZ interlayers relative to devices with no interlayer (bare Ag control), corresponding to larger J_{SC} (**Figure 3.22**). Absorption from the CPZ interlayers (**Figure 3.14**) cannot account for the observed changes in reflectance spectra or EQE. Thus, the CPZs are considered as optical spacers that redistribute the optical field within the device and enhance active layer absorption.[15]
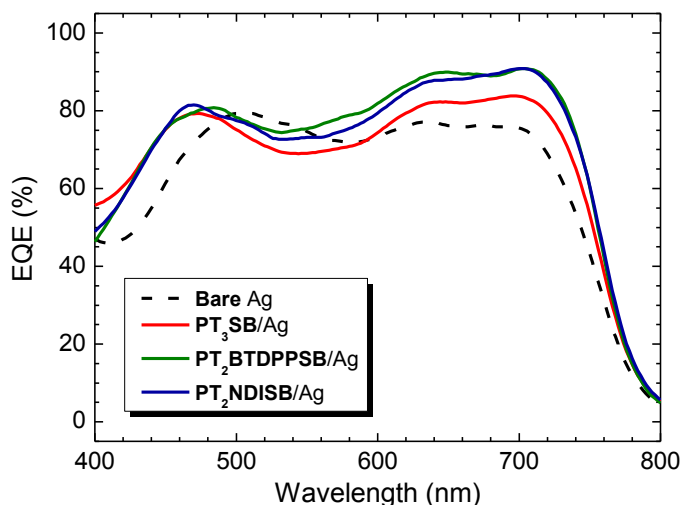
Figure 3.22 External quantum efficiency (EQE) spectra of optimized OPV devices containing CPZ interlayers vs. devices having no interlayer.

3.4 Summary and future outlook

In summary, seven novel narrow energy gap CPZs were synthesized, containing DPP, *i*In and NDI backbones, and sulfobetaine zwitterionic pendent groups. The photophysical properties of the CPZs were characterized by UV-Vis absorption and UPS to determine E_g, I_P, E_A and Δ as thin layers on Ag. These properties were compared with analogous polymers having aliphatic side chains, finding similar electronic properties of the polymers but substantially larger Δ values derived from the CPZs ($\Delta_{CPZ} \approx 0.87$ eV vs. $\Delta_{alkyl} \approx 0.37$ eV). This reduction in work function of the metal allowed it to be used as a

cathode in OPVs, affording efficient devices containing Ag cathodes, where the incorporation of DPP- and iIn-based interlayers (PTB7/PC$_{71}$BM active layer) led to PCE values on the order of 7%. For the case of **PT$_2$BTDPPSB** interlayers, thicker films could be introduced to the devices while maintaining efficient performance, which led to the development of **PT$_2$NDISB**. Optimized PCE values from 3.17% for devices containing no interfacial layer (bare Ag cathode) to 5.09%, 9.49% and 10.19% for devices containing **PT$_3$SB**, **PT$_2$BTDPPSB** and **PT$_2$NDISB** interlayers, respectively, were obtained. The dramatic improvement in device performance for the DPP and NDI-based interlayers stems from a combination of their ability to effectively lower the work function of the metal cathode, increase the built-in electrostatic device potential, and maintain a low R_s due to more efficient electron transport across the interlayer. The less efficient electron transport properties of **PT$_3$SB** leads to interfacial charge build-up and lower PCE values, while both **PT$_2$DPPSB** and **PT$_2$NDISB** maintain high PCE values for interlayer thickness exceeding 20 nm, due to their higher intrinsic electron mobilities. The CPZs act as optical spacers to enhance total photocurrent generated within the active layer. In particular, the NDI-based CPZ interlayers led to very high efficiencies, even exceeding 10% PCE. More importantly, the structure-property relationships revealed in this chapter provide guidelines for future development of functional interfaces and interlayers towards further enhancement of polymer-based solar cell technology.

3.5 References

1. Gendron, D.; Leclerc, M. *Energy Environ. Sci.* **2011**, *4*, 1225-1237.

2. Coffin, R. C.; Peet, J.; Rogers, J.; Bazan, G. C. *Nat. Chem.* **2009**, *1*, 657-661.

3. Henson, Z. B.; Zhang, Y.; Nguyen, T.-Q.; Seo, J. H.; Bazan, G. C. *J. Am. Chem. Soc.* **2013**, *135*, 4163-4166.

4.   Yip, H.-L.; Jen, A. K.-Y. *Energy Environ. Sci.* **2012**, *5*, 5994-6011.

5.   He, Z.; Wu, H.; Cao, Y. *Adv. Mater.* **2014**, *26*, 1006-1024.

6.   He, Z.; Zhong, C.; Su, S.; Xu, M.; Wu, H.; Cao, Y. *Nat. Photonics* **2012**, *6*, 591-595.

7.   Yao, K.; Salvador, M.; Chueh, C.; Xin, X.; Xu, Y.; Dane, W.; Hu, T.; Chen, Y.; Ginger, D. S.; Jen, A. K. *Adv. Energy Mater.* **2014**, *4*, 1400206.

8.   Zhang, W.; Wu, Y.; Bao, Q.; Gao, F.; Fang, J. *Adv. Energy Mater.* **2014**, *4*, 1400359.

9.   Guo, X.; Zhang, M.; Ma, W.; Ye, L.; Zhang, S.; Liu, S.; Ade, H.; Huang, F.; Hou, J. *Adv. Mater.* **2014**, *26*, 4043-4049.

10.   Li, C.-Z.; Chang, C.-Y.; Zang, Y.; Ju, H.-X.; Chueh, C.-C.; Liang, P.-W.; Cho, N.; Ginger, D. S.; Jen, A. K.-Y. *Adv. Mater.* **2014**, *26* (36), 6262-6267.

11.   Peumans, P.; Yakimov, A.; Forrest, S.R. *J. Appl. Phys.* **2003**, 93, 3693-3723.

12.   Schlaf, R.; Parkinson, B.A.; Lee, P.A.; Nebesny, K.W.; Jabbour, G.; Kippelen, B.; Peyghambarian, N.; Armstrong, N.R. *J. Appl. Phys.* **1998**, 84, 6729-6736.

13.   White, M.S.; Olson, D.C.; Shaheen, S.E.; Kopidakis, N.; Ginley, D.S. *Appl. Phys. Lett.* **2006**, 89, 143517.

14.   Dou, L. You, J. Yang, J. Chen, C.-C. He, Y. Murase, S. Moriarty, T. Emery, K. Li, G.; Yang, Y. *Nat. Photonics* **2012**, *6*, 180-185.

15.   Kim, J.Y.; Kim, S.H.; Lee, H.-H.; Lee, K.; Ma, W.; gong, X.; Heeger, A.J. *Adv. Mater.* **2006**, 18, 572-576.

16.   Liu, F.; Page, Z. A; Duzhko, V. V.; Russell, T. P.; Emrick, T. *Adv. Mater.* **2013**, *25*, 6868-6873.

17.   Seo, J. H.; Nguyen, T.-Q. *J. Am. Chem. Soc.* **2008**, 130, 10042-10043.

18.   Worfolk, B.J.; Hauger, T.C.; Harris, K.D.; Rider, D.A.; Fordyce, J.A.M.; Beaupre, S.; Leclerc, M.; and Buriak, J.M. *Adv. Energy Mater.* **2012**, 2, 361-368.

19.   He, Z.; Zhong, C.; Huang, X.; Wong, W.-Y.; Wu, H.; Chen, L.; Su, S.; and Cao, Y. *Adv. Mater.* **2011**, 23, 4636-4643.

20.   Krebs, F. C. *Sol. Energ. Mat. Sol. Cells* **2009**, *93*, 465-475.

21.   Krebs, F. C.; Gevorgyan, S. A.; Alstrup, J. *J. Mater. Chem.* **2009**, *19*, 5442-5451.

22.   O'Malley, K. M.; Li, C.-Z.; Yip, H.-L.; and Jen, A. K.-Y. *Adv. Energy Mater.* **2012**, 2, 82-86.

23.   Page, Z. A.; Liu, Y.; Duzhko, V. V.; Russell, T. P.; Emrick, T. *Science.* **2014**, *346*, 441-444.

24.   Yang, X.; Chueh, C.; Li, C.; Yip, H.; Yin, P.; Chen, H.; Chen, W.; Jen, A. K. *Adv. Energy Mater.* **2013**, *3*, 666-673.

25.   Chueh, C.; Chien, S.; Yip, H.; Salinas, J. F.; Li, C.; Chen, K.; Chen, F.; Chen, W.; Jen, A. K. *Adv. Energy Mater.* **2013**, *3*, 417-423.

26.   Mei, Q.; Li, C.; Gong, X.; Lu, H.; Jin, E.; Du, C.; Lu, Z.; Jiang, L.; Meng, X.; Wang, C.; Bo, Z. *ACS Appl. Mater. Interfaces* **2013**, *5*, 8076-8080.

27.   Li, S.; Lei, M.; Lv, M.; Watkins, S. E.; Tan, Z.; Zhu, J.; Hou, J.; Chen, X.; Li, Y. *Adv. Energy Mater.* **2013**, *3*, 1569-1574.

28.   Lai, Y.-Y.; Shih, P.-I.; Li, Y.-P.; Tsai, C.-E.; Wu, J.-S.; Cheng, Y.-J.; Hsu, C.-S. *ACS Appl. Mater. Interfaces* **2013**, *5*, 5122-5128.

29.   Li, X.; Zhang, W.; Wu, Y.; Min, C.; Fang, J. *J. Mater. Chem.* **2013**, *1*, 12413-12416.

30.   Duan, C.; Zhong, C.; Liu, C.; Huang, F.; Cao, Y. *Chem. Mater.* **2012**, *24*, 1682-1689.

31.   Zhang, Z.-G.; Qi, B.; Jin, Z.; Chi, D.; Qi, Z.; Li, Y.; Wang, J. *Energy Environ. Sci.* **2014**, *7*, 1966-1973.

32.   Chen, D.; Nakahara, A.; Wei, D.; Nordlund, D.; Russell, T. P. *Nano Lett.* **2011**, *11*, 561-567.

33.   Zhou, Y.; Fuentes-Hernandez, C.; Shim, J.; Meyer, J.; Giordano, A.J.; Li, H.; Winget, P.; Papadopoulos, T.; Cheun, H.; Kim, J.; Fenoll, M; Dindar, A.; Haske, W.; Najafabadi, E.; Khan, T. M.; Sojoudi, H.; Barlow, S.; Graham, S.; Brédas, J.-L.; Marder, S.R.; Kahn, A.; Kippelen, B.; *Science* **2012**, 336, 327-332.

34.   Yang, Y.; Wudl, F. *Adv. Mater.* **2009**, *21*, 1401-1403.

35.   Cowan, S. R.; Banerji, N.; Leong, W. L.; Heeger, A. J. *Adv. Funct. Mater.* **2012**, *22*, 1116-1128.

36.   Beaujuge, P. M.; Amb, C. M.; Reynolds, J. R. *Acc. Chem. Res.* **2010**, *43*, 1396-1407.

37.   Woo, S.; Hyun Kim, W.; Kim, H.; Yi, Y.; Lyu, H.-K.; Kim, Y. *Adv. Energy Mater.* **2014**, *4*, 1301692.

38. Gu, C.; Chen, Y.; Zhang, Z.; Xue, S.; Sun, S.; Zhong, C.; Zhang, H.; Lv, Y.; Li, F.; Huang, F.; Ma, Y. *Adv. Energy Mater.* **2014**, *4*, 1301771.

39. Page, Z. A.; Duzhko, V. V.; Emrick, T. *Macromolecules* **2013**, *46*, 344-351.

40. Page, Z. A.; Liu, F.; Russell, T. P.; Emrick, T. *Chem. Sci.* **2014**, *5*, 2368-2373.

41. Page, Z. A.; Liu, F.; Russell, T. P.; Emrick, T. *J. Polym. Sci., Part A Polym. Chem.***2015**, *53,* 327-336.

42. Liu, Y.; Page, Z. A.; Russell, T. P.; Emrick, T. *Submitted*, **2015**.

43. Mei, J.; Graham, K. R.; Stalder, R.; Reynolds, J. R. *Org. Lett.* **2010**, *12*, 660-663.

44. Overman, L. E.; Peterson, E. a *Tetrahedron* **2003**, *59*, 6905-6919.

45. Wu, X.-M.; Gu, Y.-B. *Lett. Org. Chem.* **2012**, *9*, 396-400.

46. Betancur, R.; Romero-gomez, P.; Martinez-otero, A.; Elias, X.; Maymo, M.; Martorell, J. *Nat. Photonics* **2013**, *7*, 995-1000.

47. Hau, S. K.; Yip, H.; Acton, O.; Baek, S.; Jen, A. K. *J. Mater. Chem.* **2008**, *18*, 5113-5119.

48. Mor, G. K.; Shankar, K.; Paulose, M.; Varghese, O. K.; Grimes, C. A. *Appl. Phys. Lett.* **2011**, *91*, 152111.

49. Li, Y.; Sonar, P.; Murphy, L.; Hong, W. *Energy Environ. Sci.* **2013**, *6*, 1684-1710.

50. Yan, H.; Chen, Z.; Zheng, Y.; Newman, C.; Quinn, J. R.; Dötz, F.; Kastler, M.; Facchetti, A. *Nature* **2009**, *457*, 679-686.

51. Hwang, Y.-J.; Earmme, T.; Courtright, B. a E.; Eberle, F. N.; Jenekhe, S. a. *J. Am. Chem. Soc.* **2015**, *137*, 4424-4434.

CHAPTER 4

FUNCTIONAL FULLEROPYRROLIDINE ZWITTERIONS

4.1 Introduction

Dramatic recent improvements in design and fabrication of bulk heterojunction (BHJ) polymer solar cells (PSCs) have produced devices with power conversion efficiency (PCE) values exceeding 9%.[1-5] However, achieving such high efficiencies often requires increasingly complex polymer synthesis and device architectures (*e.g.* tandem devices). In addition, the most common metal used as the device cathode, aluminum, is prone to rapid oxidation and cannot be processed from solution. More stable metals, such as silver, copper, and gold, can be deposited from solution, but their high work-function (Φ) limits attainable open circuit voltage (V_{OC}), short circuit current density (J_{SC}), and fill factor (*FF*) due to a low built-in electrostatic potential difference across the device.[6-8] To circumvent this limitation, a thin buffer layer, inserted between the active layer and cathode, tailors the interface to maximize V_{OC} and minimize contact resistance. Numerous inorganic buffer layers have been studied, such as Ca and LiF, while organic interlayers are often better suited to solution-based device fabrication.[9-11] Conductive interlayers, such as Ca, advantageous for their intrinsically low Φ; suffer from their sensitivity to oxygen and water. Polar organic interlayers permit layer-by-layer solution deposition, but often have poor adhesion to low-surface-energy active layers,[12] thus limiting their utility in conventional device architectures (as fabricated from anode-to-cathode). Furthermore, buffer layers are typically very thin (< 5 nm), so as to prevent charge build-up due to large injection barriers at the active layer/buffer layer interface or

slow charge transport through the buffer layer. However, from a processing standpoint, the need to reproduce precise nm or sub-nm interlayer thicknesses is in itself problematic.

An ideal cathode design for OPVs might consist of a metal with a high intrinsic work function to provide stability, and a readily tailored surface to lower the effective work function for the sake of device performance. This chapter shows that functionalized fullerenes bearing tertiary amine or sulfobetaine groups are easy to process from solution, manifest excellent adhesion to the photoactive layer, and afford OPV devices with outstanding PCE values even when employing high work function metals as cathodes.

Buffer layers, or interlayers, positioned at the active layer-cathode interface lower the work function of the cathode, with a magnitude frequently described as an interfacial dipole (Δ),[13] where large negative Δ values have produced some of the most effective reported OPVs. For example, solution-processed tertiary-amine substituted polyfluorene (PFN) yielded a maximum PCE of 9.21% in an inverted device,[1] and poly(ethyleneimine) (PEI) and its derivatives enabled all-solution-processed inverted devices with maximum PCE values of 8.9%.[14,15] In each case, the amine functionality of the interlayer is responsible for the large negative Δ values (< -0.5 eV).[14] However, these interlayers have their own drawbacks; the PFN backbone is intrinsically p-type, whereas PEI is insulating and exhibits poor adhesion to the active layer. Interest is thus emerging in fullerene-based interlayers that can transport electrons and promote π-π interactions with the active layer for enhanced adhesion;[5,16-24] these favorable properties hold promise for eliminating the undesirable effects often associated with interlayers.

With respect to electrode selection, recent reports of BHJ PSCs using a bathocuproine (BCP) interlayer with a Ag cathode achieved PCEs of 7.7 and 8.1%,

representing benchmark values for standard single-junction PSCs containing Ag cathodes.[25,26] However, BCP requires a thermal deposition step and a precisely defined interlayer thickness (3.5 nm).[26] In previous chapters conjugated polymer zwitterions (CPZs) were reported to cause large negative Δ values (-0.5 eV to -0.9 eV) on metals.[27-29] Spin-coating CPZs and the active layer polymer from orthogonal solvents (i.e., exclusively dissolving only one of the components) provides good control over interlayer thickness with little disruption of the underlying surface. The subsequent sections of this chapter report the synthesis, characterization and utility of two trisubstituted polar fulleropyrrolidines as effective interlayers in PSCs, providing an alternative to previously described CPZs.

4.2 Synthesis and structural characterization

The tris(dimethylamino) and tris(sulfobetaine) substituted fullerenes (C_{60}-N, **72**, and C_{60}-SB, **73**, respectively) were prepared by connecting the corresponding trisubstituted phenyl groups through a pyrrolidine ring (**Scheme 4.1**). For C_{60}-N, Mitsunobu coupling[30] of 2,3,4-trihydroxybenzaldehyde (**70**) with 3-dimethylaminopropan-1-ol in the presence of triphenylphosphine and diisopropyl azodicarboxylate gave a tris[3-(dimethylamino)propoxy]benzaldehyde (**71**). The tri-substituted benzaldehyde was then connected through the Prato reaction[31,32] to fullerene-C_{60} in the presence of N-methylglycine), to give C_{60}-N (**72**). Matrix-assisted laser desorption time of flight (MALDI-TOF) mass spectroscopy was used to confirm the structure of C_{60}-N (**Figure 4.1**).
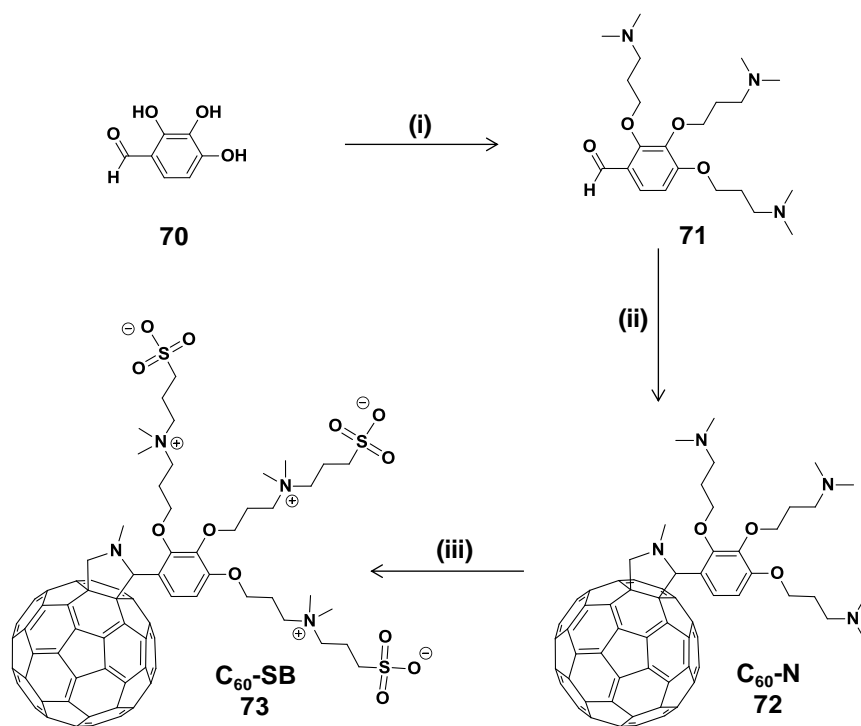
Scheme 4.1 Synthesis of fullerene interlayer materials **C$_{60}$-N** and **C$_{60}$-SB**. Reagents and conditions: (i) 3-dimethylamino-1-propanol, DIAD, PPh$_3$, THF; (ii) fullerene C$_{60}$, sarcosine, oDCB; (iii) 1,3-propane sultone, Na$_2$CO$_3$, TFE. Reproduced from reference: Page, Z. A. et. al. *Science.* **2014**, p.441.
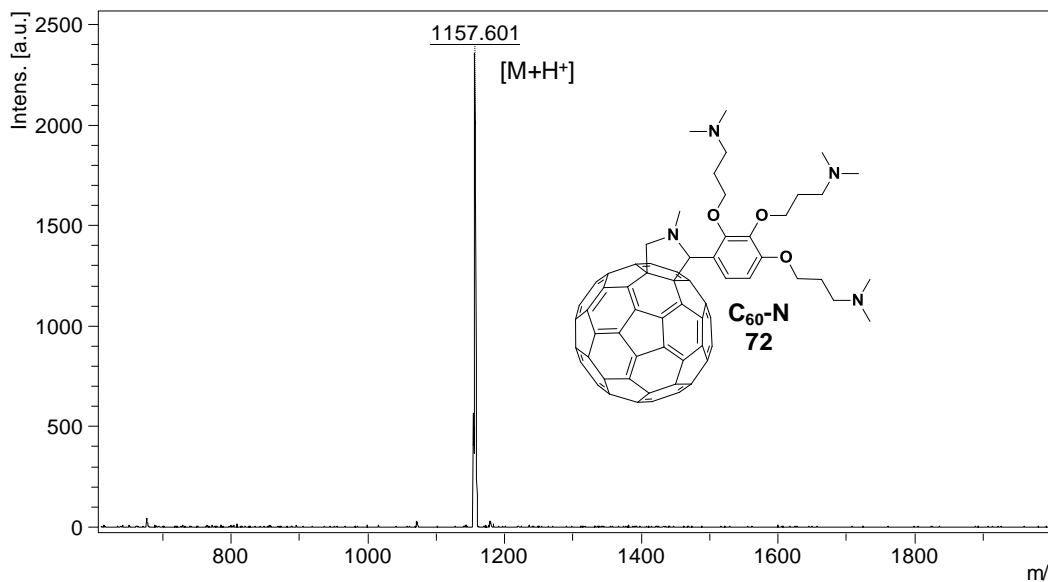
Figure 4.1 MALDI-TOF mass spectrum of **C$_{60}$-N** (**72**). Reproduced from reference: Page, Z. A. et. al. *Science.* **2014**, p.441.

C$_{60}$-N served as a precursor to **C$_{60}$-SB** (**73**) through use of the tertiary amines in ring-opening of 1,3-propanesultone. In order to reach full conversion and obtain **C$_{60}$-SB**

with three sulfobetaine groups per fullerene it was necessary to use trifluoroethanol (TFE) as the solvent containing a non-nucleophilic base (in this case sodium carbonate, Na_2CO_3, was chosen). This solvent and base combination maintained complete miscibility of both **C$_{60}$-N**, intermediate functional fullerenes and **C$_{60}$-SB**, while preventing protonation of the tertiary amines by TFE. MALDI-TOF mass spectroscopy was utilized to observe the various products that are formed over time when undertaking the ring-opening reaction in TFE (**Figure 4.2** and **4.3**). It is interesting to note that the pyrrolidine heterocycle does not appear to participate in the ring-opening of 1,3-propanesultone even given extended time and excess sultone, as suggested by both ^{1}H-NMR and MALDI-TOF mass spectroscopies. Overall, these syntheses proved rapid and efficient, while precluding the need for methanofullerene derivatives prepared through unstable diazo intermediates.[33]
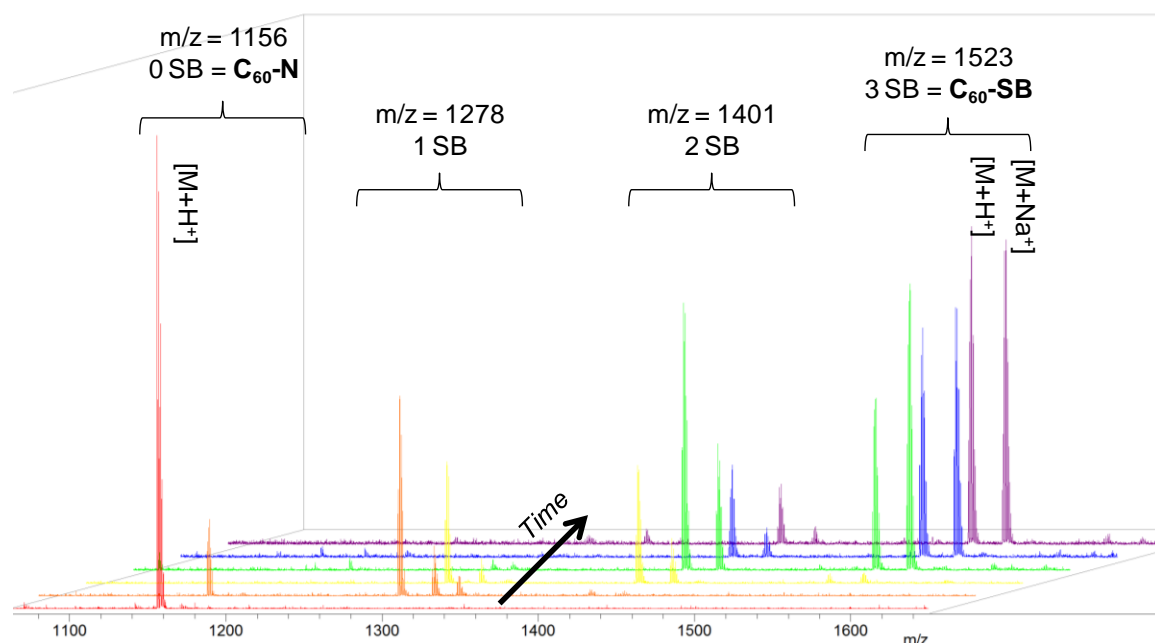
Figure 4.2 MALDI-TOF mass spectra of zwitterion formation as a function of time in TFE, without added Na_2CO_3, showing the presence of residual bis(sulfobetaine)fulleropyrrolidine derivatives at 1402 g / mol (purple signals). Addition of Na_2CO_3 is necessary to achieve full conversion. Reproduced from reference: Page, Z. A. et. al. *Science.* **2014**, p.441.
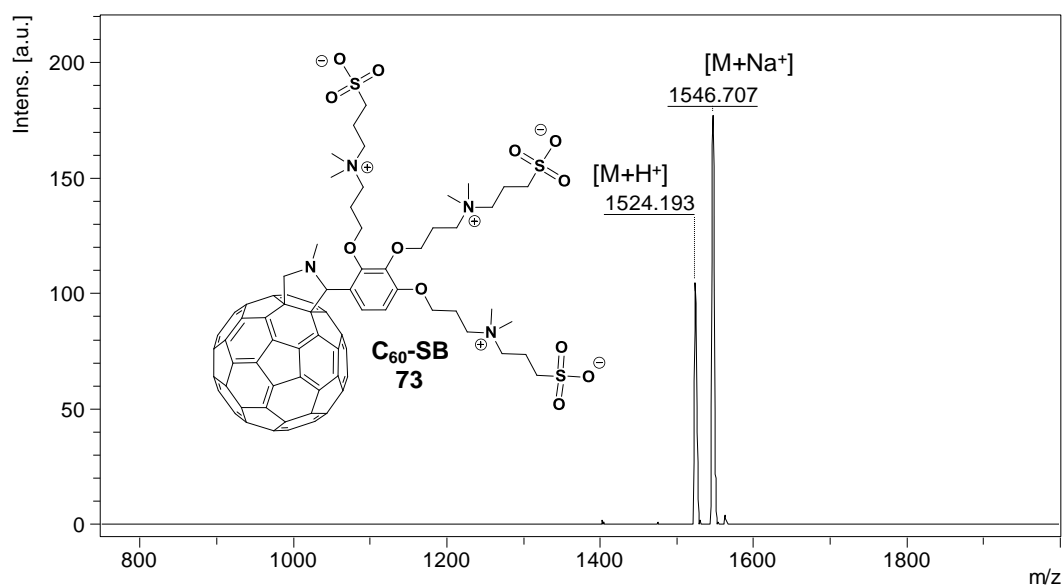
Figure 4.3 MALDI-TOF mass spectrum of **C₆₀-SB** (**73**). Reproduced from reference: Page, Z. A. et. al. *Science.* **2014**, p.441.

As an inexpensive alternative to using pure fullerene C_{60} ($50/gram) for the synthesis of **C₆₀-N**, the use of an unrefined mixture ($13/gram), composed largely of C_{60} and C_{70}, was investigated for use in an analogous synthetic procedure (using the Prato reaction) to produce mixed **C₆₀-N/C₇₀-N** (**mixed F-N**) (**72/74**) (**Figure 4.4**). MALDI-TOF mass spectroscopy was used to identify the presence of both **C₆₀-N** (**72**) and **C₇₀-N** (**74**) in the **mixed F-N** sample, while no higher order adducts were detected.
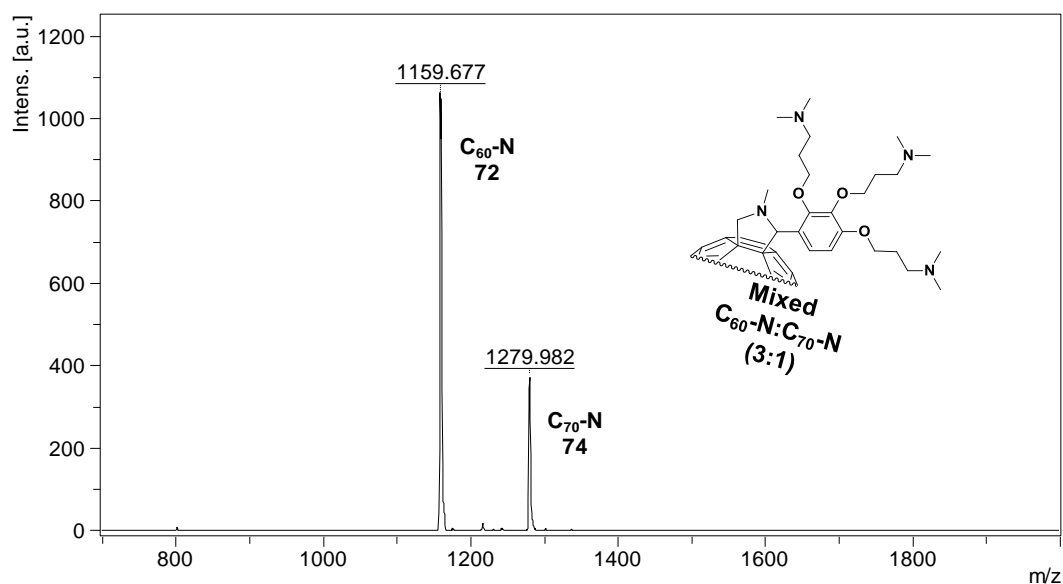
Figure 4.4 MALDI-TOF mass spectrum of **mixed F-N** (**72/74**).

In order to determine the composition more precisely pure **C_{70}-N** (**74**) was synthesized from C_{70} using the Prato reaction, and UV-Vis absorption spectra of pure **C_{60}-N**, pure **C_{70}-N** and **mixed F-N** were recorded (**Figure 4.5**). Given that **mixed F-N** only contains **C_{60}-N** and **C_{70}-N** a ratio between the two was calculated using the equation shown as an inset in **Figure 4.5**, finding 58:42 for **C_{60}-N:C_{70}-N**.
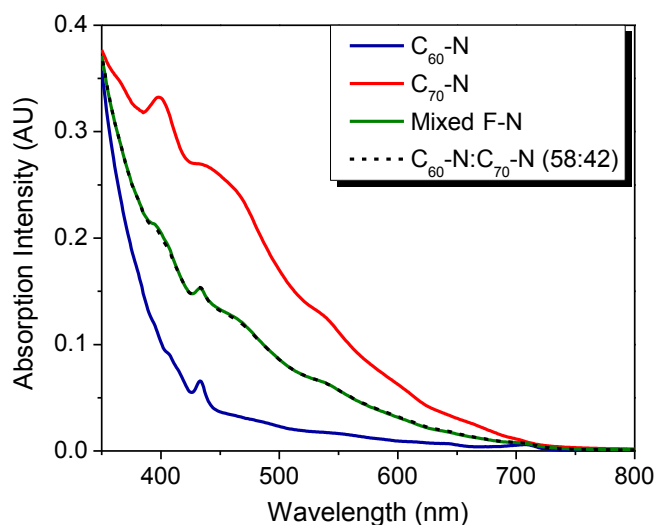
Figure 4.5 UV-Vis absorption spectra of **C_{60}-N**, **C_{70}-N** and **mixed F-N**. The ratio of **C_{60}-N:C_{70}-N** in **mixed F-N** was determined from these spectra to be 58:42, shown to overlap well at all wavelengths with the mathematically generated dashed line.

4.3 Solar cell device integration

Single junction OPVs were fabricated with a BHJ active layer containing a blend of [6,6]-phenyl C_{71}-butyric acid methyl ester ($PC_{71}BM$) (**38**) as the acceptor and a low bandgap conjugated polymer thieno[3,4-*b*]thiophene-*a*-benzodithiophene with either 2-(ethylhexyl)oxy (PTB7)[34] (**37**) or 2-(ethylhexyl)thienyl (PBDTT-TT) (**69**) side chains as the donor (**Figure 4.6**).
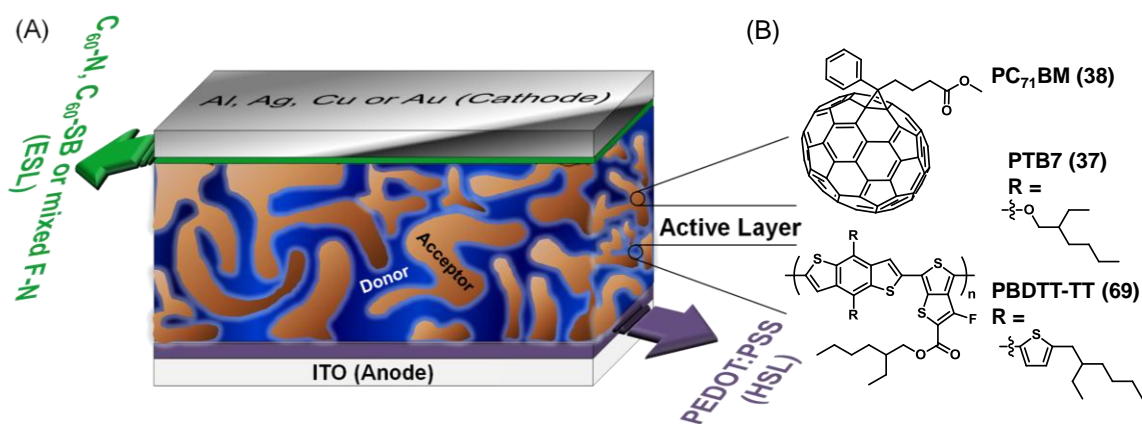
Figure 4.6 Solar cell device architecture and components. (A) Device configuration, consisting of indium tin oxide (ITO)/poly(ethylenedioxythiophene):poly(styrene sulfonate) (PEDOT:PSS)/active layer/**C_{60}-N**, **C_{60}-SB**, or **mixed F-N**/cathode, where PEDOT:PSS is the hole selective layer (HSL) and anode modifier, and Al, Ag, Cu or Au were used as the cathode; (B) Active layer components, with $PC_{71}BM$ as the acceptor and PTB7 (**37**) or PBDTT-TT (**69**) as the donor. Reproduced from reference: Page, Z. A. et. al. *Science.* **2014**, p.441.

In a device, **C_{60}-N** or **C_{60}-SB** was deposited by spin coating onto the active layer from TFE, followed by deposition of the metal cathode (Al, Ag, Cu or Au). A device fabricated in this fashion, containing a **C_{60}-N/**Ag cathode, was examined and certified by the National Renewable Energy Laboratory (NREL) at a PCE of 8.91% (**Figure 4.7**), identical to the efficiency obtained in our laboratories for that particular device (**Figure 4.8**).

UMASS
organic Cell

Device ID: S1
Mar 05, 2014 12:31
Spectrum: ASTM G173 global

Device Temperature: 30.0 ± 10.0 °C
Device Area: 0.03025 cm^2
Irradiance: 1000.0 W/m^2

X25 IV System
PV Performance Characterization Team

V_{oc} = 0.7959 V
I_{sc} = 0.47267 mA
J_{sc} = 15.628 mA/cm^2
Fill Factor = 71.66 %

I_{max} = 0.40876 mA
V_{max} = 0.6595 V
P_{max} = 0.26957 mW
Efficiency = 8.91 %

UMASS
organic Cell

Device ID: S2
Mar 05, 2014 12:48
Spectrum: ASTM G173 global

Device Temperature: 30.0 ± 10.0 °C
Device Area: 0.05418 cm^2
Irradiance: 1000.0 W/m^2

X25 IV System
PV Performance Characterization Team

V_{oc} = 0.8099 V
I_{sc} = 0.85031 mA
J_{sc} = 15.695 mA/cm^2
Fill Factor = 69.24 %

I_{max} = 0.72297 mA
V_{max} = 0.6596 V
P_{max} = 0.47684 mW
Efficiency = 8.80 %

Figure 4.7 NREL certified OPV devices with an architecture of ITO/PEDOT:PSS/PBDTT-TT:PC$_{71}$BM/**C$_{60}$-N**/Ag. (A) Device area of 0.03025 cm^2 resulting in a PCE of 8.91%. (B) Device area of 0.05418 cm^2 resulting in a PCE of 8.80%. Reproduced from reference: Page, Z. A. et. al. *Science.* **2014**, p.441.
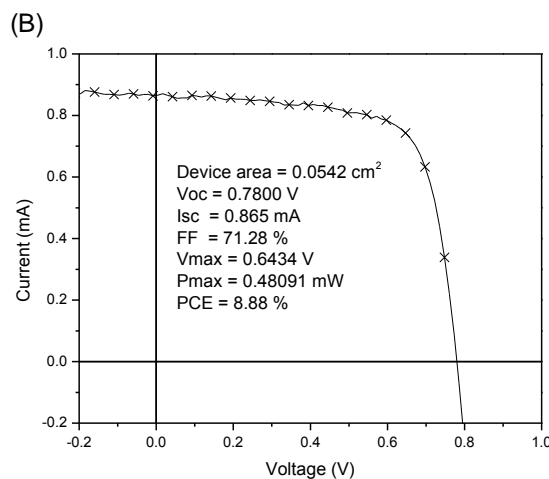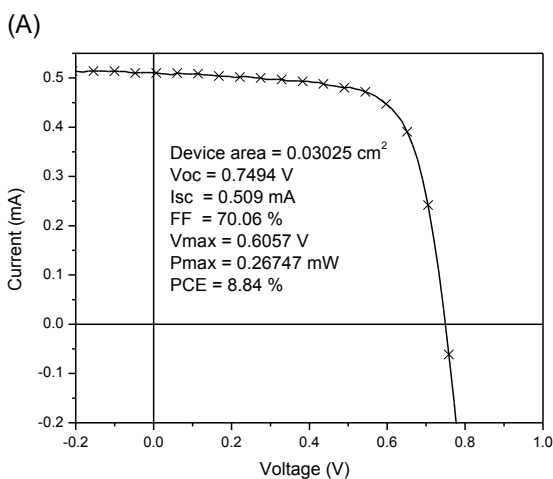
Figure 4.8 *J–V* curve of the certified device after it was returned from NREL, showing good agreement of device metrics using the calibration procedure for our solar simulator with a silicon reference cell and KG5 filter. (A) Device area of 0.03025 cm^2 resulting in a PCE of 8.84%. (B) Device area of 0.05418 cm^2 resulting in a PCE of 8.88%. Reproduced from reference: Page, Z. A. et. al. *Science.* **2014**, p.441.

We subsequently optimized further the donor:acceptor ratio and interlayer thickness, giving devices with even higher PCE values. The optimized PBDTT-TT:PC$_{71}$BM OPV devices fabricated with bare Ag cathodes (control devices, no cathode modification layer) gave a PCE of 2.76 ± 0.59% (maximum PCE 3.72%), whereas devices with **C$_{60}$-N** or **C$_{60}$-SB** interlayers yielded PCE values of 9.35 ± 0.13% (maximum PCE 9.78%) and 8.57 ± 0.15% (maximum PCE 8.92%), respectively (**Figure 4.9** and **Table 4.1**). This large efficiency improvement stems from higher V_{OC} and *FF* values. Devices with bare Ag cathodes suffer from the high work function of Ag and the resultant weak built-in electrostatic potential difference. **Figure 4.9** shows that devices fabricated with **C$_{60}$-N** interlayers outperform those with **C$_{60}$-SB** interlayers owing to higher V_{OC} (0.75 to 0.78 V) and *FF* (68 to 71%) values. Devices were also fabricated using a standard Ca/Al cathode, giving PCE values of 8.36 ± 0.21% (**Table 4.1**).
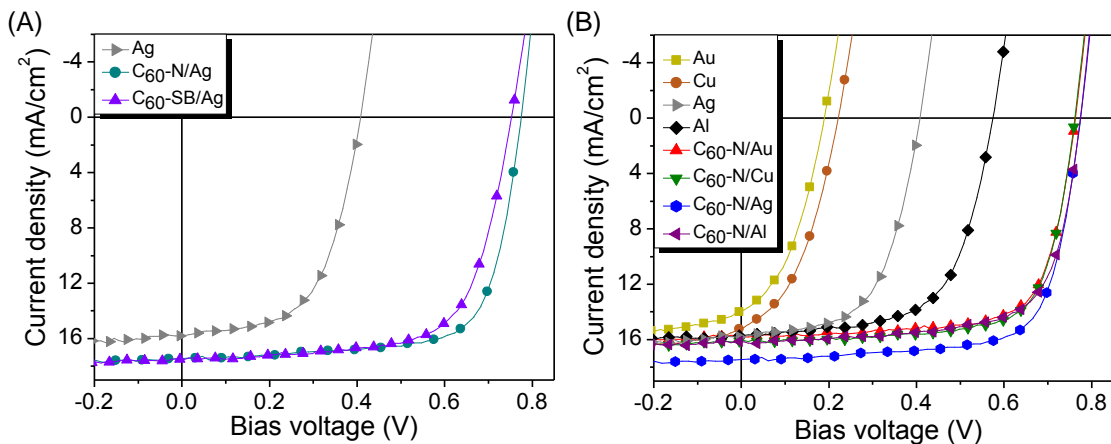
Figure 4.9 OPV device performance for ITO/PEDOT:PSS/PBDTT-TT:PC$_{71}$BM/(fulleropyrrolidine)/cathode architecture. (A) Representative *J–V* curves for OPVs with bare Ag cathodes, and ~15 nm-thick **C$_{60}$-N** and **C$_{60}$-SB** interlayers; (B) Representative *J–V* curves showing the effect of cathode work function on V_{OC} for the bare metal devices, and impact on OPVs containing a thin layer (~15 nm) of **C$_{60}$-N** between the active layer and top cathode. Reproduced from reference: Page, Z. A. et. al. *Science.* **2014**, p.441.

Table 4.1 Summarized photovoltaic performance of device architectures and compositions of ITO/PEDOT:PSS/PBDTT-TT:PC$_{71}$BM/(X)/cathode, where X represents either Ca, **C$_{60}$-N**, **C$_{60}$-SB** or no interlayer (*i.e.*, bare metal). Al, Ag, Cu and Au were employed as cathodes. Error represents ± 1 standard deviation for averages obtained over six devices; PCE$_{max}$ is given parenthetically. Reproduced from reference: Page, Z. A. et. al. *Science.* **2014**, p.441.

Cathode	Interlayer	V_{OC} (V)	J_{SC} (mA/cm^2)	*FF* (%)	*PCE* (%)
Al	None	0.56	15.76	63.11	5.59 ± 0.05 (5.66)
	Ca	0.75	15.88	70.49	8.36 ± 0.21 (8.71)
	C$_{60}$-SB	0.75	16.42	67.61	8.29 ± 0.11 (8.44)
	C$_{60}$-N	0.76	16.29	69.71	8.65 ± 0.11 (8.79)
Ag	None	0.33	15.30	53.40	2.76 ± 0.59 (3.72)
	C$_{60}$-SB	0.75	16.89	68.07	8.57 ± 0.15 (8.92)
	C$_{60}$-N	0.78	16.83	71.35	9.35 ± 0.13 (9.78)
Cu	None	0.21	15.25	40.62	1.29 ± 0.06 (1.38)
	C$_{60}$-N	0.75	16.01	71.91	8.67 ± 0.17 (8.88)
Au	None	0.18	13.92	40.21	0.99 ± 0.05 (1.07)
	C$_{60}$-N	0.76	15.75	71.27	8.56 ± 0.21 (8.83)

Comparable PCE values were obtained for devices with **C$_{60}$-N**/Al and **C$_{60}$-SB**/Al, with averages of 8.65 ± 0.11 % and 8.29 ± 0.11 % respectively, thus eliminating the need for thermal deposition of Ca. Devices with PTB7:PC$_{71}$BM active layer performed similarly, albeit with smaller PCEs (**Table 4.2**).

Table 4.2 Summarized photovoltaic performances for device architectures and compositions of ITO/PEDOT:PSS/PTB7:PC$_{71}$BM/(X)/Cathode, where X is either Ca as a control, **C$_{60}$-N**, **C$_{60}$-SB** or not included (bare metal as control). Error represents ± 1 standard deviation for averages obtained over six to eight devices; PCE$_{max}$ is given in parenthases. Reproduced from reference: Page, Z. A. et. al. *Science.* **2014**, p.441.

Cathode	Buffer Layer	V_{OC} (V)	J_{SC} (mA/cm^2)	*FF* (%)	*PCE* (%)
Al	Ca	0.71	15.71	69.08	7.72 ± 0.29 (8.05)
Ag	None	0.47	15.08	50.21	3.54 ± 0.32 (3.88)
	C$_{60}$-SB	0.70	16.02	66.68	7.47 ± 0.12 (7.65)
	C$_{60}$-N	0.72	16.37	72.94	8.59 ± 0.19 (8.96)

OPV devices with a Ag cathode containing **mixed F-N** as a buffer layer were fabricated and compared with devices containing **C$_{60}$-N**, finding that both equally enhance device performance to a PCE ≈ 9.5 % (**Figure 4.10**). The comparable PCE

values obtained for both **C₆₀-N** and **mixed F-N** shows the potential for **mixed F-N** to be used as a viable, and inexpensive, substitute for **C₆₀-N** in PSCs.
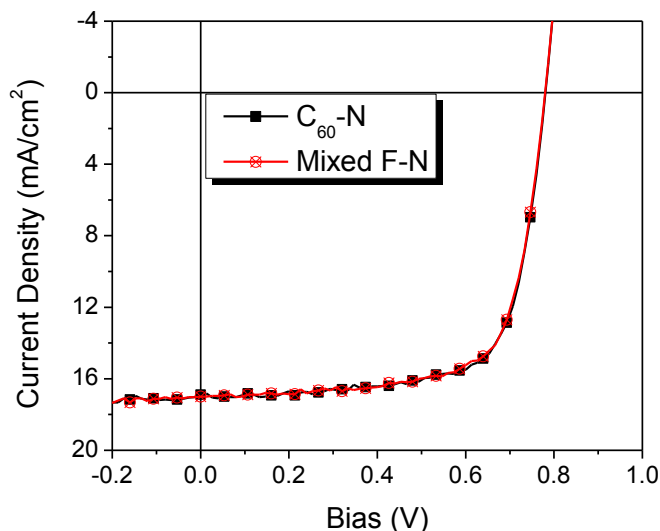
Figure 4.10 OPV device performance for ITO/PEDOT:PSS/PBDTT-TT:PC₇₁BM/(fulleropyrrolidine)/cathode architecture, comparing **C₆₀-N** and **mixed F-N** as cathode modification layers.

OPV devices fabricated with Cu or Au cathodes, omitting a cathode-modifying interlayer, had low PCE values of $1.29 \pm 0.06\%$ and $0.99 \pm 0.05\%$ respectively, as expected from the high Φ values of Cu (4.7 eV) and Au (5.1 eV). However, by casting a ~15 nm thick layer of **C₆₀-N** onto the active layer prior to cathode deposition, the V_{OC} increased to 0.75 V for Cu and 0.76 V for Au, producing devices with PCE values of 8.67 $\pm$ 0.17% (PCE$_{max}$ = 8.88%) and 8.56 $\pm$ 0.21 % (PCE$_{max}$ = 8.83%), respectively. The higher PCE values obtained for Ag-cathode devices stem from their higher J_{SC}: 16.83 mA/cm² for Ag, 16.01 mA/cm² for Cu, and 15.75 mA/cm² for Au. In addition, the large FF ($\approx$ 70%) obtained, independent of the metal cathode, underscores the universal nature of these **C₆₀-N** interlayers. Although LiF/Al and Ca/Al are common cathode configurations, Ag, Cu or Au with LiF or Ca layers give significantly lower PCE values (**Figure 4.11** and **Table 4.3**).
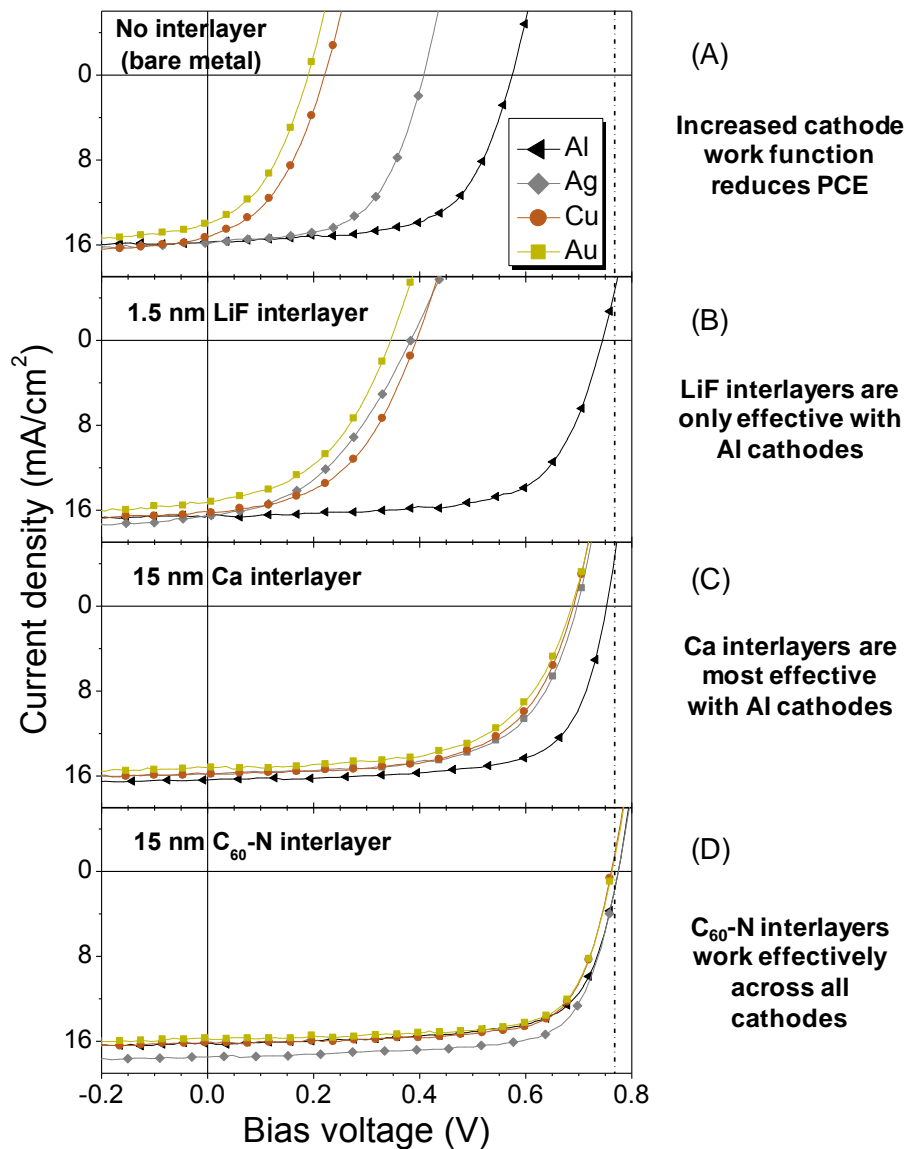
Figure 4.11 OPV device performance for ITO/PEDOT:PSS/PBDTT-TT:PC$_{71}$BM/(interlayer)/cathode architecture, with Al, Ag Cu and Au cathodes. (A) No interlayer, bare metal cathodes; (B) 1.5 nm LiF interlayers; (C) 15 nm Ca interlayer; (D) 15 nm **C$_{60}$-N** interlayer.

Table 4.3 Summarized photovoltaic performance of control devices with architectures of ITO/PEDOT:PSS/PBDTT-TT:PC$_{71}$BM/(X)/cathode, where X represents either Ca or LiF. Al, Ag, Cu and Au were employed as cathodes. Error represents ± 1 standard deviation for averages obtained over six devices; PCE$_{max}$ is given parenthetically. Reproduced from reference: Page, Z. A. et. al. *Science.* **2014**, p.441.

Cathode	Interlayer	V_{OC} (V)	J_{SC} (mA/cm^2)	*FF* (%)	*PCE* (%)
Al	Ca	0.75	15.88	70.49	8.36 ± 0.21 (8.71)
	LiF	0.75	16.86	65.42	8.24 ± 0.09 (8.37)
Ag	Ca	0.70	15.92	61.89	6.87 ± 0.06 (6.99)
	LiF	0.39	17.22	47.25	3.15 ± 0.40 (3.38)
Cu	Ca	0.69	15.66	61.20	6.65 ± 0.10 (6.74)
	LiF	0.40	16.22	48.50	3.12 ± 0.06 (3.19)
Au	Ca	0.69	15.05	60.37	6.28 ± 0.08 (6.36)
	LiF	0.35	15.27	47.42	2.56 ± 0.29 (2.90)

As shown in **Figure 4.11** and **Table 4.3**, control devices were fabricated containing either 15 nm Ca or 1.5 nm LiF interlayers between the active layer and metal (Al, Ag, Cu or Au) cathode. Devices with **C$_{60}$-N** interlayers outperformed all those made with Ca and LiF, due to a higher V_{OC} and *FF*. While devices containing **C$_{60}$-N** interlayers maintained an average V_{OC} and *FF* of 0.75 V and 70% irrespective of cathode work function, the V_{OC} and *FF* for devices containing the higher work function Ag, Cu and Au cathodes with a Ca interlayer dropped to approximately 0.7 V and 60%, respectively, and with a LiF interlayer to 0.4 V and 48%, respectively.

In combination with **C$_{60}$-N** interlayers, devices with Ag, Cu or Au cathodes not only yielded higher PCE relative to devices with LiF/Al or Ca/Al cathodes, but also exhibit improved stability in air (**Figure 4.12**). Whereas little-to-no degradation occurred for the devices with Ag, Cu or Au cathodes after 24 hours under ambient conditions, the Al-based devices had 25% depreciation in PCE (**Figure 4.12A**). Device stability under normal operation conditions (AM1.5G irradiation, +0.5 V forward bias, in air) was studied for Ca/Al, LiF/Al and **C$_{60}$-N**/Ag devices, revealing enhanced stability for the devices containing **C$_{60}$-N** interlayers relative to those containing Ca or LiF interlayers

(**Figure 4.12B**). These high work function metals have the important advantages of increasing device lifetime and offering a pathway to all-solution-processing that can be translated to roll-to-roll (R2R) techniques wherein devices are printed from solution onto a flexible substrate such as a metal foil or plastic.
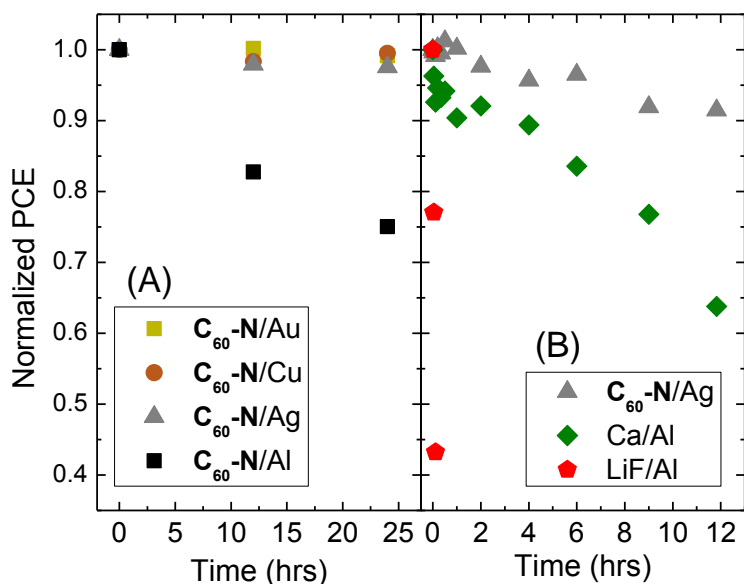
Figure 4.12 OPV device stability. (A) PBDTT-TT:PC$_{71}$BM devices containing a **C$_{60}$-N** interlayer with either Al, Ag, Cu or Au cathode stored in air under ambient conditions, showing the enhanced stability for the higher work function cathodes relative to the more commonly utilized Al cathode. (B) PBDTT-TT:PC$_{71}$BM devices containing a Ca/Al, LiF/Al or **C$_{60}$-N**/Ag interlayer/cathode measured over time under AM1.5G irradiation, with a +0.5 V forward bias and in ambient air, showing the enhanced stability of **C$_{60}$-N**/Ag devices under accelerated aging conditions. Reproduced from reference: Page, Z. A. et. al. *Science.* **2014**, p.441.

Seven different interlayer thicknesses were investigated, ranging from 5 to 55 nm (**Figures 4.13**). Both **C$_{60}$-N** and **C$_{60}$-SB** produced peak PCE devices at ~15 nm interlayer thickness. For **C$_{60}$-N**, V_{OC} and *FF* plateaued at approximately 0.75 V and 70%, respectively, in accord with interlayer thickness, whereas **C$_{60}$-SB** devices maintained a constant V_{OC} (≈ 0.75 V) and a slight decline in *FF* (from 68 to 65%) for films thicker than ~15 nm, and a decrease in J_{SC} from ~17 mA/cm^2 (thickness ≤ 15 nm) to ~13 mA/cm^2 (thickness ~55 nm). Thus, these interlayers offer substantial advantages over other

interlayers, such as the CPZs we previously reported, in which thickness must be controlled and >10 nm interlayers produced S-shaped *J–V* curves and reduced PCE.[28] Unlike the CPZ interlayers, these fulleropyrrolidine interlayers afford efficient devices even when the film thickness exceeds 50 nm.
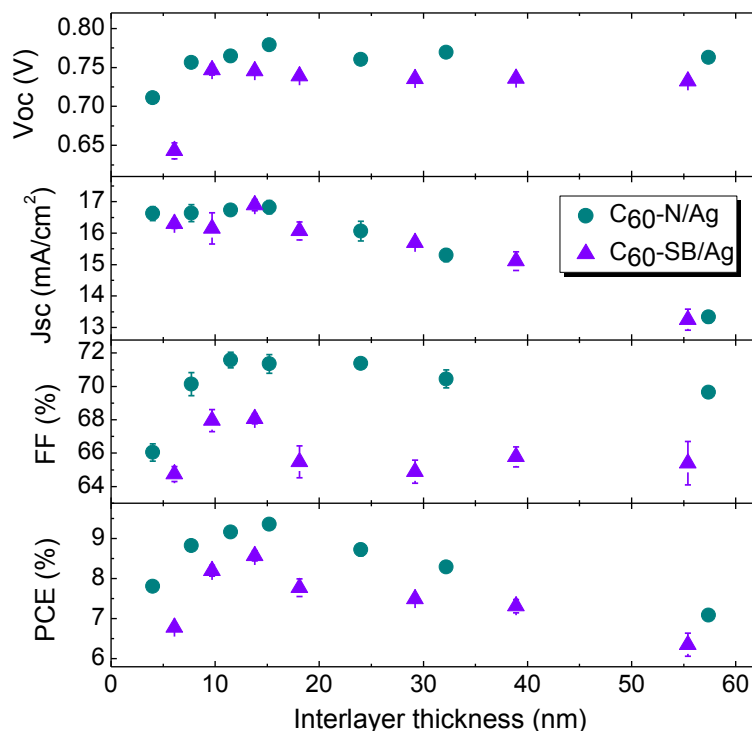
Figure 4.13 OPV device metrics for ITO/PEDOT:PSS/PBDTT-TT:PC$_{71}$BM/(fulleropyrrolidine)/cathode architecture, obtained at varying interlayer thickness (from ~5 to 55 nm). Error represents ±1 standard deviation over six devices. Reproduced from reference: Page, Z. A. et. al. *Science.* **2014**, p.441.

The approximate interlayer thicknesses for **C$_{60}$-N** and **C$_{60}$-SB** were determined through a combination of UV-Vis absorption spectroscopy and profilometry. First, absorption coefficients were determined by casting three relatively thick films (~150 nm) onto clean glass substrates, measuring their absorption profiles with UV-Vis absorption spectroscopy, determining thickness using profilometry and taking the average values from both measurements as *A* (absorption, AU) and *l* (path length, cm) to determine the attenuation coefficient (α, cm^{-1}) using the Beer-Lambert law for films: $\alpha = A/l$. After

determining attenuation coefficients thin films of both **C$_{60}$-N** and **C$_{60}$-SB** were spun-coat on glass from dilute solutions, using TFE as the solvent. The UV-Vis absorption spectra were measured and film thicknesses were calculated using the Beer-Lambert law and predetermined attenuation coefficients, providing a linear relationship between film thickness and solution concentration from which the films were spun-coat from (**Figure 4.14**).
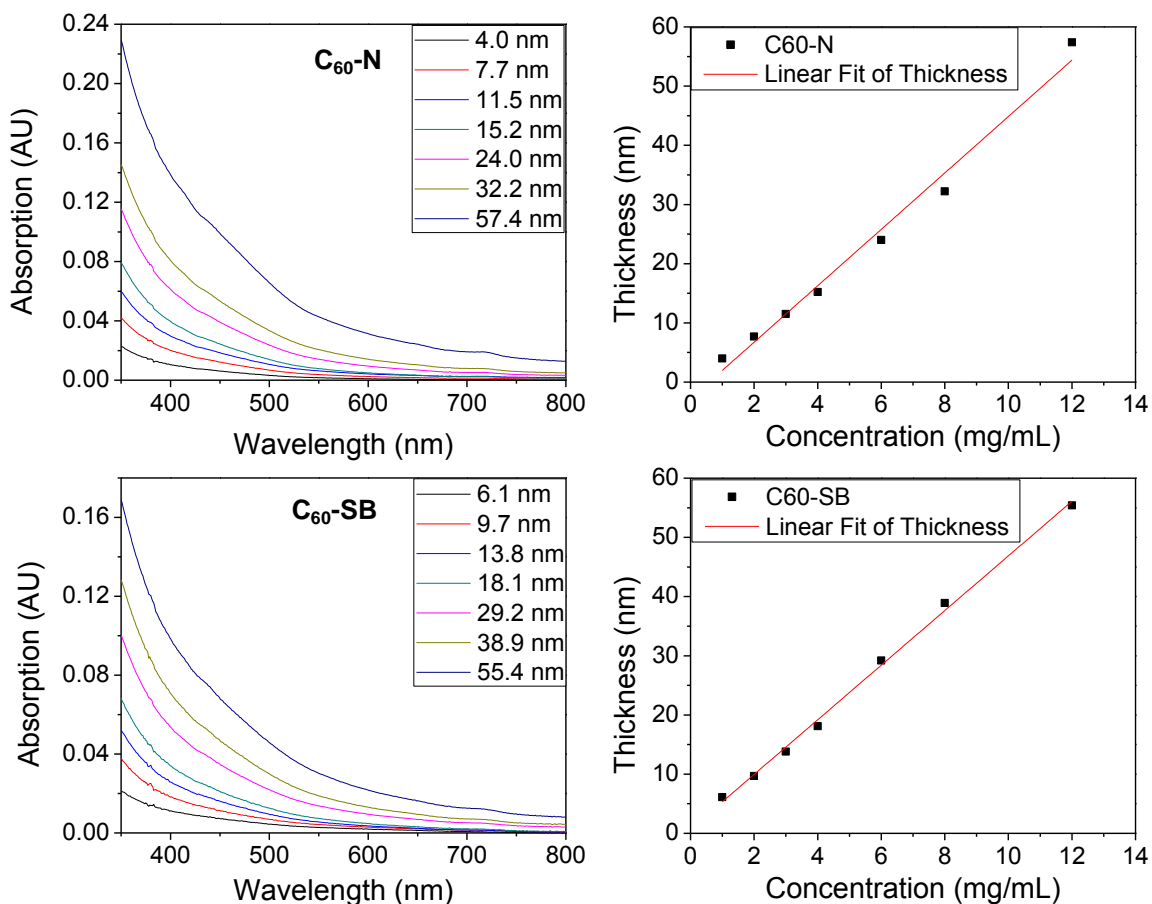
Figure 4.14 UV-Vis absorption (left) and concentration vs. thickness profiles for fulleropyrrolidine films spun coat on glass (right). Reproduced from reference: Page, Z. A. et. al. *Science.* **2014**, p.441.

For confirmation of interlayer thickness profilometry was performed directly on OPV devices by removing a thin layer of material using a razor blade, followed by at least 10 measurements around the active device area (**Table 4.4**). Measurements were

done between the Ag cathodes, such that the thickness data includes the following layers (where PEDOT:PSS was measured to be ~30 nm thick): PEDOT:PSS/PBDTT-TT:PC$_{71}$BM/(**C$_{60}$-N**). The thickness of the interlayer was then calculated by taking the difference between the average control thickness (no interlayer) and measured thicknesses for devices containing interlayers. The results match well with those obtained using UV-Vis absorption spectroscopy (**Table 4.4**).

Table 4.4 Average thicknesses determined using profilometry directly from OPV devices with an architecture of ITO/PEDOT:PSS/PBDTT-TT:PC$_{71}$BM/(fulleropyrrolidine)/cathode containing either no interlayer (0 mg/mL control) or **C$_{60}$-N** spun from TFE at 4000 rpm onto the active layer at the concentrations noted (4 mg/mL, 8 mg/mL and 12 mg/mL). Reproduced from reference: Page, Z. A. et. al. *Science.* **2014**, p.441.

Concentration of **C$_{60}$-N** used for spin-coating→	0 mg/mL (control)	4 mg/mL	8 mg/mL	12 mg/mL
Average thickness (nm)	129 ± 3	146 ± 5	162 ± 6	183 ± 6
Thickness of C$_{60}$-N (nm)	0	17	33	55

4.4 Electronic characterization

The interactions of **C$_{60}$-N** and **C$_{60}$-SB** layers with metal surfaces were investigated and compared to interlayers consisting of 2,3,4-tris(hexyloxy)fulleropyrrolidine (**C$_{60}$-alkyl**) (**76**) which lacks amine or sulfobetaine functionality, yet synthesized in a similar fashion to both **C$_{60}$-N** and **C$_{60}$-SB** (**Scheme 4.2**).
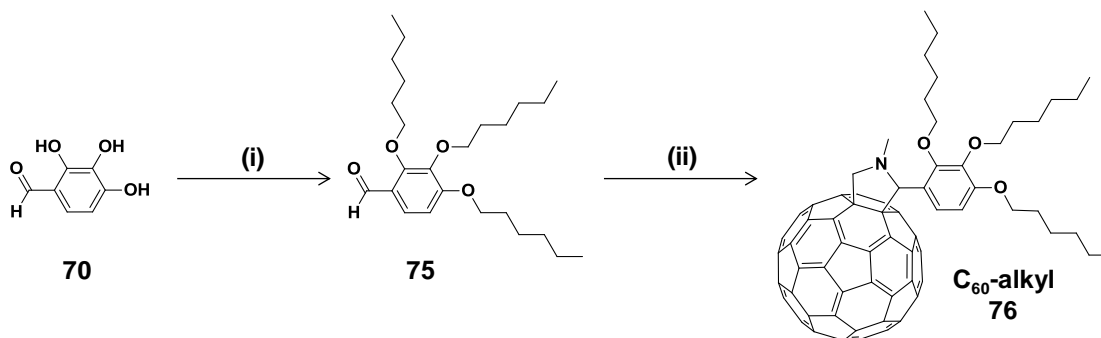
Scheme 4.2 Synthesis of **C$_{60}$-alkyl** (**76**), as an analogous fulleropyrrolidine for comparison of electronic properties with **C$_{60}$-N** and **C$_{60}$-SB**. Reagents and conditions: (i) 1-hexanol, DIAD, PPH$_3$, THF. (ii) fullerene C$_{60}$, sarcosine, *o*DCB. Reproduced from reference: Page, Z. A. et. al. *Science.* **2014**, p.441.

C$_{60}$-N, **C$_{60}$-SB** and **C$_{60}$-alkyl** exhibit similar optoelectronic properties, with UV absorption onsets indicating optical energy gaps (E_g) of approximately 1.8 eV for each (**Figure 4.15**), and cyclic voltammetry (CV) giving electron affinity (E_A) values of 3.8-3.9 eV (**Figure 4.16**).
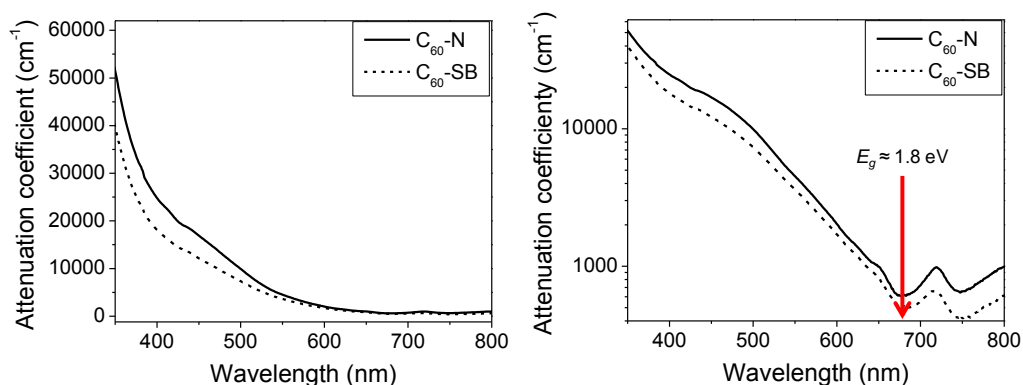
Figure 4.15 UV-Vis absorption spectra of fulleropyrrolidines. Right spectra plotted against attenuation coefficient as a logarithmic scale to help identify an approximate onset of absorption, providing an E_g equal to 1.8 eV for **C$_{60}$-N** and **C$_{60}$-SB**. Reproduced from reference: Page, Z. A. et. al. *Science.* **2014**, p.441.
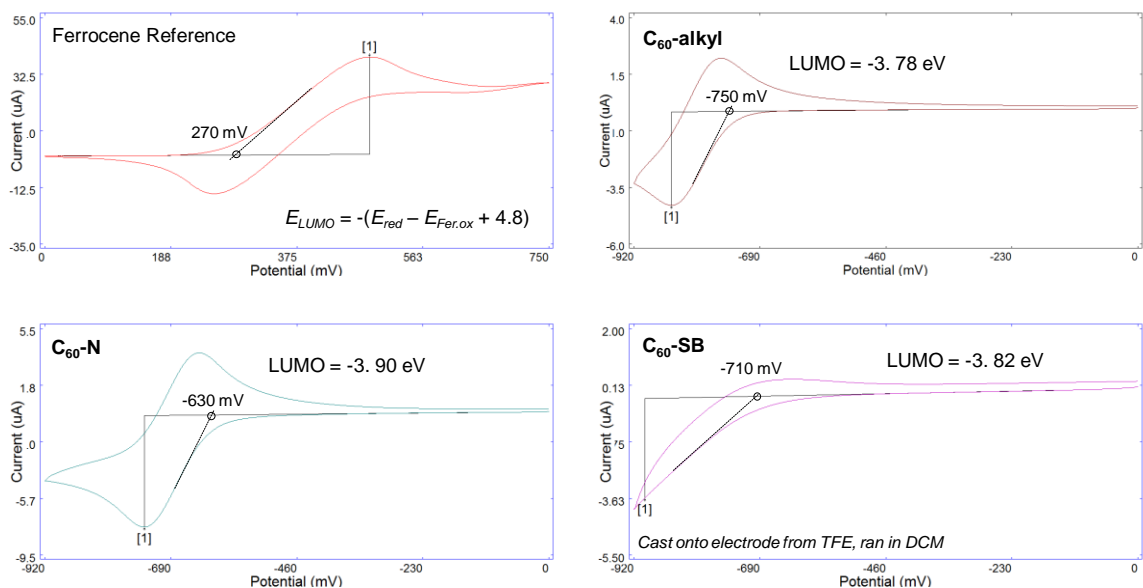
Figure 4.16 CV of fulleropyrrolidines (**C$_{60}$-alkyl**, **C$_{60}$-N** and **C$_{60}$-SB**) used to determine LUMO energy ($= -E_A$) from the reduction onset, using the equation given in the bottom right corner of the ferrocene reference. **C$_{60}$-SB** was cast from solution directly onto the working electrode. Reproduced from reference: Page, Z. A. et. al. *Science.* **2014**, p.441.

120

The high and low binding energy onsets measured by ultraviolet photoelectron spectroscopy (UPS) showed that the ionization potential (I_P) for the fulleropyrrolidines ranged from 5.6 to 5.7 eV (**Figure 4.17**). E_g values, calculated from the difference between E_A and I_P, correlated closely to the E_g values determined by UV-Vis absorbance spectroscopy (~1.8 ± 0.1 eV) (**Figure 4.15**). The similarities of the E_A values of these fullerenes to that of $PC_{71}BM$ suggests that there is little to no energy barrier for electron transfer at the active layer/interlayer interface. An appreciable energy barrier at this interface would reduce *FF* due to interfacial charge build-up; as such, these substituted fullerenes combine the benefits of unhindered electron transfer with polar, surface-interacting functionality for improved device performance.

The high binding-energy region of UPS provides interfacial dipole (Δ) values that reflect the difference in the high binding energy onsets, or E_{SEC}, of bare *vs* coated metals. UPS characterization of **C$_{60}$-N**, **C$_{60}$-SB** and **C$_{60}$-alkyl** on freshly prepared Ag substrates revealed **C$_{60}$-N** to have the largest Δ value (**Figure 4.17**), which remained constant for films thicker than 8 nm, and declined for very thin films (in keeping with the reduced V_{OC} values for those devices, **Table 4.5**). The larger Δ for **C$_{60}$-N** relative to **C$_{60}$-SB** accounts for the higher V_{OC} in those devices, as this increases the built-in electrostatic potential difference in the device, improving charge extraction and reducing recombination losses, consistent with higher J_{SC} and *FF* values for devices with **C$_{60}$-N** relative to **C$_{60}$-SB**. The difference in work function of the electrodes coated with **C$_{60}$-alkyl** and **C$_{60}$-SB** (0.24 eV) arises from a permanent dipole due to interaction between the zwitterionic sulfobetaine groups with the metal surfaces.[28] The larger Δ for **C$_{60}$-N** is

likely due to electron transfer from the nitrogen lone pair of the tertiary amines to the metal substrate,[35-37] a mechanism not available to the nitrogen of the sulfobetaine groups.
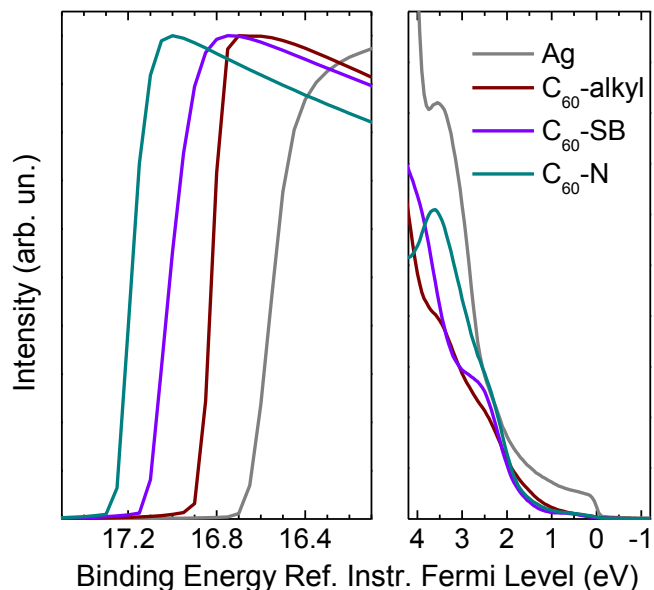
Figure 4.17 UPS of of **C_{60}-alkyl**, **C_{60}-N** and **C_{60}-SB** (~1 nm layers) on Ag. Δ values extracted from the high binding energy region near the E_{SEC} (left) are -0.54 eV for **C_{60}-N**, -0.39 eV for **C_{60}-SB**, and -0.15 eV for **C_{60}-alkyl**. The low binding energy region provides I_P values for **C_{60}-alkyl**, **C_{60}-N** and **C_{60}-SB**, of 5.70 eV, 5.62 eV and 5.72 eV respectively. Binding energies are given with reference to the instrument Fermi level. Reproduced from reference: Page, Z. A. et. al. *Science.* **2014**, p.441.

Table 4.5 UPS of **C_{60}-N** on Ag, varying fullerene thickness. Interfacial dipole increases by approximately 0.1 eV when going from 4.0 nm to 7.7 nm, but plateaus past this thickness, giving an interfacial dipole around -0.83 eV. This result agrees with the lower V_{OC} obtained for OPV devices fabricated with a ~4 nm interlayer thickness of **C_{60}-N**, compared to those fabricated with thicker films. Reproduced from reference: Page, Z. A. et. al. *Science.* **2014**, p.441.

Thickness (nm)	4.0	7.7	11.5	15.2	24.0	32.2
Δ_{Ag} (eV)	-0.74 ± 0.01	-0.83 ± 0.02	-0.82 ± 0.03	-0.84 ± 0.02	-0.85 ± 0.01	-0.84 ± 0.01
I_P (eV)	5.65	5.62	5.64	5.62	5.62	5.63

UPS, UV-Vis absorption and CV characterization were also accomplished to compare **C_{60}-N**, **C_{70}-N** and **mixed F-N** (**Figure 4.18** and **Table 4.6**). As expected due to

its red-shifted absorption C_{70}-N has a narrower E_g (1.68 eV) compared to C_{60}-N (1.83 eV). Interactions of all three amino-fulleropyrrolidines with Ag led to substantial reductions in work function, having Δ values ranging from -0.8 to -0.9 eV. Deep E_A values were identified (3.8-3.9 eV) and highlight the strong electron accepting ability of the fullerene portion in these derivatives. The electronic similarities between C_{60}-N and **mixed F-N** correspond well with their ability to act as effective cathode modification layers in OPV devices (**Figure 4.18** and **Table 4.6**).
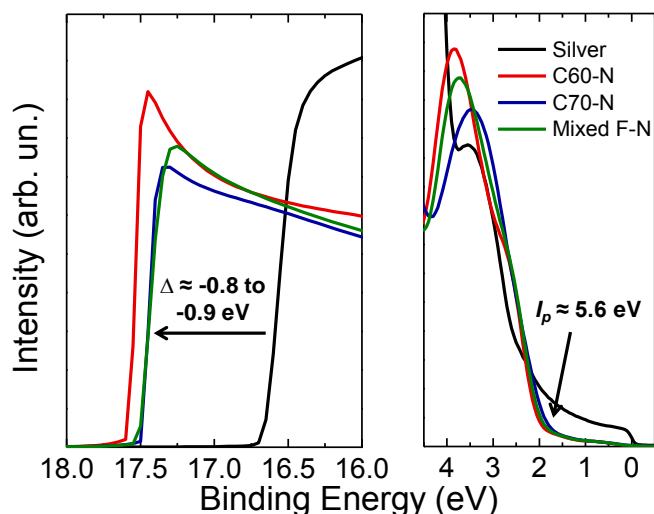
Figure 4.18 UPS of C_{60}-N, C_{70}-N and mixed **mixed F-N** on silver, showing comparable Δ and I_P values.

Table 4.6 Energy levels and Δ values with Ag for C_{60}-N, C_{70}-N and **Mixed F-N**.

Fullerene	E_g (eV)	I_P (eV)	E_A (eV)	Δ_{Ag} (eV)
C_{60}-N	1.83	5.59	3.76	-0.91 ± 0.02
C_{70}-N	1.68	5.57	3.89	-0.82 ± 0.01
Mixed F-N	1.83; 1.68	5.63	3.80 ; 3.95	-0.84 ± 0.01

The magnitude of Δ for C_{60}-N films on metal substrates depended critically on film thickness (**Figure 4.19A**). However, for ultrathin films (1 nm nominal thickness) of C_{60}-N on Ag, Cu or Au, the effective work function remained constant at 3.9 eV, independent of the metal composition. Observing this effect for such thin films indicates

that work function pinning originates at the metal/C_{60}-N interface, though the exact mechanism of this interaction is not understood fully.[38] With increasing C_{60}-N thickness, work function values saturated at 3.65 eV on Ag, Cu or Au (**Figure 4.19B**). This effect is independent of the metal substrate, yielding an effective work function of 3.65 eV for C_{60}-N-modified Ag, Cu and Au electrodes (**Figure 4.19B**). This observation in turn suggests that C_{60}-N provides Ohmic contact for electron injection, and a large built-in electrostatic potential difference for efficient charge extraction in OPVs. The effect of these fullerenes on different metals confirms the general utility of these interfacial layer materials, and successful interfacial tailoring independent of the work function inherent to each metal electrode.

Such a gradual change of Δ within ~5 nm of the interface indicates a narrow space charge region in C_{60}-N films, similar to a depletion region at the metal/doped semiconductor interface. The formation of a positive space charge in C_{60}-N is consistent with electron transfer from tertiary amines to the metal (equation 4.1), whereas the Δ values for C_{60}-alkyl gave no indication of electron transfer (**Figure 4.20**).[35-37,39]
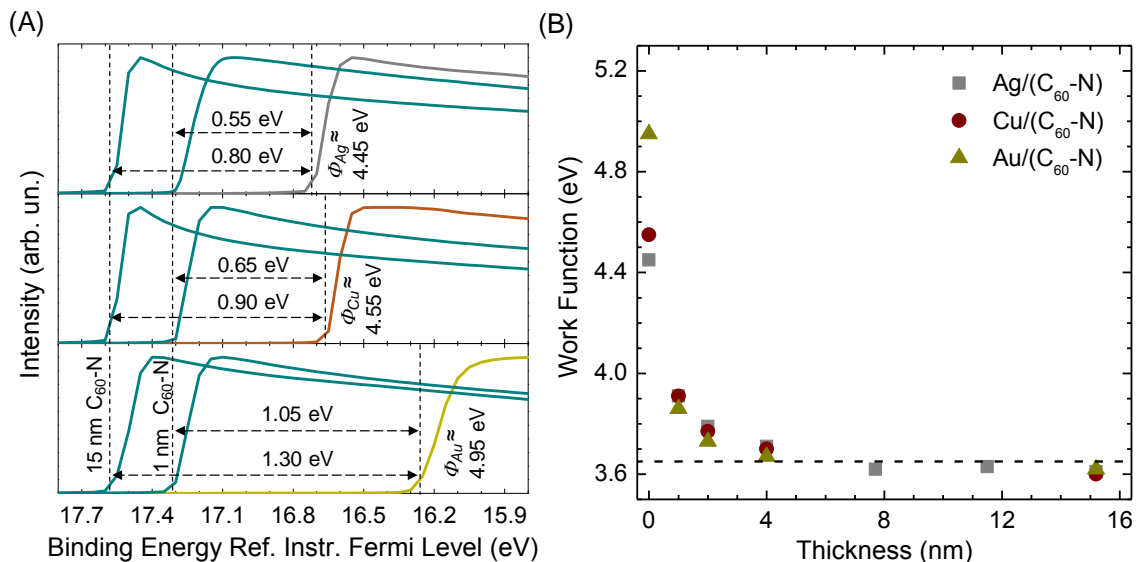
Figure 4.19 UPS of fulleropyrrolidine layers on metal substrates. (A) Representative high binding energy region spectra for **C$_{60}$-N** films on freshly prepared Ag, Cu and Au substrates that pin the work function of each modified metal surface at ~3.9 eV or ~3.65 eV for 1 nm and 15 nm films, respectively. (B) Work function modification of Ag, Cu and Au with **C$_{60}$-N** films of various thicknesses. Pinning of the effective work function is observed for very thin films (nominally 1 nm), and large modification of work function (to 3.65 eV) is achieved for interlayers > 4 nm. Reproduced from reference: Page, Z. A. et. al. *Science.* **2014**, p.441.

Equation 4.1 provides an expression for a depletion layer width (w), where V_{bi} (= Δ) is the built-in potential, q is the elementary charge, $\varepsilon_0 = 8.85\times10^{-12}$ F/m, and ε_r (=5) is the dielectric constant.[39]

$$w = \sqrt{\frac{2\varepsilon_r\varepsilon_0 V_{bi}}{qN_D}} \qquad 4.1$$

The exponential decrease of the work function for the interface of Ag with **C$_{60}$-N** indicates formation of a space charge due to quantum mechanical tunneling of electrons, consistent with electron transfer from amine groups to metal. Using a depletion layer width w of 5 nm, the density of positive charges N_D that resulted from the electron transfer can be estimated at 1×10^{19} cm^{-3} (equation 4.1). Taking the volume of a single **C$_{60}$-N** molecule as ~1 nm^3, approximately 1 in 300 amines in the layer participates in

electron donation to the metal. Therefore, an ultrathin layer of **C$_{60}$-N** near the metal surface effectively works as a highly-doped n-type semiconductor.
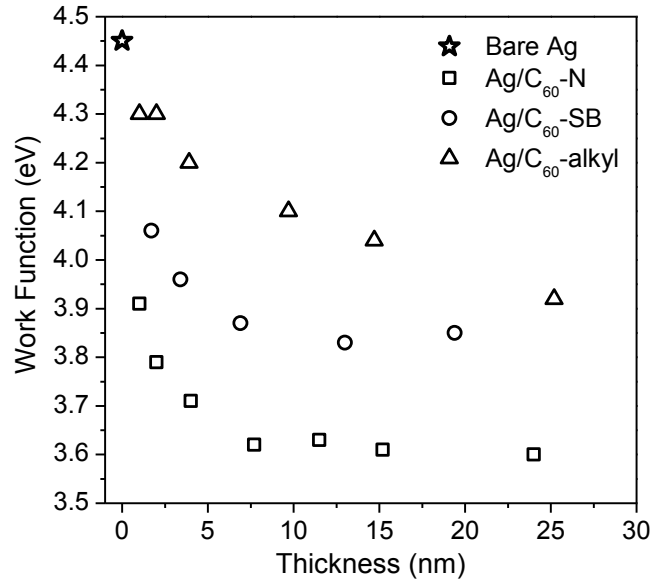
Figure 4.20 Φ modification of Ag with **C$_{60}$-alkyl**, **C$_{60}$-SB** and **C$_{60}$-N** films of various thicknesses, indicating different spatial profiles of electrostatic potential. Reproduced from reference: Page, Z. A. et. al. *Science.* **2014**, p.441.

Although device efficiency exceeded 6% for interlayers ranging from 5 to 55 nm, optimum PCE values were obtained at ~15 nm thickness, followed by a gradual decline in efficiency for thicker interlayers (**Figure 4.13**). To better understand the role of these polar fullerene interlayers, single-carrier devices were prepared to determine electron mobility using the modified Mott-Gurney law (equation 4.2) (where $\gamma \leq 1$ is the contact non-ideality factor) for the space charge limited current (SCLC) regime of device operation (**Figure 4.21**). Electron-only devices were constructed using an ITO bottom electrode and Ca/Al top electrode with PC$_{71}$BM, **C$_{60}$-N** or **C$_{60}$-SB** as the bulk transport material.

$$J = \gamma \frac{9}{8} \varepsilon_r \varepsilon_0 \mu \frac{V^2}{L^3} \qquad\qquad 4.2$$
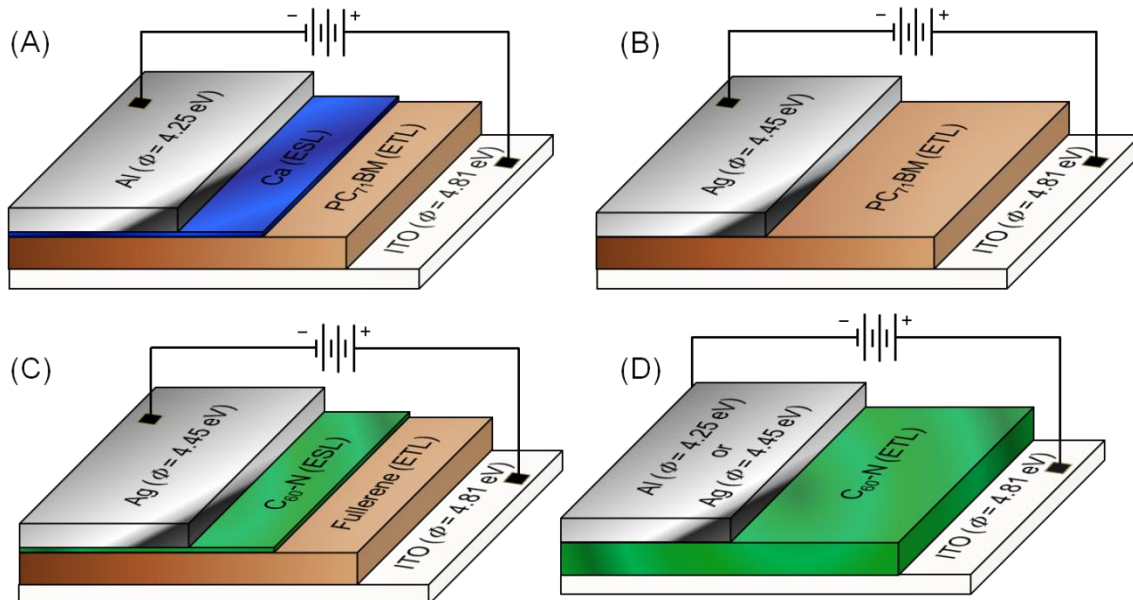
Figure 4.21 Representative device architectures used for SCLC. (A) ITO/PC$_{71}$BM/Ca/Al architecture to measure charge mobility of PC$_{71}$BM; (B) ITO/PC$_{71}$BM/Ag architecture to show the effect of a Schottky barrier at Ag/PC$_{71}$BM interface; (C) ITO/PC$_{71}$BM/**C$_{60}$-N**/Ag architecture to show Ohmic contact at **C$_{60}$-N**/Ag interface, removing barrier to injection into PC$_{71}$BM; (D) ITO/**C$_{60}$-N**/Ag architecture to show Ohmic contact at **C$_{60}$-N**/Ag interface and measure charge mobility of **C$_{60}$-N**. Reproduced from reference: Page, Z. A. et. al. *Science.* **2014**, p.441.

UPS suggests that hole injection from ITO to the HOMO of **C$_{60}$-N** is negligible due to a high energy barrier at the ITO/**C$_{60}$-N** interface (**Figure 4.22**), such that the devices shown in **Figure 4.21** are expected to only provide transport for electrons. Additionally, **C$_{60}$-N** was shown to pin the work the work function of ITO to ~3.65 eV, like Ag, Cu and Au, suggesting that inverted PSC architectures using **C$_{60}$-N** as an ITO (cathode) modification layer should work (**Figure 4.22**).
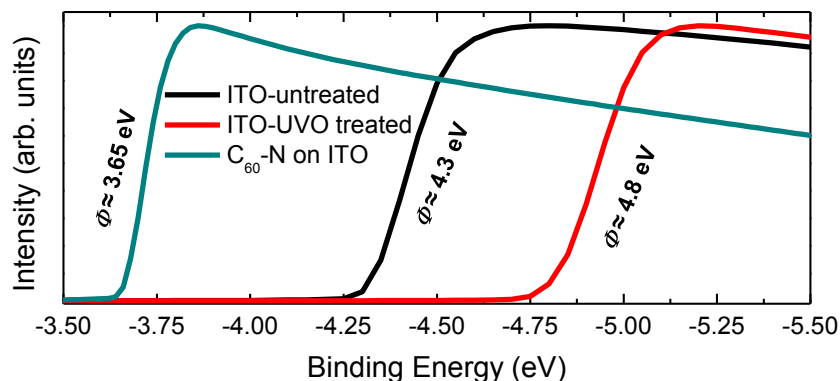
Figure 4.22 Representative high binding energy region spectra for bare ITO, UV-ozone treated ITO and ~15 nm thick film of **C$_{60}$-N** on ITO substrates where **C$_{60}$-N** pins the work function at ~3.65 eV. Binding energy scale provides ionization potentials by removing bias and subtracting the energy of the UV-light source (21.2 eV). Reproduced from reference: Page, Z. A. et. al. *Science.* **2014**, p.441.

Assuming Ca/Al electrodes provide Ohmic contact ($\gamma = 1$) for electron injection, electron mobilities of 1.3 x 10^{-3}, 1.8 x 10^{-3} and 1.0 x 10^{-5} cm^2/V-s were estimated for PC$_{71}$BM, **C$_{60}$-N** and **C$_{60}$-SB**, respectively (the dielectric constants, ε_r, were determined by impedance spectroscopy to be 3.5 for PC$_{71}$BM and 5.0 for **C$_{60}$-N** and **C$_{60}$-SB**) (**Figure 4.23**). The higher electron mobility of **C$_{60}$-N** compared to **C$_{60}$-SB** explains its higher efficiency as thicker interlayers in OPVs; less efficient electron extraction through **C$_{60}$-SB** interlayers imparts a series resistance that reduces *FF* and *J$_{SC}$*.
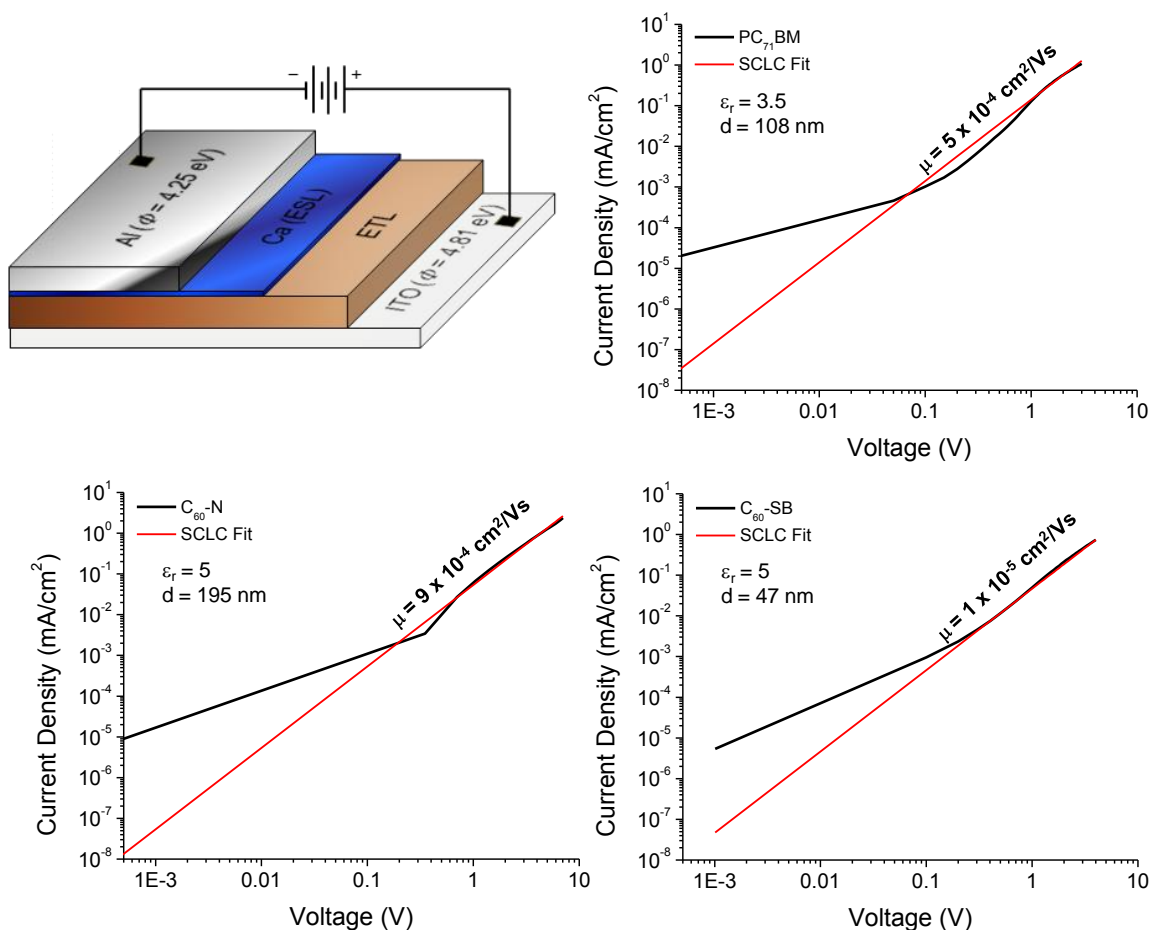
Figure 4.23 Representative *J-V* curves for diodes with an architecture of ITO/(PC₇₁BM, **C₆₀-N** or **C₆₀-SB**)/Ca/Al to estimate electron mobilities using an SCLC model. Reproduced from reference: Page, Z. A. et. al. *Science.* **2014**, p.441.

To determine whether Ag forms Ohmic contact with PC₇₁BM directly and whether a **C₆₀-N** interlayer improves its properties, devices were fabricated with a Ag top electrode and a PC₇₁BM, PC₇₁BM/**C₆₀-N** or **C₆₀-N** electron transport layer (**Figure 4.24**). Devices with only PC₇₁BM showed evidence of a Schottky barrier, resulting in a γ×μ product of 3.0 x 10⁻⁷ cm²/V-s, where γ ≤ 0.001 (more than 3 orders of magnitude lower than diodes with Ca/Al electrode). This is consistent with the high work function of Ag (4.45 eV) compared to the LUMO of PC₇₁BM (3.9 eV). Inserting a layer of **C₆₀-N** (13 nm, 25 nm or 48 nm) between PC₇₁BM and Ag improved mobility by four orders of magnitude, to 2.5 x 10⁻³ cm²/V-s, suggesting an Ohmic contact for **C₆₀-N**/Ag that

promotes electron injection into PC$_{71}$BM. With OPVs, a lower potential barrier for electron injection at Ohmic contact translates to larger built-in potential, faster electron extraction, and thus higher J_{SC} and *FF*. Additionally, single-carrier devices with only **C$_{60}$-N** as the bulk transport material and top Ag electrodes gave electron mobility values (1.1 x 10^{-3} cm^2/V-s) approximately equal to those measured using Ca/Al electrodes. Since the electron mobility of PC$_{71}$BM is independent of **C$_{60}$-N** interlayer thickness and comparable to the electron mobility in **C$_{60}$-N** itself, electron transport through **C$_{60}$-N** does not lead to an increased series resistance in OPV devices, and thus is not likely responsible for compromised PCE at greater interlayer thickness.
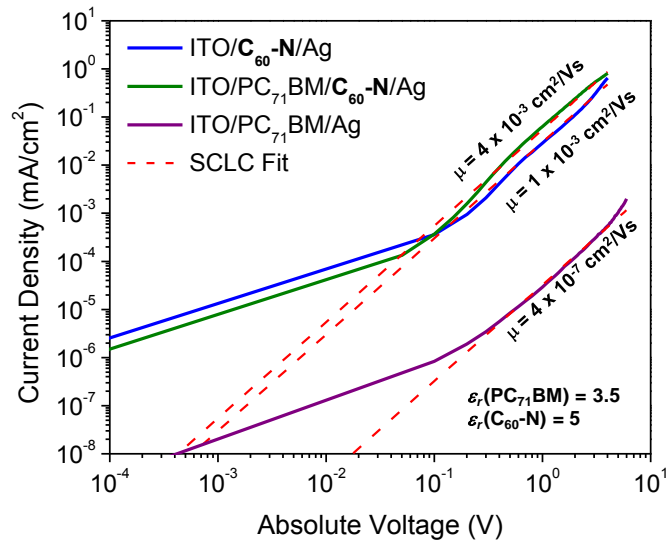
Figure 4.24 Representative *J–V* curves for electron-only devices with PC$_{71}$BM, PC$_{71}$BM/**C$_{60}$-N** and **C$_{60}$-N** layers in-between ITO and Ag electrodes, revealing that **C$_{60}$-N** removes the barrier for electron injection from Ag into the bulk organic layer, forming Ohmic contact. The dashed lines show fits to the Mott-Gurney law in the range of a SCLC regime of device operation. Reproduced from reference: Page, Z. A. et. al. *Science.* **2014**, p.441.

We further probed OPV devices fabricated with **C$_{60}$-N** interlayers on Ag (**Figure 4.25**) by UV-Vis reflectance spectroscopy, measured through the ITO substrate at 5° with respect to the surface normal. Devices with interlayers thicker than 7.7 nm exhibited

higher reflectance (reduced absorption) from 600 to 740 nm, where PBDTT-TT absorbs most strongly and C_{60}-N does not absorb. This represents direct evidence of an optical spacer effect,[40] where C_{60}-N redistributes the optical field within the device. The reduced absorption in the photoactive layer from 600 to 740 nm explains the reduced J_{SC}, and lower PCE, for OPV devices having thicker interlayers.
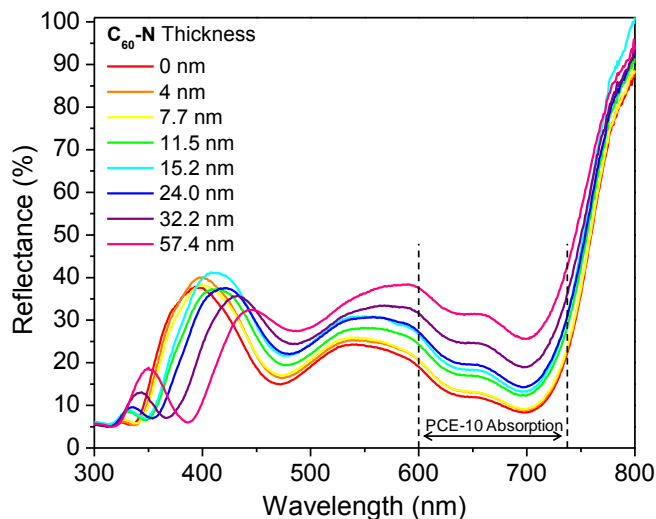
Figure 4.25 UV-Vis reflectance spectroscopy of OPV devices with C_{60}-N interlayer thicknesses varying from 4 to 57 nm (as well as a control device with no interlayer). The increased reflectance from 600 to 740 nm for devices containing interlayers thicker than 7.7 nm is direct evidence of an optical spacer effect, which explains the reduced J_{SC} for OPV devices with thicker interlayers. Reproduced from reference: Page, Z. A. et. al. *Science.* **2014**, p.441.

In addition, UV-Vis reflectance spectroscopy of bare metal cathodes (**Figure 4.26A**) reveals that the lower PCE obtained for devices with Cu (8.67 ± 0.17%) or Au (8.56 ± 0.21 %) cathodes, relative to Ag (9.35 ± 0.13 %) cathodes, can be attributed to the lower reflectivity of Au and Cu. Direct correlation between the metal reflectivity below 550 nm and external quantum efficiency of devices with different metal cathodes, both with and without C_{60}-N interlayers (**Figures 4.26B** and **4.26C**), indicates that metal reflectivity is responsible for lower short circuit current densities in devices with Au and Cu cathodes, as compared to devices with Al or Ag cathodes.
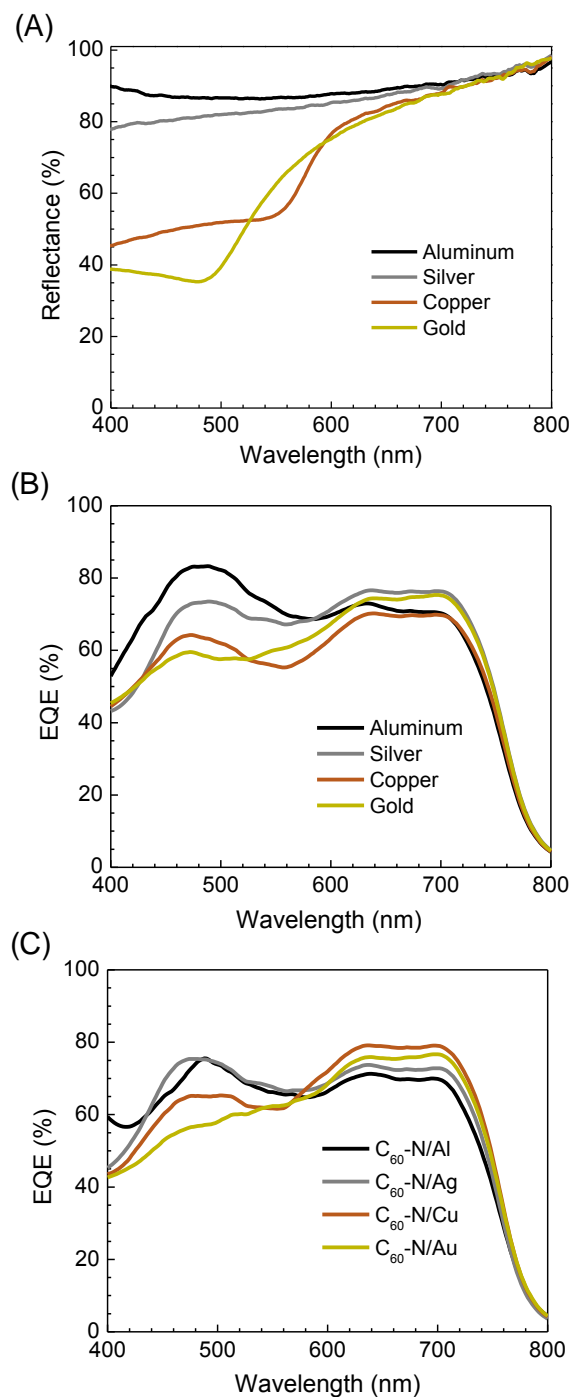
Figure 4.26 Reflectance and EQE measurements highlighting the optical effects associated with different metal cathodes. (A) Reflectance spectra showing reduced reflectance of visible light for copper and gold relative to aluminum and silver below 550 nm, which in-part explains the slightly reduced device performance (*Jsc* and PCE) for OPVs fabricated with Cu and Au cathodes compared to OPVs with Al and Ag cathodes. (B,C) External quantum efficiency (EQE) measurements for OPV devices containing Al, Ag, Cu and Au cathodes, without (B) and with (C) **C_{60}-N** interlayers. Reproduced from reference: Page, Z. A. et. al. *Science.* **2014**, p.441.

4.5 Summary and future outlook

In summary, novel fulleropyrrolidines bearing tertiary amines or sulfobetaines were prepared and found to open new routes to high efficiency devices in conjunction with numerous active layer polymers and electrode compositions. Simple, single-junction OPVs fabricated utilizing **C$_{60}$-N** and **C$_{60}$-SB** interlayers provided very high PCE values, and unprecedented efficiency (9.78%) for Ag cathode devices. PCE values exceeding 8.5% were obtained irrespective of the choice of cathode, even for high work function metals such as Au (Φ = 5.1 eV), confirming a universal utility of these interlayers. UPS revealed a pinning of the work-function at 3.65 eV; this is responsible for the observed cathode independent V_{OC} values ($\approx$ 0.75 V), and the significantly higher J_{SC} and *FF* values. UPS, charge mobility measurements, and reflectance spectroscopy explain 1) the high efficiency found in devices using **C$_{60}$-N** over that of **C$_{60}$-SB** interlayers; 2) the apparent insensitivity of device performance (PCE > 6%) as a function of interlayer thicknesses, and 3) the exceptional performance of OPV devices with a Ag cathode (PCE = 9.35 $\pm$ 0.13 %) over other metals. The synthetic accessibility of **C$_{60}$-N** and **C$_{60}$-SB**, their ability to mod-ify the electronic properties of metal substrates, and the resultant high efficiency OPV devices using C$_{60}$-N and C$_{60}$-SB as interlayers, makes these fulleropyrrolidines an excellent platform for electrode modification in OPVs as well as organic electronic devices in general.

4.6 References

1.   He, Z. *et al.* Enhanced power-conversion efficiency in polymer solar cells using an inverted device structure. *Nat. Photonics* **6**, 591–595 (2012).

2.   You, J. *et al.* A polymer tandem solar cell with 10.6% power conversion efficiency. *Nat. Commun.* **4**, 1410–1446 (2013).

3. Liu, Y. *et al.* Solution-processed small-molecule solar cells: breaking the 10% power conversion efficiency. *Sci. Rep.* **3**, 3356 (2013).

4. You, J. *et al.* 10.2% Power conversion efficiency polymer tandem solar cells consisting of two identical sub-cells. *Adv. Mater.* **25**, 3973–3978 (2013).

5. Yao, K. *et al.* A General Route to Enhance Polymer Solar Cell Performance using Plasmonic Nanoprisms. (2014).doi:10.1002/aenm.201400206.

6. Krebs, F. C. Polymer solar cell modules prepared using roll-to-roll methods: Knife-over-edge coating, slot-die coating and screen printing. *Sol. Energ. Mat. Sol. Cells* **93**, 465–475 (2009).

7. Krebs, F. C., Gevorgyan, S. a. & Alstrup, J. A roll-to-roll process to flexible polymer solar cells: model studies, manufacture and operational stability studies. *J. Mater. Chem.* 19, 5442–5451 (2009).

8. Guo, F. *et al.* ITO-Free and Fully Solution-Processed Semitransparent Organic Solar Cells with High Fill Factors. *Adv. Energy Mater.* **3**, 1062–1067 (2013).

9. Yip, H.-L. & Jen, A. K.-Y. Recent advances in solution-processed interfacial materials for efficient and stable polymer solar cells. *Energy Environ. Sci.* **5**, 5994–6011 (2012).

10. Duan, C., Zhang, K., Zhong, C., Huang, F. & Cao, Y. Recent advances in water/alcohol-soluble π-conjugated materials: new materials and growing applications in solar cells. *Chem. Soc. Rev.* **42**, 9071–9104 (2013).

11. Gu, C., Chen, Y., Zhang, Z., Xue, S. & Sun, S. Achieving High Efficiency of PTB7-Based Polymer Solar Cells via Integrated Optimization of Both Anode and Cathode Interlayers. *Adv. Energy Mater.* (2014).doi:10.1002/ aenm.201301771

12. Zhang, Z. *et al.* Amine group functionalized fullerene derivatives as cathode buffer layers for high performance polymer solar cells. *J. Mater. Chem. A* **1**, 9624–9629 (2013).

13. Worfolk, B. J. *et al.* Work function control of interfacial buffer layers for efficient and air-stable inverted low-bandgap organic photovoltaics. *Adv. Energy Mater.* **2**, 361–368 (2012).

14. Zhou, Y. *et al.* A universal method to produce low-work function electrodes for organic electronics. *Science* **336**, 327–332 (2012).

15. Woo, S. *et al.* 8.9% Single-stack inverted polymer solar cells with electron-rich polymer nanolayer-modified inorganic electron-collecting buffer layers. *Adv. Energy Mater.* (2014).doi:10.1002/aenm.201301692

16. O'Malley, K. M., Li, C.-Z., Yip, H.-L. & Jen, A. K.-Y. Enhanced Open-Circuit Voltage in High Performance Polymer/Fullerene Bulk-Heterojunction Solar Cells

by Cathode Modification with a C60 Surfactant. *Adv. Energy Mater.* **2**, 82–86 (2012).

17. Yang, X. *et al.* High-Efficiency Polymer Solar Cells Achieved by Doping Plasmonic Metallic Nanoparticles into Dual Charge Selecting Interfacial Layers to Enhance Light Trapping. *Adv. Energy Mater.* **3**, 666–673 (2013).

18. Chueh, C. *et al.* Toward high-performance semi-transparent polymer solar cells : optimization of ultra-thin light absorbing layer and transparent cathode architecture. *Adv. Energy Mater.* **3**, 417–423 (2013).

19. Mei, Q. *et al.* Enhancing the performance of polymer photovoltaic cells by using an alcohol soluble fullerene derivative as the interfacial layer. *ACS Appl. Mater. Interfaces* **5**, 8076–8080 (2013).

20. Li, S. *et al.* [6,6]-Phenyl-C 61 -Butyric Acid Dimethylamino Ester as a Cathode Buffer Layer for High-Performance Polymer Solar Cells. *Adv. Energy Mater.* **3**, 1569–1574 (2013).

21. Lai, Y.-Y. *et al.* Interface engineering to enhance the efficiency of conventional polymer solar cells by alcohol-/water-soluble C60 materials doped with alkali carbonates. *ACS Appl. Mater. Interfaces* **5**, 5122–5128 (2013).

22. Li, X., Zhang, W., Wu, Y., Min, C. & Fang, J. High performance polymer solar cells with a polar fullerene derivative as the cathode buffer layer. *J. Mater. Chem.* **1**, 12413–12416 (2013).

23. Duan, C., Zhong, C., Liu, C., Huang, F. & Cao, Y. Highly efficient inverted polymer solar cells based on an alcohol soluble fullerene derivative interfacial modification material. *Chem. Mater.* **24**, 1682–1689 (2012).

24. Wei, Q., Nishizawa, T., Tajima, K. & Hashimoto, K. Self-organized buffer layers in organic solar cells. *Adv. Mater.* **20**, 2211–2216 (2008).

25. Betancur, R. *et al.* Transparent polymer solar cells employing a layered light-trapping architecture. *Nat. Photonics* **7**, 995–1000 (2013).

26. Martínez-Otero, A., Elias, X., Betancur, R. & Martorell, J. High-Performance Polymer Solar Cells Using an Optically Enhanced Architecture. *Adv. Optical Mater.* **1**, 37–42 (2013).

27. Page, Z. A., Duzhko, V. V. & Emrick, T. Conjugated Thiophene-Containing Polymer Zwitterions: Direct Synthesis and Thin Film Electronic Properties. *Macromolecules* **46**, 344–351 (2013).

28. Liu, F., Page, Z., Duzhko, V. V., Russell, T. P. & Emrick, T. Conjugated Polymeric Zwitterions as Efficient Interlayers in Organic Solar Cells. *Adv. Mater.* **25**, 6868–6873 (2013).

29. Page, Z. A., Liu, F., Russell, T. P. & Emrick, T. Rapid, facile synthesis of conjugated polymer zwitterions in ionic liquids. *Chem. Sci.* **5**, 2368-2373, (2014).

30. Mitsunobu, O. & Yamada, M. Preparation of Esters of Carboxylic and Phosphoric Acid via Quaternary Phosphonium Salts. *Bull. Chem. Soc. Jpn.* **40**, 2380-2382 (1967).

31. Maggini, M. & Scorrano, G. Addition of Azomethine Ylides to C60: Synthesis, Characterization, and Functionalization of Fulleroene Pyrrolidines. *J. Am. Chem. Soc.* **115**, 9798-9799 (1993).

32. Prato, M. & Maggini, M. Fulleropyrrolidines : A Family of Full-Fledged Fullerene Derivatives. *Acc. Chem. Res.* **31**, 519-526 (1998).

33. Hummelen, J. C., Knight, B. W., LePeq, F. & Wudl, F. Preparation and Characterization of Fulleroid and Methanofullerene Derivatives. *J. Org. Chem.* **60**, 532-538 (1995).

34. Liang, Y. Y. *et al.* For the bright future-bulk heterojunction polymer solar cells with power conversion efficiency of 7.4%. *Adv. Mater.* 22, E135-E138 (2010).

35. Bröker, B. *et al.* Gold work function reduction by 2.2 eV with an air-stable molecular donor layer. *Appl. Phys. Lett.* **93**, 243303 (2008).

36. Lindell, L. *et al.* Integer charge transfer at the tetrakis(dimethylamino)ethylene/Au interface. *Appl. Phys. Lett.* **92**, 163302 (2008).

37. Lindell, L. *et al.* Transparent, Plastic, Low-Work-Function Poly(3,4-ethylenedioxythiophene) Electrodes. *Chem. Mater.* **18**, 4246–4252 (2006).

38. Braun, B. S., Salaneck, W. R. & Fahlman, M. Energy-Level Alignment at Organic/Metal and Organic/Organic Interfaces. *Adv. Mater.* **21**, 1450–1472 (2009).

39. Sze, S. M. & Ng, K. K. *Physics of Semiconductor Devices*. (John Wiley & Sons, Inc.: 2007).

40. Kim, J. Y. *et al.* New Architecture for High-Efficiency Polymer Photovoltaic Cells Using Solution-Based Titanium Oxide as an Optical Spacer. *Adv. Mater.* **18**, 572–576 (2006).

CHAPTER 5

ARYLENE-VINYLENE CONJUGATED POLYMER ZWITTERIONS

5.1 Introduction

Hydrophilic conjugated polymers are interesting from the standpoint of their optoelectronic activity and processibility in non-toxic polar solvents such as water and alcohols. Conjugated polymers of this type are further enticing for their facile structural tunability, surface wettability and mechanical flexibility. As such, hydrophilic conjugated polymers are of growing interest as organic field effect transistors (OFETs), light-emitting diodes (OLEDs), photovoltaics (OPVs) and sensors.[1] For example, conjugated polyelectrolytes (CPEs) and conjugated polyzwitterions (CPZs) integrate polar functionality pendent to conjugated aromatic backbones. Researchers have identified the utility of CPEs in optoelectronic and sensing applications,[1-3] while recent syntheses of CPZs by Huang, Huck, our group, and others show promise for producing polar, charge-neutral (counterion-free) electronically active materials for devices.[4-11]

In poly(arylene-vinylene)s (PAVs),[12,13] the vinylene linkages planarize the polymer backbone by removing torsional interactions between aryl rings, thus extending conjugation and tuning the band gap. Rotational flexibility about the vinyl group imparts solubility and solution processing.[14] PAVs are synthesized from appropriate polymer precursors, or directly by polymerization of suitable monomers. The precursor routes begin by polymerization of quinodimethane monomers,[15] followed by post-polymerization elimination to generate the conjugated structure. These routes often lead to structural defects, such as the formation of triple bonds and incomplete elimination.

Direct routes to PAVs include transition-metal catalyzed polymerizations (i.e., Heck and Stille couplings), metathesis polymerizations,[16] and transition-metal free polymerizations.[17-21] Horner-Wadsworth-Emmons (HWE) coupling represents a simple and effective approach to PAVs, giving reasonably high molecular weight and defect-free polymers, with a high degree of *trans*-olefins, without the need for metals or catalysts.[22-27] PAV production by HWE coupling is typically performed in organic solvents using electron-rich monomers and strongly basic conditions.

This chapter describes a route to aqueous HWE coupling on electron deficient bisphosphonate monomers to afford hydrophilic PAVs. Three different bisphosphonate monomers, containing thiadiazole and/or fluorine substituents, were coupled with anionic, cationic and zwitterionic terephthalaldehydes. In addition, discrete arylene vinylenes (AVs) were prepared to better understand the kinetics and regioselectivity of the coupling chemistry. Characterization of these hydrophilic PAVs in devices revealed their potential utility in organic electronics and sensing.

5.2 Synthesis

The hydrophilic PAVs were synthesized by polymerization of the aromatic bisphosphonates shown in **Scheme 5.1**. (1,4-Phenylenebis(methylene))bis(phosphonate) (**78**) was synthesized from dibromo-*p*-xylene by Michaelis-Arbuzov[28-30] (M-A) coupling to give the corresponding dialkylphosphate. Bisphosphonates **78**, **81**, **84** and **88** were obtained in this manner, and isolated in pure form and high yield (73-95%) by crystallization.
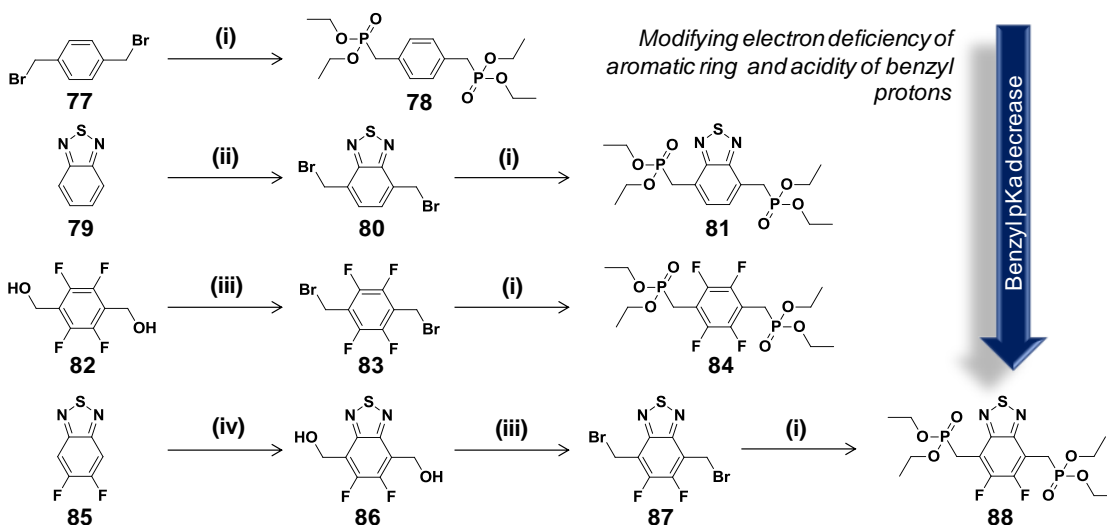
Scheme 5.1 Aromatic bisphosphonate monomer preparation: (i) P(OEt)$_3$, 73-95%; (ii) trioxane, myristyltrimethylammonium bromide, HBr (48 wt% in water), H$_2$SO$_4$, 92%; (iii) PBr$_3$, CH$_2$Cl$_2$, 38-65%; (iv) LDA, formaldehyde, THF, HMPA, 78%.

Dibenzylbromide **80**, the precursor to monomer **81**, was synthesized by bromomethylation of benzothiadiazole (**79**) under phase transfer conditions, using H$_2$SO$_4$ in place of CH$_3$COOH[31] to accelerate the reaction. Bis(bromomethyl) tetrafluorobenzene **83**, the precursor to **84**, was synthesized from commercially available tetrafluorobenzenedimethanol (**82**) with PBr$_3$. Monomer **88** was then prepared by hydroxymethylation of difluorobenzothiadiazole (**85**),[32] followed by bromination with PBr$_3$, and finally a M-A reaction. The hydroxymethylation reaction worked particularly well (78%) using lithium diisopropylamide (LDA)[33] in the presence of hexamethylphosphoramide (HMPA) to stabilize the dianionic benzothiadiazole intermediate, followed by reacting the intermediate with molecular formaldehyde instead of paraformaldehyde owing to improved solubility/reactivity in THF at -78 °C.[34,35] The electron withdrawing benzothiadiazole and fluorine groups increase the acidity of the benzyl protons positioned α to the phosphonate, according to calculations that place the pKa values in the order **78** > **81** > **84** > **88** (**88** is most acidic, **Figure 5.1**).
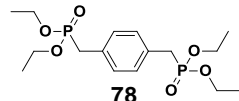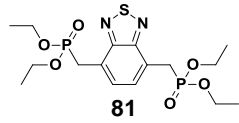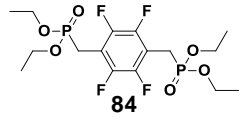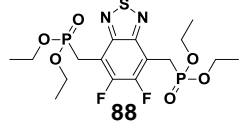
Theoretical pKa

78 25.9

81 23.3

84 20.7

88 20.6

Figure 5.1 Theoretical acid dissociation constants were calculator using JChem and ACE online software: <https://epoch.uky.edu/ace/public/pKa.jsp>.

The terephthalaldehyde monomers were synthesized with zwitterionic (**92**), cationic (**93**), and anionic (**94**) components from diol **89**,[36] as shown in **Scheme 5.2**. Zwitterion **92** was synthesized by reaction of **89** with 1,6-dibromohexane (used in excess) to give **90**, followed by treatment with dimethylamine to give **91**, and ring-opening of 1,3-propanesultone. The cationic derivative, **93**, was synthesized similarly, using trimethylamine in place of dimethylamine. The anionic derivative, **94**, was synthesized in one step from **89**, utilizing the sodium phenoxide salt to ring open 1,4-butane sultone and afford the bis-sulfonate product. Monomers **92** and **93** were purified simply by precipitation and filtration; isolation of **94** from residual salts was achieved by reverse phase chromatography (**Figure 5.2**).
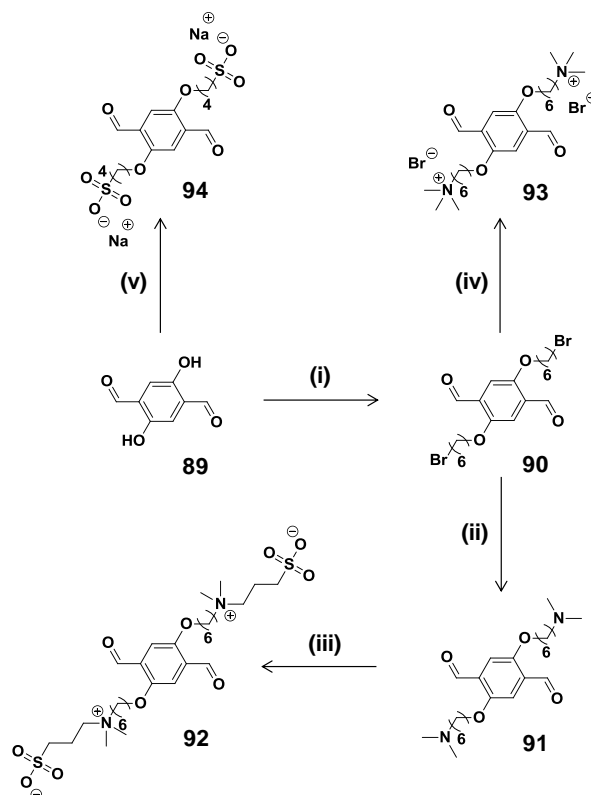
Scheme 5.2 Synthesis of monomers **92-94**: (i) 1,6-dibromohexane, K_2CO_3, CH_3CN, 69%; (ii) dimethylamine, THF, 87%; (iii) 1,3-propane sultone, CH_3CN, 98%; (iv) trimethylamine, CH_3CN, 96%; (v) 1,4-butane sultone, Na_2CO_3, DMF, 74%.
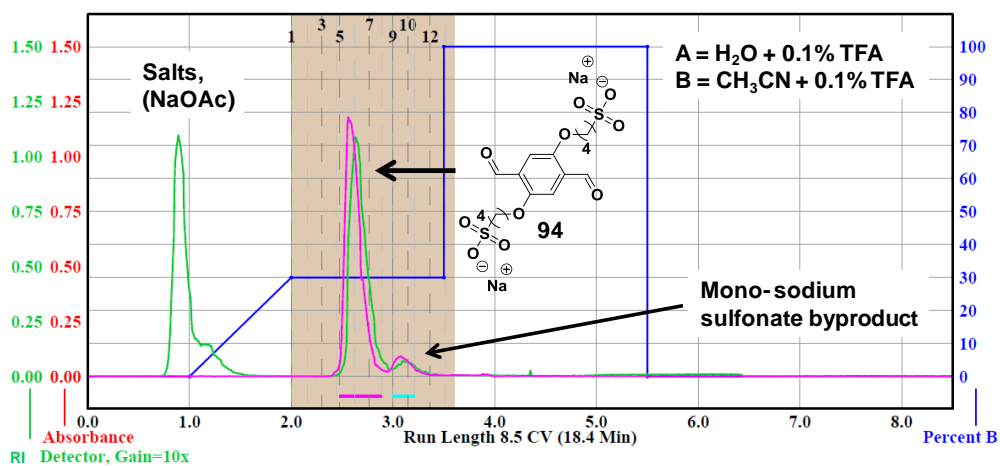
Figure 5.2 Representative reverse-phase chromatograph on C18-derivatized silica eluting initially with water (+0.1% TFA) and over-time the percent of acetonitrile(+0.1% TFA) is increased. Clear separation between non-UV active salts, desired product **94** and byproduct, sodium 4-(2,5-diformyl-4-hydroxyphenoxy)butane-1-sulfonate, that arises from incomplete ring-opening is shown.

141

Attempted HWE coupling/polymerization of bisphosphonate monomers **78**, **81**, **84** and **88** with terephthalaldehydes **92-94** (**Figure 5.3**) using sodium hydroxide as base were generally unfavorable. Monomer **78** did not react under these conditions, likely due to its weakly acidic benzyl protons, while monomers **81**, **84**, and **88** afforded only low molecular weight polymers ($M_n \approx$ 2-16 kDa) as estimated by size exclusion chromatography (SEC) in trifluoroethanol (TFE).
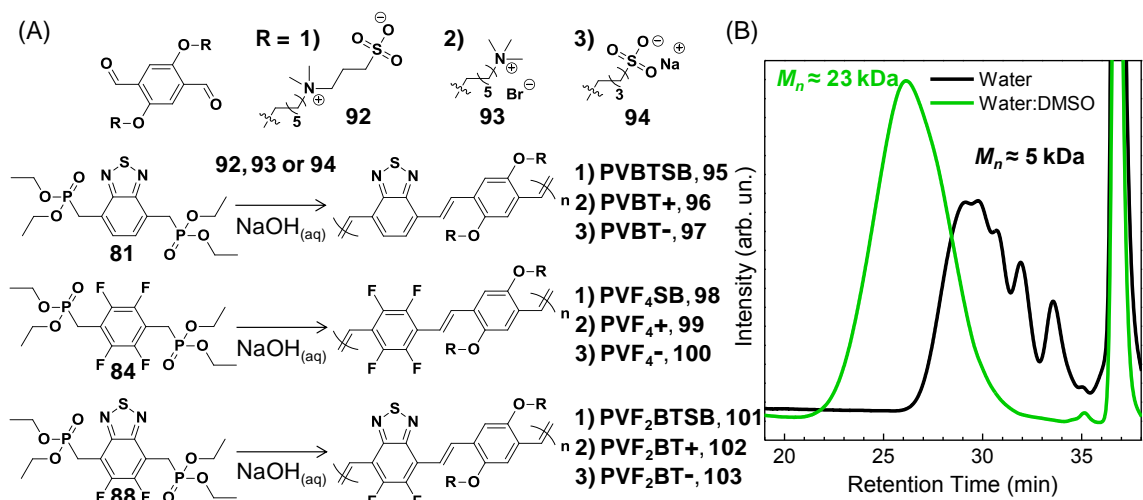
Figure 5.3 (A) HWE polymerization of bisphosphonate monomers **81**, **84**, and **88** with terephthalaldehyde monomers **92**-**94** in water, or 1:1 water:DMSO, yielding zwitterionic PAVs **PVBTSB** (**95**), **PVF$_4$SB** (**98**), and **PVF$_2$BTSB** (**101**); cationic PAVs **PVBT+** (**96**), **PVF$_4$+** (**99**), and **PVF$_2$BT+** (**102**); and anionic PAVs **PVBT-** (**97**), **PVF$_4$-** (**100**), and **PVF$_2$BT-** (**103**). (B) Representative size exclusion chromatograms of **PVBTSB**, eluting with 2,2,2-trifluoroethanol (the signal at 37 minutes corresponds to the methanol flow-marker, and poly(methyl methacrylate) calibration standards were employed).

Fortunately, performing HWE polymerizations in 1:1 H$_2$O:DMSO proved more successful.   Mixing   benzothiadiazole-phosphonate   **81**   and   zwitterionic terephthalaldehyde **92** under basic conditions led to a rapid change in the reaction mixture from yellow to blue, with extended polymer conjugation obtained in minutes as opposed to days for the polymerizations run in pure water. SEC of the polymer product confirmed the higher molecular weight achieved (up to 50 kDa) when using DMSO as cosolvent. The benzothiadiazole-based polymers reached higher molecular weights (20-

142

50 kDa) than the fluorinated derivatives (8-25 kDa), the latter precipitating during the course of the polymerization. The insensitivity of this HWE method to ambient conditions (*i.e.*, oxygen and moisture) and the absence of transition-metal catalysts and initiators are advantageous. The cationic and anionic CPEs displayed good solubility in pure water, while the CPZs were soluble in salt water and TFE. Solution aggregation of PAVs in DMSO, water and TFE resulted in weak fluorescence and substantial peak broadening in the ^{1}H-NMR spectra, making it impossible to determine the degree of *cis* vs *trans* vinyl linkages by NMR.

Benzaldehydes **104**-**106** (**Figure 5.4**) were synthesized in analogous fashion to the terephthalaldehydes described above, and coupled to aromatic bisphosphonates **81**, **84**, and **88** to afford AV oligomers as discrete model systems. The 9 AVs (3 each of cationic, anionic, and zwitterionic) prepared are shown in **Figure 5.4**. These structures fluoresce brightly in DMSO, suggesting their lack of aggregation relative to the corresponding polymers in DMSO. Additionally, the utility of different central aromatic units, (benzothiadiazole, tetrafluorobenzene and difluorobenzothiadiazole) provides a wide range of color tunability, as shown in **Figure 5.5**.
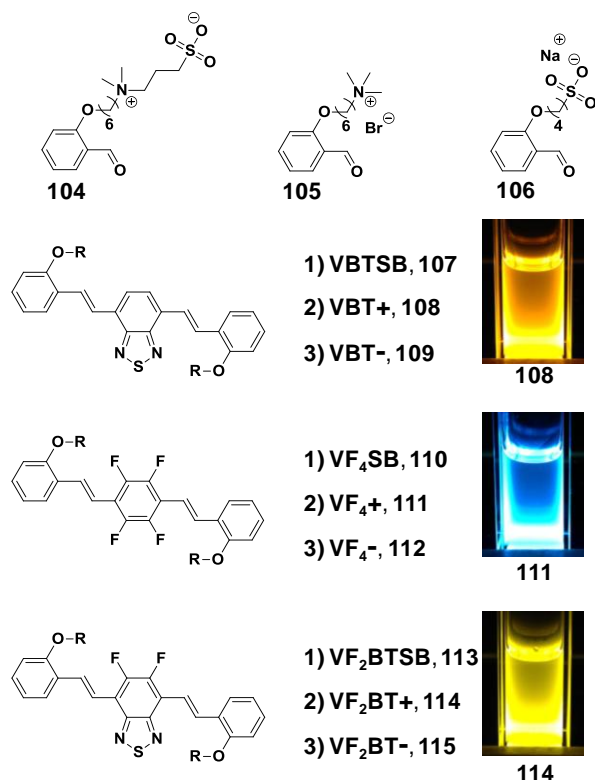
Figure 5.4 Discrete AV oligomers synthesized by HWE coupling of **81**, **84** and **88** with salicylaldehydes **104**, **105**, and **106**, yielding zwitterionic **VBTSB** (**107**), **VF₄SB** (**110**), and **VF₂BTSB** (**113**), cationic **VBT**+ (**108**), **VF₄**+ (**111**), and **VF₂BT**+ (**114**) and anionic **VBT**- (**109**), **VF₄**- (**112**), and **VF₂BT**- (**115**). The photographs are of cuvettes containing the indicated AVs as 0.2 mM DMSO solutions irradiated at 354 nm.
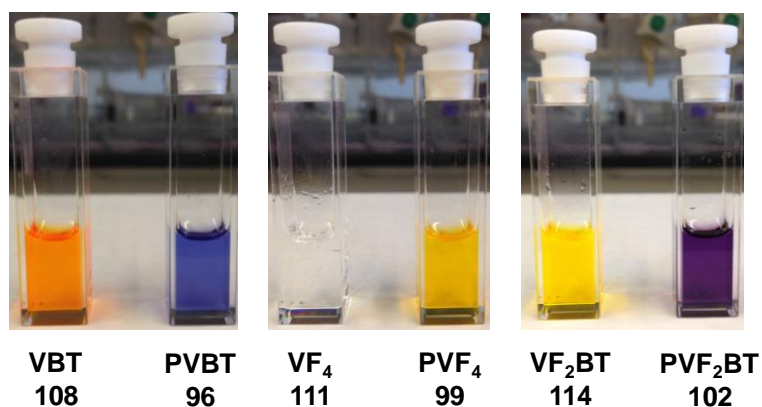
Figure 5.5 Images of cationic trimers and PAVs in DMSO, where the change in color from trimer to corresponding polymer indicates a bathochromic shift in absorption due to an increased conjugation length. Trimers are at a concentration of 0.2 mM and PAVs at 0.05 mg / mL.

144

5.3 Characterization

The AV synthesis allowed for facile characterization of these aqueous HWE reactions containing charged and zwitterionic side chains. ^{1}H-NMR spectroscopy lends insight to the regioselectivity of the AVs from the vinylene coupling constants. The spectra of the zwitterionic AVs shown in **Figure 5.6** indicate the presence of *trans* alkenes, with coupling constants of ~17 Hz in all cases (benzothiadiazole, tetrafluorobenzene and difluoro-benzothiadiazole). Smaller coupling constants, 5-10 Hz, would be expected for *cis* alkenes.[37] The *cis/trans* ratio in AVs and PAVs significantly impacts optoelectronic properties, where *trans* linkages typically improve planarity to maximize conjugation and minimize the energy gap (E_g).[38]
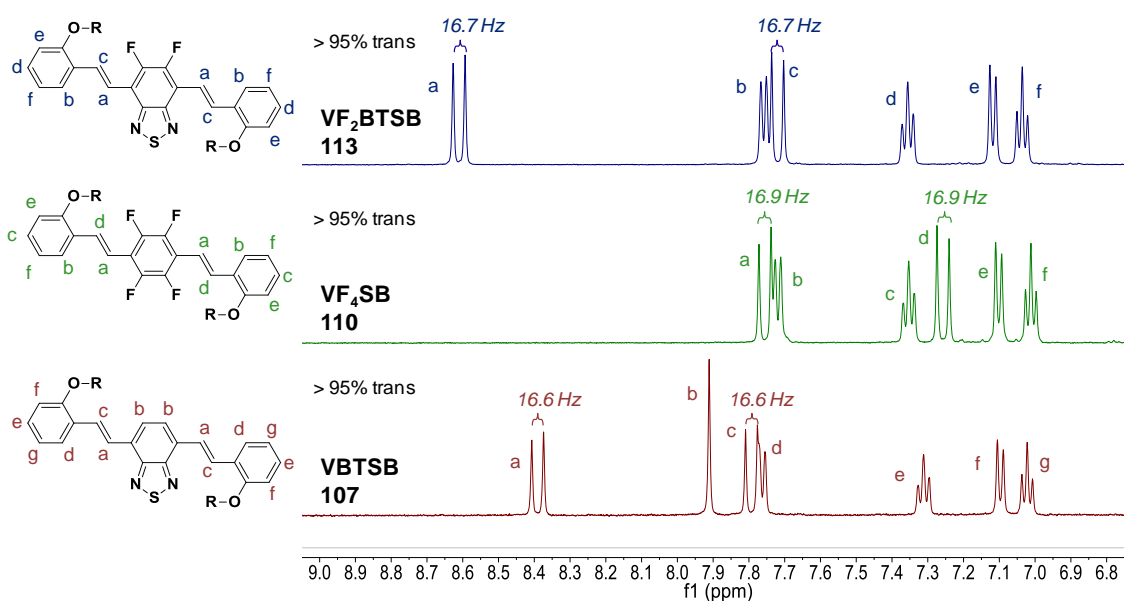
Figure 5.6 Partial ^{1}H-NMR spectra of **VBTSB**, **VF$_4$SB** and **VF$_2$BTSB**, with labels indicating coupling constants from *trans* alkene protons, indicating a high degree of regioselectivity.

NMR spectroscopy was used to monitor the kinetics of the HWE reactions (**Figures 5.7** and **5.8**). ^{31}P-NMR spectra were recorded on reaction performed in basic

(NaOH) D$_2$O in an NMR tube, specifically noting signals for benzylphosphonates (20-30 ppm) and sodium phosphonate salt by-product (0.5 ppm) (**Figure 5.8**).

$$Rate = k_{obs}[A][P][B] \text{ where } k_{obs} = \frac{k_1 k_2 K_{eq}}{k_2 + k_{-1}}$$
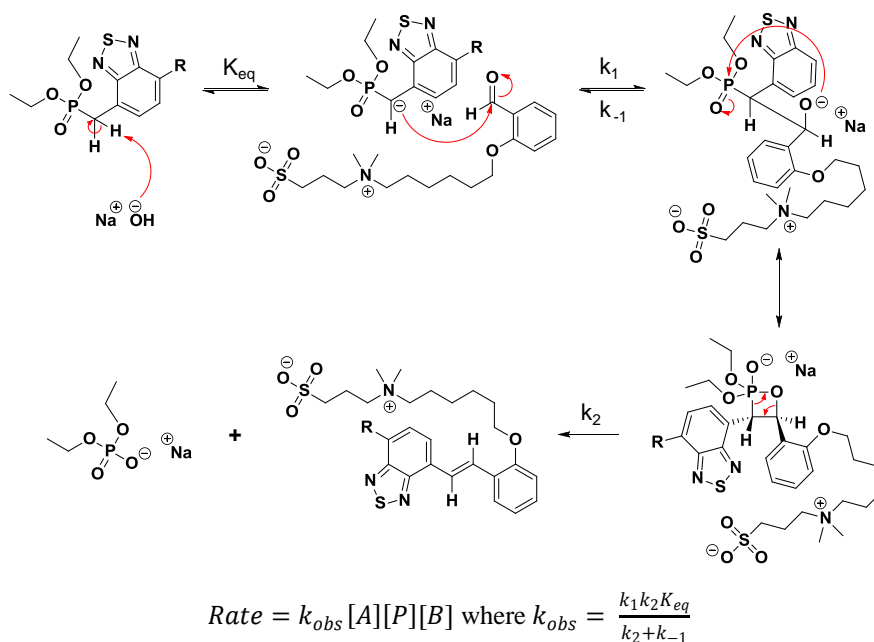
Figure 5.7 Mechanism of HWE coupling and corresponding rate equation[39-41] (derived using the steady state approximation), where [A] = aldehyde concentration, [P] = phosphonate concentration, and [B] = base concentration.
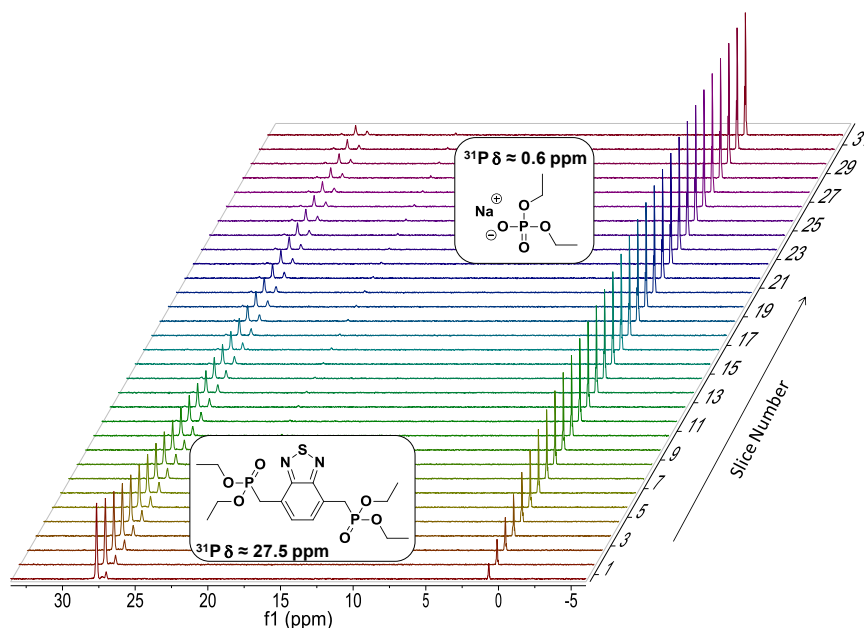
Figure 5.8 ^{31}P-NMR kinetics spectra for the reaction between bisphosphonate benzothiadiazole monomer (**81**) and sulfobetaine benzaldehyde (**104**) in water with four equivalents of NaOH. Spectra were recorded every 20 minutes, monitoring the disappearance of the peak at 25 ppm and concurrent appearance of the peak at 0.6 ppm.

146

HWE reactions are typically overall third order (first order in each aldehyde [A], phosphonate [P], and base [B]); carbanion addition to the aldehyde is the rate-limiting step (**Figure 5.7**).[39-41] The reaction of phosphonate **81** with zwitterionic benzaldehyde **104** was monitored with varying reactant concentration, finding the expected linear relationship between reaction rate and [A][P][B] (**Figure 5.9** and **Table 5.1**).
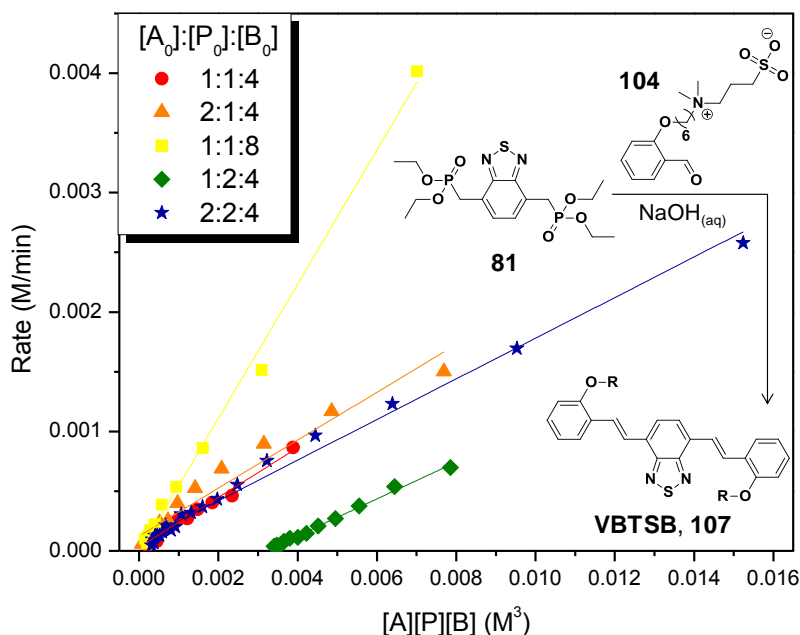
Figure 5.9 HWE kinetics for the trimerization reaction between bisphosphonate benzothiadiazole monomer, **81**, and sulfobetaine-benzaldehyde **104** with NaOH as the base and water as the solvent, yielding **VBTSB**, **107**. Initial reactant concentrations are varied, resulting in no observable change in rate constant (k_{obs}) irrespective of the initial aldehyde, [A_0], or phosphonate, [P_0], concentrations, but changes upon increasing the initial base concentration, [B_0].

Table 5.1 Observed rate constants for HWE trimerization reactions between benzothiadiazole-phosphonate, **81**, and zwitterionic benzaldehyde, **104**, to give **VBTSB**, **107**. All reactions were done in water at room temperature. Data shown is an average from two experiments.

	VBTSB				
[A_0] (M)	0.1	0.2	0.2	0.1	0.1
[P_0] (M)	0.1	0.2	0.1	0.2	0.1
[B_0] (M)	0.4	0.4	0.5	0.4	0.8
k_{obs} (M^{-2} min^{-1})	0.21	0.17	0.19	0.15	0.56
r^2	0.98	0.99	0.95	0.99	0.99

Subsequent kinetics experiments compared reaction rates of the aromatic bisphosphonates **81**, **84** and **88** (**Figure 5.10**) and hydrophilic benzaldehydes **104**-**106** (**Figure 5.11A** and **Tables 5.2** and **5.3**), with additional examination of the effect of DMSO as a co-solvent with water (**Figure 5.11B** and **Table 5.4**). The reactivities of the bisphosphonate monomers tracked closely with calculated pKa values, with the more acidic **88** reacting 6-10 times faster than the less acidic **81** (**Figures 5.1** and **5.10**).
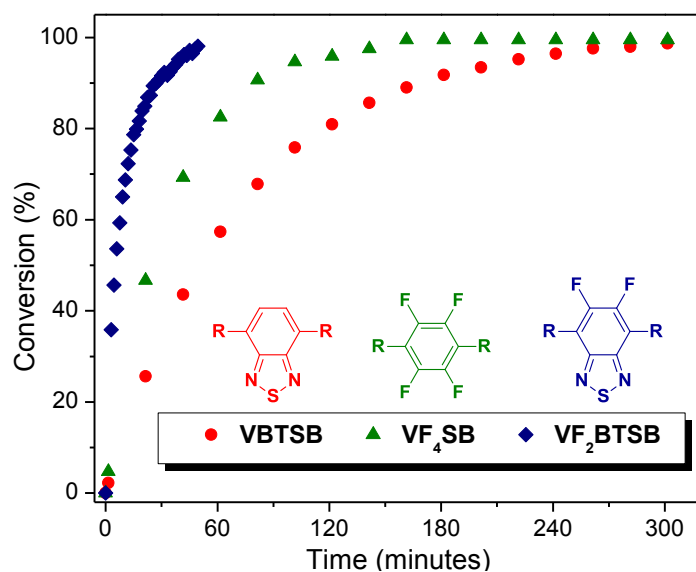
Figure 5.10 HWE coupling kinetics for aromatic bisphosphonates **88**, **84** and **81**, with zwitterionic benzaldehyde **104**, revealing the following reaction rate trend: **88** > **84** > **81**. All experiments were run in duplicate and done at room temperature, in H_2O (H_2O:DMSO) with four equivalents of NaOH as the base, using ^{31}P-NMR to determine conversion.

For the benzaldehydes, the cationic example was most reactive, followed by the zwitterionic and anionic versions (**Figure 5.11A**). Since the rate-limiting step of HWE coupling is nucleophilic attack on the aldehyde, we speculate that the cation of **105** interacts with the transient anion of the benzyl phosphonate derivatives, drawing it closer to the aldehyde. In contrast, charge repulsion slows the reaction of **106**. Increasing the DMSO:water ratio to 3:1 (**Figure 5.11B**) accelerated the reaction rate by > 100 times (the

reaction went to completion in < 2 minutes, corresponding to the higher molecular weight

PAVs obtained for polymerizations in DMSO:water, **Figure 5.3**). We speculate that

DMSO accelerates the reaction rate by reducing the influence of solution aggregation.
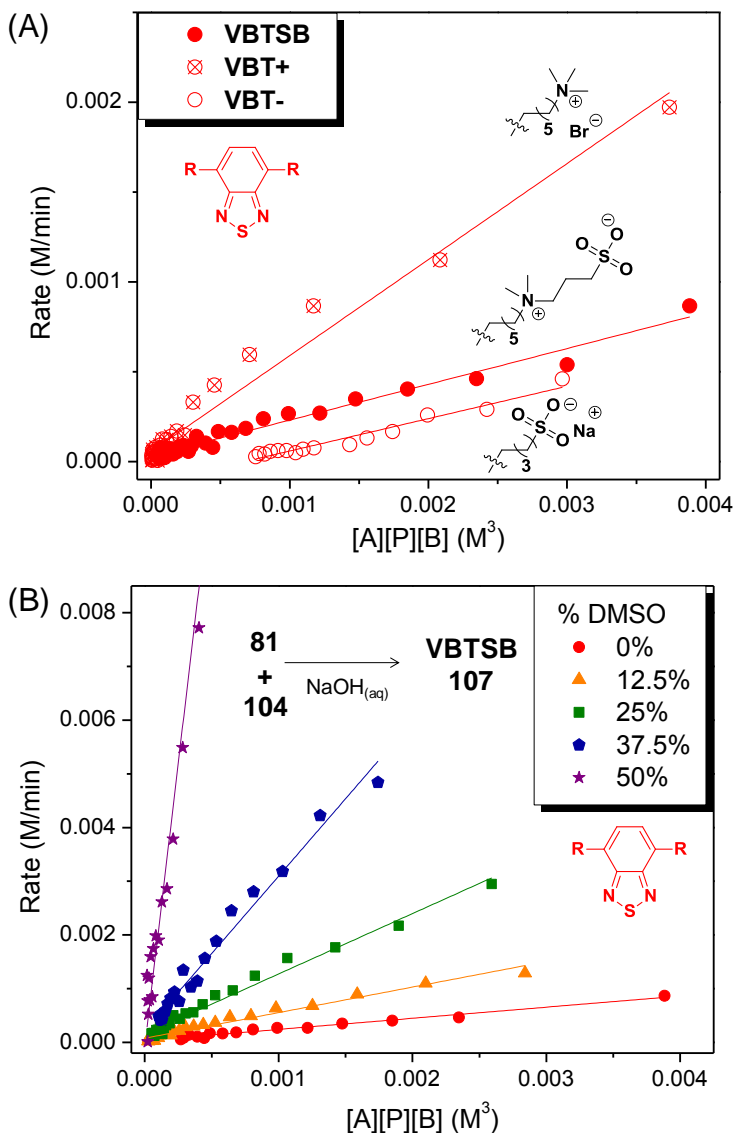
Figure 5.11 HWE coupling kinetics for (A) zwitterionic (**104**), cationic (**105**) and anionic (**106**) benzaldehydes, and (B) H$_2$O and H$_2$O:DMSO solvents. The following reaction rate trends are revealed: cation > zwitterion > anion and DMSO:H$_2$O > H$_2$O. All experiments were run in duplicate and done at room temperature, in H$_2$O (H$_2$O:DMSO) with four equivalents of NaOH as the base, using ^{31}P-NMR to determine conversion.

Table 5.2 Observed rate constants for HWE trimerization reactions done in water at room temperature, with equivalent amounts of aldehyde ($[A_0] = 0.1$ M) and phosphonate ($[P_0]$ = 0.1 M) and excess base ($[B_0]$ = 0.4 M). Data shown is an average from two experiments.

	VBT			VF$_4$			VF$_2$BT		
	SB	+	-	SB	+	-	SB	+	-
k_{obs} (M^{-2} min^{-1})	0.21	0.53	0.18	0.43	0.68	0.24	1.29	3.22	1.39
r^2	0.98	0.98	0.95	0.99	0.95	0.85	0.91	0.89	0.88

Table 5.3 Observed rate constants for HWE trimerization reactions done in water at room temperature, with two equivalents of aldehyde ($[A_0] = 0.2$ M) relative to phosphonate ($[P_0] = 0.1$ M) and excess base ($[B_0]$ = 0.4 M). Data shown is an average from two experiments.

	VBT			VF$_4$			VF$_2$BT		
	SB	+	-	SB	+	-	SB	+	-
k_{obs} (M^{-2} min^{-1})	0.19	0.23	0.09	0.44	0.54	0.15	1.89	2.29	1.00
r^2	0.95	0.84	0.89	0.96	0.94	0.88	0.95	0.85	0.94

Table 5.4 Observed rate constants for trimerization reactions done in H$_2$O:(DMSO) at room temperature between benzothiadiazole-phosphonate, **81**, and zwitterionic benzaldehyde, **104**, to give **VBTSB**, with equivalent amounts of aldehyde ($[A_0] = 0.1$ M) and phosphonate ($[P_0] = 0.1$ M) and excess base ($[B_0]$ = 0.4 M).Data shown is an average from two experiments.*Reaction was complete by the time one ^{31}P NMR scan could be measured (~2 mins).

VBTSB	DMSO (%)					
	0	12.5	25	37.5	50	75*
k_{obs} (M^{-2} min^{-1})	0.21	0.48	1.12	2.88	21.11	---
r^2	0.98	0.97	0.98	0.98	0.98	---

The solid state energy levels were determined for the nine PAVs using UV-Vis absorption spectroscopy (**Figures 5.12** and **5.13**) to determine the energy gap (E_g) from the onset of absorption, and ultraviolet photoelectron spectroscopy (UPS) to determine ionization potential (I_P) from the low-binding energy onset (**Table 5.5**).
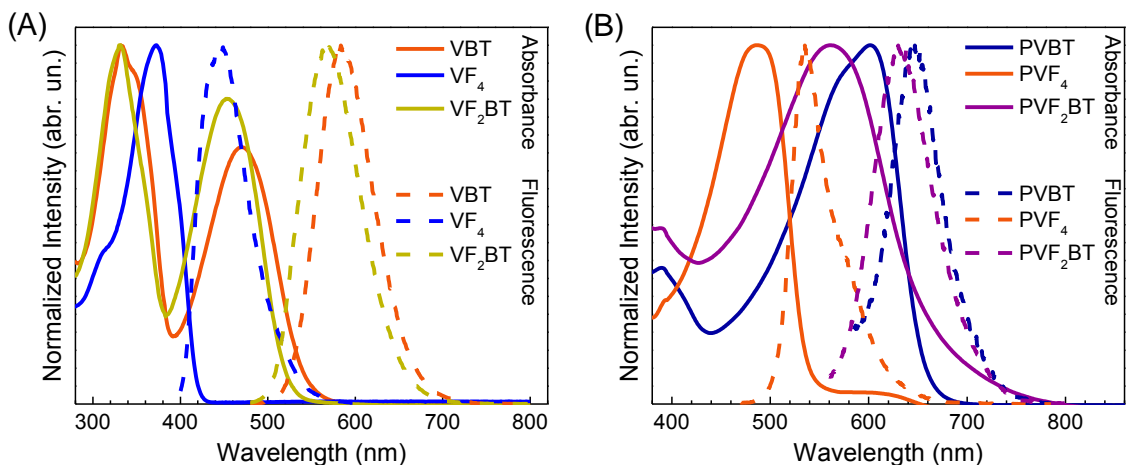
Figure 5.12 Normalized absorption and fluorescence spectra of cationic AVs (A) and PAVs (B) in DMSO. Excitation for fluorescence spectra was at peak absorption, λ_{max} (second, red-shifted peaks for **VBT** and **VF₂BT**). The anionic and zwitterionic materials show very similar absorption and fluorescence features to the representative cationic AVs and PAVs.
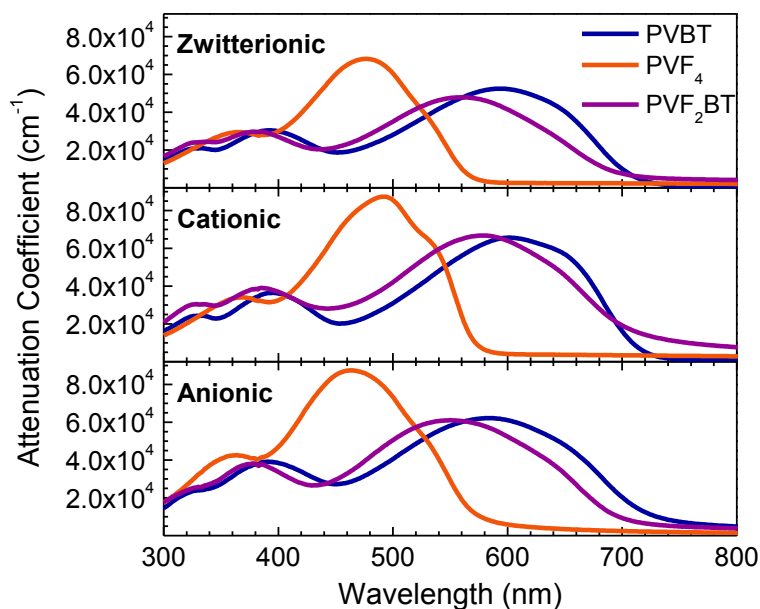
Figure 5.13 UV-Vis absorption spectra of PAV films spun-coat onto glass substrates. Thickness of the films was determined after measuring absorption profiles using a profilometer, followed by calculating the shown attenuation coefficients using Beer's law (ε = A / l, where ε is attenuation coefficient, A is absorption and l is thickness). E_g's were determined from the absorption onset.

UPS also probes interactions between a conductive substrate and an ultra-thin coating, providing information about work function (Φ) from the high binding energy region in the spectrum. This is calculated from the difference between the secondary

151

electron cutoff energies (E_{SEC}) of the bare and coated conductive substrate, denoted as an interfacial dipole (Δ).

Table 5.5 Hydrophilic PAV energy levels and Δ values measured on Ag, determined with UV-Vis absorption spectroscopy and UPS. Δ values given are averages from ≥ 3 measurements, with ± 1 standard deviation.

PAVs	E_g (eV)	I_P (eV)	E_A (eV)	Δ_{Ag} (eV)
PVBTSB	1.74	5.18	3.44	-0.56 ± 0.05
PVF$_4$SB	2.19	5.48	3.29	-0.67 ± 0.02
PVF$_2$BTSB	1.79	5.30	3.51	-0.63 ± 0.03
PVBT+	1.71	5.09	3.38	-0.70 ± 0.05
PVF$_4$+	2.17	5.46	3.29	-0.77 ± 0.06
PVF$_2$BT+	1.74	5.19	3.45	-0.73 ± 0.07
PVBT-	1.72	5.19	3.47	0.03 ± 0.03
PVF$_4$-	2.16	5.68	3.52	0.13 ± 0.03
PVF$_2$BT-	1.78	5.34	3.56	0.05 ± 0.03

We showed previously that CPZs reduce the Φ of Ag (-Δ), a stable high work function metal, facilitating its use as a cathode in OSCs in place of less stable Ca/Al. For CPEs, cationic polymers similarly induce a negative Δ, while anionic polymers lead to a positive Δ (increase Φ), and thus find utility as both cathode and anode modification layers in optoelectronics.[42] The three zwitterioinc, cationic and anionic PAVs were coated as ultra-thin layers (< 5 nm) onto freshly deposited Ag substrates and characterized by UPS (**Figure 5.14**).
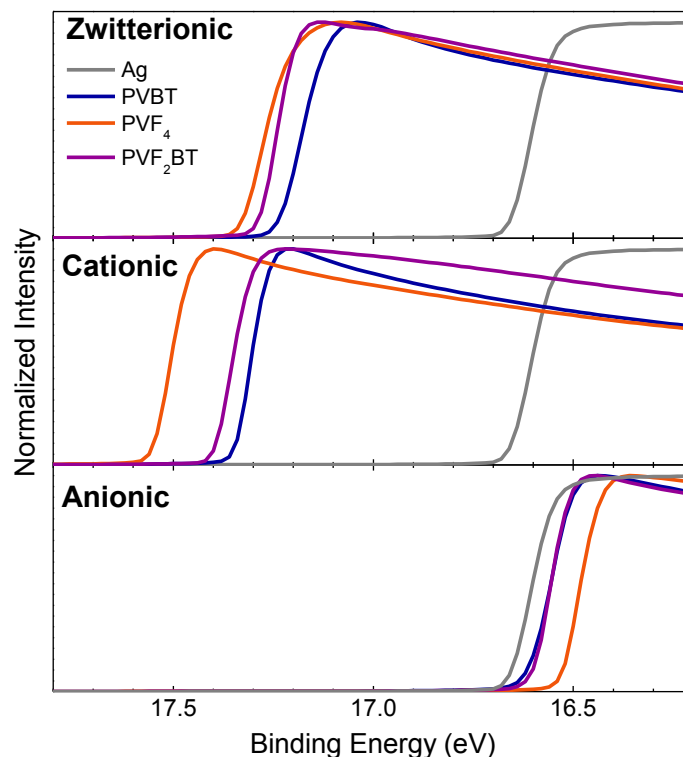
Figure 5.14 Representative ultraviolet photoelectron spectra of thin PAV layers (< 5 nm) on silver substrates. Δ values are extracted from the high binding energy region at the onset (E_{SEC}). The zwitterionic and cationic PAVs reduce the work function of Ag by ~0.6 to 0.8 eV and the anionic PAVs lead to a small increase in work function of ≤ 0.1 eV. Binding energies are given with reference to the instrument Fermi level and UPS experiments were run in triplicate.

The zwitterionic and cationic PAVs resulted in a substantial decrease in Φ ($\Delta \approx$ -0.6 to -0.8 eV), while the anionic CPEs produced a minor increase in Φ of both Ag and ITO ($\Delta \leq 0.1$ eV) (**Table 5.6** for UPS data of anionic PAVs on ITO).

Table 5.6 Anionic PAV energy levels and Δ values measured on ITO, determined with UV-Vis absorption spectroscopy and UPS. Δ values given are averages from ≥ 3 measurements, with ± 1 standard deviation.

PAVs	E_g (eV)	I_P (eV)	E_A (eV)	Δ_{ITO} (eV)
PVBT-	1.72	5.19	3.47	-0.02 ± 0.04
PVF$_4$-	2.16	5.68	3.52	0.15 ± 0.02
PVF$_2$BT-	1.78	5.34	3.56	0.00 ± 0.04

5.4 Applications

Due to their inherent photoluminescence and structural tunability, CPEs are now entering applications in chemo- and bio-sensing. Sensing based on electrostatic, van der

Waals, and specific substrate (antigen-antibody, biotin-avidin) interactions has been explored, where fluorescence 'turn-on' and 'turn-off' is exploited.[3] Implementation of these platforms in sensing relies on amplified quenching, where high photoluminescence quenching efficiency is achieved at very low quencher/analyte concentrations. The tetrafluorobenzene polymer family (**PVF$_4$**) was subjected to Stern-Volmer photoluminescence quenching experiments using methyl viologen (MV^{2+}) as a cationic quencher (**Figures 5.15** and **5.16**). Notably, **PVF$_4$-** exhibited a relatively strong amplified quenching response with $K_{sv} = 4 \times 10^6 \, M^{-1}$, comparable to state of the art CPEs ($\sim 10^6$-10^7 M^{-1}).[43] Additionally, it was observed that ca. 3 µM MV^2 effectively quenched 95% of the PL intensity.
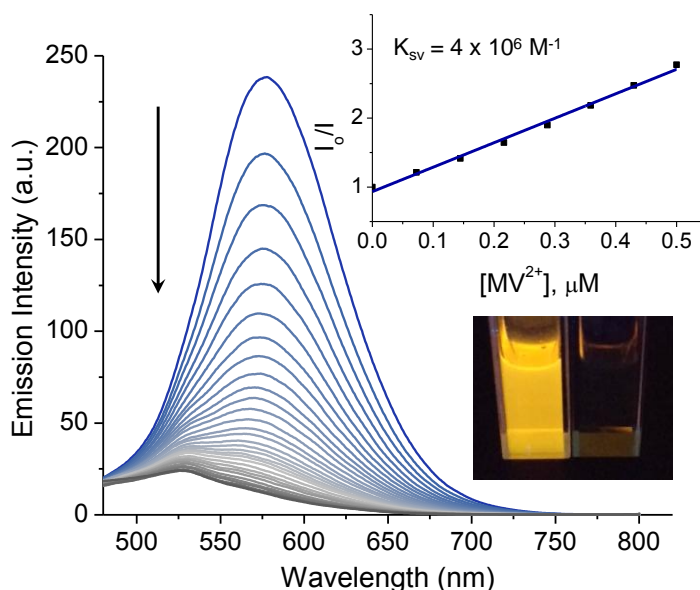
Figure 5.15 Evolution of the PL spectrum of Polymer **PVF$_4$-** upon the addition of MV^{2+} quencher, the respective Stern-Volmer plot, and photograph of the polymer solutions in water with and without quencher.

The high quenching efficiency of the **PVF$_4$-** is attributed to the ion-complexation between the oppositely charged MV^{2+} and polymer repeat units, effectively increasing the local concentration of the quencher ion. More importantly, it indicated exciton

delocalization and rapid migration along the polymer chain, increasing the effective sphere of action of the quencher molecule. High MV^{2+} concentrations led to enhanced quenching (as shown in **Figure 5.16**), which likely arises from complexation (and thus aggregation) of two polymer chains with one MV^{2+} quencher.[44] Only moderate amplification was exhibited by the zwitterionic derivative, **PVF₄SB**, (K_{sv} = 2 x 10^5 M^{-1}), with the PL intensity attenuation essentially similar to that exhibited by the cationic polyelectrolyte, **PVF₄+** (16% and 18% PL quenching at ca. 3 µM MV^{2+}) (**Figure 5.16**). Negative deviation from the Stern-Volmer relationship was characteristic of both polymers, in accord with the hindered chromophore access, possibly due to the electrostatic repulsion between the quencher ion and the polymer side chains.[45]
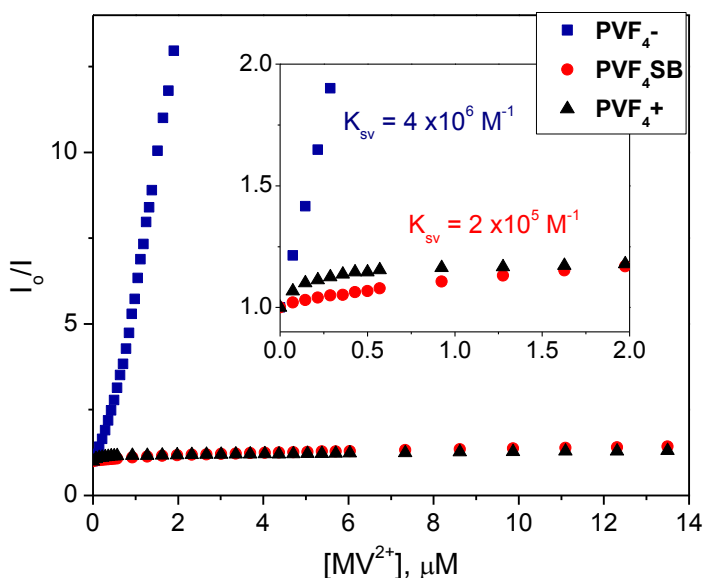
Figure 5.16 Stern-Volmer plots for polymers **PVF₄SB** (zwitterion), **PVF₄+** (cation), and **PVF₄-** (anion) and the respective Stern-Volmer quenching constants.

To probe the value of these PAVs in polymer solar cells (PSCs) they were incorporated as interfacial layers between the photoactive layer and electrode. The PSCs were fabricated with Ag cathodes rather than Al, to demonstrate their utility in conjunction with stable high Φ metal electrodes. Based on the Δ values determined by

UPS (**Figure 5.14** and **Tables 5.5** and **5.6**), we used the zwitterionic and cationic polymers as cathode modifiers (in place of C_{60}-N^{46}) and anionic polymers as anode modifiers (in place of poly(ethylenedioxythiophene):poly(styrene sulfonate), PEDOT:PSS) (**Figures 5.17** and **5.18** and **Tables 5.7** and **5.8**). Specifically, the zwitterionic and cationic PAVs were cast from TFE onto the photoactive layer (PBDTT-TT/PC_{71}BM BHJ) followed by thermal deposition of Ag, while the anionic PAVs were cast from water onto indium tin oxide (ITO), followed by spin-coating the photoactive layer from chlorobenzene. Unlike devices made with PEDOT:PSS, thermal annealing was not required after casting the anionic PAVs. The cationic PAV cathode interlayers led to improved PSC device performance compared to bare Ag control devices (from 4.3% to 9.0% PCE), while the anionic PAV anode interlayers led to improved PSC performance relative to control devices containing bare ITO (from 6.1% to 8.0% PCE).
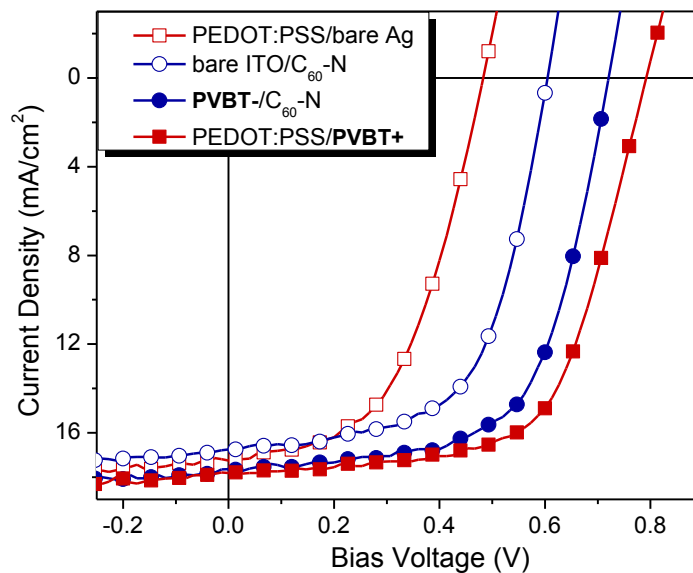
Figure 5.17 OPV device performance for ITO/**AML**/PBDTT-TT:PC_{71}BM/**CML**/Ag architecture, where **AML** represents anode modification layer (either PEDOT:PSS or **PVBT-**) and **CML** represents cathode modification layer (C_{60}-N or **PVBT+**).

Table 5.7 Summarized photovoltaic performance of devices with architectures: ITO/**AML**/PBDTT-TT:PC$_{71}$BM/**CML**/Ag, where **AML** represents anode interlayer (either PEDOT:PSS or **PVBT-**) and **CML** represents cathode interlayer (C$_{60}$-N or **PVBT+**). Values given correspond to optimized PSC devices, with J-V curves shown in **Figure 7**.

AML/**CML** composition	V_{OC} (V)	J_{SC} (mA/cm^2)	*FF* (%)	PCE (%)
PEDOT:PSS/bare Ag	0.48	17.2	51.5	4.26
bare ITO/C$_{60}$-N	0.60	16.8	60.4	6.12
PVBT-/C$_{60}$-N	0.72	17.7	63.0	8.03
PEDOT:PSS/**PVBT+**	0.79	17.9	63.3	8.95

Table 5.8 Summarized average photovoltaic performance of devices with architectures: ITO/**AML**/PBDTT-TT:PC$_{71}$BM/**CML**/Ag, where **AML** represents the anode interlayer and **CML** represents cathode interlayer. Error represents $\pm$ 1 standard deviation for averages obtained over six devices.

AML/**CML** composition	V_{OC} (V)	J_{SC} (mA/cm^2)	*FF* (%)	PCE (%)
PEDOT:PSS/bare Ag	0.48	17.2	53.1	4.35 ± 0.13
bare ITO/C$_{60}$-N	0.61	16.6	58.7	5.93 ± 0.22
PEDOT:PSS/**PVBTSB**	0.72	16.3	36.0	4.21 ± 0.31
PEDOT:PSS/**PVF$_4$SB**	0.31	15.9	44.3	2.20 ± 0.16
PEDOT:PSS/**PVF$_2$BTSB**	0.47	17.0	39.0	3.15 ± 0.18
PEDOT:PSS/**PVBT+**	0.80	17.0	64.2	8.72 ± 0.17
PEDOT:PSS/**PVF$_4$+**	0.73	16.1	53.7	6.35 ± 0.59
PEDOT:PSS/**PVF$_2$BT+**	0.80	16.9	66.5	9.03 ± 0.16
PVBT-/C$_{60}$-N	0.71	17.5	61.3	7.59 ± 0.33
PVF$_4$-/C$_{60}$-N	0.73	16.5	48.3	5.82 ± 0.90
PVF$_2$BT-/C$_{60}$-N	0.70	16.5	54.77	6.27 ± 0.24
PVBT-/**PVBT+**	0.72	16.4	52.9	6.22 ± 0.42
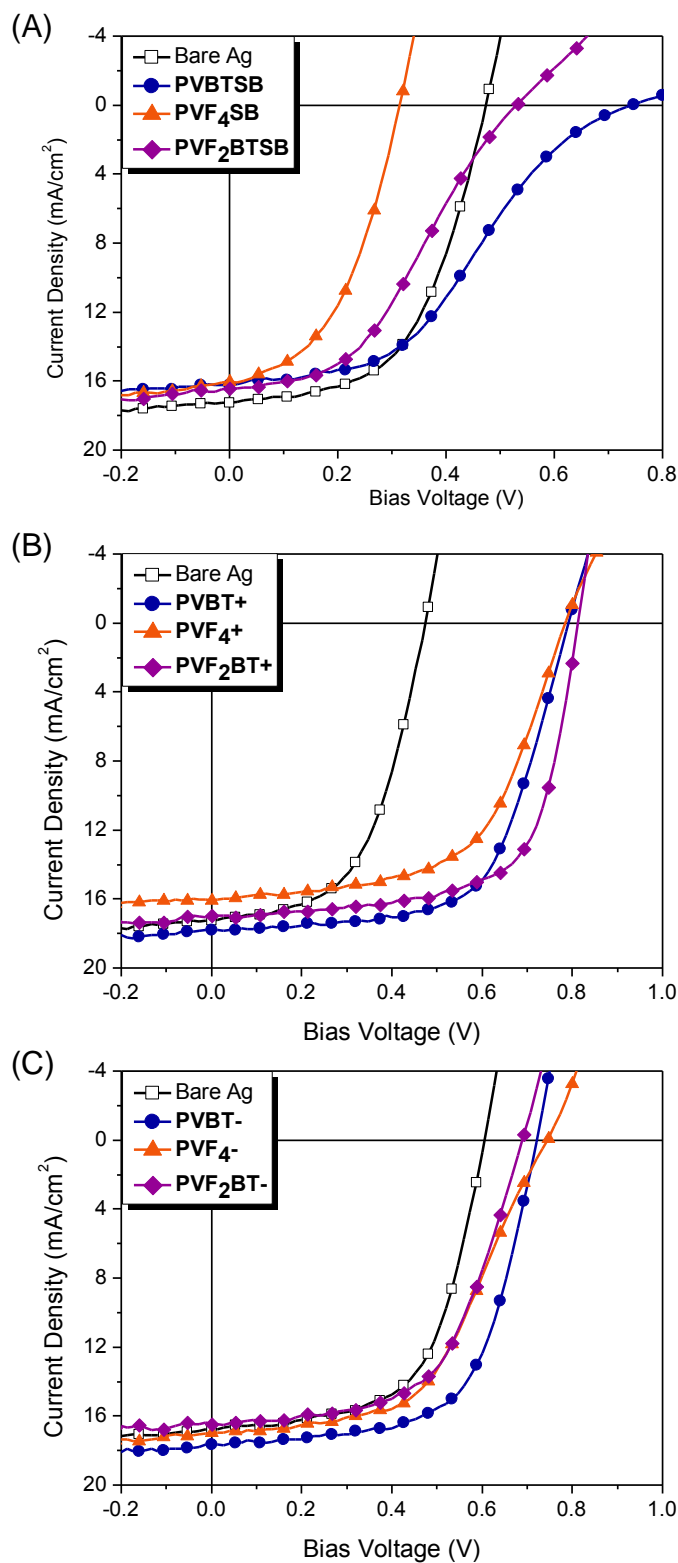
Figure 5.18 OPV device performance for ITO/**AML**/PBDTT-TT:PC$_{71}$BM/**CML**/Ag architecture, where **AML** represents anode interlayer (either PEDOT:PSS or PAV) and **CML** represents cathode interlayer (C$_{60}$-N or PAV). (A) zwitterionic PAVs; (B) cationic PAVs; (C) anionic PAVs.

The larger improvement in device efficiency for the cationic PAV cathode modifiers relative to the anionic PAV anode modifiers (compared to bare Ag and ITO controls, respectively) correlates with the absolute change in Φ ($|\Delta|$) measured with UPS; the anionic PAVs produce a smaller change in electrode Φ ($|\Delta| \leq 0.1$ eV) than the cationic PAVs Φ ($|\Delta| \approx 0.8$ eV). Additionally, UPS measurements of the zwitterionic and cationic PAVs on Ag indicate a similar reduction in Φ ($\Delta \approx$ -0.6 to -0.8 eV). Surprisingly, the CPZ interlayers did not perform at the level anticipated for such structures,[8-11] instead giving "S-shaped" J-V curves and reduced PCEs relative to the anionic and cationic interlayers (**Figure 5.18**). The presence of an "S-shaped" J-V curve for devices containing the zwitterionic PAVs suggests a charge extraction imbalance, which may arise from poor electron transport through the interlayer.[9] The CPEs may remedy this with improved conductivity from self-doping by the transient counterions.[47] The distinct advantage of these PAV interlayers in PSCs over more traditional Ca cathode interlayers and PEDOT:PSS anode interlayers is the ease of solution processing that precludes thermal evaporation (*eg* Ca) and annealing (*eg* PEDOT:PSS) procedures.

5.5 Summary and future outlook

In summary, novel hydrophilic PAVs containing zwitterionic, cationic and anionic side-chains were synthesized by HWE coupling in the presence of water. Strong electron withdrawing fluorine and thiadiazole substituents on the benzylphosphonates proved vital for successful coupling. The reaction rates and regioselectivity of the HWE reaction in water was studied by the formation of AV trimers. The addition of DMSO as a cosolvent greatly enhanced reaction rate and, as a result, higher molecular weight polymers were obtained. The energy levels and metal interactions of the PAVs were

probed using UV-Vis absorption and UPS, finding that zwitterionic and cationic PAVs reduce the Φ of Ag, while the anionic PAVs cause a slight increase in metal Φ. Stern-Volmer photoluminescence quenching experiments showed the potential of the anionic PAVs to be used in sensing applications. Integration of the cationic and anionic PAVs as cathode and anode modification layers (respectively) in PSCs clearly represented their potential to improve device efficiency. Moreover, the described scope and limitations of HWE coupling in water provides a platform from which novel and useful hydrophilic PAVs can be developed.

5.6 References

1.   Hu, Z.; Zhang, K.; Huang, F.; Cao, Y. *Chem. Commun.* **2015**, *51*, 5572-5585.

2.   Duarte, A.; Pu, K.-Y.; Liu, B.; Bazan, G. C. *Chem. Mater.* **2011**, *23* (3), 501-515.

3.   Jiang, H.; Taranekar, P.; Reynolds, J. R.; Schanze, K. S. *Angew. Chem. Int. Ed.* **2009**, *48* (24), 4300-4316.

4.   Duan, C.; Wang, L.; Zhang, K.; Guan, X.; Huang, F. *Adv. Mater.* **2011**, *23*, 1665-1669.

5.   Duan, C.; Zhang, K.; Guan, X.; Zhong, C.; Xie, H.; Huang, F.; Chen, J.; Peng, J.; Cao, Y. *Chem. Sci.* **2013**, *4* (3), 1298-1307.

6.   Fang, J.; Wallikewitz, B. H.; Gao, F.; Tu, G.; Müller, C.; Pace, G.; Friend, R. H.; Huck, W. T. S. *J. Am. Chem. Soc.* **2011**, *133* (4), 683-685.

7.   Kumar, A.; Pace, G.; Bakulin, A. a.; Fang, J.; Ho, P. K. H.; Huck, W. T. S.; Friend, R. H.; Greenham, N. C. *Energy Environ. Sci.* **2013**, *6* (5), 1589-1596.

8.   Page, Z. A.; Duzhko, V. V.; Emrick, T. *Macromolecules* **2013**, *46* (2), 344-351.

9.   Liu, F.; Page, Z.; Duzhko, V.; Russell, T. P.; Emrick, T. *Adv. Mater.* **2013**, *25*, 6868-6873.

10.   Page, Z. A.; Liu, F.; Russell, T. P.; Emrick, T. *Chem. Sci.* **2014**, *5*, 2368-2373.

11.   Page, Z. A.; Liu, F.; Russell, T. P.; Emrick, T. *J. Polym. Sci., Part A Polym. Chem.* **2015**, *53* (2), 327-336.

12. Burroughes, J. H.; Bradley, D. D. C.; Brown, A. R.; Marks, R. N.; Mackay, K.; Friend, R. H.; Burns, P. L.; Holmes, A. B. *Nature* **1990**, *347* (11), 539-541.

13. Grimsdale, A. C.; Chan, K. L.; Martin, R. E.; Jokisz, P. G.; Holmes, A. B. *Chem. Rev.* **2009**, *109* (3), 897-1091.

14. Feng, X.; Liu, M.; Pisula, W.; Takase, M.; Li, J.; Müllen, K. *Adv. Mater.* **2008**, *20* (14), 2684-2689.

15. Junkers, T.; Vandenbergh, J.; Adriaensens, P.; Lutsen, L.; Vanderzande, D. *Polym. Chem.* **2012**, *3* (2), 275-285.

16. Buchmeiser, M. R. *Adv. Polym. Sci.* **2005**, *176*, 89-119.

17. Cho, N. H.; Kim, D. Y.; Kim, Y. C.; Lee, Y. J.; Kim, Y. C. *Adv. Mater.* **1997**, *9* (4), 326-328.

18. Greenham, N. C.; Moratti, S. C.; Bradley, D. D. C.; Friend, R. H.; Holmes, A. B. *Nature* **1993**, *365*, 628-630.

19. Pfeiffer, S.; Horhold, H.-H. *Synt. Met.* **1999**, *101*, 109-110.

20. Pfeiffer, S.; Horhold, H. *Macromol. Chem. Phys.* **1999**, *200*, 1870-1878.

21. Synthesis and Properties of Poly(arylene vinylene)s, chapter 4. In: *Handbook of Conducting Polymers*. 3rd ed. Skotheim, T. A., Reynolds, J. R., Eds.; Taylor & Francis Group, LLC, **2007**; pp 1–6.

22. Drury, A.; Maier, S.; Rüther, M.; Blau, W. J. *J. Mater. Chem.* **2003**, *13* (3), 485-490.

23. Anuragudom, P.; El-daye, J.; Chinwangso, P.; Advincula, R. C.; Phanichphant, S.; Lee, T. R. *Polym. Int.* **2011**, *60* (4), 660-665.

24. Laughlin, B. J.; Smith, R. C. *Macromolecules* **2010**, *43* (8), 3744-3749.

25. Auragudom, P.; Tangonan, A. a.; Namboothiry, M. a. G.; Carroll, D. L.; Advincula, R. C.; Phanichphant, S.; Lee, T. R. *J. Polym. Res.* **2009**, *17* (3), 347-353.

26. Anuragudom, P.; Newaz, S. S.; Phanichphant, S.; Lee, T. R. *Macromolecules* **2006**, *39*, 3494-3499.

27. Davey, A. P.; Drury, A.; Maier, S.; Byrne, H. J.; Blau, W. J. *Synt. Met.* **1999**, *103*, 2478-2479.

28. Michaelis, A.; Kaehne, R. *Berichte* **1898**, *31*, 1048.

29. Arbuzov, A. E. *J. Russ. Phys. Chem. Soc.* **1906**, *38*, 687.

30.   Arbuzov, A. E. *Chem. Zentr.* **1906**, *II*, 1639.

31.   Mitchell, R. H.; Iyer, V. S. *Synlett* **1989**, No. 1, 55-57.

32.   Zhou, H.; Yang, L.; Stuart, A. C.; Price, S. C.; Liu, S.; You, W. *Angew. Chem. Int. Ed.* **2011**, *50* (13), 2995-2998.

33.   Kularatne, R. S.; Taenzler, F. J.; Magurudeniya, H. D.; Du, J.; Murphy, J. W.; Sheina, E. E.; Gnade, B. E.; Biewer, M. C.; Stefan, M. C. *J. Mater. Chem. A* **2013**, *1* (48), 15535-15543.

34.   Schlosser, M.; Jenny, T.; Guggisberg, Y. *Synlett* **1990**, 704.

35.   Rodriguez, L.; Lu, N.; Yang, N.-L. *Synlett* **1990**, No. 4, 227-228.

36.   Hiremath, U. S. *Tetrahedron Lett.* **2013**, *54* (26), 3419-3423.

37.   Organic Chemistry, 5th ed. Brown, W. H.; Foote, C. S.; Iverson, B. L.; Anslyn, E. V. Brooks/Cole Cengage Learning. **2009**. pp 495.

38.   Cacialli, F.; Daik, R.; Feast, W. J.; Friend, R. H.; Lartigau, C. *Opt. Mater.* **1999**, *12* (2-3), 315-319.

39.   Li, Z.-K.; He, C.; Yang, M.; Xia, C.-Q.; Yu, X.-Q. *ARKIVOC* **2005**, *1*, 98-104.

40.   Larsen, R. O.; Aksnes, G. *Phosphorus and Sulfur* **1983**, *15*, 219-228.

41.   Larsen, R. O.; Aksnes, G. *Phosphorus and Sulfur* **1983**, *15*, 229.

42.   Seo, J. H.; Nguyen, T. *J. Am. Chem. Soc.* **2008**, *130*, 10042-10043.

43.   Conjugated Polyelectrolytes: Fundamentals and Applications. Liu, B.; Bazan, G. C., Eds. Wiley-VCH. **2013**. pp 418.

44.   Wang, D.; Wang, J.; Moses, D.; Bazan, G. C.; Heeger, A. J. Langmuir **2001**, *17*, 1262-1266.

45.   Principles of Fluorescence Spectroscopy, 3rd ed. Lakowicz, J.R. Springer, **2006**, pp 954.

46.   Page, Z. A.; Liu, Y.; Duzhko, V. V.; Russell, T. P.; Emrick, T. *Science* **2014**, *346*, 441-444.

47.   Chueh, C.-C.; Li, C.-Z.; Jen, A. K.-Y. *Energy Environ. Sci.* **2015**, *8* (4), 1160-1189.

CHAPTER 6

EXPERIMENTAL SECTION

6.1 Materials

1,2-Dichlorobenzene (99.5%), 1,3,5-trioxane (≥99%), 1,3-propanesultone (99%), 1,4-butane sultone (≥99%), 1,4-dibromobutane (99%), 1,6-dibromohexane (99%), 1,8-diiodoctane (98%), 1-methyl-2-pyrrolidinone (anhydrous, 99.5%), 2-bromothiophene (98%), 2,5-dibromothiophene (98%), 2-isopropoxy-4,4,5,5-tetramethyl-1,3,2-dioxaborolane (98%), 2-methyl-2-butanol (anhydrous, >99%), 2-thiophenecarbonitrile (99%), 3-bromothiophene (97%), 3-dimethylamino-1-propanol (99%), α,α'-Dibromo-*p*-xylene (**70**) (97%), Aliquat 336, aluminum oxide (activated, basic, Brockmann I), acetonitrile (anhydrous, 99.8%), benzophenone (≥99%), bis(pinacolato)diboron (99%), bis(triphenylphosphine)palladium(II) dichloride (99%), calcium hydride (≥97%), cesium carbonate (98%), diethyl succinate (99%), diisopopylamine (99.95%), diisopropyl azodicarboxylate (98%), dimethylamine (40 wt% solution in water), dimethylamine (2M solution in THF), hydrobromic acid (ACS reagent, 48%), lithium fluoride (99.99%), myristyltrimethylammonium bromide (≥99%), *N*,*N*-dimethylformamide (anhydrous, 99.8%), *N*,*N*,*N*',*N*'-tetramethylethylenediamine (>99.5%), *N*-iodosuccinimide (95%), paraquat dichloride hydrate (PESTANAL®, analytical standard), phosphorus tribromide (99%), potassium acetate (99%), potassium *tert*-butoxide (>98%), salicylaldehyde (98%), sarcosine (99%), silver trifluoroacetate (98%), sodium bromide (>99%), sodium cubes (99.9%), sodium iodide (99%), sodium thiosulfate (99%), tetrabutylammonium bisulfate (99%), tetra-n-butylammonium fluoride (75 wt. % in H_2O), thionyl chloride (≥99%),

triethylamine (>99%), triethyl phosphite (98%), trimethylamine (anhydrous, ≥99%), and triphenylphosphine (99%) were purchased from Sigma Aldrich and used without further purification. Hexamethylphosphoramide (99%, Sigma Alrich) was dried over calcium hydride and distilled before use. Tris(dibenzylideneacetone)-dipalladium(0) ($Pd_2(dba)_3$) (99%), 2-(dicyclohexylphosphino)-2',4',6'-tri-*iso*-propyl-1,1'-biphenyl (XPhos) (98%), bis(tir-*ortho*-tolylphosphine)palladium(0) (98%) were purchased from STREM. Bis(tri-*o*-tolylphosphine)palladium(0) ($Pd[P(o\text{-}tol)_3]_2$) (98%), dichloro[1,1'-bis(diphenylphosphino)ferrocene]-palladium(II) dichloromethane adduct $Pd(dppf)Cl_2 \cdot DCM$ (99%) and, palladium(II) acetate $Pd(OAc)_2$ (99+ %) were purchased from STREM Chemicals. Chloroform-D (99.8%), methylene chloride-D2 (99%), 1,2-dichlorobenzene-D4 (99%), methanol-D4 (99.8%), deuterium oxide (99.9%) and 2,2,2-trifluorethanol-D3 (99%) were purchased from Cambridge Isotope Laboratories. *n*-Butyllithium (2.5 M in hexane), sodium bicarbonate (99%), 2,2,2-Trifluoroethanol (99+%), paraformaldehyde (97%) and 3-thiophenemethanol (98%) were purchased from Alfa Aesar. Silica gel (200 x 400 mesh) was purchased from Sorbent Technologies. Sephadex LH-20 was purchased from GE Healthcare Life Sciences. Spectra/Por dialysis tubing was purchased from Spectrum Labs. *N*-bromosuccinimide (NBS) (99%, Acros Organics) was recrystallized from water. 2,3,4-Trihydroxybenzaldehyde (**70**) (98%), 2,2'-bithiophene (98%), 6-bromoisatin (97%), 6-bromooxindole (97%) and 2,1,3-benzothiadiazole (**79**) (98%) were purchased from Combi-Blocks and used without further purification. 2,5-bis-thiopheneboronic acid pinacol ester (**25**) (98 %, Combi-Blocks) was purified by column chromatography on silica with hexanes:ethyl acetate (9:1) as the eluent followed by recrystallization from hexanes and 2,1,3-benzothiadiazole-

4,7-diboronic acid pinacol ester (**26**) (97%, Combi-Blocks) was sublimed. 6-(Dimethylamino)hexylamine (97%) was purchased from Matrix Scientific and used without further purification. Anhydrous magnesium sulfate (97%), glacial acetic acid (99%) anhydrous diethyl ether (99%), sodium hydroxide (99%), sodium carbonate (99 %), potassium carbonate (99%), ethyl acetate, hexanes, chloroform, methanol, acetonitrile, water, acetic acid, hydrochloric acid (conc. aq.), acetone, diethyl ether and dichloromethane were purchased from Fisher Scientific. Tetrahydrofuran (99%, Fisher Scientific) (THF) was dried over sodium/benzophenone ketyl and dichloromethane (99%, Fisher Scientific) was dried over calcium hydride (under nitrogen) and distilled before use. All ionic liquids were purchased from Ionic Liquids Technologies (Io-li-tec) and used without further purification. PTB7 and PCE-10 (PBDTT-TT) were purchased from 1-Material. $PC_{61}BM$ and $PC_{71}BM$ was purchased from American Dye Source and Nano-C. Fullerene-C_{60} (99.95%), fullerene-C_{70} (99.0%) and mixed fullerenes was purchased from Materials Technologies Research (MTR) and used without further purification. RediSep Rf Reversed-phase columns composed of C18-derivatized silica were purchased from Teledyne Isco. 2,3,5,6-Tetrafluoro-1,4-benzenedimethanol (99%) (**75**) was purchased from AK Scientific.

6.2 Instrumentation

^{1}H-NMR spectra were recorded at 300 MHz, ^{19}F-NMR at 282 MHz on a Brüker-spectrospin and ^{13}C-NMR at 101 MHz on a Brüker-spectrospin or 176 MHz on an Agilent Technologies Varian. Some NMR spectra were recorded on a Bruker 500 AVANCE III HD with a CryoProbe Prodigy and at 500 MHz for ^{1}H, 176 MHz for ^{13}C, 202 MHz for ^{31}P and 471 MHz for ^{19}F. UV/Vis absorbance measurements were taken on

a Perkin-Elmer Lambda 25 UV/vis spectrometer. Fluorescence spectra were recorded on a Perkin-Elmer LS 55 luminescence spectrometer. Centrifugation was done using an eppendorf centrifuge 5804. Lyophilization used a Labconco FreeZone® 4.5 Liter Freeze Dry System (model 77500). Molecular weights and dispersities (Đ) were estimated by size exclusion chromatography (SEC) in sodium nitrate (0.1 M with 0.02 wt% of NaN_3) aqueous solution at 45 °C, calibrated against poly(ethylene oxide) standards, operating at 1.0 mL/min with an HP Series 1050 Pump, HP 1047A refractive index detector, and three Waters Ultrahydrogel linear columns (each 300 × 7.8 mm) for the **PTSB-1** (**13**) and **PTBTSB-1** (**15**) samples and in 2,2,2-trifluoroethanol with 0.02 M sodium trifluoroacetate at 40 °C using an Agilent 1200 system, calibrated against poly(methyl methacrylate) standards, equipped with an isocratic pump operated at 1 mL/min, a degasser, an Agilent 1260 infinity autosampler, one 50 mm x 8 mm PSS PFG guard column (Polymer Standards Service), three 300 mm x 7.5 mm PSS PFG analytical linear M columns with a 7 μm particle size (Polymer Standards Service), and an Agilent 1200 refractive index detector and Agilent 1200 VWD UV detector for all other polymers unless noted otherwise. Molecular weights and Đ of the anionic poly(arylene vinylenes), **PVBT-** (**90**), **PVF₄-** (**93**) and **PVF₂BT-** (**96**), were estimated by SEC in water:CH_3CN 1/1 v/v with 0.01 % NaN_3 at 35 °C, calibrated against poly(ethylene oxide) standards. The system was equipped with a Waters Ultrahydrogel^{TM} guard column (6 mm x 40 mm), 2 Waters Ultrahydrogel^{TM} linear columns (10 μm, 7.8 mm x 300 mm), an Agilent 1100 series isocratic pump operated at 1 mL/min and an Optilab rEX^{TM} differential refractive index detector (Wyatt Technology Corporation). Atomic force microscopy (AFM) was performed on a Digital Instruments Dimension 3100, operating in tapping

mode. UPS measurements were performed on the Omicron Nanotechnology, Model ESCA+S, consisting of a helium discharge lamp (He I line, 21.2 eV) as the UV excitation source and a hemispherical SPHERA energy analyzer. All samples were negatively biased by -3V during the measurements. This bias compensated for the instrument work function difference repelling the low-kinetic energy electrons. The energy scale of experimental graphs was shifted by 3 eV. Polymer film thickness was determined by the surface profiler KLA Tencor, model Alpha-Step IQ. High-resolution fast atom bombardment (FAB) data was obtained on a JEOL JMS700 MStation. Matrix assisted laser desorption ionization time of flight (MALDI-TOF) data were obtained on a Brüker microflex using a microScout Ion Source and linear mode detection. The matrix used was [2-(4-hydroxyphenylazo)-benzoic acid] (HABA) which was dropcast from a 40 mg/mL solution in THF containing approximately $0.1 - 1$ mg/mL of the analyte added to the mixture as a solution in TFE. Electrospray ionization (ESI) measurements were taken on a Bruker micrOTOF II. Current-voltage (I-V) characteristics were measured in a N_2 atmosphere (unless otherwise stated) using a Keithley 2400 source-meter under simulated AM1.5G irradiation using a 300 W Xe lamp solar simulator (Newport 91160). The light intensity was adjusted with an NREL-calibrated Si reference solar cell and KG-5 filter. The illuminated area (0.03025 cm^2 unless otherwise stated) was defined by a photomask with an aperture, the area of which was measured at NREL, and used in all reported PCE measurements. Impedance spectroscopy was performed on an Agilent Precision Impedance Analyzer (4294A). The PCE values of devices that were measured without the photomask, using 0.06 cm^2 as the device area, were typically about 1-1.5% higher for 8-9% devices due to an underestimation of the illuminated device area. In particular, the

device with a PCE of 9.35% produced 10.6% when measured without the aperture. Teledyne Isco CombiFlashR$_f$ automated chromatography system with internal UV-Vis detection and external refractive index detection (model 340CF ELSD) was used for purification of the anionic compounds **87** and **99**.

6.3 Methods

- **General Suzuki polycondensation for the preparation of thiophene-based conjugated polymer zwitterions (13, 14, 15 and 16).**

| **13** | **14** | **15** | **16** |
| PTSB-1 | PTSB-2 | PTBTSB-1 | PTBTSB-2 |
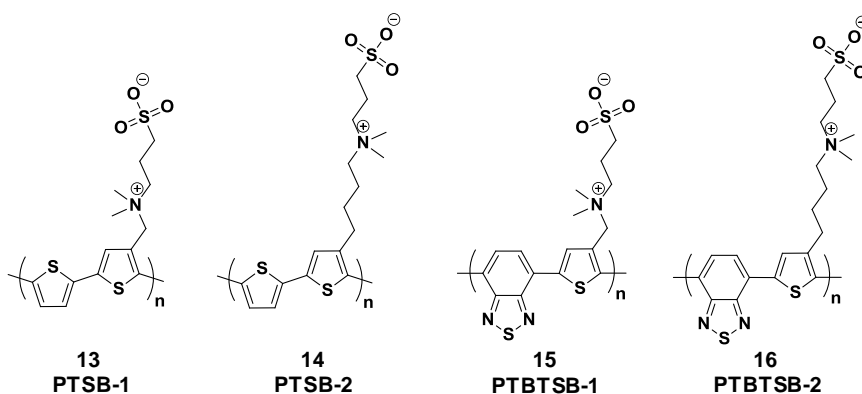
Method A. To a 5 mL pressure tube equipped with a magnetic stir-bar was added dichloro-bis(triphenylphosphine)palladium(II) (0.005 mmol), zwitterionic A$_2$ monomer (**21** or **24**) (0.25 mmol), diboronicester B$_2$ monomer (**25** or **26**) (0.25 mmol) and one drop of Aliquat 336. The atmosphere was flushed with argon and toluene (2 mL) and 2 M K$_2$CO$_3$: 2M NaBr (aq) (1 mL) (previously degassed with argon) were added. The cap was sealed tightly, the tube wrapped with aluminum foil and the mixture heated to 90 ˚C with vigorous stirring for 24 hours. The contents were cooled to room temperature and precipitated into methanol:THF (2:1), centrifuged and washed with THF (4x), dried under reduced pressure, dissolved in 1 M NaCl (aq) and transferred to a dialysis membrane (cellulose, 1 KDa cutoff). The polymer was dialyzed against water for 4 days, changing the water three times daily. The contents within the dialysis bag were collected

and lyophilized to give the SB-polymer as bright orange (PTSB-1), red (PTBTSB-1 / PTSB-2) or purple (PTBTSB-2) solids. Isolated yields of polymer ranged from 70-90 %.

Method B. Palladium(II) acetate (1 mg, 0.0045 mmol), sodium carbonate (80 mg, 0.75 mmol), ionic liquid (0.75 g) and 2M NaBr (aq, 0.3 mL) were added to a 7 mL scintillation vial containing a magnetic stir-bar. The mixture was stirred and heated to 100 °C for 5 minutes, followed by addition of monomers **21** (57.5 mg, 0.125 mmol) and **25** (42 mg, 0.125 mmol) (we note that the reaction works if all of the reagents are added prior to any heating). The reaction was stirred at 100 °C for 2 hours, then 1 mL of H_2O was added and the polymer was precipitated into MeOH, giving a bright orange solid. Soxhlet extraction with MeOH was used to fully remove residual ionic liquid, suggested by a lack of fluorine signal from ^{19}F-NMR spectroscopy.

Poly(thiophene-*alt*-thiophenemethylenesulfobetaine) **(PTSB-1)** **(13)** was obtained as a bright orange solid after lyophilization (60 mg, 70%). (GPC) M_n = 15,500 g / mol, Đ = 2.2; ^{1}H NMR (300 MHz, 2,2,2-Trifluoroethanol-d3) δ 7.60 − 6.89 (br, 3H), 4.92 − 4.26 (br, 2H), 3.55 − 3.29 (br, 2H), 3.27 − 2.71 (br, 8H), 2.52 − 2.02 (br, 2H).

Poly(thiophene-*alt*-thiophenebutylenesulfobetaine) **(PTSB-2)** **(14)** was obtained as a red solid after lyophilization (77 mg, 80%). (GPC) M_n = 22,000 g / mol, Đ = 2.0; ^{1}H NMR (300 MHz, 2,2,2-Trifluoroethanol-d3) δ 7.24 − 6.65 (br, 3H), 3.55 − 3.28 (br, 2H), 3.28 − 3.11 (br, 2H), 3.10 − 2.51 (br, 10H), 2.41 − 2.00 (br, 2H), 1.95 − 1.49 (br, 4H).

Poly(benzothiadiazole-*alt*-thiophenemethylenesulfobetaine) (PTBTSB-1) (15) was obtained as a red solid after lyophilization (80 mg, 80%). (GPC) M_n = 10,500 g /

mol, Đ = 2.4; ^{1}H NMR (300 MHz, 2,2,2-Trifluoroethanol-d3) δ 8.78 – 8.23 (br, 1H), 8.23 – 7.66 (br, 2H), 5.09 – 4.38 (br, 2H), 3.80 – 1.94 (br, 12H).

Poly(benzothiadiazole-*alt*-thiophenebutylenesulfobetaine) (PTBTSB-2) (16) was obtained as a dark purple solid after lyophilization (100 mg, 90%). (GPC) M_n = 47,000 g / mol, Đ = 2.2; ^{1}H NMR (300 MHz, 2,2,2-Trifluoroethanol-d3) δ 8.75 – 6.64 (br, 3H), 3.72 – 1.07 (br, 20H).

- **General Suzuki polycondensation procedure to alkylated polymers (17 and 18).**

17
POT-*a*-T

18
POT-*a*-BT
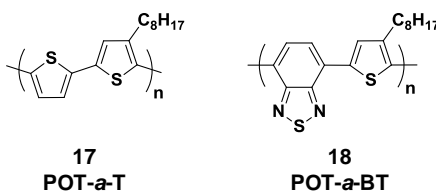
A 5 mL pressure tube equipped with a magnetic stir-bar was obtained and bis(tri-*o*-tolylphosphine)palladium(0) (0.005 mmol), 2,5-diiodo-3-octylthiophene[1] (112 mg, 0.25 mmol), diboronic ester B$_2$ monomer (**25** or **26**) (0.25 mmol) and one drop of Aliquat 336 were added. The atmosphere was flushed with argon, then toluene (3 mL) and 2 M K_2CO_3 (aq) (1 mL), previously degassed with argon were added. The cap was sealed tightly, the tube wrapped with aluminum foil and the mixture was heated to 90 ˚C with vigorous stirring for 24 hours. The contents were cooled to room temperature and precipitated into MeOH. The solid was filtered into a Soxhlet thimble and extracted with MeOH, acetone, Hex and CHCl$_3$ subsequently. The CHCl$_3$ fraction was collected and solvent removed under reduced pressure.

Poly(octylthiophene-*alt*-thiophene) (POT-*a*-T) (17) was obtained as a red-gold, lustrous solid (40 mg, 58%) (GPC) M_n = 7,800 g / mol, Đ = 1.6; ^{1}H NMR (300 MHz,

Chloroform-d) δ 7.20 – 6.58 (br, 3H), 3.00 – 2.44 (br, 2H), 1.92 – 1.48 (br, 2H), 1.53 – 0.97 (br, 10H), 1.05 – 0.62 (br, 3H).

Poly(octylthiophene-*alt*-benzothiadiazole) (POT-*a*-BT) (18) was obtained as a purple-gold, lustrous solid (63 mg, 77%). (GPC) M_n = 18,600 g / mol, Đ = 1.9; ^{1}H NMR (300 MHz, CDCl$_3$) δ 8.26 – 8.11 (br, 1H), 8.04 – 7.92 (br, 1H), 7.81 – 7.65 (br, 1H), 3.02 – 2.63 (br, 2H) 1.87 – 1.63 (br, 2H), 1.45 – 1.11 (br, 10H), 0.93 – 0.80 (br, 3H).

- **2,5-dibromo-3-(bromomethyl)thiophene (19)**
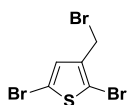
Synthesized in a similar fashion to that reported by our group.[2] A dry 2-neck, 500 mL round-bottom flask equipped with a magnetic stir bar, inlet-adapter and septum was flushed with nitrogen and anhydrous CH$_2$Cl$_2$ (200 mL) and (2,5-dibromothiophen-3-yl)methanol[3] (10.0 g, 36.8 mmol) were added. The mixture was cooled to 0 ˚C with an ice bath and phosphorus tribromide (3.5 mL, 36.8 mmol) was added slowly by syringe. The mixture was stirred at 0 ˚C for 30 minutes and at room temperature for 12 hours. The reaction was slowly quenched with saturated aqueous sodium bicarbonate, and the product extracted into CH$_2$Cl$_2$, dried with MgSO$_4$, filtered and concentrated to give a yellow oil. The crude product was purified by column chromatography on silica-gel, eluting with hexanes then ethylacetate:hexanes (10:90). Removal of the solvent under reduced pressure gave **19** as a white solid (10.7 g, 87%). ^{1}H NMR (300 MHz, CDCl$_3$) δ 7.00 (s, 1H), 4.36 (s, 2H). ^{13}C NMR (101 MHz, CDCl$_3$) δ 25.09, 111.91, 112.27, 131.06, 137.97 ppm.

- **1-(2,5-dibromothiophen-3-yl)-N,N-dimethylmethanamine (20).**
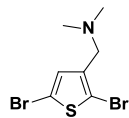
Tetrabutylammonium bisulfate (0.3 g, 0.9 mmol), CHCl$_3$ (15 mL) and dimethylamine (40 wt% in water, 15 mL) were added to a 1-neck, 100 mL round-bottom flask equipped with a magnetic stir bar, inlet-adapter and condenser. Compound **19** (3.0 g, 9.0 mmol) was added and the mixture was heated to reflux with vigorous stirring for two hours. The mixture was cooled to room temperature and the product extracted with CH$_2$Cl$_2$. The organic fractions were combined, dried over MgSO$_4$, filtered and concentrated to obtain a crude oil. The oil was purified by column chromatography on alumina (activated basic, Brockmann I), eluting with CH$_2$Cl$_2$:hexanes (1:1). Removal of the solvent under reduced pressure gave **20** as a colorless oil (2.2 g, 82%). ^{1}H NMR (300 MHz, CDCl$_3$) δ 6.95 (s, 1H), 3.33 (s, 2H), 2.25 (s, 6H). ^{13}C NMR (101 MHz, CDCl$_3$) δ 45.33, 57.17, 110.09, 110.90, 131.60, 139.65 ppm.

- **3-(((2,5-dibromothiophen-3-yl)methyl)dimethylammonio)propane-1-sulfonate (21).**
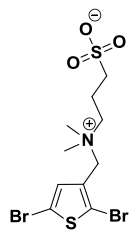
A dry 1-neck, 100 mL round-bottom flask, equipped with a magnetic stir bar, condenser and inlet adapter was flushed with nitrogen and **20** (3.0 g, 10.0 mmol) and 1,3-propanesultone (4.9 g, 40.1 mmol) were added. Anhydrous acetonitrile (60 mL) was added, and the mixture was heated to reflux for one hour, during which time a white

precipitate formed. The mixture was cooled to room temperature, filtered and washed with anhydrous acetonitrile. The product was dried under reduced pressure to afford **21** as a fluffy white solid (3.9 g, 93%).^{1}H NMR (300 MHz, D_2O) δ 7.25 (s, 1H), 4.46 (s, 2H), 3.67 – 3.41 (m, 2H), 3.11 (s, 6H), 2.97 (t, J = 7.2 Hz, 2H), 2.40 – 2.16 (m, 2H). ^{13}C NMR (101 MHz, D_2O) δ 18.41, 47.32, 49.78, 61.05, 62.72, 112.81, 119.19, 128.42, 132.74 ppm. HRMS-FAB (m/z): [M+H]$^+$ calculated for $C_{10}H_{16}Br_2NO_3S_2$: 421.8918, found: 421.8898.

- **2,5-dibromo-3-(4-bromobutyl)thiophene (22).**
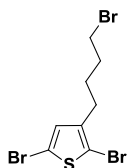
Compound **22** was synthesized in a 250 mL, 2-neck round-bottom flask, equipped with a magnetic stir bar, septum, addition funnel and inlet adapter. The atmosphere was flushed with nitrogen and 3-(4-bromobutyl)thiophene[4] (3.0 g, 13.7 mmol) was added and dissolved in DMF (40 mL). NBS (6.1 g, 34.2 mmol) was dissolved in DMF (20 mL) and added to the addition funnel. The reaction was covered with aluminum foil and the contents in the addition funnel were added drop-wise, while stirring at room temperature. After complete addition the reaction was stirred at room temperature under nitrogen for 12 hours, followed by quenching with saturated sodium carbonate (aq) solution. The product was extracted into Et_2O (3 x 50 mL) and the organic fractions were combined and washed with water (5 x 100 mL), dried with anhydrous $MgSO_4$, filtered and the concentrated to obtain a crude oil. The product was purified by column chromatography on silica gel with hexanes as the eluent. Removal of the solvent gave **22** as a colorless oil (4.18 g, 81%). ^{1}H NMR (300 MHz, Methylene Chloride-d2) δ 6.87 (s, 1H), 3.47 (t, J =

6.6 Hz, 2H), 2.60 (t, J = 7.4 Hz, 2H), 2.00 – 1.84 (m, 2H), 1.83 – 1.67 (m, 2H). ^{13}C NMR (176 MHz, CDCl$_3$) δ 28.17, 28.64, 32.03, 33.42, 108.55, 110.86, 130.86, 142.04.

- **4-(2,5-dibromothiophen-3-yl)-N,N-dimethylbutan-1-amine (23).**
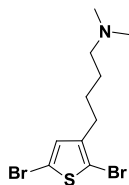
A dry 150 mL pressure flask was equipped with a magnetic stir bar, flushed with nitrogen and **22** (3.0 g, 8.0 mmol) and dimethylamine (2M solution in THF, 80 mL, 160 mmol) were added. The mixture was heated to 60 ˚C for 12 hours, during which time a white salt precipitated. The mixture was cooled to room temperature and the salt removed by filtration and washed with Et$_2$O. The solvent was removed under reduced pressure to obtain a crude oil that was purified by column chromatography on silica gel with Hex:EtOAc (1:1) and 1% TEA as the eluent. The solvent was removed under reduced pressure to give **23** as a colorless oil (1.40 g, 51%). ^{1}H NMR (300 MHz, Chloroform-d) δ 6.81 (s, 1H), 2.55 (t, J = 7.4 Hz, 2H), 2.28 (t, J = 7.4 Hz, 2H), 2.23 (s, 6H), 1.63 – 1.48 (m, 4H). ^{13}C NMR (176 MHz, CDCl$_3$) δ 27.36, 27.55, 29.48, 45.68, 59.61, 108.20, 110.52, 131.01, 142.72.

- **3-((4-2,5-dibromothiophen-3-yl)butyl)dimethylammonio)propane-1-sulfonate (24).**
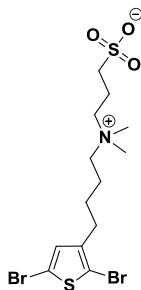
A dry 1-neck, 25 mL round-bottom flask, equipped with a magnetic stir bar, condenser and inlet adapter was flushed with nitrogen and **23** (500 mg, 1.47 mmol) and 1,3-propanesultone (716 mg, 5.86 mmol) were added. Anhydrous acetonitrile (10 mL) was added to the mixture and heated to reflux for two hours, during which time a white precipitate formed. The mixture was cooled to room temperature, filtered and washed with anhydrous acetonitrile followed by anhydrous diethyl ether. The product was dried under reduced pressure to afford **24** as a fluffy white solid (626 mg, 92%). ^{1}H NMR (700 MHz, 2,2,2-Trifluoroethanol-d3) δ 6.81 (s, 1H), 3.43 – 3.36 (m, 2H), 3.24 – 3.16 (m, 2H), 2.98 (s, 6H), 2.90 (t, J = 6.8 Hz, 2H), 2.65 (t, J = 7.4 Hz, 2H), 2.22 – 2.16 (m, 2H), 1.77 (dd, J = 10.7, 6.2 Hz, 2H), 1.66 (p, J = 7.5 Hz, 2H). ^{13}C NMR (176 MHz, 2,2,2-Trifluoroethanol-d3) δ 20.08, 23.25, 27.27, 29.71, 48.71, 51.98, 65.13, 66.60, 110.12, 112.56, 132.53, 143.29. HRMS-FAB (m/z): [M+H]$^+$ calculated for $C_{13}H_{22}Br_2NO_3S_2$: 461.9408, found: 461.9408.

- **4,7-bis(4,4,5,5-tetramethyl-1,3,2-dioxaborolan-2-yl)benzo[c][1,2,5]thiadiazole (26).**
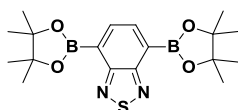
Following the procedure of Müllen and coworkers,[5] to a dry 1-neck, 25 mL round-bottom flask equipped with a magnetic stir bar and septum, and flushed with argon, was added 4,7-dibromobenzo[c][1,2,5]thiadiazole[6] (1.0 g, 3.4 mmol), bis(pinacolato)diboron (2.0 g, 7.9 mmol), anhydrous potassium acetate (2.0 g, 20 mmol) and [1,1'bis(diphenylphosphine)ferrocene]dichloropalladium-DCM adduct (0.25 g, 0.3 mmol). The flask was evacuated and backfilled with argon (3x). The contents were

dissolved upon stirring with anhydrous 1,4-dioxane (10 mL) (degassed with argon). The mixture was stirred and heated to 80 ˚C for 24 hours. The mixture was cooled to room temperature and water was added to quench the reaction, followed by extraction of the crude product into ethyl acetate. The organic fractions were combined, dried over anhydrous $MgSO_4$, filtered and concentrated to obtain a dark red / brown solid. The product was purified by column chromatography on silica-gel, eluting with hexanes then ethyl acetate:hexanes (5:95). Removal of the solvent gave **26** as a light yellow solid (0.98 g, 74%). ^{1}H NMR (300 MHz, Methylene Chloride-d2) δ 8.10 (s, 2H), 1.40 (s, 28H). ^{13}C NMR (101 MHz, CD_2Cl_2) δ 25.27, 84.86, 138.10, 157.52.

- **General Suzuki polycondensation for the preparation of diketopyrrolopyrrole-based polymer zwitterions (39, 40 and 41).**
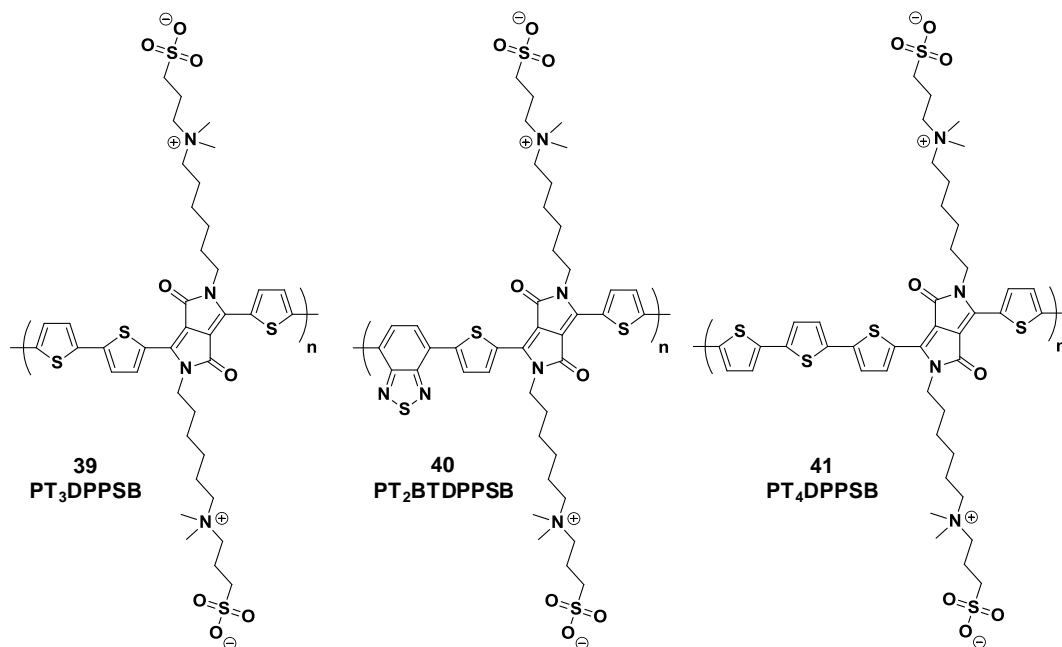
A 20 mL thick walled glass pressure tube equipped with a magnetic stir bar was brought into a nitrogen filled glove-box. Tris(dibenzylideneacetone)-dipalladium(0) ($Pd_2(dba)_3$) (6.9 mg, 0.0075 mmol) and 2-(dicyclohexylphosphino)-2',4',6'-tri-*iso*-propyl-1,1'-

biphenyl (XPhos) (10.7 mg, 0.0225 mmol) were added to the tube, followed by capping the tube and removing it from the glove-box. Dibromo monomer, diboronic-ester monomer (0.375 mmol), AQ336 (6 drops), toluene (6 mL), tetrabutylammonium fluoride solution (75 wt. % in H_2O, 2.2 mL) and NaBr (2 M aq, 0.8 mL) were added to the pressure tube and degassed with argon for 5 minutes. The pressure tube was capped tightly and the mixture stirred vigorously at 110 °C for 24 hours. The polymerization mixture was then cooled to room temperature and precipitated into MeOH. The polymer was isolated by centrifugation and extracted with MeOH for 16 hours then 2,2,2-trifluoroethanol (TFE) for 4 hours using a Soxhlet apparatus. The TFE solution containing polymer was run through a plug of Sephadex LH-20, then added to a dialysis membrane (10 kDa cutoff) and dialyzed in a 4 L beaker against water for 24 hours (changing > 4 times). The contents of the dialysis bag were lyophilized yielding a colored fluffy polymer.

PT₃DPPSB (39) was obtained as a blue-green solid (249 mg, 75 %). M_n = 11,800 g / mol, Đ = 1.3; ^1H NMR (300 MHz, 2,2,2,-Trifluoroethanol-d_3) δ 9.43 − 8.34 (br, 2H), 7.60 − 6.37 (br, 4H), 4.40 − 2.59 (br, m, 28H), 2.58 − 0.96 (br, m, 20H).

PT₂BTDPPSB (40) was obtained as a blue solid (303 mg, 87 %). M_n = 20,300 g / mol, Đ = 1.6; ^1H NMR (300 MHz, 2,2,2,-Trifluoroethanol-d_3) δ 9.43 − 8.23 (br, 2H), 8.23 − 6.74 (br, 4H), 4.32 − 2.59 (br, m, 28H), 2.58 − 0.91 (br, m, 20H).

PT₄DPPSB (41) was obtained as a green solid (339 mg, 94 %). M_n = 21,400 g / mol, Đ = 1.7; ^1H NMR (300 MHz, 2,2,2,-Trifluoroethanol-d_3) δ 9.46 − 8.00 (br, 2H), 7.38 − 5.89 (br, 6H), 4.51 − 2.59 (br, m, 28H), 2.58 − 0.83 (br, m, 20H).

- **General Suzuki polycondensation for the preparation of isoindigo-based polymer zwitterions (42, 43 and 44).**

42
PTiInSB

43
PBTiInSB

44
PT₂iInSB
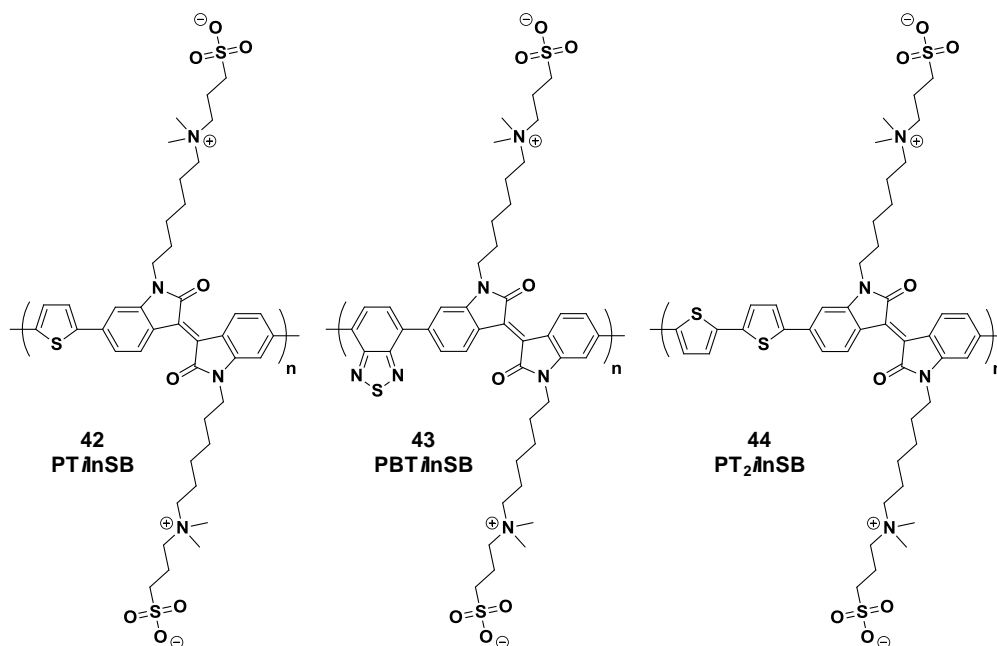
Followed the same procedure as described for the DPP-based CPZs (**39**, **40** and **41**) except the reactions were run at 90 °C for 10 hours instead of 110 °C for 24 hours.

PT*i*InSB (42) was obtained as a blue-green solid (103 mg, 33 %). M_n = 13,900 g / mol, Đ = 1.6; ^{1}H NMR (300 MHz, 2,2,2,-Trifluoroethanol-d_3) δ 9.52 − 8.23 (br, 2H), 8.00 − 5.95 (br, 6H), 3.90 − 3.58 (br, 4H), 3.48 − 3.33 (br, 4H), 3.32 − 3.12 (br, 4H), 3.11 − 2.71 (br, m, 16H), 2.33 − 2.00 (br, 4H), 1.98 − 1.20 (br, m, 16H).

PBT*i*InSB (43) was obtained as a brown-red solid (173 mg, 52%). (GPC) M_n = 16,300 g / mol, Đ = 1.7; ^{1}H NMR (300 MHz, 2,2,2,-Trifluoroethanol-d_3) δ 9.49 − 8.42 (br, 2H), 8.42 − 6.18 (br, 6H), 3.94 − 2.53 (br, m, 28H), 2.53 − 1.14 (br, m, 20H).

PT₂*i*InSB (44) was obtained as a blue-green solid (191 mg, 55 %). (GPC) M_n = 15,400 g / mol, Đ = 1.8; ^{1}H NMR (300 MHz, 2,2,2,-Trifluoroethanol-d_3) δ 9.54 − 8.29

(br, 2H), 8.42 – 5.70 (br, 8H), 4.03 – 2.48 (br, m, 28H), 2.41 – 1.98 (br, 4H), 1.96 – 0.88 (br, m, 16H).

- **Branched-alkyl diketopyrrolopyrrole-based polymers (45, 46 and 47).**

45	46	47
PT$_3$DPP-alkyl	PT$_2$BTDPP-alkyl	PT$_4$DPP-alkyl

Branched-alkyl dikeotpyrrolopyrrole-based polymers were prepared according to literature.[7]

- **Branched-alkyl isoindigo-based polymers (48, 49 and 50).**

48	49	50
PT*i*In-alkyl	PBT*i*In-alkyl	PT$_2$*i*In-alkyl
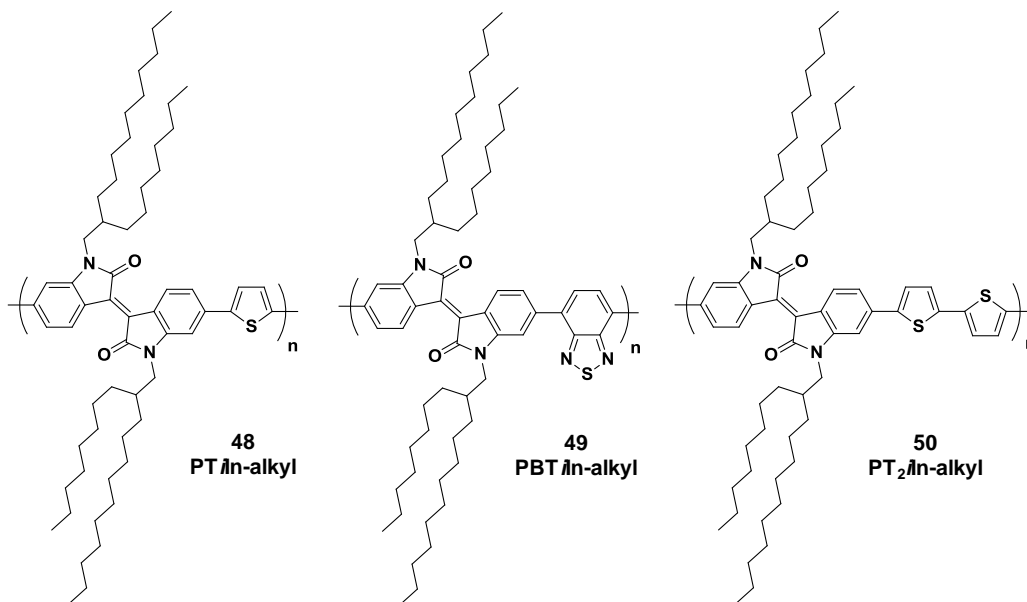
Branched-alkyl isoindigo-based polymers were prepared according to literature.[8]

- **3,6-di(thiophen-2-yl)pyrrolo[3,4-c]pyrrole-1,4(2H,5H)-dione (51).**
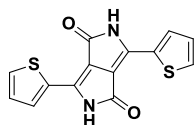
Compound **51** was prepared according to literature.[9]

- **2,5-bis(6-iodohexyl)-3,6-di(thiophen-2-yl)pyrrolo[3,4-c]pyrrole-1,4(2H,5H)-dione (52).**
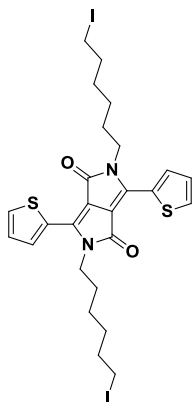
A 2-neck, 250 mL round-bottom flask equipped with a magnetic stir bar, inlet adapter and septum was flushed with nitrogen, followed by addition of 1,6-diiodohexane (prepared by the Finkelstein reaction)[10] (3.0 g, 10 mmol), cesium carbonate (13.0 g, 40 mmol) and NMP (anhydrous, 120 mL). The reaction was heated to 70 °C with stirring, followed by addition of 1,6-diiodohexane (27.0 g, 13.2 mL, 80 mmol). The reaction was stirred at 70 °C for 4 hours, then cooled to room temperature. The product was extracted with DCM, the organic fractions combined, washed with water, dried over MgSO$_4$, filtered and concentrated to obtain a red solid. This was purified by column chromatography on silica-gel, eluting with DCM:hexanes mixtures. The solvent was removed by rotary evaporation to afford a red solid that was recrystallized from

DCM:hexanes (≈1:5) to give **52** as red needles (3.62 g, 50 %). ^{1}H NMR (300 MHz, Chloroform-*d*) δ 8.92 (d, *J* = 3.9 Hz, 2H), 7.65 (d, *J* = 5.0 Hz, 2H), 7.29 (dd, *J* = 5.1, 3.9 Hz, 2H), 4.15 – 4.01 (m, 4H), 3.18 (t, *J* = 6.9 Hz, 4H), 1.93 – 1.66 (m, 8H), 1.51 – 1.39 (m, 8H). ^{13}C NMR (176 MHz, Chloroform-*d*) δ 161.46, 140.09, 135.47, 130.88, 129.79, 128.82, 107.82, 42.12, 33.43, 30.24, 29.88, 25.94, 6.98. [Note that use of dibromohexane in place of diiodohexane required higher temperatures (> 90 °C) to achieve substitution, and competing elimination chemistry was observed, as seen in the appearance of vinyl protons in the ^{1}H-NMR spectra.]

- **3,6-bis(5-bromothiophen-2-yl)-2,5-bis(6-iodohexyl)pyrrolo[3,4-c]pyrrole-1,4(2H,5H)-dione (53).**
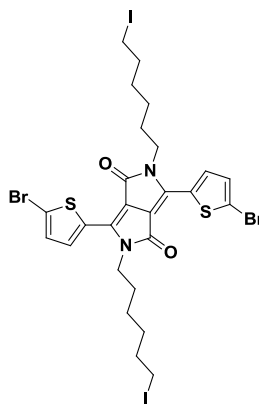
A 2-neck, 250 mL round-bottom flask equipped with a magnetic stir bar, inlet adapter and septum was flushed with nitrogen gas, followed by addition of **52** (2.56 g, 3.55 mmol) and CHCl$_3$ (62 mL). The reaction mixture was protected from light by covering the glassware with aluminum foil, and *N*-bromosuccinimide (NBS, 1.58 g, 8.88 mmol) was added under a stream of nitrogen. The mixture was heated to 35 °C and stirred in the dark for 24 hours, then cooled to room temperature. The product was isolated by precipitation into MeOH, then filtered and washed with MeOH to afford **53** as a purple

solid (2.43 g, 78 %). ^{1}H NMR (400 MHz, 98 °C, *o*-dichlorobenzene-d_4) δ 8.66 (d, *J* = 4.2 Hz, 2H), 7.04 (d, *J* = 4.1 Hz, 2H), 3.93 (t, *J* = 7.6 Hz, 4H), 2.98 (t, *J* = 7.0 Hz, 4H), 1.85 – 1.48 (m, 8H), 1.43 – 1.26 (m, 8H). ^{13}C NMR (101 MHz, 98°C, CDCl$_3$) δ 160.49, 138.29, 134.75, 131.44, 131.33, 118.48, 108.28, 41.81, 33.29, 29.93, 29.64, 25.61, 5.20.

- **3,6-bis(5-bromothiophen-2-yl)-2,5-bis(6-(dimethylamino)hexyl)pyrrolo[3,4-c]pyrrole-1,4(2H,5H)-dione (54).**
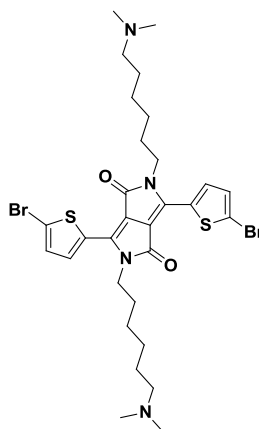
A 500 mL pressure flask equipped with a magnetic stir bar was flushed with nitrogen, followed by addition of **53** (3.0 g, 3.4 mmol) and dimethylamine (2M in THF, 250 mL). The pressure flask was capped tightly and heated to 60 °C for 1 hour with stirring. The mixture was cooled to room temperature, water was added and the product was extracted with DCM. The organic fractions were combined and dried over MgSO$_4$, filtered and concentrated. The crude product was purified by column chromatography on silica-gel, eluting with DCM:MeOH:TEA mixtures. The solvent was removed under reduced pressure, giving a purple/red solid that was purified further by recrystallization from acetone to give **54** as a purple/red solid (1.82 g, 75 %). ^{1}H NMR (300 MHz, methylene chloride-d_2) δ 8.66 (d, *J* = 4.2 Hz, 2H), 7.27 (d, *J* = 4.2 Hz, 2H), 3.97 (t, *J* = 7.6 Hz, 4H), 2.30 – 2.22 (m, 4H), 2.18 (s, 12H), 1.80 – 1.62 (m, 4H), 1.56 – 1.29 (m, 12H). ^{13}C NMR

(176 MHz, chloroform-*d*) δ 161.17, 139.12, 135.52, 131.82, 131.20, 119.32, 107.96, 59.79, 45.54, 42.32, 30.11, 27.58, 27.21, 26.92.

- **3,3'-(((3,6-bis(5-bromothiophen-2-yl)-1,4-dioxopyrrolo[3,4-c]pyrrole-2,5(1H,4H)-diyl)bis(hexane-6,1   diyl))bis(dimethylammonionediyl))bis(propane-1-sulfonate) (55).**
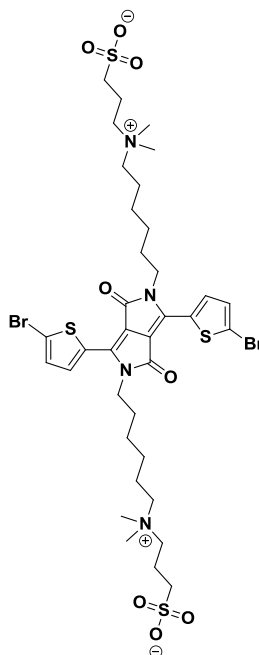
A 2-neck, 250 mL round-bottom flask equipped with a magnetic stir bar, inlet adapter, condenser and septum was flushed with nitrogen, followed by addition of **54** (1.75 g, 2.46 mmol), 1,3-propanesultone (2.40 g, 19.65 mmol) and THF (anh, 175 mL). The reaction was heated to reflux while stirring for 24 hours, then cooled to room temperature. The product (**55**) precipitated during the course of the reaction and was obtained by filtration and purified by washing with THF. Further purification can be done by recrystallizing **55** from water, yielding lustrous gold / purple flakes (2.21 g, 94 %). ^{1}H NMR (300 MHz, 2,2,2,-Trifluoroethanol-*d*₃) δ 8.36 (d, *J* = 3.7 Hz, 2H), 7.23 (d, *J* = 3.8 Hz, 2H), 3.95 (s, 4H), 3.46 − 3.33 (m, 4H), 3.27 − 3.15 (m, 4H), 3.00 (s, 12H), 2.91 (t, *J* = 6.1 Hz, 4H),),

2.37 – 2.03 (m, 4H), 1.83 – 1.60 (m, 8H), 1.55 – 1.33 (m, 8H). ^{13}C NMR (176 MHz, 2,2,2,-Trifluoroethanol-d_3) δ 163.84, 141.96, 137.15, 133.56, 132.52, 122.32, 109.66, 69.70, 67.01, 64.97, 52.13, 48.84, 30.88, 27.56, 27.20, 24.02, 20.18. MALDI-TOF (m/z): [M+H]$^+$ calculated for $C_{36}H_{53}Br_2N_4O_8S_4$: 957.10, found: 957.31.

- **(E)-6,6'-dibromo-[3,3'-biindolinylidene]-2,2'-dione (56)**
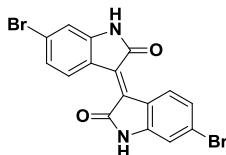
Compound **56** was prepared according to literature.[11]

- **(E)-6,6'-dibromo-1,1'-bis(6-iodohexyl)-[3,3'-biindolinylidene]-2,2'-dione (57).**
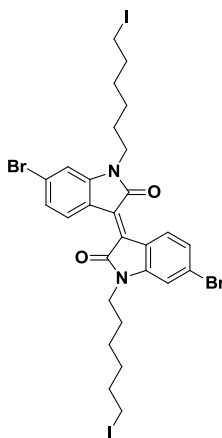
A 2-neck, 250 mL roundbottom flask equipped with a magnetic stir bar, inlet adapter and septum was flushed with nitrogen, followed by addition of **56** (3.0 g, 7.1 mmol), cesium carbonate (9.3 g, 29 mmol) and NMP (anhydrous, 90 mL). The mixture was heated to 70 °C with stirring, followed by addition of 1,6-diiodohexane (27.0 g, 13.2 mL, 80 mmol). The mixture was stirred at 70 °C for 4 hours, and then cooled to room temperature. The product was precipitated in water, filtered and washed with water, MeOH, EtOH and hexanes. The crude red solid was purified by column chromatography on silica-gel,

eluting with DCM:hexanes mixtures. The solvent was removed by rotary evaporation, and the residue recrystallized from CHCl$_3$:heptane (≈2:3) to give **57** as a lustrous red solid (2.22 g, 37 %). ^{1}H NMR (300 MHz, Chloroform-*d*) δ 9.07 (d, *J* = 8.6 Hz, 2H), 7.18 (dd, *J* = 8.6, 1.6 Hz, 2H), 6.93 (s, 2H), 3.75 (t, *J* = 7.1 Hz, 4H), 3.18 (t, *J* = 6.9 Hz, 4H), 1.83 (p, *J* = 7.1 Hz, 4H), 1.71 (p, *J* = 7.3 Hz, 4H), 1.53 − 1.36 (m, 8H). ^{13}C NMR (176 MHz, Chloroform-*d*) δ 167.92, 145.81, 132.77, 131.39, 126.99, 125.41, 120.57, 111.43, 40.24, 33.44, 30.28, 27.39, 26.10, 6.89.

- **(E)-6,6'-dibromo-1,1'-bis(6-(dimethylamino)hexyl)-[3,3'-biindolinylidene]-2,2'-dione (58).**
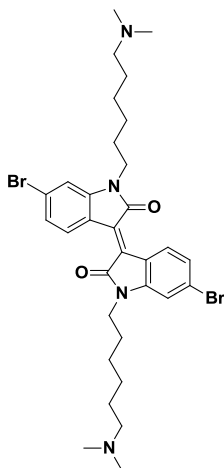
A 500 mL thick walled glass pressure flask equipped with a magnetic stir bar was flushed with nitrogen, followed by addition of **57** (2.2 g, 2.6 mmol) and dimethylamine (2M in THF, 180 mL). The flask was capped tightly and heated to 60 °C for 1 hour with stirring. The reaction was cooled to room temperature, water was added and the product extracted with DCM. The organic fractions were combined and dried with MgSO$_4$, then filtered and concentrate by rotary evaporation. The crude product was purified by column chromatography on silica-gel, eluting with DCM:MeOH:TEA mixtures. The solvent was removed under reduced pressure to yield **58** as a red solid (1.74 g, 98 %). ^{1}H NMR (300

185

MHz, Chloroform-*d*) δ 9.06 (d, *J* = 8.6 Hz, 2H), 7.16 (d, *J* = 8.6 Hz, 2H), 6.92 (s, 2H), 3.73 (t, *J* = 7.4 Hz, 4H), 2.35 – 2.16 (m, 16H), 1.69 (p, *J* = 7.1 Hz, 4H), 1.44 – 1.31 (m, 8H). ^{13}C NMR (176 MHz, Chloroform-*d*) δ 167.88, 145.89, 132.78, 131.35, 126.91, 125.31, 120.57, 111.45, 59.86, 45.66, 40.35, 27.75, 27.52, 27.28, 27.10.

- **(E)-3,3'-(((6,6'-dibromo-2,2'-dioxo-[3,3'-biindolinylidene]-1,1'-diyl)bis(hexane-6,1-diyl))bis(dimethylammonionediyl))bis(propane-1-sulfonate) (59).**
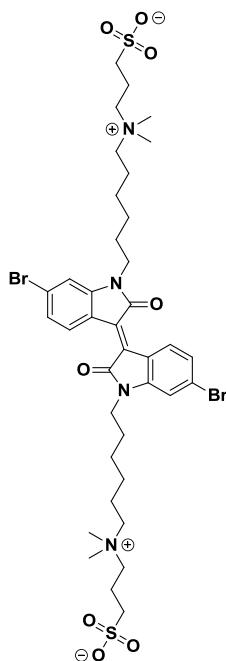
A 2-neck, 250 mL round-bottom flask equipped with a magnetic stir bar, inlet adapter, condenser and septum was flushed with nitrogen, followed by addition of **58** (1.70 g, 2.52 mmol), 1,3-propanesultone (2.46 g, 20.16 mmol) and THF (anhydrous, 175 mL). The stirring mixture was heated to reflux for 24 hours, then cooled to room temperature. The product (**59**) precipitated during the course of the reaction, and was isolated by filtration and purified by washing with THF, yielding **59** as a red solid (2.27 g, 98 %). ^{1}H NMR (700 MHz, 2,2,2,-Trifluoroethanol-*d*$_3$) δ 8.73 (d, *J* = 8.1 Hz, 2H), 7.17 (d, *J* = 8.8 Hz, 2H), 6.94 (s, 2H), 3.75 – 3.55 (m, 4H), 3.47 – 3.34 (m, 4H), 3.24 – 3.14 (m, 4H), 2.99 (s,

12H), 2.90 (t, J = 6.7 Hz, 4H), 2.26 – 2.15 (m, 4H), 1.79 – 1.71 (m, 4H), 1.71 – 1.62 (m, 4H), 1.52 – 1.37 (m, 8H). ^{13}C NMR (176 MHz, 2,2,2,-Trifluoroethanol-d_3) δ 170.19, 147.23, 134.72, 132.21, 128.93, 127.26, 122.01, 113.84, 69.68, 66.95, 64.94, 52.13, 48.82, 28.48, 27.75, 27.28, 24.02, 20.16. MALDI-TOF (m/z): [M+H]$^+$ calculated for C$_{38}$H$_{55}$Br$_2$N$_4$O$_8$S$_2$: 919.17, found: 919.04.

- **5,5'-bis(4,4,5,5-tetramethyl-1,3,2-dioxaborolan-2-yl)-2,2'-bithiophene (63).**
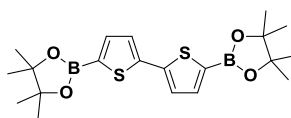
Compound **63** was prepared according to literature.[12]

- **2,6-Dibromo-1,4,5,8-naphthalenetetracarboxylic dianhydride (64).**
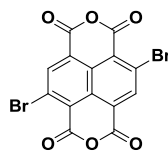
Compound **64** was synthesized according to a published procedure.[13]

- **4,9-dibromo-2,7-bis(6-(dimethylamino)hexyl)benzo[lmn][3,8]phenanthroline-1,3,6,8(2H,7H)-tetraone (65).**
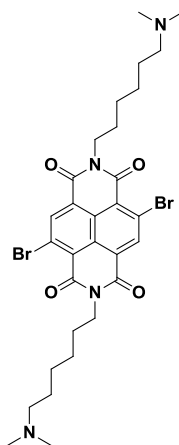
A 2-neck, 250 mL roundbottom flask equipped with a magnetic stir bar, inlet adapter, condenser and septum was flushed with nitrogen, followed by addition of **64** (3.30 g, 7.8 mmol), glacial acetic acid (82 mL) and 6-(dimethylamino)hexylamine (3.90 g, 27.1 mmol). The mixture was heated to reflux and stirred for 2 hours. The flask was immersed in an ice bath, and saturated Na_2CO_3 (aq) was added slowly. The product was extracted into dichloromethane (DCM), washed with saturated Na_2CO_3 (aq), then brine, dried with $MgSO_4$ (anh), filtered and concentrated to obtain a red/brown solid. The crude product was purified further using basic alumina (activated Brockman I) eluting with DCM:MeOH (99.5:0.5) yielding a red/yellow solid that was dissolved in DCM and precipitated into acetone to afford **65** as a beige solid (0.95 g, 18%) ^{1}H NMR (700 MHz, Chloroform-*d*) δ 8.93 (s, 2H), 4.16 (t, *J* = 7.8 Hz, 4H), 2.23 (t, *J* = 7.5 Hz, 4H), 2.19 (s, 12H), 1.72 (p, *J* = 7.7 Hz, 4H), 1.48 – 1.45 (m, 4H), 1.45 – 1.40 (m, 4H), 1.40 – 1.36 (m, 4H). ^{13}C NMR (176 MHz, Chloroform-*d*) δ 160.64, 160.60, 138.98, 128.27, 127.63, 125.27, 124.00, 59.75, 45.50, 41.48, 27.83, 27.64, 27.13, 27.03. MALDI-TOF (m/z): [M+H][+] calculated for $C_{30}H_{39}Br_2N_4O_4$: 679.12, found: 678.90.

- **3,3'-(((4,9-dibromo-1,3,6,8-tetraoxobenzo[lmn][3,8]phenanthroline-2,7(1H,3H,6H,8H)-diyl)bis(hexane-6,1-diyl))bis(dimethylammonionediyl))bis(propane-1-sulfonate) (66).**
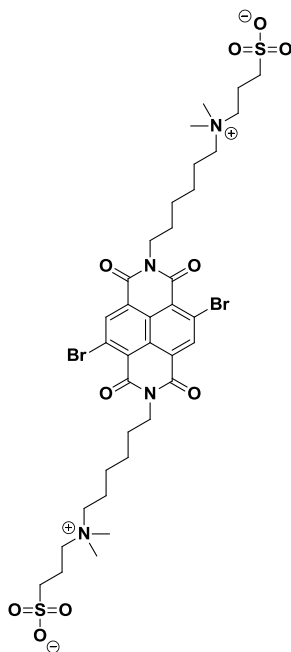
A 2-neck, 250 mL round-bottom flask equipped with a magnetic stir bar, inlet adapter, condenser and septum was flushed with nitrogen, followed by addition of **65** (1.1 g, 1.6 mmol), 1,3-propanesultone (1.58 g, 13.0 mmol) and anhydrous THF (100 mL). The mixture was heated to reflux while stirring for 24 hours, then cooled to room temperature. The product precipitated during the course of the reaction, and was isolated by filtration, then purified by washing with THF to obtain a light orange/yellow solid (1.34 g, 90%). Further purification was performed by recrystallization from water, yielding **66** as pale yellow flakes (1.02 g, 68 %). ^{1}H NMR (700 MHz, 2,2,2-Trifluoroethanol-d_3) δ 8.87 (d, J = 2.6 Hz, 2H), 4.18 (t, J = 7.9 Hz, 4H), 3.46 – 3.40 (m, 4H), 3.29 – 3.21 (m, 4H), 3.04 (s, 12H), 2.92 (td, J = 6.9, 2.6 Hz, 4H), 2.27 – 2.18 (m, 4H), 1.86 – 1.74 (m, 8H), 1.59 – 1.48 (m, 8H). ^{13}C NMR (176 MHz, 2,2,2-Trifluoroethanol-d_3) δ 163.65, 163.41, 140.79,

130.04, 129.56, 126.01, 67.00, 64.96, 52.19, 48.86, 42.92, 28.66, 27.61, 27.05, 23.86, 20.20. MALDI-TOF (m/z): $[M+H]^+$ calculated for $C_{36}H_{51}Br_2N_4O_{10}S_2$: 923.13, found: 923.30.

- **General Suzuki polymerization procedure for PT$_2$NDISB (67) and PT$_3$SB (68).**

67
PT$_2$NDISB

68
PT$_3$SB
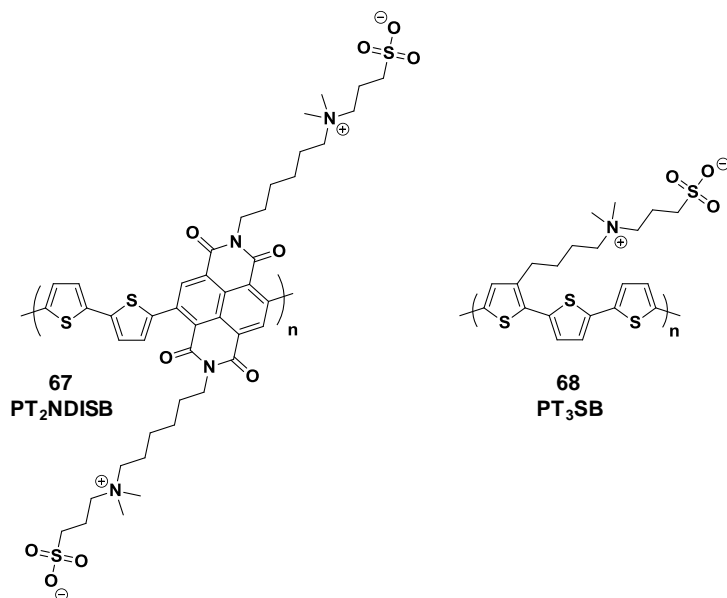
A 20 mL thick walled glass pressure tube equipped with a magnetic stir bar was transferred into a nitrogen filled glove-box. Tris(dibenzylideneacetone)-dipalladium(0) (Pd$_2$(dba)$_3$) (6.9 mg, 0.0075 mmol) and 2-(dicyclohexylphosphino)-2',4',6'-tri-*iso*propyl-1,1'-biphenyl (XPhos) (10.7 mg, 0.0225 mmol) were added to the tube, followed by capping the tube and removing it from the glove-box. The dibromo and diboronic-ester monomers (0.375 mmol), AQ336 (6 drops), toluene (6 mL), tetra-*n*-butylammonium fluoride solution (75 wt.% in H$_2$O, 2.2 mL) and NaBr (2 M aq, 0.8 mL) were added to the tube and degassed with argon for 5 minutes. The pressure tube was capped securely and the mixture stirred vigorously at 110 °C in the absence of light for 24 hours. The polymerization mixture was cooled to room temperature, and precipitated into MeOH.

The polymer was isolated by centrifugation and extracted first with MeOH for 16 hours then with 2,2,2-trifluoroethanol (TFE) for 4 hours using a Soxhlet apparatus. The TFE solution containing polymer was passed through a plug of Sephadex LH-20, then added to a dialysis membrane (10 kDa cutoff) and dialyzed in a 4 L beaker against water for 24 hours. The contents of the dialysis bag were lyophilized to afford a colored fluffy polymer.

PT$_2$NDISB (67) was obtained as a blue solid (319 mg, 92%). M_n = 11,700 – 55,800 g / mol, Đ = 1.6 – 4.7; ^{1}H NMR (300 MHz, 2,2,2-Trifluoroethanol-d_3) δ 9.27 – 8.23 (br, 2H), 7.34 – 7.13 (br, 2H), 6.98 – 6.12 (br, 2H), 4.69 – 4.03 (br, 4H), 3.43 – 3.32 (br, 4H), 3.31 – 3.15 (br, 4H), 3.12 – 2.83 (br, 16H), 2.28 – 2.07 (s, 4H), 1.96 – 1.70 (br, 8H), 1.71 – 1.38 (br, 8H).

PT$_3$SB (68) was obtained as a deep red-gold solid (164 mg, 93%). M_n = 21,500 – 52,900 g / mol, Đ = 1.5 – 2.2; ^{1}H NMR (700 MHz, 2,2,2-trifluoroethanol-d_3) δ 7.20 – 6.60 (br, 5H), 3.42 – 3.25 (br, 2H), 3.22 – 3.08 (br, 2H), 3.07 – 2.57 (br, 10H), 2.20 – 2.01 (br, 2H), 1.92 – 1.45 (br, 4H).

- **2,3,4-tris(3-(dimethylamino)propoxy)benzaldehyde (71).**
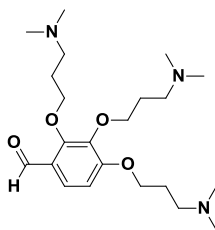
A 2-neck, 250 mL roundbottom flask equipped with a magnetic stir bar, inlet adapter, addition funnel and septa was flushed with nitrogen, followed by addition of 2,3,4-trihydroxybenzaldehyde (**70**) (2.00 g, 13.0 mmol), 3-dimethylaminopropan-1-ol (4.55 g, 44.1 mmol), triphenylphosphine (11.57 g, 44.1 mmol) and THF (anh, 45 mL). The

mixture was cooled to 0 °C with an ice bath while stirring under nitrogen. Diisopropyl azodicarboxylate was added to the addition funnel, dissolved in THF (anh, 15 mL) and added dropwise to the reaction mixture. After complete addition the flask was removed from the ice bath and stirred at room temperature for five hours. The reaction was concentrated and the resulting crude mixture was washed with Hex:Et$_2$O (1:1), filtering off the white phosphine-oxide byproduct through Celite. The filtrate was concentrated, dissolved in DCM and washed with 1M HCl (aq) (50 mL, 3x). The aqueous fractions were combined and washed with DCM until the organic phase no longer contained a UV-active compound (tested on UV-active TLC plates under short-wave 254 nm light). The acidic aqueous layer was neutralized with sodium carbonate (sat., aq.) and the product was extracted into DCM. The combined organic phases were dried with MgSO$_4$ (anh), filtered and concentrated to obtain a brown oil. The crude product was further purified using basic alumina (activated Brockman I) eluting with DCM:MeOH:TEA (98:1:1) yielding (once concentrated) **71** as a light yellow oil (3.88g, 73 %). ^{1}H NMR (700 MHz, Chloroform-*d*) δ 10.20 (s, 1H), 7.52 (d, *J* = 8.8 Hz, 1H), 6.70 (d, *J* = 8.8 Hz, 1H), 4.18 (t, *J* = 6.5 Hz, 2H), 4.06 (t, *J* = 6.5 Hz, 2H), 4.00 (t, *J* = 6.5 Hz, 2H), 2.55 − 2.35 (m, 6H), 2.33 − 2.01 (m, 18H), 1.97 (p, *J* = 6.8 Hz, 2H), 1.91 (ddt, *J* = 12.9, 8.5, 6.3 Hz, 4H). ^{13}C NMR (176 MHz, Chloroform-*d*) δ 189.05, 158.98, 156.47, 140.94, 123.99, 123.58, 108.37, 73.58, 72.09, 67.28, 56.66, 56.44, 56.26, 45.63, 45.61, 45.59, 28.62, 28.54, 27.51.

- **2,3,4-tris(3-(dimethylamino)propoxy)fulleropyrrolidine (C$_{60}$-N) (72).**
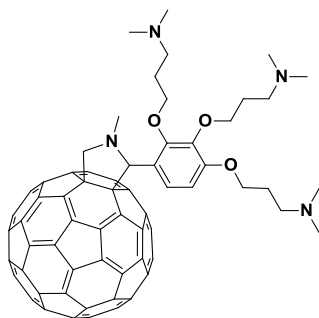
A 1-neck, 250 mL round-bottom flask equipped with a magnetic stir bar, inlet adapter, and Vigreux column was flushed with nitrogen, followed by addition of **2** (300 mg, 0.73 mmol), fullerene-C$_{60}$ (792 mg, 1.10 mmol), sarcosine (200 mg, 2.2 mmol) and 1,2-dichlorobenzene (110 mL). The mixture was degassed with nitrogen and then heated to reflux for 1 hour. The reaction was concentrated, dissolved in chloroform and filtered. The resulting filtrate was concentrated and then dissolved in carbon disulfide (CS$_2$). The crude mixture was added to silica gel, wet packed with hexanes, and eluted with CS$_2$, followed by CH$_2$Cl$_2$:TEA:MeOH (95:5:5). The first brown band that eluted was collected and concentrated, dissolved in chloroform, filtered through a 1 μm PTFE filter and precipitated into acetone. The precipitate was washed with acetone and dried to obtain the **C$_{60}$-N** (**72**) as a brown solid (374 mg, 44 %). ^{1}H NMR (300 MHz, Chloroform-*d*) δ 7.61 (d, *J* = 8.8 Hz, 1H), 6.78 (d, *J* = 8.8 Hz, 1H), 5.37 (s, 1H), 4.97 (d, *J* = 9.3 Hz, 1H), 4.26 (d, *J* = 9.4 Hz, 1H), 4.16 (t, *J* = 6.2 Hz, 2H), 4.09 − 3.99 (m, 2H), 3.94 (t, *J* = 6.5 Hz, 2H), 2.78 (s, 3H), 2.58 − 2.46 (m, 4H), 2.45 − 2.37 (m, 2H), 2.31 (s, 6H), 2.26 (s, 6H), 2.21 (s, 6H), 2.07 − 1.91 (m, 4H), 1.87 − 1.75 (m, 2H). ^{13}C NMR (176 MHz, Chloroform-*d*) δ 156.85, 155.05, 154.31, 154.19, 152.98, 152.58, 147.40, 147.06, 146.83, 146.42, 146.36, 146.35, 146.29, 146.23, 146.18, 146.17, 146.05, 146.04, 145.85, 145.67, 145.64, 145.42, 145.40, 145.37, 145.35, 145.24, 145.20, 144.71, 144.70, 144.54, 144.46, 143.19, 143.10,

142.74, 142.73, 142.67, 142.64, 142.40, 142.38, 142.27, 142.26, 142.22, 142.17, 142.09, 141.97, 141.80, 141.79, 141.72, 141.33, 140.26, 140.21, 139.62, 139.60, 136.69, 136.58, 136.07, 134.97, 124.56, 122.77, 108.92, 76.36, 72.23, 71.77, 70.03, 67.08, 56.98, 56.75, 56.62, 45.87, 45.70, 45.66, 40.23, 28.93, 28.39, 27.81. MALDI-TOF (m/z): $[M+H]^+$ calculated for: $C_{84}H_{45}N_4O_3$: 1157.34, found: 1157.60.

- **2,3,4-tris(3-(propylsulfobetaine)propoxy)fulleropyrrolidine (C_{60}-SB) (73).**
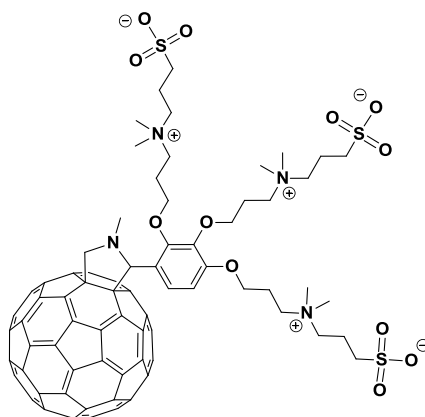
A 1-neck, 15 mL round-bottom flask equipped with a magnetic stir bar, inlet adapter, condenser and septum was flushed with nitrogen, followed by addition of **17** (250 mg, 0.22 mmol), 1,3-propanesultone (250 mg, 2.05 mmol), Na_2CO_3 (70 mg, 0.65 mmol) and TFE (5 mL). The reaction was heated to reflux while stirring for 24 hours, then cooled to room temperature. The product was precipitated into THF, filtered and washed with THF, followed by re-dissolving into TFE (5 mL), centrifuging and filtering through a 1 μm PTFE syringe filter into a dialysis membrane (1 kDa cutoff). The contents of the dialysis bag were dialyzed against pure water in a 4L beaker for 24 hours (changing the water five times) and then the water was removed by lyophilization. **C_{60}-SB** (**73**) was obtained as a pure light brown fluffy solid (286 mg, 87 %). ^{1}H NMR (700 MHz, 2,2,2,-Trifluoroethanol-d_3) δ 7.90 (br, 1H), 6.99 (br, 1H), 5.32 (br, 1H), 5.05 (br, 1H), 4.42 –

4.24 (m, 3H), 4.24 – 4.15 (m, 2H), 4.11 – 4.00 (m, 2H), 3.69 – 3.58 (m, 3H), 3.58 – 3.40 (m, 9H), 3.14 (br, 6H), 3.12 – 2.99 (m, 12H), 2.99 – 2.90 (m, 6H), 2.80 (br, 3H), 2.32 (br, 4H), 2.23 (br, 6H), 2.14 (br, 2H). MALDI-TOF (m/z): $[M+H]^+$ calculated for: $C_{93}H_{63}N_4O_{12}S_3$: 1524.36, found: 1524.19.

- **2,3,4-tris(hexyloxy)benzaldehyde (75).**
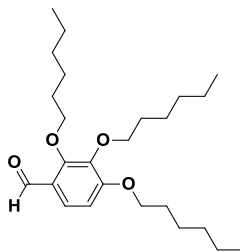
A 2-neck, 250 mL round-bottom flask equipped with a magnetic stir bar, inlet adapter, addition funnel and septa was flushed with nitrogen, followed by addition of 2,3,4-trihydroxybenzaldehyde (2.00 g, 13.0 mmol), 1-hexanol (4.51 g, 44.1 mmol), triphenylphosphine (11.57 g, 44.1 mmol) and THF (anh, 45 mL). The mixture was cooled to 0 °C with an ice bath while stirring under nitrogen. Diisopropyl azodicarboxylate was added to the addition funnel, dissolved in THF (anh, 15 mL) and added dropwise to the reaction mixture. After complete addition the flask was removed from the ice bath and stirred at room temperature for five hours. The reaction was concentrated and the resulting crude mixture was washed with hexanes, filtering off the white phosphine-oxide byproduct through celite. The filtrate was concentrated to obtain a light brown oil. The oil was subjected to silica gel chromatography for further purification, eluting with Hex:EtOAc (95:5) to obtain the product as the first UV-active band to elute. After concentrating the solution **75** was obtained as a clear light yellow oil (1.73 g, 33 %). ^{1}H NMR (700 MHz, Chloroform-d) δ 10.26 (s, 1H), 7.57 (d, J = 8.7 Hz, 1H), 6.71 (d, J = 8.8 Hz, 1H), 4.17 (t, J = 6.7 Hz, 2H), 4.04 (t, J = 6.5 Hz, 2H), 3.97 (t, J = 6.7 Hz, 2H), 1.84

(dt, J = 15.1, 6.6 Hz, 2H), 1.77 (ddt, J = 15.7, 9.2, 6.7 Hz, 4H), 1.52 − 1.42 (m, 6H), 1.38 − 1.31 (m, 12H), 0.91 (t, J = 7.3 Hz, 9H). ^{13}C NMR (176 MHz, Chloroform-d) δ 189.27, 159.29, 156.83, 141.17, 123.85, 123.61, 108.21, 75.46, 73.90, 69.07, 31.84, 31.76, 31.65, 30.38, 30.26, 29.27, 25.90, 25.85, 25.81, 22.79, 22.73, 22.72, 14.18, 14.15, 14.13.

- **2,3,4-tris(hexyloxy)fulleropyrrolidine (C$_{60}$-alkyl) (76).**
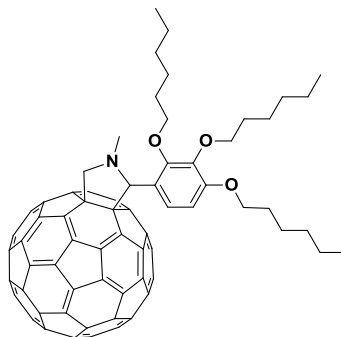
A 1-neck, 250 mL round-bottom flask equipped with a magnetic stir bar, inlet adapter, and Vigreux column was flushed with nitrogen, followed by addition of **3** (298 mg, 0.73 mmol), fullerene-C$_{60}$ (792 mg, 1.10 mmol), sarcosine (200 mg, 2.2 mmol) and 1,2-dichlorobenzene (110 mL). The mixture was degassed with nitrogen and then heated to reflux for 1 hour. The reaction was concentrated, dissolved in chloroform and filtered. The resulting filtrate was concentrated and then dissolved in carbon disulfide (CS$_2$). The crude mixture was added to silica gel, wet packed with hexanes, and eluted with CS$_2$, followed by Hex:CH$_2$Cl$_2$ (1:1). The first brown band that eluted was collected and concentrated, dissolved in chloroform, filtered through a 1 μm PTFE filter and precipitated into acetone. The precipitate was washed with acetone and dried to obtain **C$_{60}$-alkyl** (**76**) as a brown solid (446 mg, 53 %). ^{1}H NMR (700 MHz, Chloroform-d) δ 7.60 (d, J = 8.8 Hz, 1H), 6.74 (d, J = 8.9 Hz, 1H), 5.38 (s, 1H), 4.96 (d, J = 9.3 Hz, 1H), 4.26 (d, J = 9.3 Hz, 1H), 4.11 (qt, J = 9.3, 6.5 Hz, 2H), 3.97 (ddt, J = 32.7, 9.4, 6.5 Hz,

2H), 3.91 – 3.84 (m, 2H), 2.78 (s, 3H), 1.84 – 1.71 (m, 4H), 1.64 – 1.57 (m, 2H), 1.52 – 1.43 (m, 4H), 1.41 – 1.30 (m, 10H), 1.29 – 1.19 (m, 4H), 0.91 (dh, J = 18.2, 4.5, 4.1 Hz, 6H), 0.85 (t, J = 7.0 Hz, 3H). ^{13}C NMR (176 MHz, Chloroform-d) δ 156.92, 155.19, 154.48, 154.20, 153.19, 152.76, 147.42, 147.40, 147.18, 146.87, 146.54, 146.37, 146.36, 146.31, 146.24, 146.19, 146.17, 146.06, 145.87, 145.71, 145.67, 145.43, 145.42, 145.37, 145.36, 145.34, 145.23, 145.20, 144.72, 144.71, 144.58, 144.46, 143.19, 143.10, 142.75, 142.73, 142.68, 142.64, 142.42, 142.39, 142.31, 142.26, 142.22, 142.19, 142.08, 141.99, 141.79, 141.78, 141.75, 141.45, 140.24, 140.20, 139.59, 139.57, 136.74, 136.55, 136.15, 134.87, 124.33, 122.57, 108.56, 76.49, 73.94, 73.40, 70.09, 69.31, 68.76, 40.27, 31.94, 31.84, 31.77, 30.61, 30.10, 29.53, 26.13, 25.97, 25.86, 22.96, 22.80, 22.75, 14.37, 14.23, 14.18. MALDI-TOF (m/z): [M+H]$^{+}$ calculated for: $C_{87}H_{47}N_4NO_3$: 1153.36, found: 1154.35.

- **Tetraethyl (1,4-phenylenebis(methylene))bis(phosphonate) (78).**
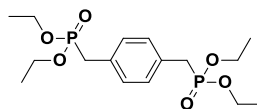
Compound **78** was prepared according to literature.[14]

- **4,7-Bis(bromomethyl)benzo[c][1,2,5]thiadiazole (80).**
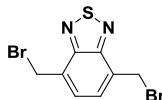
Following a modified literature procedure[15]: To a 1-neck, 500 mL roundbottom flask equipped with a magnetic stir bar and condenser was added 2,1,3-benzothiadiazole (**79**) (10.0 g, 73 mmol), hydrobromic acid (48 wt% in water, 200 mL) and sulfuric acid (conc., 50 mL). 1,3,5-Trioxane (33.1 g, 367 mmol) and myristyltrimethylammonium bromide

(2.5 g, 7 mmol) were added to the flask while stirring the mixture. The reaction was heated to reflux and stirred for 16 hours. The reaction was cooled to room temperature and the precipitate was filtered, washed with water then ethanol and dried under reduced pressure. The resulting off-white solid was further purified using silica gel column chromatography eluting with dichloromethane:hexanes (1:3), yielding **80** (once concentrated) as a white crystalline solid (21.7 g, 92%). ^{1}H NMR (500 MHz, Chloroform-*d*) δ 7.62 (s, 2H), 4.96 (s, 4H). ^{13}C NMR (126 MHz, Chloroform-*d*) δ 153.66 , 131.33 , 129.46 , 28.21.

- **Tetraethyl (benzo[c][1,2,5]thiadiazole-4,7-diylbis(methylene))bis(phosphonate) (81).**
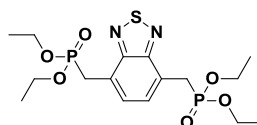
Michaelis-Arbuzov reaction[16-18]: To a 2-neck, 25 mL roundbottom flask equipped with a magnetic stir bar, Vigreaux column, inlet adapter and septum was added **80** (4.0 g, 12 mmol) and triethyl phosphite (12.4 g, 75 mmol). The reaction was brought under a nitrogen atmosphere and heated to 120°C with stirring for 4 hours. The reaction was cooled and added to boiling hexanes while stirring. Upon cooling the hexanes mixture **81** crystallized out as white needles, which were isolated by filtration and dried under reduced pressure (5.1 g, 95%). ^{1}H NMR (500 MHz, Chloroform-*d*) δ 7.60 (s, 2H), 4.06 (p, *J* = 7.3 Hz, 8H), 3.73 (d, *J* = 20.8 Hz, 4H), 1.19 (t, *J* = 7.0 Hz, 12H). ^{13}C NMR (126 MHz, Chloroform-*d*) δ 154.78 (t, *J* = 2.0 Hz), 129.91 – 129.67 (m), 124.31 – 124.04 (m), 62.30 (t, *J* = 3.3 Hz), 29.69 (d, *J* = 2.0 Hz), 28.57 (d, *J* = 2.1 Hz), 16.40 (t, *J* = 3.0 Hz).

^{31}P NMR (202 MHz, Chloroform-*d*) δ 25.15. High resolution ESI (m/z): [M•H]$^-$ calculated for: $C_{16}H_{26}N_2O_6P_2S$: 435.0914, found: 435.0909.

- **1,4-Bis(bromomethyl)-2,3,5,6-tetrafluorobenzene (83).**
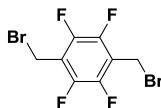
A dry 2-neck, 250 mL roundbottom flask equipped with a magnetic stir bar, inlet adapter and septum was flushed with nitrogen and **82** (6.0 g, 29 mmol) was added followed by dichloromethane (anhydrous, 90 mL). The mixture was cooled to 0°C with an ice bath followed by the dropwise addition of phosphorus tribromide (5.4 mL, 57 mmol) through a syringe. The reaction was removed from the ice bath and allowed to warm to room temperature. After stirring for 3 hours the flask was again cooled to 0°C and sodium bicarbonate was added slowly to quench the reaction. When the generation of carbon dioxide ceased the mixture was washed with brine, followed by drying the organic layer with anhydrous magnesium sulfate, filtering and concentrating to obtain the crude product. Further purification was done by running the product through a plug of silica gel eluting with dichloromethane:hexanes (1:3). After concentrating under reduced pressure the product, **83**, was obtained as a white crystalline solid (3.7 g, 38%). ^{1}H NMR (500 MHz, Chloroform-*d*) δ 4.50 (s, 4H). ^{13}C NMR (126 MHz, Chloroform-*d*) δ 145.79 – 143.43 (m), 117.62 (tdd, *J* = 10.6, 7.3, 4.3 Hz), 16.38 (p, *J* = 3.1 Hz). ^{19}F NMR (471 MHz, Chloroform-*d*) δ -142.38.

- **Tetraethyl ((perfluoro-1,4-phenylene)bis(methylene))bis(phosphonate) (84).**
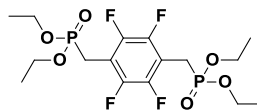
Following the same Michaelis-Arbuzov reaction used to make compound **81**: Product **84** was obtained as white needles (3.3 g, 73%). ^{1}H NMR (500 MHz, Chloroform-*d*) δ 4.12 (pt, *J* = 7.2, 3.4 Hz, 8H), 3.26 (d, *J* = 20.5 Hz, 4H), 1.30 (t, *J* = 7.0 Hz, 12H). ^{13}C NMR (126 MHz, Chloroform-*d*) δ 146.06 – 143.26 (m), 110.99 – 110.37 (m), 62.56 (t, *J* = 3.3 Hz), 21.52 (d, *J* = 142.6 Hz), 16.25 (t, *J* = 3.1 Hz). ^{19}F NMR (471 MHz, Chloroform-*d*) δ -142.49. ^{31}P NMR (202 MHz, Chloroform-*d*) δ 21.92. High resolution ESI (m/z): [M•H][-] calculated for: $C_{16}H_{24}F_4O_6P_2$: 449.0911, found: 449.0907.

- **5,6-Difluorobenzo[c][1,2,5]thiadiazole (85).**
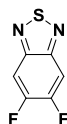
Following a modified literature procedure[19] A dry 3-neck, 500 mL roundbottom flask equipped with a magnetic stir bar, inlet adapter, condenser, addition funnel and septa was flushed with nitrogen and 1,2-diamino-4,5-difluorobenzene (10.0 g, 69 mmol) was added followed by chloroform (anhydrous, 200 mL) and triethylamine (38.7 mL, 278 mmol). Thionyl chloride (10.6 mL, 146 mmol) was diluted in chloroform (anhydrous, 50 mL) and added dropwise to the mixture while stirring at room temperature. After complete addition the reaction was heated to reflux for 5 hours, then cooled to room temperature and quenched with water. The product was extracted with dichloromethane and the organic fractions were combined, dried with anhydrous magnesium sulfate, filtered and concentrated. The crude product was further purified using silica gel column

chromatography eluting with dichloromethane:hexanes (1:3). The product **85** was obtained as an off-white solid and sublimed at room temperature to obtain a white crystalline solid (10.5 g, 87%). ^{1}H NMR (500 MHz, Chloroform-d) δ 7.75 (t, J = 8.7 Hz, 2H). ^{13}C NMR (126 MHz, Chloroform-d) δ 154.86 (d, J = 20.0 Hz), 152.79 (d, J = 20.0 Hz), 150.86 (t, J = 5.6 Hz), 106.17 (dd, J = 15.6, 6.0 Hz). ^{19}F NMR (471 MHz, Chloroform-d) δ -127.98 (t, J = 8.7 Hz).

- **(5,6-Difluorobenzo[c][1,2,5]thiadiazole-4,7-diyl)dimethanol (86).**
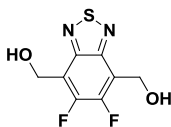
Following a modified literature procedure[20]: A dry 2-neck, 250 mL roundbottom flask equipped with a magnetic stir bar, inlet adapter and septum was evacuated and refilled with nitrogen and anhydrous tetrahydrofuran (THF, 65 mL) and diisopropylamine (7.9 mL, 56 mmol) were added. The mixture was cooled to -78°C with a dry ice / acetone bath and n-butyllithium (2.5 M in hexanes, 19.2 mL, 48 mmol) was added carefully. The contents of the flask were stirred for 40 minutes at -78°C to generate lithium diisopropylamide (LDA). A second 2-neck, 500 mL roundbottom flask equipped with a magnetic stir-bar, jacketed addition funnel, inlet adapter and septum was evacuated and refilled with nitrogen and THF (65 mL) and **85** (3.44 g, 20 mmol) were added. The mixture was cooled to -78°C with a dry ice / acetone bath and the freshly prepared LDA solution was added dropwise by cannulating it over directly from the first flask. The reaction immediately turned a dark red / brown color. Anhydrous hexamethylphosphoramide (HMPA, 11 mL) was added dropwise at -78°C and the stirred at this temperature for one hour, during which time the reaction mixture turned dark

green. THF (20 mL) was added to the jacketed addition funnel and chilled to -78°C with dry ice / acetone, followed by the addition of formaldehyde* (1.3 M in THF, 49 mL, 64 mmol). The formaldehyde in THF was added dropwise, maintaining a temperature of -78°C for the reaction flask and addition funnel. After complete addition the reaction mixture was warmed to -45°C using a dry ice / acetonitrile bath and then allowed to warm to -30°C over the course of one hour. After the dry ice / acetonitrile cooling bath had reached -30°C it was replaced with an ice bath and the reaction mixture was stirred for 20 minutes at 0°C followed by quenching with 1 M HCl. The product was extracted with dichloromethane, dried with anhydrous magnesium sulfate, filtered and concentrated to obtain an orange oil. The crude product was further purified using silic gel column chromatography eluting with ethyl acetate:hexanes (3:7 gradient to 8:2). After concentrating under reduced pressure the product **86** was obtained as a yellow solid (3.61 g, 78%). ^{1}H NMR (500 MHz, DMSO-d_6) δ 5.49 (t, J = 5.8 Hz, 2H), 4.94 (d, J = 5.6 Hz, 4H). ^{13}C NMR (126 MHz, DMSO-d_6) δ 151.69 (d, J = 20.3 Hz), 150.07 (t, J = 4.5 Hz), 149.64 (d, J = 20.2 Hz), 118.56 (dd, J = 11.7, 4.5 Hz), 53.22 (t, J = 2.4 Hz). ^{19}F NMR (471 MHz, DMSO-d_6) δ -134.70.

*Formaldehyde solutions[21,22] were generated by cracking paraformaldehyde thermally under reduced pressure and trapping it in anhydrous tetrahydrofuran (THF) at -78°C. The solutions were filtered to remove repolymerized material and stored under an inert atmosphere at -80°C, where they were stable for months. The molar concentration of formaldehyde in THF was determined using ^{1}H-NMR spectroscopy.

- **4,7-Bis(bromomethyl)-5,6-difluorobenzo[c][1,2,5]thiadiazole (87).**
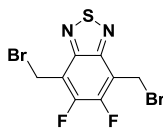
A dry 2-neck, 500 mL roundbottom flask equipped with a magnetic stir bar, inlet adapter and septum was flushed with nitrogen and **86** (3.6 g, 16 mmol) was added followed by tetrahydrofuran (anhydrous, 300 mL). The mixture was cooled to 0°C with an ice bath followed by the dropwise addition of phosphorus tribromide (2.9 mL, 31 mmol) through a syringe. The reaction was removed from the ice bath and allowed to warm to room temperature. After stirring for 3 hours the flask was again cooled to 0°C and sodium bicarbonate was added slowly to quench the reaction. When the generation of carbon dioxide ceased the mixture was washed with brine, followed by drying the organic layer with anhydrous magnesium sulfate, filtering and concentrating to obtain the crude product. Further purification was done by running the product through a plug of silica gel eluting with ethyl acetate:hexanes (1:4). After concentrating under reduced pressure the product, **87**, was obtained as a yellow crystalline solid (3.6 g, 65%). ^{1}H NMR (500 MHz, Chloroform-*d*) δ 4.95 (s, 4H). ^{13}C NMR (126 MHz, Chloroform-*d*) δ 152.31 (d, *J* = 19.6 Hz), 150.22 (d, *J* = 19.8 Hz), 149.58 (t, *J* = 3.7 Hz), 116.91 (dd, *J* = 11.4, 4.8 Hz), 19.36 (t, *J* = 3.1 Hz). ^{19}F NMR (471 MHz, Chloroform-*d*) δ -129.80.

- **Tetraethyl ((5,6-difluorobenzo[c][1,2,5]thiadiazole-4,7-diyl)bis(methylene))bis(phosphonate) (88).**
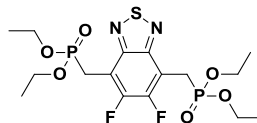
Following the same Michaelis-Arbuzov reaction used to make compound **81**: Product **88** was obtained as light yellow crystals (3.5 g, 75%). ^{1}H NMR (500 MHz, Chloroform-d) δ 4.20 – 4.04 (m, 8H), 3.71 (d, $J = 20.8$ Hz, 4H), 1.23 (t, $J = 7.0$ Hz, 12H). ^{13}C NMR (126 MHz, Chloroform-d) δ 152.96 – 152.58 (m), 150.88 – 150.52 (m), 110.64 – 110.11 (m), 62.56 (t, $J = 3.2$ Hz), 24.57 (d, $J = 1.6$ Hz), 23.44 (d, $J = 2.3$ Hz), 16.38 (t, $J = 3.2$ Hz). ^{19}F NMR (471 MHz, Chloroform-d) δ -130.34 (d, $J = 5.5$ Hz). ^{31}P NMR (202 MHz, Chloroform-d) δ 22.81 (d, $J = 6.0$ Hz). High resolution ESI (m/z): [M•H]$^{-}$ calculated for: $C_{16}H_{24}F_2N_2O_6P_2S$: 471.0726, found: 471.0709.

- **2,5-dihydroxyterephthalaldehyde (89).**
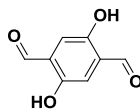
Compound **89** was prepared according to literature.[23]

- **2,5-bis((6-bromohexyl)oxy)terephthalaldehyde (90).**
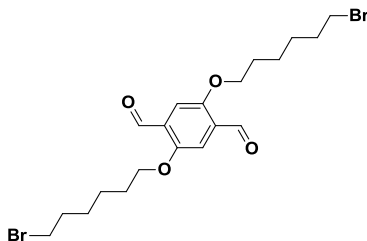
A dry 2-neck, 250 mL roundbottom flask equipped with a magnetic stir bar, inlet adapter, condenser and septum was flushed with nitrogen and **89** (1.6 g, 10 mmol) and potassium

carbonate (5.3 g, 39 mmol) were added followed by acetonitrile (anhydrous, 80 mL) and 1,6-dibromohexane (8.9 mL, 58 mmol). The mixture was degassed with nitrogen and heated to reflux while stirring for 14 hours. Initially the reaction becomes dark red (formation of phenoxide anions), but turns bright yellow over time. The reaction mixture was cooled to room temperature, concentrated under reduced pressure, dissolved in dichloromethane, washed with aqueous sodium carbonate then water. The organic phase was dried with anhydrous magnesium sulfate, filtered and concentrated. The crude product was subjected to silica gel column chromatography eluting with dichlromethane:hexanes (1:1). After concentration under reduced pressure the product **90** was obtained as a bright yellow crystalline solid (3.28 g, 69%). ^{1}H NMR (500 MHz, Chloroform-*d*) δ 10.50 (s, 2H), 7.42 (s, 2H), 4.09 (t, *J* = 6.4 Hz, 4H), 3.42 (t, *J* = 6.7 Hz, 4H), 1.95 − 1.78 (m, 8H), 1.58 − 1.46 (m, *J* = 4.2 Hz, 8H). ^{13}C NMR (126 MHz, Chloroform-*d*) δ 189.43, 155.22, 129.28, 111.67, 77.16, 69.02, 33.88, 32.69, 29.01, 27.96, 25.38.

- **2,5-bis((6-(dimethylamino)hexyl)oxy)terephthalaldehyde (91).**
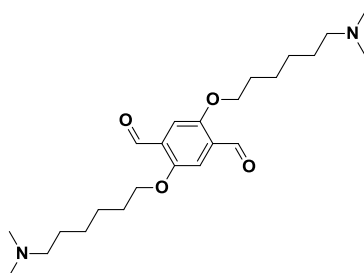
A dry, 250 mL pressure flask equipped with a magnetic stir bar and Teflon screw cap with a rubber *O*-ring was flushed with nitrogen and **90** (3.2 g, 7 mmol) was added, followed by dimethylamine (2 M solution in THF, 65 mL, 130 mmol). The Teflon cap was closed tightly and the reaction mixture was heated to 60°C, while stirring, for 5

hours. Shortly after heating the reaction turns from yellow to almost colorless and a white precipitate is formed. The salt is likely dimethylammonium bromide and the change in color is thought to arise from aminal formation, which may occur if dimethylamine reacts with benzaldehyde, reducing conjugation. After 5 hours, the reaction mixture is allowed to cool and a couple milliliters of aqueous 1 M hydrochloric acid is added while stirring. The solution quickly changes back to its original yellow color, indicating that conjugation through the aldehyde was restored. The reaction mixture was neutralized with aqueous sodium carbonate, extracted with dichloromethane and the combined organic extracts were washed with brine, dried with anhydrous magnesium sulfate, filtered and concentrated under reduced pressure to obtain the product **91** as a bright yellow solid (2.4 g, 87%). ^{1}H NMR (500 MHz, Chloroform-*d*) δ 10.51 (s, 2H), 7.42 (s, 2H), 4.08 (t, *J* = 6.4 Hz, 4H), 2.28 (t, *J* = 7.5 Hz, 4H), 2.24 (s, 12H), 1.84 (p, *J* = 6.7 Hz, 4H), 1.50 (h, *J* = 7.0 Hz, 8H), 1.43 − 1.34 (m, 4H). ^{13}C NMR (126 MHz, Chloroform-*d*) δ 189.52, 155.33, 129.39, 111.76, 77.16, 69.26, 59.81, 45.57, 29.16, 27.67, 27.28, 26.14.

- **3,3'-(((((2,5-Diformyl-1,4-phenylene)bis(oxy))bis(hexane-6,1-diyl))bis(dimethylammonionediyl)) bis(propane-1-sulfonate) (92).**
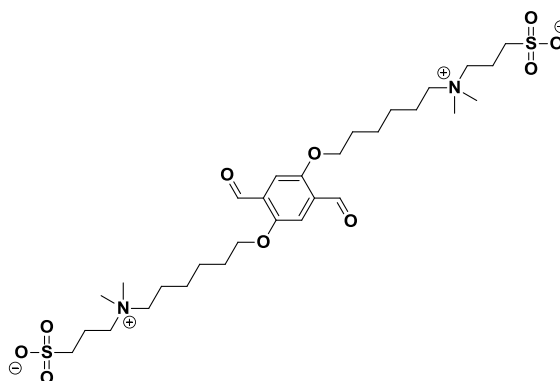
A dry 2-neck, 500 mL roundbottom flask equipped with a magnetic stir bar, inlet adapter, condenser and septum was flushed with nitrogen and **91** (2.4 g, 6 mmol), 1,3-propane

sultone (5.5 g, 45 mmol) and anhydrous acetonitrile (200 mL) were added. The mixture was degassed with nitrogen, then heated to reflux while stirring for 14 hours. The reaction mixture was cooled to room temperature and the yellow precipitate was filtered and washed with acetonitrile, tetrahydrofuran and diethyl ether sequentially. After drying under reduced pressure the product **92** was isolated as a bright yellow solid (3.7 g, 98%). ^{1}H NMR (500 MHz, DMSO-d_6) δ 10.42 (s, 2H), 7.42 (s, 2H), 4.15 (t, J = 6.2 Hz, 4H), 3.43 – 3.35 (m, 4H), 3.28 – 3.22 (m, 12H), 2.99 (s, 4H), 2.45 (t, J = 6.9 Hz, 4H), 1.96 (p, J = 7.3, 6.8 Hz, 4H), 1.81 (p, J = 6.8 Hz, 4H), 1.70 (p, J = 7.7 Hz, 4H), 1.51 (p, J = 7.6 Hz, 4H), 1.35 (p, J = 7.6 Hz, 4H). ^{13}C NMR (126 MHz, DMSO-d_6) δ 189.07, 154.59, 128.93, 112.01, 68.80, 67.04, 62.84, 62.20, 50.06, 47.65, 39.52, 28.25, 25.49, 25.16, 25.01. High resolution ESI (m/z): [M•2Na]$^{2+}$ calculated for: $C_{30}H_{52}N_2O_{10}S_2$: 355.1424, found: 355.1425.

- **6,6'-((2,5-Diformyl-1,4-phenylene)bis(oxy))bis(N,N,N-trimethylhexan-1-aminium) bromide (93).**
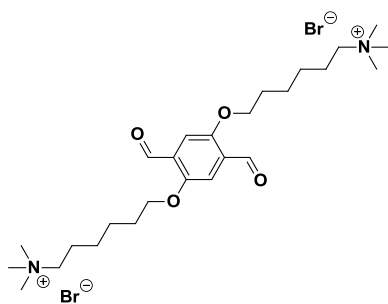
A dry, 250 mL pressure flask equipped with a magnetic stir bar and Teflon screw cap with a rubber *O*-ring was flushed with nitrogen and **90** (3.2 g, 7 mmol) was added and dissolved in anhydrous acetonitrile (65 mL). The flask and contents were cooled to -10°C with a salt / ice bath and trimethylamine (2.5 mL, 26 mmol) was quickly added followed by tightly capping the pressure flask. The reaction mixture was heated to 60°C, while

stirring, for 4 hours. The bright yellow precipitate that formed was filtered, washed with tetrahydrofuran and diethyl ether and concentrated under reduced pressure to obtain the product **93** (3.7 g, 96%) as a bright yellow solid. ^{1}H NMR (500 MHz, DMSO-d_6) δ 10.41 (s, 2H), 7.41 (s, 2H), 4.14 (t, J = 6.3 Hz, 4H), 3.36 – 3.30 (m, 4H), 3.08 (s, 18H), 1.80 (p, J = 6.4 Hz, 4H), 1.70 (dq, J = 12.0, 8.2, 6.2 Hz, 4H), 1.51 (p, J = 7.5 Hz, 4H), 1.34 (p, J = 7.5 Hz, 4H). ^{13}C NMR (126 MHz, DMSO-d_6) δ 189.04, 154.55, 128.88, 112.00, 68.79, 65.12, 52.09, 39.52, 28.23, 25.45, 24.99, 22.00. High resolution ESI (m/z): [M]$^{2+}$ calculated for: $C_{26}H_{46}N_2O_4$: 225.1723, found: 225.1724.

- **Sodium 4,4'-((2,5-diformyl-1,4-phenylene)bis(oxy))bis(butane-1-sulfonate) (94).**
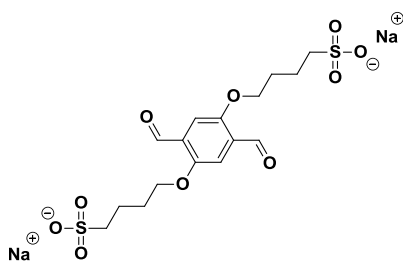
A dry 2-neck, 100 mL roundbottom flask equipped with a magnetic stir bar, inlet adapter, condenser and septum was flushed with nitrogen and **89** (1.0 g, 6 mmol) and sodium carbonate (2.55 g, 24 mmol) were added followed by acetonitrile (anhydrous, 50 mL) and 1,4-butane sultone (3.3 g, 24 mmol). The mixture was degassed with nitrogen and heated to 80°C while stirring for 18 hours. Initially the reaction becomes dark red (formation of phenoxide anions), but turns orange over time. The reaction mixture was cooled to room temperature, poured into tetrahydrofuran, filtered and the filtrate was washed with tetrahydrofuran. The yellow-orange solid was dried under reduced pressure then dissolved in water containing 0.1% trifluoroacetic acid (TFA) to give a concentration of

~100 mg/mL. Acetic acid was added dropwise to the aqueous mixture while stirring until the evolution of carbon dioxide ceased or when the pH was determined to be ~5 - 7. The mixture was subjected to reverse phase chromatography with C18-derivatized silica as the stationary phase and mixed water:acetonitrile (+ 0.1% TFA) as the mobile phase (see **Figure 5.2** for details). After removing acetonitrile and TFA under reduced pressure the water was removed by lyophelization, yielding the product **94** (2.1 g, 74%) as a yellow fluffy solid. ^{1}H NMR (500 MHz, DMSO-d_6) δ 10.40 (s, 2H), 7.42 (s, 2H), 4.13 (t, J = 6.3 Hz, 4H), 2.62 (t, J = 7.5 Hz, 4H), 1.84 (p, J = 6.6 Hz, 4H), 1.74 (p, J = 7.2, 6.6 Hz, 4H). ^{13}C NMR (126 MHz, DMSO-d_6) δ 189.01, 154.64, 128.98, 112.09, 68.76, 50.95, 39.52, 27.68, 21.57. High resolution ESI (m/z): $[M]^{2-}$ calculated for: $C_{16}H_{20}O_{10}S_2$: 218.0254, found: 218.0269.

- **General procedure for HWE polymerization to PAVs 95-103**

To a scintillation vial equipped with a magnetic stir-bar was added bis(methylphosphonate) A_2 monomer **81**, **84** or **88** (0.4 mmol) and functionalized terephthalaldehyde B_2 monomer **92**, **93** or **94** (0.4 mmol), followed by 0.1 mL of water and 0.5 mL of DMSO. The reaction mixture was rapidly stirred and sodium hydroxide (3.2 mmol) in 0.4 mL of water was quickly added. The color changes immediately from bright yellow to orange (PVF_4 derivatives) or blue/purple (PVBT and PVF_2BT derivatives). The vial was capped and the mixture was stirred at room temperature for 24 hours. The fluorinated polymers tended to precipitate out of the reaction, limiting the attainable molecular weight. After 24 hours the reaction mixtures were diluted with water and added to a dialysis membrane (molecular weight cutoff 3,500 Da). The zwitterionic and anionic polymers were dialyzed against pure water and the cationic polymers were

dialyzed against water alternating with water containing sodium chloride (0.5 M) in order to exchange out the bromide and phosphonate counterions for chloride (the dialysis was done in an alternating fashion because the PAV cationic polyelectrolytes precipitated in the bag when the salt solutions were being used, but readily redissolved after switching back to pure water; exemplifying the *polyelectrolyte effect*). The contents of the dialysis bags were lyophilized to obtain the polymers as brightly colored and fluffy solids, with yields typically ≥95%.

PVBT-SB, 95   **PVBT-TMA, 96**   **PVBT-SO$_3$, 97**
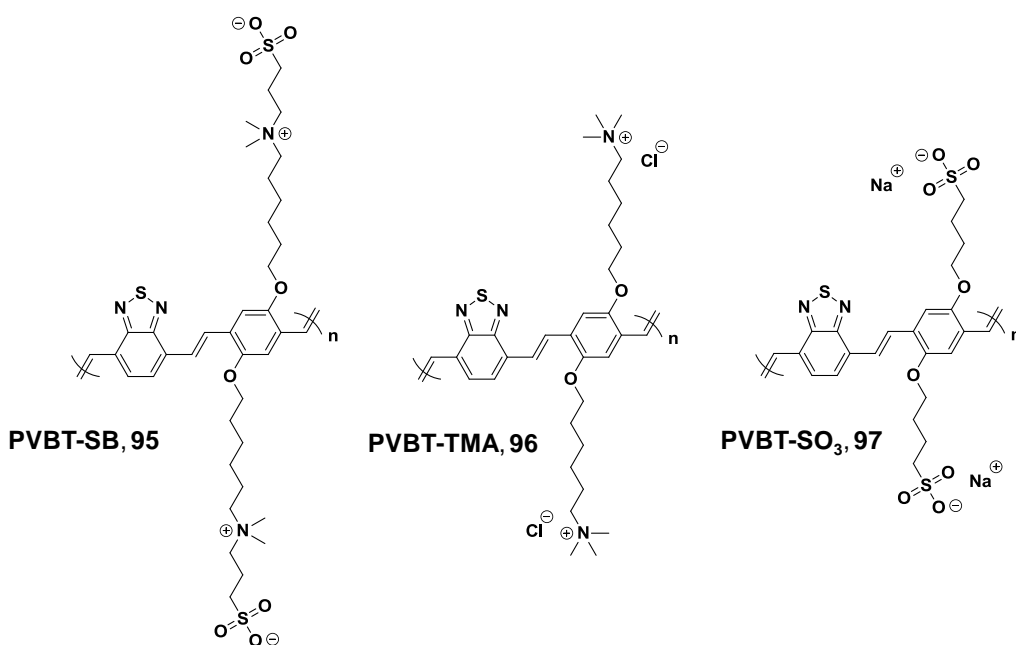
PVBT-SB was obtained as a dark blue solid. M_n = 22,800 Da, Đ = 2.0; ^{1}H NMR (500 MHz, TFE-d_3) δ 9.13 − 6.13 (br, 8H), 4.66 − 3.96 (br, 4H), 3.55 − 3.10 (br, 8H), 3.15 − 2.69 (br, 16H), 2.39 − 1.32 (br, 20H).

PVBT+ was obtained as a dark blue solid. M_n = 48,600 Da, Đ = 1.6 ^{1}H NMR (500 MHz, Deuterium Oxide) δ 8.16 − 6.43 (br, 8H), 4.03 − 2.84 (br, 26H), 2.42 − 1.12 (br, 16H).

PVBT- was obtained as a dark purple/blue solid. M_n = 50,100 Da, Đ = 1.5 ^{1}H NMR (500 MHz, Deuterium Oxide) δ 8.44 − 6.40 (br, 8H), 4.53 − 3.78 (br, 4H), 3.60 − 2.93 (br, 4H), 2.59 − 1.51 (br, 8H).

PVF$_4$-SB, 98   PVF$_4$-TMA, 99   PVF$_4$-SO$_3$, 100
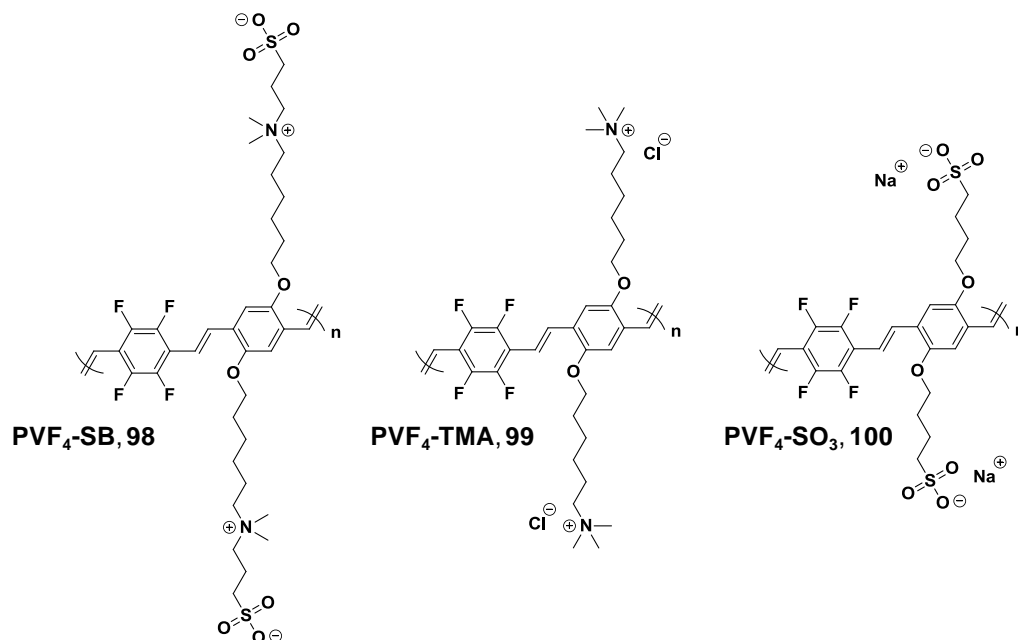
PVF$_4$-SB was obtained as a bright orange solid. M_n = 8,300 Da, Đ = 2.0 ^{1}H NMR (500 MHz, TFE-d_3) δ 8.02 − 6.04 (br, 6H), 4.38 − 3.92 (br, 4H), 3.52 − 3.36 (br, 4H), 3.35 − 3.16 (br, 4H) 3.14 − 2.96 (br, 12H), 2.95 − 2.81 (br, 4H), 2.29 − 2.11 (br, 4H), 2.10 − 1.77 (br, 8H), 1.76 − 1.63 (br, 4H), 1.62 − 1.45 (br, 4H).

PVF$_4$+ was obtained as a bright orange solid. M_n = 26,000 Da, Đ = 1.4 ^{1}H NMR (500 MHz, Deuterium Oxide) δ 7.76 − 6.38 (br, 6H), 4.55 − 3.80 (br, 4H), 3.76 − 2.84 (br, 22H), 2.27 − 1.05 (br, 16H).

PVF$_4$- was obtained as a bright orange solid. M_n = 42,600 Da, Đ = 1.3 ^{1}H NMR (500 MHz, Deuterium Oxide) δ 7.57 − 6.04 (br, 6H), 4.38 − 3.55 (br, 4H), 3.35 − 2.70 (br, 4H), 2.46 − 1.56 (br, 8H).

PVF₂BT-SB, 101 **PVF₂BT-TMA, 102** **PVF₂BT-SO₃, 103**
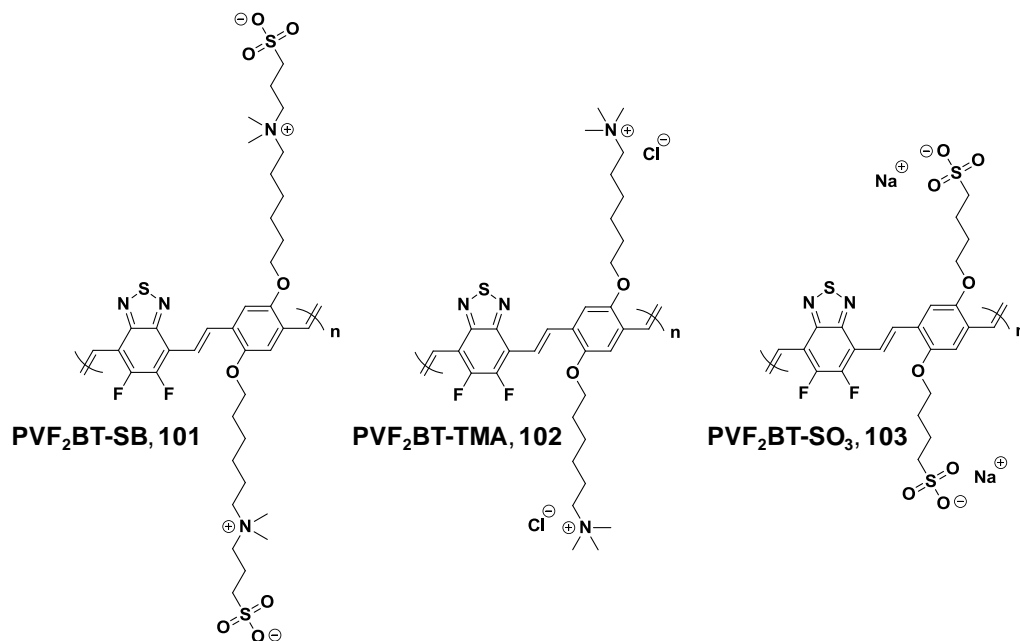
PVF₂BT-SB was obtained as a dark purple solid. M_n = 9,700 Da, Đ = 2.0 ^{1}H NMR (500 MHz, TFE-d_3) δ 8.82 − 6.41 (br, 6H), 4.60 − 3.95 (br, 4H), 3.53 − 3.17 (br, 8H), 3.13 − 2.65 (br, 16H), 2.52 − 1.27 (br, 20H).

PVF₂BT+ was obtained as a dark purple solid. M_n = 25,500 Da, Đ = 1.3 ^{1}H NMR (500 MHz, Deuterium Oxide) δ 7.65 − 5.89 (br, 6H), 4.48 − 2.62 (br, 26H), 2.20 − 0.85 (br, 16H).

PVF₂BT- was obtained as a dark purple solid. M_n = 43,300 Da, Đ = 1.3 ^{1}H NMR (500 MHz, Deuterium Oxide) δ 8.21 − 5.52 (br, 8H), 4.51 − 3.53 (br, 4H), 3.42 − 2.65 (br, 4H), 2.52 − 1.38 (br, 8H).

212

- **3-((6-(2-Formylphenoxy)hexyl)dimethylammonio)propane-1-sulfonate (104).**
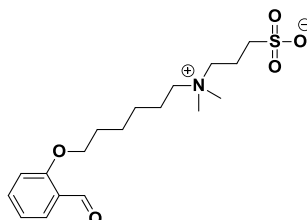
Starting from salicylaldehyde compound **104** was synthesized in an analogous procedure as that given for compound **92** (details above).

- Salicylaldehyde was reacted under basic conditions (potassium carbonate in refluxing acetonitrile) with 1,6-dibromohexane through an S_N2 substitution, yielding *2-((6-bromohexyl)oxy)benzaldehyde* (8.0 g, 86%) as a colorless clear oil. ^{1}H NMR (500 MHz, Chloroform-*d*) δ 10.50 (s, 1H), 7.82 (d, *J* = 7.8 Hz, 1H), 7.53 (t, *J* = 7.9 Hz, 1H), 7.01 (t, *J* = 7.5 Hz, 1H), 6.97 (d, *J* = 8.4 Hz, 1H), 4.08 (t, *J* = 6.3 Hz, 2H), 3.42 (t, *J* = 6.7 Hz, 2H), 1.94 − 1.82 (m, 4H), 1.58 − 1.47 (m, 4H). ^{13}C NMR (126 MHz, Chloroform-*d*) δ 189.95, 161.52, 136.07, 128.35, 124.89, 120.65, 112.51, 77.16, 68.29, 33.93, 32.69, 29.03, 27.95, 25.40.

- 2-((6-bromohexyl)oxy)benzaldehyde was reacted with excess dimethylamine in tetrahydrofuran in a pressure flask at 60°C, yielding *2-((6-(dimethylamino)hexyl)oxy)benzaldehyde* (1.3 g, 99%) as a light yellow oil. ^{1}H NMR (500 MHz, Chloroform-*d*) δ 10.51 (s, 1H), 7.82 (d, *J* = 7.8 Hz, 1H), 7.52 (t, *J* = 7.8 Hz, 1H), 6.99 (t, *J* = 7.5 Hz, 1H), 6.96 (d, *J* = 8.4 Hz, 1H), 4.07 (t, *J* = 6.3 Hz, 2H), 2.27 (t, *J* = 7.3 Hz, 2H), 2.22 (s, 6H), 1.85 (p, *J* = 6.7 Hz, 2H), 1.57 − 1.45 (m, 4H), 1.43 − 1.34 (m, 2H). ^{13}C NMR (126 MHz, Chloroform-*d*) δ 190.01, 161.65, 136.03, 128.34, 125.02, 120.60, 112.60, 77.16, 68.54, 59.85, 45.62, 29.19, 27.76, 27.30, 26.18.

- 2-((6-(dimethylamino)hexyl)oxy)benzaldehyde was reacted with 1,3-propane sultone in refluxing acetonitrile, yielding **104** (1.7 g, 94 %) as a white solid. ^{1}H NMR (500 MHz, DMSO-d_6) δ 10.39 (s, 1H), 7.68 (dd, J = 7.7, 1.4 Hz, 1H), 7.65 (t, J = 7.8 Hz, 1H), 7.23 (d, J = 8.4 Hz, 1H), 7.06 (t, J = 7.5 Hz, 1H), 4.13 (t, J = 6.3 Hz, 2H), 3.44 − 3.35 (m, 2H), 3.32 − 3.18 (m, 2H), 3.00 (s, 6H), 2.47 (t, J = 7.0 Hz, 2H), 2.01 − 1.91 (m, 2H), 1.81 (p, J = 6.7 Hz, 2H), 1.75 − 1.63 (m, 2H), 1.51 (p, J = 7.6 Hz, 2H), 1.34 (p, J = 7.7 Hz, 2H). ^{13}C NMR (126 MHz, DMSO-d_6) δ 189.22, 161.07, 136.54, 127.61, 124.18, 120.58, 113.54, 68.16, 62.83, 62.18, 50.04, 47.68, 39.52, 28.27, 25.52, 25.07, 21.61, 18.95. High resolution ESI (m/z): [M•Na]$^+$ calculated for: $C_{18}H_{29}NO_5S$: 394.1659, found: 394.1658.

- **6-(2-Formylphenoxy)-N,N,N-trimethylhexan-1-aminium bromide (105).**
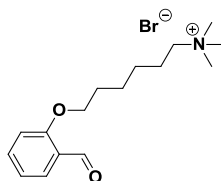
Starting from salicylaldehyde compound **105** was synthesized using an analogous procedure to that given for compound **93** (details above). 2-((6-bromohexyl)oxy)benzaldehyde was reacted with excess trimethylamine in acetonitrile in a pressure flask at 60°C, yielding **105** (2.2 g, 93%) as a white solid. ^{1}H NMR (500 MHz, DMSO-d_6) δ 10.39 (s, 1H), 7.68 (d, J = 7.7 Hz, 1H), 7.65 (t, J = 7.9 Hz, 1H), 7.23 (d, J = 8.4 Hz, 1H), 7.06 (t, J = 7.5 Hz, 1H), 4.14 (t, J = 6.3 Hz, 2H), 3.35 − 3.29 (m, 2H), 3.07 (s, 9H), 1.81 (p, J = 6.6 Hz, 2H), 1.76 − 1.66 (m, 2H), 1.51 (p, J = 7.5 Hz, 2H), 1.34 (p, J = 7.6 Hz, 2H). ^{13}C NMR (126 MHz, DMSO-d_6) δ 189.22, 161.06, 136.57, 127.62,

124.14, 120.59, 113.54, 68.15, 65.13, 52.10, 39.52, 28.27, 25.50, 25.11, 22.04. High resolution ESI (m/z): [M]$^+$ calculated for: $C_{16}H_{26}NO_2$: 264.1958, found: 264.1958.

- **Sodium 4-(2-formylphenoxy)butane-1-sulfonate (106).**
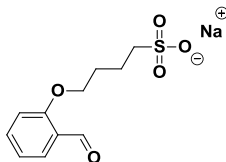
Starting from salicylaldehyde compound **106** was synthesized using an analogous procedure to that given fo compound **94** (details above). Salicylaldehyde was reacted under basic conditions (sodium carbonate in N,N-dimethylformamide at 80°C) with 1,4-butane sultone, and purified with reverse-phase chromatography on C18-derivativzed silica eluting with acetonitrile:water (containing 0.1% trifluoroacetic acid), yielding **106** (1.8 g, 78%) as a yellow oil (material is deliquescent) after lyophilization. ^{1}H NMR (500 MHz, DMSO-d_6) δ 10.39 (s, 1H), 7.68 (dd, J = 7.7, 1.8 Hz, 1H), 7.67 − 7.62 (m, 1H), 7.24 (d, J = 8.4 Hz, 1H), 7.06 (t, J = 7.5 Hz, 1H), 4.14 (t, J = 6.3 Hz, 2H), 2.60 (t, J = 7.7 Hz, 2H), 1.87 (p, J = 6.6 Hz, 2H), 1.77 (p, J = 7.2, 6.6 Hz, 2H). ^{13}C NMR (126 MHz, DMSO-d_6) δ 189.18, 161.14, 136.53, 127.54, 124.22, 120.57, 113.64, 68.12, 50.94, 39.52, 27.63, 21.60. High resolution ESI (m/z): [M]$^-$ calculated for: $C_{11}H_{13}O_5S$: 257.0489, found: 257.0491.

- **General procedure for HWE trimerization to AVs 107-115**

To a scintillation vial equipped with a magnetic stir-bar was added bis(methylphosphonate) A$_2$ monomer **81**, **84** or **88** (0.2 mmol) and functionalized benzaldheyde B terminators **104**, **105** or **106** (0.4 mmol), followed by 0.9 mL of water and 1 mL of DMSO. The reaction mixture was rapidly stirred and sodium hydroxide (0.8 mmol) in 0.1 mL of water was quickly added. The color changes immediately from

colorless to yellow (VF$_4$ derivatives) or orange (VBT and VF$_2$BT derivatives). The vial was capped and the mixture was stirred at room temperature for 24 hours. The fluorinated trimers tended to precipitate out of the reaction. After 24 hours the reaction mixtures were diluted with water and added to a dialysis membrane (molecular weight cutoff 1,000 Da). Only a small amount of color leached out of the bags, suggesting that the trimers, which have molecular weights < 1,000 Da, may aggregate in solution, significantly reducing their rate of diffusion through the dialysis membrane. The zwitterionic and anionic trimers were dialyzed against pure water and the cationic trimers were dialyzed against water alternating with water containing sodium chloride (0.5 M) in order to exchange out the bromide and phosphonate counterions for chloride. The contents of the dialysis bags were lyophilized to obtain the trimers as brightly colored and fluffy solids, with yields typically ≥95%.

VBT-SB, 107   **VBT-TMA, 108**   **VBT-SO$_3$, 109**
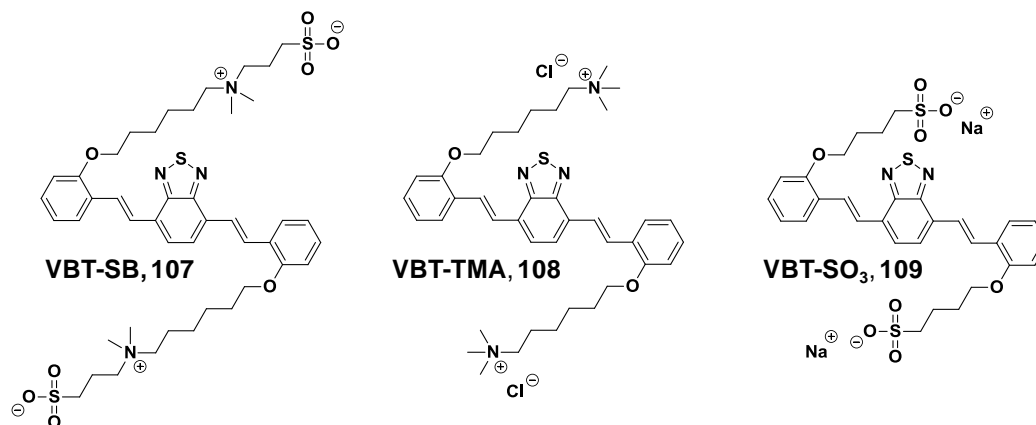
VBT-SB was obtained as a bright orange solid. ^{1}H NMR (500 MHz, DMSO-d_6) δ 8.39 (d, J = 16.6 Hz, 2H), 7.91 (s, 2H), 7.79 (d, J = 16.7 Hz, 2H), 7.76 (d, J = 8.6 Hz, 2H), 7.31 (t, J = 7.8 Hz, 2H), 7.09 (d, J = 8.3 Hz, 2H), 7.02 (t, J = 7.5 Hz, 2H), 4.11 (t, J = 6.4 Hz, 4H), 3.44 − 3.35 (m, 4H), 3.30 − 3.24 (m, 4H), 2.99 (s, 12H), 2.46 (t, J = 7.0 Hz, 4H), 1.97 (dt, J = 14.6, 7.2 Hz, 4H), 1.89 (dt, J = 13.6, 6.8 Hz, 4H), 1.77 − 1.69 (m,

4H), 1.65 (dt, J = 13.7, 7.2 Hz, 4H), 1.43 (p, J = 7.6 Hz, 4H). ^{13}C NMR (126 MHz, TFE-d_3) δ 158.76, 155.59, 131.38, 129.84, 128.73, 128.48, 126.29, 114.70, 70.28, 66.91, 64.94, 61.50, 52.03, 48.82, 30.60, 27.44, 27.08, 24.13, 20.16. ESI (m/z): [M•Na]$^+$ calculated for: $C_{44}H_{62}N_4O_8S_3$: 893.362, found: 893.379; [M•2Na]$^{2+}$ calculated: 458.176, found: 458.188.

VBT+ was obtained as a bright orange solid. ^{1}H NMR (500 MHz, DMSO-d_6) δ 8.38 (d, J = 16.6 Hz, 2H), 7.90 (s, 2H), 7.79 (d, J = 16.8 Hz, 2H), 7.76 (d, J = 8.4 Hz, 2H), 7.31 (t, J = 7.2 Hz, 2H), 7.09 (d, J = 8.3 Hz, 2H), 7.02 (t, J = 7.5 Hz, 2H), 4.12 (t, J = 6.3 Hz, 4H), 3.35 – 3.31 (m, 4H), 3.06 (s, 18H), 1.89 (p, J = 6.7 Hz, 4H), 1.73 (p, J = 8.4 Hz, 4H), 1.65 (p, J = 7.5 Hz, 4H), 1.42 (p, J = 7.6 Hz, 4H). ^{13}C NMR (126 MHz, DMSO-d_6) δ 156.44, 153.32, 129.60, 129.11, 128.16, 127.75, 126.80, 125.74, 124.84, 120.79, 112.62, 67.81, 65.18, 52.08, 39.52, 28.59, 25.66, 25.29, 22.18. ESI (m/z): [M]$^{2+}$ calculated for: $C_{40}H_{56}N_4O_2S$: 328.206, found: 328.234.

VBT- was obtained as a bright orange solid. ^{1}H NMR (500 MHz, DMSO-d_6) δ 8.37 (d, J = 12.7 Hz, 2H), 7.90 (s, 2H), 7.81 – 7.70 (m, 4H), 7.30 (t, J = 7.6 Hz, 2H), 7.09 (d, J = 8.3 Hz, 2H), 7.01 (t, J = 7.5 Hz, 2H), 4.09 (t, J = 6.0 Hz, 4H), 2.59 (t, J = 7.3 Hz, 4H), 1.97 – 1.83 (m, 8H). ^{13}C NMR (126 MHz, DMSO-d_6) δ 156.48, 153.20, 129.48, 128.98, 128.93, 127.85, 127.76, 127.65, 126.69, 126.64, 125.77, 124.77, 120.69, 112.60, 67.97, 51.20, 39.52, 28.19, 22.11. ESI (m/z): [M]$^{2-}$ calculated for: $C_{30}H_{30}N_2O_8S_3$: 321.059, found: 321.041.

VF₄-SB, 110   **VF₄-TMA, 111**   **VF₄-SO₃, 112**
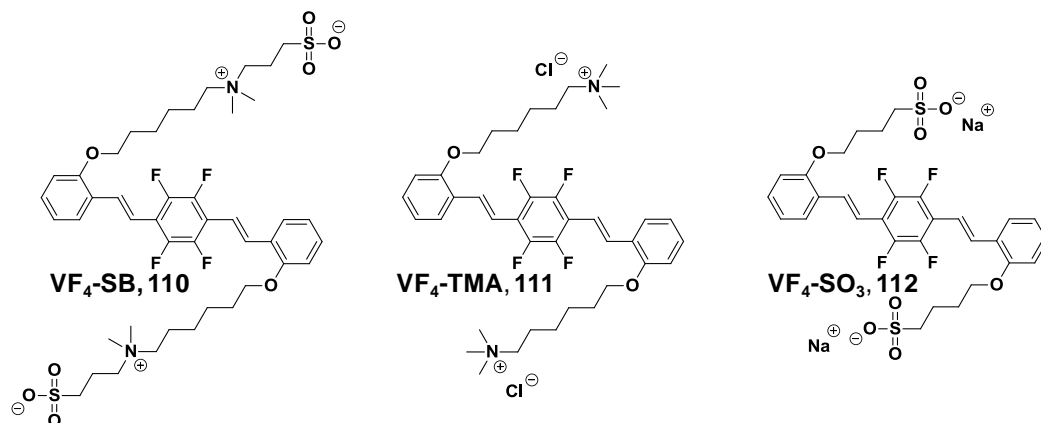
VF$_4$-SB was obtained as a bright yellow solid. ^{1}H NMR (500 MHz, DMSO-d_6) δ 7.75 (d, J = 16.9 Hz, 2H), 7.71 (d, J = 7.7 Hz, 2H), 7.35 (t, J = 8.2 Hz, 2H), 7.25 (d, J = 16.9 Hz, 2H), 7.10 (d, J = 8.3 Hz, 2H), 7.01 (t, J = 7.5 Hz, 2H), 4.08 (t, J = 6.4 Hz, 4H), 3.44 − 3.36 (m, 4H), 3.30 − 3.21 (m, 4H), 3.00 (s, 12H), 2.46 (t, J = 7.0 Hz, 4H), 2.04 − 1.90 (m, 4H), 1.83 (p, J = 6.7 Hz, 4H), 1.71 (p, J = 7.8 Hz, 4H), 1.55 (p, J = 7.4 Hz, 4H), 1.38 (p, J = 7.7 Hz, 4H). ^{13}C NMR (126 MHz, TFE-d_3) δ 158.99 , 148.10 − 145.43 (m), 134.12 , 131.98 , 128.92 , 127.64 , 122.80 , 117.47 − 117.02 (m), 115.83 , 114.42 , 70.06 , 67.04 , 65.05 , 52.12 , 48.87 , 30.59 , 27.47 , 27.29 , 24.21 , 20.23. ESI (m/z): [M•Na]$^+$ calculated for: C$_{44}$H$_{60}$F$_4$N$_2$O$_8$S$_2$: 907.362, found: 907.382; [M•2Na]$^{2+}$ calculated: 465.176, found: 465.192.

VF$_4$+ was obtained as a bright yellow solid. ^{1}H NMR (500 MHz, DMSO-d_6) δ 7.75 (d, J = 16.9 Hz, 2H), 7.70 (d, J = 7.5 Hz, 2H), 7.35 (t, J = 8.3 Hz, 2H), 7.24 (d, J = 16.9 Hz, 2H), 7.10 (d, J = 8.4 Hz, 2H), 7.01 (t, J = 7.5 Hz, 2H), 4.08 (t, J = 6.2 Hz, 4H), 3.35 − 3.30 (m, 4H), 3.07 (s, 18H), 1.83 (p, J = 6.7 Hz, 4H), 1.72 (p, J = 8.2 Hz, 4H), 1.55 (p, J = 7.5 Hz, 4H), 1.37 (p, J = 7.7 Hz, 4H). ^{13}C NMR (126 MHz, DMSO-d_6) δ 156.56 , 145.54 − 142.69 (m), 132.30 , 130.62 , 127.44 , 124.45 , 120.84 , 115.13 − 114.83 (m),

113.82 , 112.60 , 67.77 , 65.16 , 52.06 , 28.44 , 25.47 , 25.13 , 22.06. ESI (m/z): $[M]^{2+}$ calculated for: $C_{40}H_{54}F_4N_2O_2$: 335.206, found: 335.231.

VF4- was obtained as a bright yellow solid. ^{1}H NMR (500 MHz, DMSO-d_6) δ 7.74 (d, J = 12.8 Hz, 2H), 7.70 (d, J = 7.8 Hz, 2H), 7.33 (t, J = 7.8 Hz, 2H), 7.23 (d, J = 16.9 Hz, 2H), 7.09 (d, J = 8.3 Hz, 2H), 6.99 (t, J = 7.5 Hz, 2H), 4.06 (t, J = 6.6 Hz, 4H), 2.54 − 2.50 (m, 4H), 1.88 (p, J = 7.0 Hz, 4H), 1.76 (p, J = 7.3, 6.9 Hz, 4H). ^{13}C NMR (126 MHz, DMSO-d_6) δ 156.77 , 151.28 − 148.37 (m), 132.27 , 130.27 , 127.13 , 125.26 , 120.76 , 116.65 − 115.99 (m), 114.63 , 112.62 , 67.95 , 51.12 , 28.17 , 21.98. ESI (m/z): $[M]^{2-}$ calculated for: $C_{30}H_{28}F_4O_8S_2$: 328.059, found: 328.052.
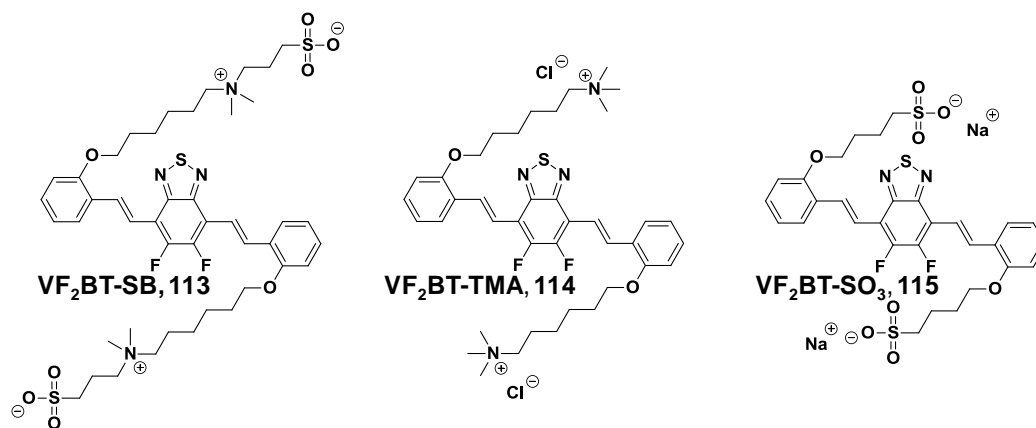
VF2BT-SB was obtained as a bright orange solid. ^{1}H NMR (500 MHz, DMSO-d_6) δ 8.61 (d, J = 16.7 Hz, 2H), 7.75 (d, J = 6.9 Hz, 2H), 7.72 (d, J = 16.7 Hz, 2H), 7.35 (t, J = 7.7 Hz, 2H), 7.12 (d, J = 8.3 Hz, 2H), 7.03 (t, J = 7.5 Hz, 2H), 4.12 (t, J = 6.3 Hz, 4H), 3.44 − 3.37 (m, 4H), 3.32 − 3.24 (m, 4H), 3.00 (s, 12H), 2.46 (t, J = 7.0 Hz, 4H), 2.01 − 1.93 (m, 4H), 1.88 (p, J = 6.6 Hz, 4H), 1.73 (td, J = 11.4, 9.9, 5.8 Hz, 4H), 1.64 (p, J = 7.6 Hz, 4H), 1.42 (p, J = 7.6 Hz, 4H). ^{13}C NMR (126 MHz, TFE-d_3) δ 159.07 , 153.66 − 151.06 (m), 134.32 , 131.75 , 128.99 , 127.92 , 122.70 , 118.21 , 116.81 , 114.37 , 69.97 , 66.90 , 64.98 , 52.01 , 48.78 , 30.61 , 27.45 , 27.11 , 24.11 , 20.13. ESI (m/z): $[M•Na]^+$

calculated for: $C_{44}H_{60}F_2N_4O_8S_3$: 929.343, found: 929.361; $[M\cdot2Na]^{2+}$ calculated: 476.166, found: 476.179.

VF$_2$BT+ was obtained as a bright orange solid. ^{1}H NMR (500 MHz, DMSO-d_6) δ 8.58 (d, J = 16.7 Hz, 2H), 7.73 (d, J = 8.0 Hz, 2H), 7.70 (d, J = 16.8 Hz, 2H), 7.36 (t, J = 7.4 Hz, 2H), 7.11 (d, J = 8.3 Hz, 2H), 7.03 (t, J = 7.5 Hz, 2H), 4.12 (t, J = 6.3 Hz, 4H), 3.34 − 3.31 (m, 4H), 3.07 (s, 18H), 1.88 (p, J = 6.3 Hz, 4H), 1.73 (p, J = 8.3 Hz, 4H), 1.64 (p, J = 7.6 Hz, 4H), 1.41 (p, J = 7.7 Hz, 4H). ^{13}C NMR (126 MHz, DMSO-d_6) δ 156.75 , 151.37 − 148.55 (m), 132.55 , 130.40 , 127.32 , 125.14 , 120.89 , 116.56 , 114.76 − 114.52 (m), 112.66 , 67.81 , 65.17 , 52.08 , 28.59 , 25.64 , 25.27 , 22.17. ESI (m/z): $[M]^{2+}$ calculated for: $C_{40}H_{54}F_2N_4O_2S$: 346.196, found: 346.223.

VF$_2$BT- was obtained as a bright orange solid. ^{1}H NMR (500 MHz, DMSO-d_6) δ 8.62 (d, J = 13.1 Hz, 2H), 7.75 (d, J = 7.7 Hz, 2H), 7.68 (d, J = 16.7 Hz, 2H), 7.34 (t, J = 7.7 Hz, 2H), 7.11 (d, J = 8.3 Hz, 2H), 7.02 (t, J = 7.5 Hz, 2H), 4.09 (t, J = 6.2 Hz, 4H), 2.57 (t, J = 7.4 Hz, 4H), 1.97 − 1.83 (m, 8H). ^{13}C NMR (126 MHz, DMSO-d_6) δ 156.77 , 151.28 − 148.37 (m), 132.27 , 130.27 , 127.13 , 125.26 , 120.76 , 116.49 , 114.81 − 114.35 (m), 112.62 , 67.95 , 51.12 , 28.17 , 21.98. ESI (m/z): $[M]^{2-}$ calculated for: $C_{30}H_{28}F_2N_2O_8S_3$: 339.049, found: 339.046.

- **Sample preparation for solid-state UV-Vis absorption measurements.**

The glass slides were cleaned with detergent (1x), water (2x), acetone (1x) and isopropanol (1x) subsequently. The slides were dried in an oven at 150 ˚C for 12 hours, cooled to room temperature, treated with UV-ozone for 20 minutes and the polymers were spun-cast from trifluoroethanol (10 mg / mL) at 1500 rpm over 60 seconds.

- **Sample preparation and UPS measurements.**

Silicon wafers (n-doped with arsenic) were cut (~7 x 7 mm) and cleaned with detergent, water, acetone and isopropanol. The substrates were dried in an oven at 150 ˚C for 12 hours, cooled to room temperature, treated with UV-ozone for 20 minutes, transferred to a nitrogen filled glove-box, and placed in a vacuum deposition chamber (2 x 10^{-6} mbar). A ~50 nm thick layer of silver or gold was deposited. Immediately after deposition the substrates were removed and the polymers spun from a 0.6 mg / mL solution of trifluoroethanol at 2000 rpm for 60 seconds. The samples were brought into the UPS analysis chamber, under ultrahigh vacuum (1 x 10^{-9} mbar). The ionization potentials were determined through two steps: first the intersection of a line tangent to the low kinetic energy onset of the spectrum with the abscissa axis was ascertained and subtracted from 21.2 eV (the UV-source energy), followed by the addition of the intersection of high kinetic energy onset with the abscissa axis. All measurements were done at a -3 V sample bias, allowing for facile collection of low kinetic energy electrons. The resolution of the UPS instrument was 0.1 eV as determined from the width of the Fermi level of silver. All samples were <10 nm thick as determined by the surface profiler (KLA Tencor, model Alpha-Step IQ).

- **Solar cell device fabrication and testing.**

Method A. The ITO-coated glass substrates (10 Ω/□, from Thin Film Devices, Inc.) were cleaned in ultrasonic bath using detergent, deionized water (twice), acetone and isopropanol for 10 minutes/step, then baked overnight and subjected to UV/Ozone for 15 minutes prior to film deposition step. PEDOT:PSS (H.C. Starck, I 4083) was spin-coated at 2000 rpm for 2 minutes and annealed at 150 °C for 15 minutes, and transferred to the

glove box (N_2 atmosphere, < 1 ppm O_2, <1 ppm H_2O) for device fabrication. A solution of PTB7 and PCBM (1:1.5 weight ratio) in 1,2-dichlorobenzene:1,8-diiodoocatane (2.5 v% DIO) was stirred at 80 °C for ~1 day. The thickness of the active layer film after spin-coating was ~100-120 nm (determined by profilometry). DIO was removed under vacuum, and the devices were placed in a glove box for spin-coating of CPZs and thermal evaporation of LiF (1.5 nm) and Al (100 nm) through a shadow mask which defined the active device area of 0.06 cm^2. Film thickness was measured by KLA-TENCOR Alpha-Step IQ Surface Profiler. Current-voltage (I-V) characteristics were measured using a Keithley 2400 source-meter under simulated AM1.5G irradiation using a 300 W Xe lamp solar simulator (Newport 91160). The light intensity was adjusted with an NREL-calibrated Si reference solar cell and KG-5 filter. An aperture that exactly matched the device geometry defined the illuminated area. Device metrics are given as averages over 18 devices with error bars representing ± 1 standard deviation.

Method B. Photovoltatic devices were fabricated by spin coating poly(ethylenedioxythiophene): poly(styrene sulfonate) (PEDOT:PSS) (H.C. Starck, I 4083) onto pre-cleaned glass substrates (14.7 x 14.7 mm), patterned with indium tin oxide (ITO) (10 Ω/□, from Thin Film Devices, Inc.) to cover half of the substrate area. Then, PEDOT:PSS was baked at 150 °C for 30 minutes in air, and transferred to the glove box (N_2 atmosphere, < 1 ppm O_2, <1 ppm H_2O) for deposition of the photoactive layer, interlayer and top electrode. A mixture of PBDTT-TT and PC$_{71}$BM (1:1.8 weight ratio) in chlorobenzene:1,8-diiodoocatane (3.2 v% DIO) was stirred at 55 °C for ~1 day. The photoactive layers were deposited by spin-coating the solution onto the PEDOT:PSS layer. The thickness of the active layer film was ~100 nm (determined by profilometry).

DIO was removed under vacuum, followed by spin-coating of CPZs. Thermal evaporation of metal electrodes through a shadow mask created four devices on each substrate. Performance characteristics of those devices were averaged. The overlap between the bottom ITO electrode and the top metal electrode defined the maximum available device area of 0.06 cm^2.

- **Polymerization kinetics study of PTBTSB-2 in IL9 (Figure 2.7).**

Aliquats from three separate reactions were removed at the denoted time points and the polymer was precipitated into MeOH and washed with MeOH 2x to remove residual ionic liquids and small molecular byproducts prior to running SEC in TFE to determine molecular weight. Averages of the three reactions are given with error bars representing ± 1 standard deviation.

- **Determination of film thickness.**

Film thickness was varied by using different concentrations of CPZ in TFE for spin coating, maintaining a constant spin-coating rate of 4000 rpm (*e.g.,* 0.5 mg/mL gave 2 nm films, 1 mg/mL gave 5 nm films, and 2 mg/mL gave 10 nm films). The average thickness was determined using a combination of profilometry and UV-Vis absorption. Pre-cleaned glass slides were treated with UV-ozone for 15 minutes prior to spin coating. First, a thick film of each CPZ was spun cast from TFE (20 mg/mL) at 2000 rpm. UV-Vis absorption spectra were measured, followed by film thickness using profilometry (each absorption and thickness measurement was performed on three different positions on each slide to obtain an average). Extinction coefficients (ε) were determined at the wavelength of maximum absorption (low energy band for alternating polymers) using Beer's law ($\varepsilon = \frac{A}{l}$), where A is the absorption intensity and l is the thickness (**Table 6.1**).

Table 6.1 Thickness and attenuation coefficients of thiophene based-CPZs. Reproduced from Liu, F. et. al. *Adv. Mater.* **2013**, p.6868.

CPZ	Thickness (nm)	A_{max} (nm)	ε (cm^{-1})
PTSB-1	115 ± 5	416	41,000
PTSB-2	60 ± 10	493	36,000
PTBTSB-1	93 ± 6	470	50,000
PTBTSB-2	90 ± 10	547	39,000

To determine the approximate film thickness of the CPZ interlayers, first a thin film of the active layer was cast onto glass using a dilute active layer solution (2 mg/mL PTB7:PC$_{71}$BM in DCB:DIO, 2.5 v% DIO) and spin rate of 1000 rpm. The films were dried under vacuum for 14 hours. 1 mg/mL solutions of the CPZs (as well as a 2 mg/mL and 4 mg/mL sample of **PTBTSB-2**) were cast from TFE at 4000 rpm on top of the active layer. A glass slide containing only the active layer was used as the background reference. Three positions on all films were measured, taking an average of absorption (**Figure 6.1**). Using the extinction coefficients and absorption intensity, Beer's law was used to calculate film thickness of the CPZ layer. A linear relationship between film thickness and concentration was shown for **PTBTSB-2**, which was extrapolated to give the film thickness values.
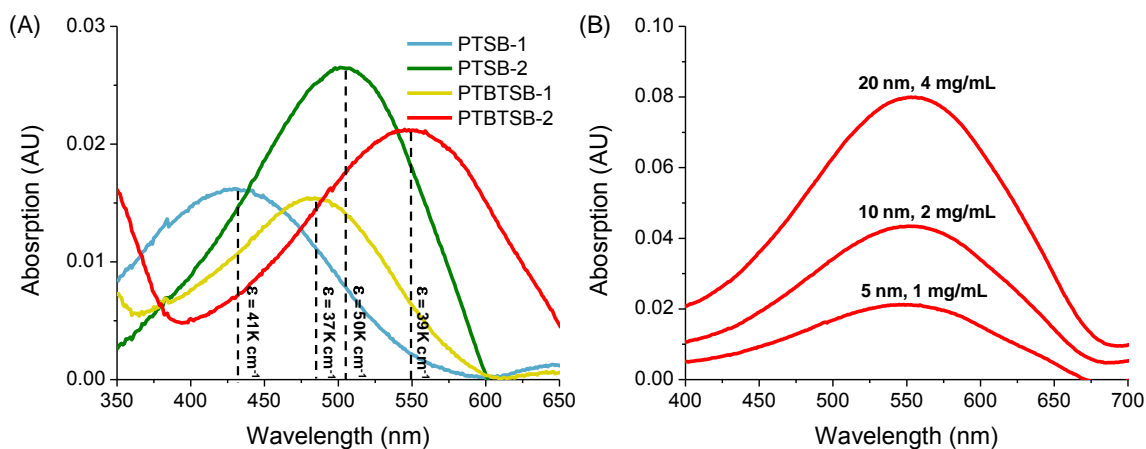
Figure 6.1 UV-Vis absorption spectra of 5 nm CPZs on thin active layer (A) and **PTBTSB-2** absorption on active layer with variable casting concentration (B). Reproduced from Liu, F. et. al. *Adv. Mater.* **2013**, p.6868.

- **Impedance spectroscopy to determine dielectric constant (ε).**

Devices were fabricated with architectures of ITO/PTB7 or CPZ/Ca/Al, where PTB7 is a control (ε = 3.5). From capacitance the ε values were calculated using the following equation $\varepsilon = Cd/\varepsilon_0 A$, where C is capacitance, d is thickness (determined using profilometry, ranging from 400 – 100 nm), ε_0 is vacuum permittivity (8.85 x 10^{-14} F/cm) and A is the area (0.06 cm^2). All fits to the equivalent circuit model had < 2 % error. Average dielectric constant values for CPZs measured were equivalent at ~5.

- **General procedure for HWE kinetics experiments**

To a scintillation vial equipped with a magnetic stir-bar was added bisphosphonate monomer **81**, **84** or **88** (0.05 mmol) and functionalized benzaldheyde **104**, **105** or **106** (0.1 mmol), followed by 0.75 mL of deuterium oxide. Sodium hydroxide (0.4 mmol) in 0.2 mL of D$_2$O was quickly added followed by transferring the homogenous contents of the vial to an NMR tube. A one scan ^{31}P-NMR spectrum was recorded at pre-designated intervals for a total of 16-32 FID slices. Each slice was Fourier transformed and peaks integrated to determine percent conversion.

- **Stern-Volmer photoluminescence quenching experiments.**

Stern-Volmer photoluminescence quenching experiments were carried out using methyl viologen dichloride (MV^{2+}) as a cationic quencher. Polymer solutions in HPLC grade water were prepared (a.u. $\approx$ 0.2 at λ_{max}). To a known volume of a polymer solution, aqueous solution of MV^{2+} was added in portions, and the photoluminescence spectra were recorded simultaneously. Stern-Volmer quenching constant was then calculated using the equation 6.1 at low quencher concentrations (linear regime):

$$I_o/I = 1 + K_{SV}[Q] \hspace{4cm} 6.1$$

Where I_o and I are photoluminescence intensities observed in the absence and presence

of the quencher, respectively, $[Q]$ is the quencher concentration, and K_{SV} is the Stern-

Volmer quenching constant.

6.4 References

1. Watanabe, Y. Mihara, T.; Koide, N. *Macromol. Chem. Phys.* **1998**, *199*, 977-983.

2. Lee, E.; Hammer, B.; Kim, J.-K.; Page, Z.; Emrick, T.; Hayward, R.C. *J. Am. Chem. Soc.* **2011**, *133*, 10390-10393.

3. Stokes, K. K. Heuze, K.; McCullough, R. D. *Macromolecules.* **2003**, *36*, 7114-7118.

4. Zhang, M.; Tsao, H. N.; Pisula, W.; Yang, C.; Mishra, A. K.; Müllen, K. *J. Am. Chem. Soc.* **2007**, *129*, 3472-3473

5. Pilgram, K.; Zupan, M.; Skiles, R. *J. Heterocycl. Chem.* **1970**, *7*, 629-633.

6. Asinger,F.; Scheuffler,B. *J. fuer Praktische Chemie (Leipzig)*, **1960** , *10*, 265-289.

7. Stas, S.; Sergeyev, S.; Geerts, Y. *Tetrahedron* **2010**, *66*, 1837-1845.

8. Mei, J.; Graham, K. R.; Stalder, R.; Reynolds, J. R. *Org. Lett.* **2010**, *12*, 660-663.

9. Usta, H.; Lu, G.; Facchetti, A.; Marks, T. J. *J. Am. Chem. Soc.* **2006**, *128*, 9034-9035.

10. Lee, J. S.; Son, S. K.; Song, S.; Kim, H.; Lee, D. R.; Kim, K.; Ko, M. J.; Choi, D. H.; Kim, B.; Cho, J. H. *Chem. Mater.* **2012**, *24*, 1316-1323.

11. Lei, T.; Cao, Y.; Fan, Y.; Liu, C.-J.; Yuan, S.-C.; Pei, J. *J. Am. Chem. Soc.* **2011**, *133*, 6099-6101.

12. Guo, X.; Watson, M. D. *Org. Lett.* **2008**, *10*, 5333-5336.

13. Page, Z. A.; Duzhko, V. V.; Emrick, T. *Macromolecules* **2013**, *46*, 344-351.

14. Li, L.; Yuan, C.; Dai, L.; Thayumanavan, S. *Macromolecules* **2014**, *47* (17), 5869-5876.

15. Mitchell, R. H.; Iyer, V. S. *Synlett* **1989**, No. 1, 55-57.

16.   Michaelis, A.; Kaehne, R. *Berichte* **1898**, *31*, 1048.

17.   Arbuzov, A. E. *J. Russ. Phys. Chem. Soc.* **1906**, *38*, 687.

18.   Arbuzov, A. E. *Chem. Zentr.* **1906**, *II*, 1639.

19.   Zhou, H.; Yang, L.; Stuart, A. C.; Price, S. C.; Liu, S.; You, W. *Angew. Chem. Int. Ed.* **2011**, *50* (13), 2995-2998.

20.   Kularatne, R. S.; Taenzler, F. J.; Magurudeniya, H. D.; Du, J.; Murphy, J. W.; Sheina, E. E.; Gnade, B. E.; Biewer, M. C.; Stefan, M. C. *J. Mater. Chem. A* **2013**, *1* (48), 15535-15543.

21.   Schlosser, M.; Jenny, T.; Guggisberg, Y. *Synlett* **1990**, 704.

22.   Rodriguez, L.; Lu, N.; Yang, N.-L. *Synlett* **1990**, No. 4, 227-228.

23.   Hiremath, U. S. *Tetrahedron Lett.* **2013**, *54* (26), 3419-3423.

APPENDIX A

EXTENDED THIOPHENE-BASED CPZ LIBRARY

The library of thiophene-based conjugated polymer zwitterions (CPZs), discussed in chapter 2, was extended through the utility of post-polymerization modifications along with the use of a trithiophene-boronic ester monomer. The synthetic strategy followed is outlined in **Scheme A.1**.
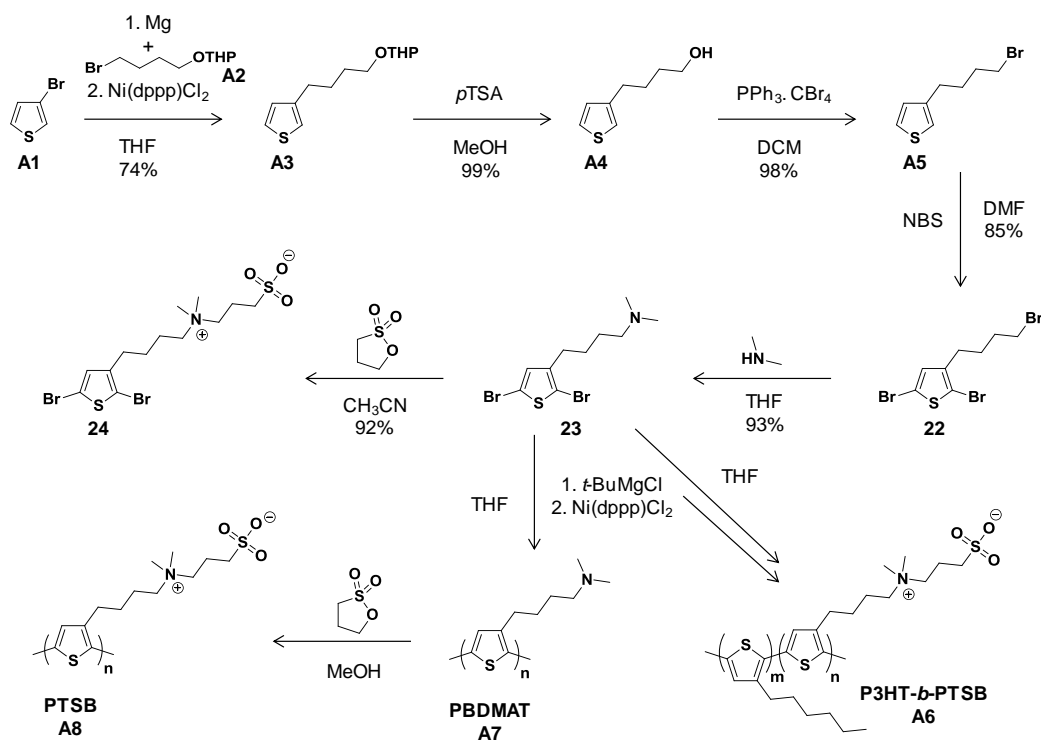
Scheme A.1 Synthesis of thiophene-based zwitterionic polymers and diblock copolymers with poly(3-hexylthiophene) (P3HT).

Scheme A.1 starts with a Kumada coupling between 3-bromothiophene (**A1**) and the Grignard of THP-protected 4-bromobutan-1-ol, (4-(((tetrahydro-2H-pyran-2-yl)oxy)butyl)magnesium bromide (**A2**), to yield 2-(4-(thiophen-3-yl)butoxy)tetrahydro-2H-pyran (**A3**). Tetrahydropyranyl (THP) ether-deprotection was accomplished under acidic conditions yielding 4-(thiophen-3-yl)butan-1-ol (**A4**), followed by an Appel

reaction to convert the primary alcohol to a bromide using triphenylphosphine (PPH$_3$) and carbon tetrabromide (CBr$_4$). The resulting 3-(4-bromobutyl)thiophene (**A5**) was brominated with *N*-bromosuccinimide (NBS) to give **22**, followed by dimethylamine substitution to **23**. Compound **23** was used for ring-opening of 1,3-propane sultone to give monomer **24** as well as a monomer for both homopolymerization and copolymerization with 2,5-dibromo-3-hexylthiophene, yielding poly(butyl dimethylamino thiophene) **PBDMAT** (**A7**) and poly(3-hexylthiophene)-*block*-poly(butyl dimethylamino thiophene) P3HT-*b*-**PBDMAT**. Subsequent post-polymerization ring-opening of 1,3-propane sultone gave the corresponding zwitterrionic polymers poly(thiophene sulfobetaine) (**PTSB**) (**A8**) and P3HT-*b*-**PTSB** (**A6**). **PTSB** represents a CPZ that has no thiophene spacers, since each thiophene in the polymer backbone contains a sulfobetaine (SB) pendant group.

The number of thiophene spacers was varied to learn about the effect this would have on the optoelectronic properties of the resultant CPZs (**Scheme A.2**). The polymerizations followed Suzuki-Miyaura (SM) polymerization conditions as discussed in chapter 3. Monomer **24** was used to generate polymers with one thiophene spacer (**PTTSB** = **PTSB-2**, **14**), two thiophene spacers (**PTTTSB** = **PT$_3$SB**, **68**) and three thiophene spacers (**PTTTTSB**, **A10**) by coupling with thiophene-boronic ester (**25**), bithiophene-boronic ester (**63**) and trithiophene-boronic (**A9**) ester respectively.
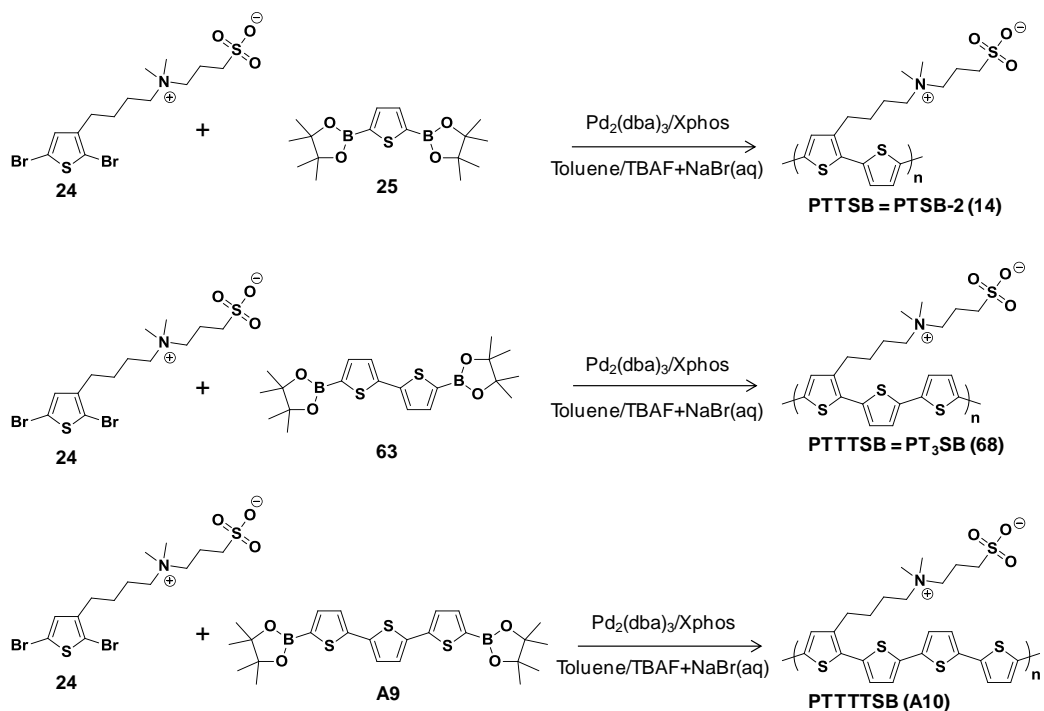
Scheme A.2 Synthesis of thiophene-based CPZs with varying numbers of alternating thiophenes (spacers).

Solution and solid-state UV-Vis absorption measurements were done on the five polymers (**PBDMAT**, **PTSB**, **PTTSB**, **PTTTSB** and **PTTTTSB**) (**Figure A.1**). In TFE solution a bathochromic shift in absorption was noted as the number of thiophene spacer units was increased, with the appearance of a second peak for the case of **PTTTTSB** that may be due to a reduced solubility causing aggregate induced π-π stacking. A similar bathochromic shift is also observed for the solid-state absorption measurements, along with a substantial increase in attenuation coefficient from approximately 40,000 cm^{-1} for **PTSB** to > 100,000 cm^{-1} for **PTTTTSB**, due to the increased concentration of thiophene chromophore relative to pendent groups (aliphatic amine or SB) for **PTTTTSB** compared to **PTSB** (**Figure A.1**).
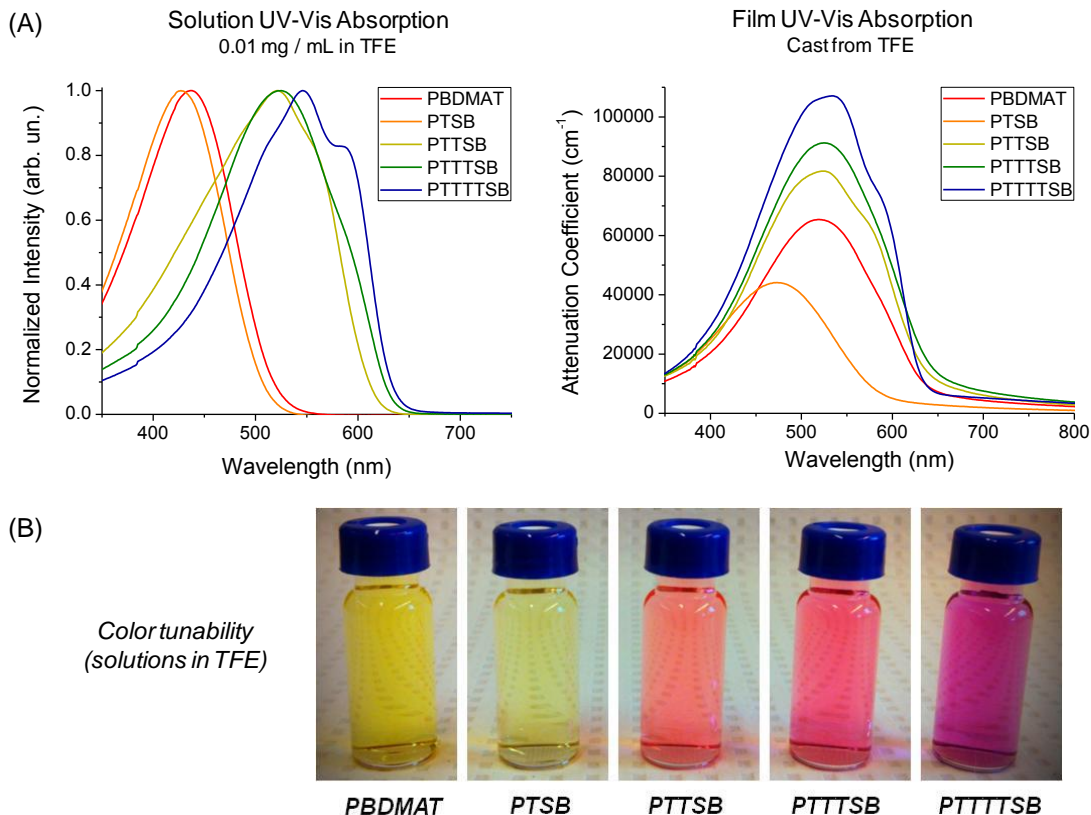
Figure A.1 Solution and solid state UV-Vis absorption of thiophene-based CPZs (A) and image of CPZs in TFE showing color tunability (B).

The energy gap (E_g) values for the five polymers were determined by taking the onset of absorption for the films and ionization potential (I_P) values were determined using ultraviolet photoelectron spectrosocopy (UPS) by taking the low binding energy onset (Table A.1). E_g values were around 2 eV and I_P values around 4.9 eV (with the exception of **PBDMAT** having an $I_P \approx 4.5$ eV, suggesting that it has a high propensity to oxidize), which is typical for poly(thiophenes). Additionally, interactions of the five polymers with Ag-surfaces were probed using UPS, specifically observing a shift in the secondary electron cutoff (E_{SEC}) energy in the high binding energy region. All of the polymers led to a negative interfacial dipole (Δ) values with Ag, thus reducing Ag's work function (Φ). The tertiary amine-functionalized polymer, **PBDMAT**, caused the largest

reduction (-1.2 eV), similar to what was observed for **C$_{60}$-N** (**72**) reducing metal Φ to a greater extent than the corresponding **C$_{60}$-SB** (**73**), as discussed in chapter 5.

Table A.1 Energy levels for extended thiophene-based CPZ library.

Polymer	E_g (eV)	I_P (eV)	E_A (ev)	Δ_{Ag} (eV)
PBDMAT	1.94	4.48	2.54	-1.20 ± 0.07
PTSB	2.09	5.06	2.97	-0.89 ± 0.07
PTTSB	1.94	4.97	3.03	-0.90 ± 0.07
PTTTSB	1.91	4.92	3.01	-0.90 ± 0.07
PTTTTSB	1.96	4.92	2.96	-0.95 ± 0.09

SYNTHESIS OF NOVEL DYADS

B.1 Introduction

Dyads are a unique class of organic semiconductors where an electron rich (donor) molecule is covalently bound to an electron deficient (acceptor) molecule. Dyads can provide helpful insight regarding charge action at donor acceptor interfaces. They also present a means to generate a one-component photoactive layer for organic solar cells, since dyads are comprised of both donor and acceptor groups. This chapter reflects on work done to synthesize novel dyads during the early stages of my dissertation research.

B.2 Oligothiophene-fullerene dyads

The synthesis of oligothiophene-fullerene dyads began with benzaldehyde functionalized thiophenes that were formed through a Williamson-ether substitution of 2,5-dibromo-3-bromomethylthiophene (**Scheme B.1**). Subsequently, the flanking substituted thiophenes were attached using Stille coupling, with palladium (II) acetate (Pd(OAc)$_2$) as the catalyst and lithium chloride (LiCl) in anhydrous dimethylformamide (DMF). The Prato reaction was used to covalently attach the terthiophenes to fullerene-C_{60}, which entails a 1,3-dipolar cycloaddition of an azomethine ylide (formed through the condensation of *N*-methylglycine with benzaldehyde making an immonium salt that decarboxylates) with fullerene to form a fulleropyrrolidine.
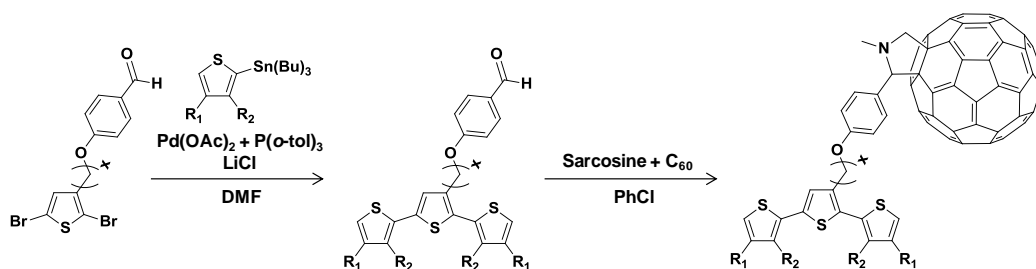
Scheme B.1 Representative synthesis of oligothiophene-fulleropyrrolidine dyads.

Using this methodology eight unique oligothiophene-fulleropyrrolidine dyads were synthesized; altering the covalent tether length binding the two moieties along with the solubilizing R_1 and R_2 side-chains (**Figure B.1**).
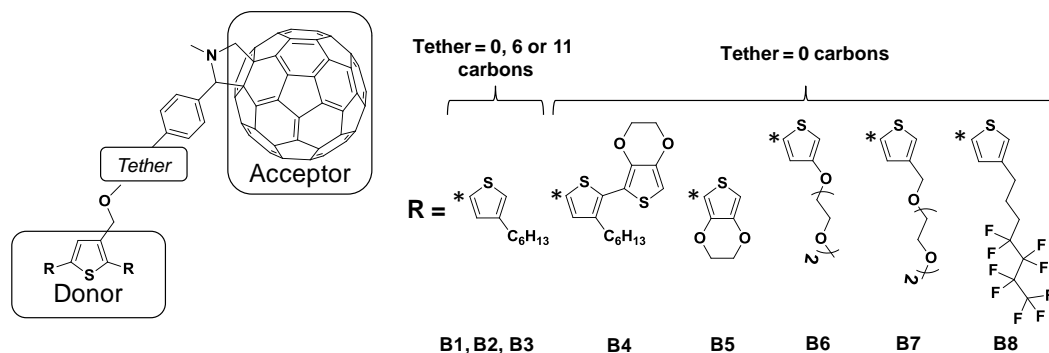
Figure B.1 Chemical composition of eight oligiothiophene-fulleropyrrolidine dyads **B1**-**B8**.

Compounds **B1**, **B2** and **B3** were synthesized by Stille coupling 2-(tributylstannyl)-4-hexylthiophene with a 2,5-dibromo-3-benzaldehyde thiophene derivative (**B13**, **B14** and **B15**), synthesized through a Williamson-ether method (**Scheme B.2**). The hydroxyl terminated hexyl and undecyl benzaldehyde precursors (**B11** and **B12** respectively) were synthesized by deprotonating 4-hydroxybenzaldehyde (**B10**) with sodium carbonate (Na_2CO_3) in a biphasic, water/chloroform (H_2O/CHCl$_3$), reaction mixture, followed by substitution of 6-bromo-1-hexanol to give **B11** and 11-bromo-1-undecanol to give **B12** (**Scheme B.2**).
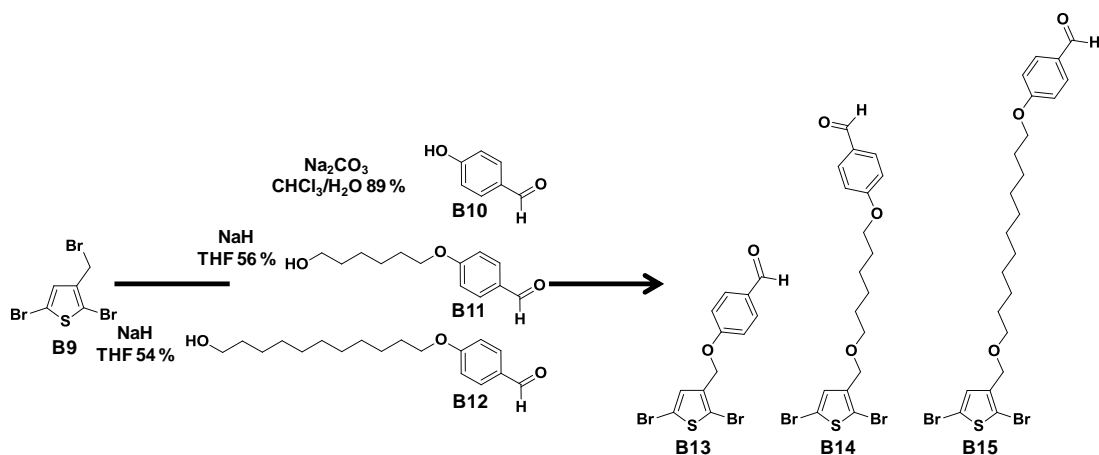
Scheme B.2 Synthesis of benzaldehyde-functionalized dibromo-thiophene compounds (**B13**, **B14** and **B15**) with different alkyl spacers.

Optimal Stille coupling conditions were found using Pd(OAc)$_2$ in DMF with LiCl (2.5 equivalents relative to benzaldehyde), giving rapid (~1 hour) formation of the desired terthiophenes. Finally the Prato reaction was used to covalently bind fullerene-C$_{60}$ to the terthiophenes, yielding dyads **B1**, **B2** and **B3** (**Figure B.2**).
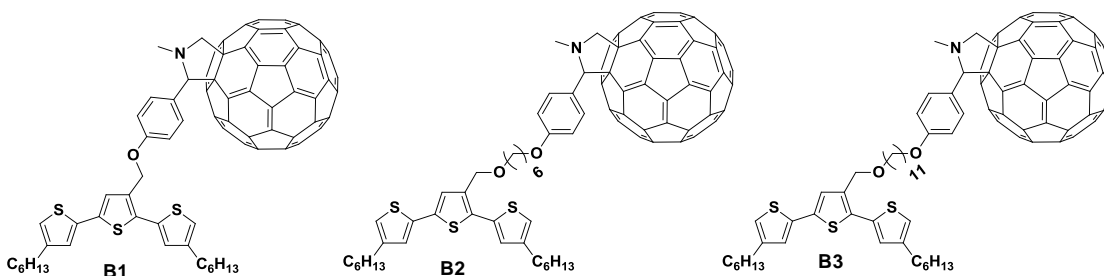
Figure B.2 Alkyl-substituted dyads with varied tether lengths (**B1**, **B2** and **B3**).

The conjugation length was extended upon the addition of two more thiophenes, giving pentathiophene. The precursor benzaldehyde (**B16**) of dyad **B1** was dibrominated with *N*-bromosuccinimide (NBS) in DMF, giving **B17**. NBS had to be added slowly as exactly two equivalents relative to the terthiophene to prevent tri-bromination, where DMF was found to provide more regiochemical control of the bromination relative to other solvents such as CHCl$_3$ or tetrahydrofuran (THF) (**Scheme B.3**). ^{1}H-NMR was used to identify the aromatic thiophene protons at 7.16, 6.89 and 6.86 ppm post-dibromination,

where the equivalent peak areas suggested little mono- or tri-bromination. Stille coupling

of 2-(tributylstannyl)-3,4-ethylenedioxythiophene (**B18)** with **B17** under the same

conditions used for formation of the benzaldehyde-terthiophenes provided

pentathiophene **B19** that was subsequently reacted with fullerene-C$_{60}$ using the Prato

reaction, yielding dyad **B4** (**Scheme B.3**). Dyad **B5** was similarly synthesized; Stille

coupling between **B13** and **B18** to yield **B20**, followed by a Prato reaction between **B20**,

fullerene-C$_{60}$ and sarcosine (**Scheme B.3**).
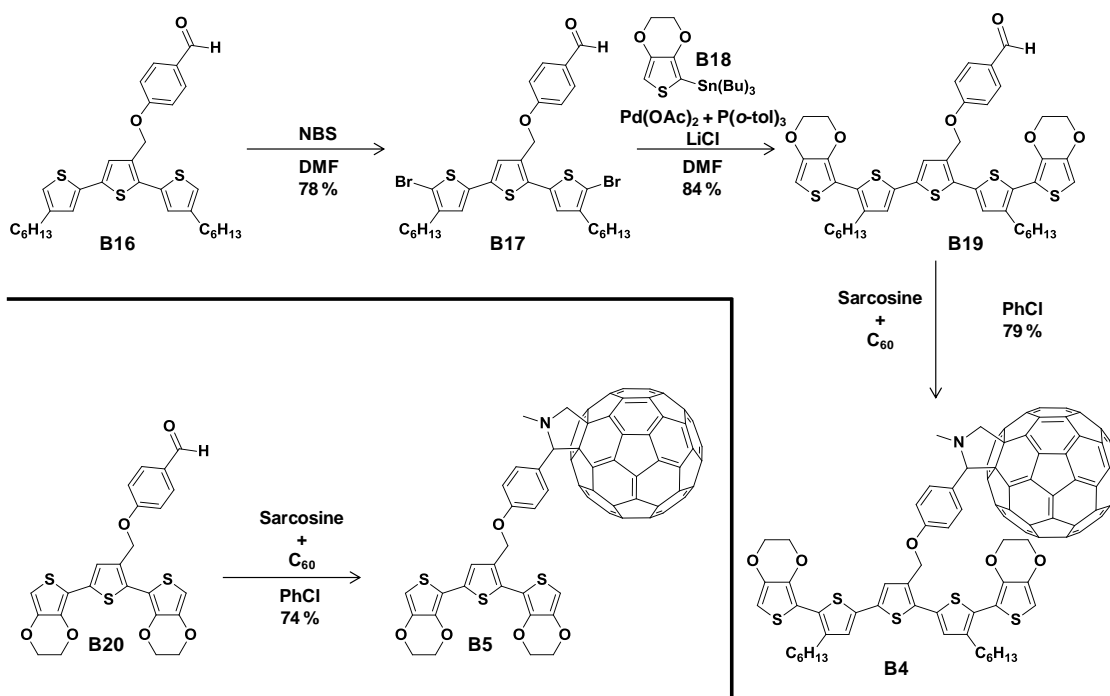
Scheme B.3 Syntheses of ethylenedioxythiophene dyads **B4** and **B5**.

In order to utilize an analogous synthetic procedure towards diethylene glyocl

functionalized dyads, **B6** and **B7**, the preparation of thiophenes **B28** and **B32** was

required, yet precluded by the effects of metal coordination (**Scheme B.4** and **Scheme**

B.5). Attempts to deprotonate the thiophene ring *meta* to the glycol chain of **B21** and **B22**

were unsuccessful, giving instead *ortho*-substituted (1,2-functionalized) products **B23**

and **B24**, irrespective of solvent choice (Et$_2$O or THF) or base used (LDA or *t*-BuLi).

236
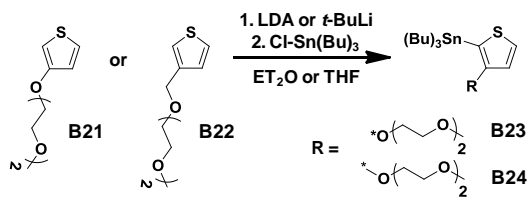
Scheme B.4 Directed *ortho*-metallation of diethylene glycol substituted thiophenes to compounds **B23** and **B24**.

Approaching the desired *meta*-substituted (1,3-functionalized) stannyl-thiophene target molecules **B28** and **B32** required a route whereby *ortho*-metallation could be exploited effectively, and the sequence shown in **Scheme B.5** was ultimately chosen. Alkoxy-functionalized thiophene **B21** was synthesized by a copper-catalyzed Ullmann-type coupling of 3-bromothiophene (**B25**) and diethyleneglycol monomethylether. Following bromination with NBS to obtain **B26**, dehalogenation to afford **B27** occurred with high chemoselectively (~95%) in a diethyl ether solution of CH_3MgBr, which proved effective relative to strong bases like *n*-BuLi, which exchanged non-selectively. Interestingly, despite the partial miscibility of CH_3MgBr in diethyl ether (the reaction mixture was a cloudy white suspension), reactions performed in more polar solvent mixtures (i.e. THF:ether (1:2)) led to lower chemoselectivity (~80% chemoselectivity for this ratio), as such solvents disrupt the intramolecular influence of the glycol side-chain. Lithium-halogen exchange between **B27** and **B28** with n-butyllithium (*n*-BuLi) followed by substitution of tributyltin chloride (Cl-Sn(Bu)$_3$) resulted in the desired 1-stannyl-3-alkoxy substituted thiophene derivative, **B28**.
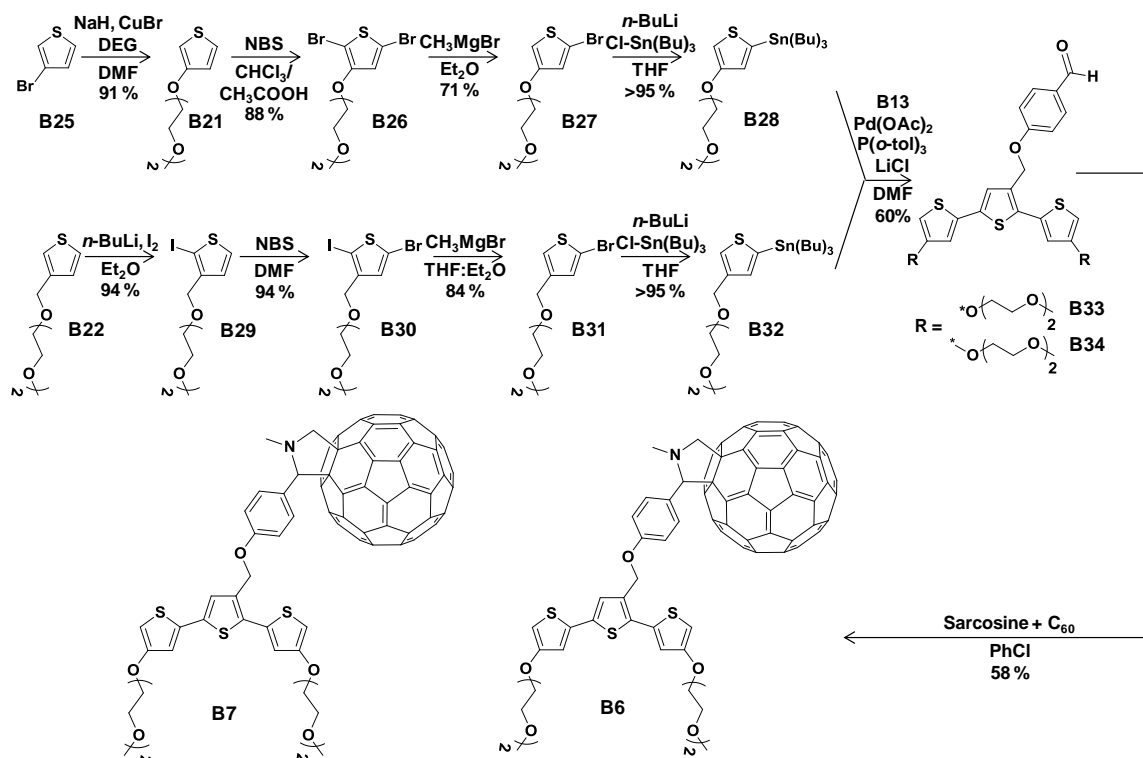
Scheme B.5 Syntheses of diethylene glycol functionalized dyads **B6** and **B7**.

This methodology was extended to prepare dyad **B7**, containing methylene spacers between the oxygen and thiophene rings. These CH$_2$ spacers were expected to reduce electron density in the aromatic rings relative to dyad **B6** (the oxygen is electron withdrawing from this position) thus lowering the highest occupied molecular orbital (HOMO) energy level and increasing the band gap (E_g). A lowered HOMO level of **B7** would raise the energy required for oxidation (both for **B7** itself and for oligomers and polymers prepared from it). The HOMO energy levels were calculated using thiophene models with a semi-empirical ZINDO/1 calculation (**Figure B.3**), which uses geometric optimization and subsequent vibration/rotation analysis to calculate orbital energies. 3-Ethoxythiophene (**B35**) and 3-(methoxymethyl)thiophene (**B37**) were used to model **B21** and **B22**, respectively, to gauge the effect of the presence and position of the oxygen (while keeping the calculation as simple as possible). **Figure B.3** shows that oxygen

attachment directly to the ring lowers the ionization potential (I_P) of the substituted thiophene compared to a 3-alkyl thiophene (**B36**), and that introducing a methylene spacer between the thiophene and the oxygen increases I_P.

B35
I_P = 7.83 eV

B36
I_P = 8.14 eV

B37
I_P = 8.29 eV
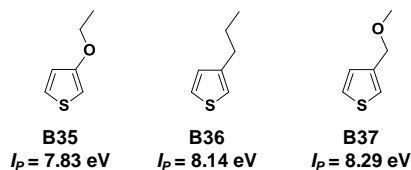
Figure B.3 Calculated ionization potential of 3-ethoxythiophene (**B35**), 3-propylthiophene (**B36**) and 3-(methoxymethyl)thiophene (**B37**).

The synthesis of dyad **B7** is outlined in **Scheme B.5**, where the initial methyloxy substituted thiophene **B22** was obtained by Williamson-ether synthesis of 3-bromomethyl thiophene and ethylene glycol. Attempted dehalogenation of a dibromo-(methyloxy)thiophene derivative **B39** (structure given in **Figure B.4**) using CH_3MgBr resulted in lower chemoselectivity (~75%) compared to the dibromo(alkoxy)thiophene derivative **B26** (~95%), owing to a weaker stabilizing effect caused by the methylene spacer. To increase selectivity in our system, we exploited the distinct reactivity of iodide and bromide. Selective iodination was attempted using *N*-iodosuccinimide (NIS) in $CHCl_3$:CH_3COOH (1:1) to obtain 2-iodo-3-methoxythiophene **B29**, but the reaction was slow (>24 hours) and an exact 1:1 ratio of thiophene:NIS was necessary to obtain pure product. As an alternative, we utilized *ortho*-lithiation of methyloxy thiophene **B22**, reacting first with *n*-BuLi followed by iodine, to obtain compound **B29**. This strategy allows excess reagent to be used, to ensure completion, while preventing diiodination. Attempted bromination of **B29** at the 5-position with NBS in $CHCl_3$:CH_3COOH (1:1) led to halogen scrambling, as seen by ^{1}H-NMR spectroscopy, noting the aromatic proton chemical shift at δ = 6.91, 6.97 and 7.02 for compounds **B38**, **B39** and **B40**, respectively (**Figure B.4**). Similar results were obtained using THF as solvent. Fortunately, in DMF,

the propensity for halogen scrambling was greatly reduced, and chemoselectivity of ~98% was achieved, as determined by ^{1}H-NMR spectroscopy. Deiodination of **B30** occurred selectively with CH$_3$MgBr, followed by quenching with aqueous ammonium chloride to give **B31**. Stannylation withy *n*-BuLi followed by Cl-Sn(Bu)$_3$ gave the desired diethyleneglycol substituted thiophene **B32**.
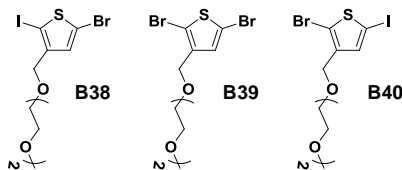
Figure B.4 Bromination products using **B29** with NBS in CHCl$_3$:CH$_3$COOH or THF as the solvent.

Novel stannyl thiophenes **B28** and **B32** are setup for Stille coupling with dibromide **B13**, such that the side-chains on the coupled products will not interact sterically with one another, thus maximizing planarity of the structure. Novel terthiophenes **B33** and **B34** were prepared (**Scheme B.5**) using Pd(OAc)$_2$ in DMF with LiCl (2.5 equivalents relative to benzaldehyde **B13**), giving rapid (~1 hour) formation of the desired terthiophenes in ~60% isolated yield. Successful terthiophene formation was noted spectroscopically by a blue fluorescence upon excitation at 350 nm. High resolution mass spectroscopy (fast atom bombardment, FAB, calcd for **B33**: 618.142, found: 618.137; calcd for **B34**: 646.173, found: 646.176) and NMR spectroscopy (integration of the aldehyde at 9.9 ppm against the thiophene and glycol protons) confirmed the desired structures. The polar ethylene oxide side-chains of these molecules impart solubility in a variety of solvents, including methanol, DMF, CHCl$_3$, dichloromethane and THF and dispersibility in H$_2$O.

The final dyad, **B8**, was synthesized by Stille coupling a novel 2-(tributylstannyl)-4-fluoroalkyl thiophene (**B44**) with benzaldehyde-thiophene **B13**, giving the fluorinated

benzaldehyde-terthiophene **B45** (**Scheme B.6**). Compound **B44** was synthesized starting with a lithium-halogen exchange of 3-bromothiophene (**B25**) with *n*-BuLi, followed by substitution of allyl bromide to give **B41**. Reacting **B41** with perfluorobutyl iodide in the presence of azobisisobutyronitrile (AIBN) afforded **B42**, which was deiodinated using sodium borohydride (NaBH$_4$) in DMSO to give **B43**. Taking the 3-fluoroalkyl thiophene precursor and reacting it with lithium diisopropylamide (LDA) followed by Cl-Sn(Bu)$_3$ in anhydrous THF at -78°C afforded **B44**. After Stille coupling to **B45** the Prato reaction was used to covalently attach fullerene-C$_{60}$, yielding the fluroinated dyad **B8** (**Scheme B.6**).
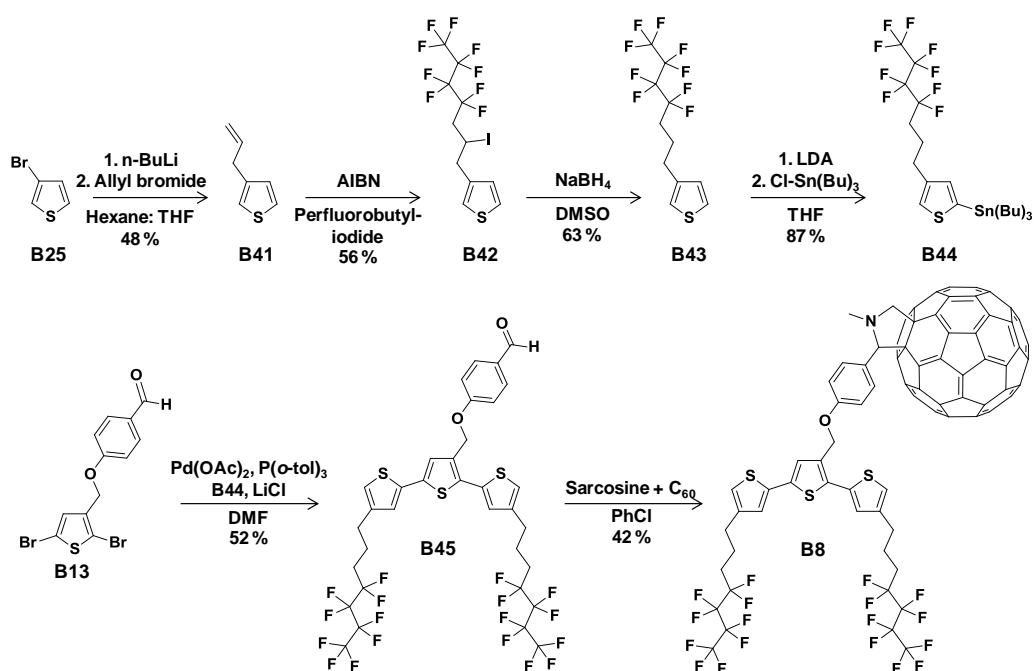
Scheme B.6 Synthesis of fluorinated dyad **B8**.

The individual donor and acceptor components were characterized with UV-Vis absorption and fluorescence spectroscopies and cyclic voltammetry (CV). The precursor benzaldehyde-oligothiophenes were characterized as references, referred to as donor compounds with respect to their fullerene-coupled dyads (donor-acceptor compounds).

Additionally, an anisole-fulleropyrrolidine, **B47**, was synthesized through the Prato reaction of anisaldehyde with *N*-methylglycine (sarcosine) and fullerene-C_{60} and characterized as an acceptor reference (FAB; calcd for **B47**: 884.108, found: 884.114) (**Scheme B.7**).
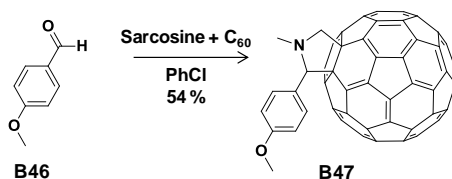
Scheme B.7 Synthesis of reference acceptor, anisole-C_{60} (**B47**), using the Prato reaction.

The optical E_g and ground state interactions of the dyads were studied with UV-Vis absorption spectroscopy, using 10 μM solutions in 1,2-dichlorobenzene (*o*DCB) as well as films on glass slides. As evidence for covalent attachment to fullerene a peak at 430 nm, characteristic of monoadducts, was noted (**Figure B.5**). A lack of ground state charge transfer for all dyads was suggested by a well matched absorption overlay of the sum of the respective parts (donor and acceptor **B47**) with the corresponding dyads (**Figure B.5**). This suggests that covalently binding fullerene to the oligothiophenes does not result in energy level hybridization, thus both donor and acceptor groups act as individual components with unique electronic properties. The dyads also have good molar absorptivities (~5 x 10^4 L mol^{-1} cm^{-1}), a trait common to organic semiconductors. For the case of dyad **B4**, the absorption extends out to 500 nm, which is an absorption range falling well within the visible, capable of more efficiently harnessing solar radiation than its terthiophene counterparts.
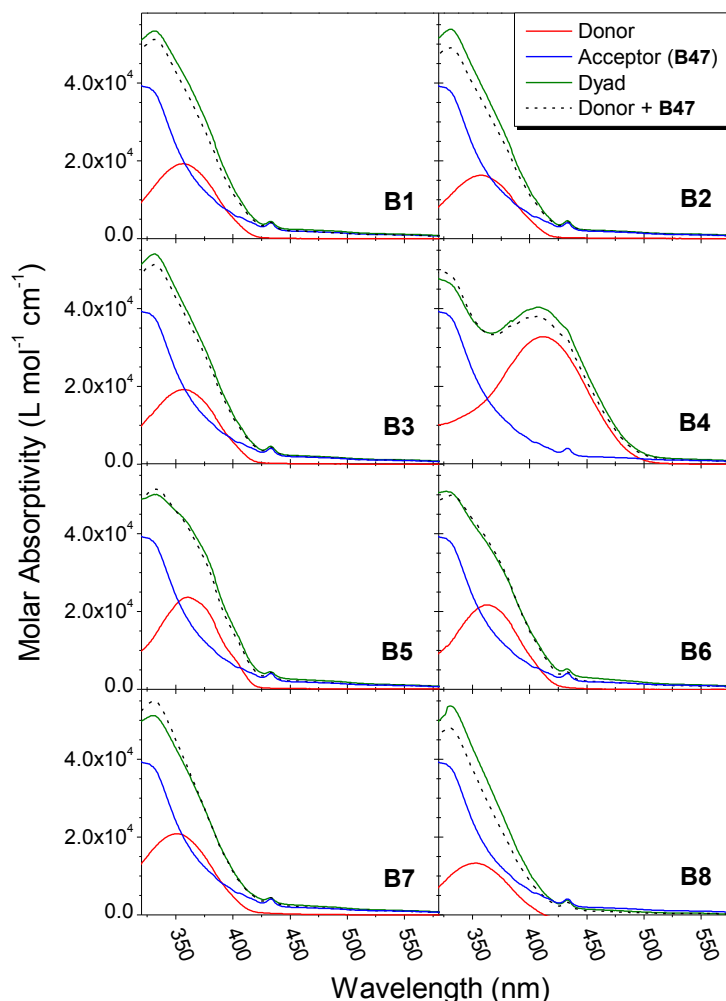
Figure B.5 UV-Vis absorption spectroscopy of dyads **B1-B8**, corresponding donor precursors and acceptor reference **B47**. All spectra were obtained with 10 µM solutions in *o*DCB. Dashed lines show the summation of the respective donor precursor and acceptor **B47**. A lack of ground state charge transfer is suggested by the high degree of overlap between the dyad absorption and the sum of its parts.

Fluorescence was also probed in dilute solution for donors and respective dyads. In all cases covalent attachment of fullerene resulted in almost complete photoluminescence quenching (**Figure B.6**). Upon extending the tether length between the donor and acceptor moieties the fluorescence quenching is reduced, suggesting a less intimate electronic communication between the terthiophene and fullerene as they are separated by longer alkyl chains. As a comparison donor **B16** was combined with acceptor **B47** (10 µM in *o*DCB), showing a reduced fluorescence intensity compared to

free **B16**, but still greater than dyad **B3**, containing the longest tether. The decrease in fluorescence of the solution containing **B16** and **B47** compared to free **B16** is likely a result of fulleropyrrolidine absorption that does not produce appreciable fluorescence, since both terthiophene and fullerene absorb at the excitation wavelength (350 nm) used for the fluorescence measurements. With no evidence showing an alteration of energy levels in the ground state (*e.g.* no ground state charge transfer) upon covalently binding fullerene to the donors we can conclude that changes in fluorescence likely occur from either charge or energy transfer from the donor oligothiophene's to the fullerene acceptor.
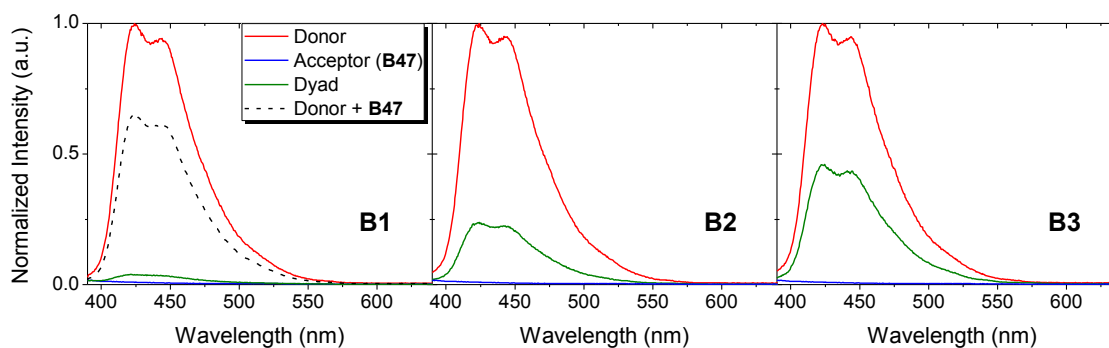
Figure B.6 Normalized fluorescence spectroscopy of dyads **B1**-**B3**, the respective donor precursors and acceptor **B47**. All fluorescence measurements were done on 10 μM solutions in *o*DCB, exciting at 350 nm. Fluorescence quenching suggests intimate electronic communication that is disrupted upon extending tether lengths, as shown with dyads **B2** and **B3**. The individual components (donor **B16** + acceptor **B47**) maintain greater fluorescence than dyad **B3** (sum given as dashed line in left figure).

CV was used to determine energy levels (*e.g.* HOMO and lowest unoccupied molecular orbital (LUMO)) of the donors, dyads and acceptor **B47** through their onsets of reduction and oxidation (**Figure B.7**). The voltammograms were obtained in dichloromethane with 0.1 M tetrabutyl ammonium hexafluorophosphate (TBAPF$_6$) using a platinum working electrode, silver reference electrode and platinum auxiliary electrode. Ferrocene onset of oxidation ($E_{Fc/Fc+}$) was used as a reference for calibration. The onset of oxidation for the donors was used to determine the HOMO energy (E_{HOMO}) and the

244

onset of reduction was used to determine the LUMO energy (E_{LUMO}) of **B47**, as shown in

equations B.1 and B.2:

$$E_{HOMO} = -(E_{ox} - E_{Fc/Fc+} + 4.8) \qquad\qquad \text{B.1}$$

$$E_{LUMO} = -(E_{red} - E_{Fc/Fc+} + 4.8) \qquad\qquad \text{B.2}$$

The dyads showed no significant change for the HOMO or LUMO levels compared to their donor precursors and acceptor **B47** respectively (**Figure B.7**). Similar to the lack of ground state charge transfer noted with UV-Vis absorption spectroscopy, the CV data also supports that covalent attachment between donor and acceptor does not alter their individual electronic properties. The significant LUMO-LUMO offset (> 1 eV) between the donors and fullerene acceptor provides an explanation for electronic communication, given that this value is much larger than the Coulombic attraction of an exciton (electron-hole pair, ~0.5 eV) (**Figure B.7**). Also, typical of fulleropyrrolidine derivatives, the LUMO energy of **B47** (-3.9 eV) is higher than for methanofullerenes, such as PCBM (-4.2 eV).
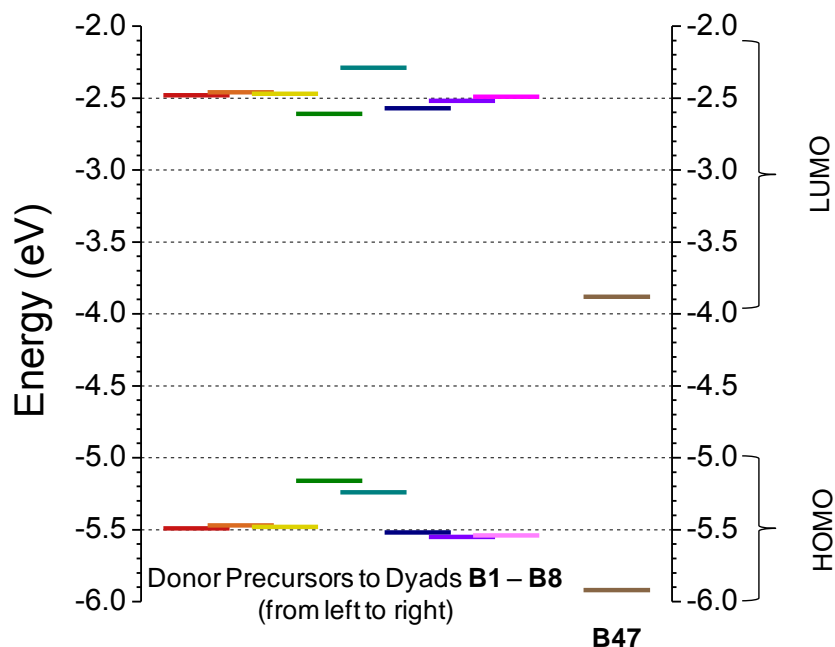
Figure B.7 HOMO-LUMO energy levels of oligothiophene donors (referred to with the corresponding dyads number) and reference acceptor **B47**. Large LUMO-LUMO offset between the donor and acceptor provides evidence for expected electronic communication either through electron transfer (represented in the figure as an example) or energy transfer.

B.3 Narrow energy gap dyads

In order for a one-component active layer to work effectively in a photovoltaic device it is crucial that the absorbing material covers a wide-region of the solar spectrum. The oligothiophene dyads discussed in the previous section do not absorb a sufficient amount of visible light. This section describes a method to overcome this limitation by synthesizing novel solution processable dyads having a reduced E_g without extension of conjugation through the addition of aromatic substituents (as was the case for pentathiophene dyad **B4**). The methodology presented relied on the development of asymmetric α-diketones (**B56**, **B57** and **B58**) that incorporate both a solubilizing group and functional handle for covalent attachment to fullerene (**Scheme B.8**). The synthesis of the asymmetric α-diketones began by converting 2-octyl-1-dodecanol (**B48**) to the

corresponding alkyl-bromide (**B49**) using the Appel reaction (PPH$_3$ + CBr$_4$). **B49** is converted into a Gilman (lithium-dioorganocopper) reagent by first producing the corresponding Grignard with magnesium turnings, followed by the addition of lithium bromide and copper(I) bromide. The freshly generated Gilman reagent is reacted with ethyl chlorooxoacetate, selectively attacking the acid chloride and leaving the ester intact, yielding **B50**. Saponification of the ethyl ester of **B50** to a carboxylic acid is readily achieved with lithium hydroxide in MeOH to give **B51**. **B51** is then converted to the acid chloride **B52** with oxalyl chloride and a catalytic amount of DMF. Immediately following isolation of **B52** a second reaction with Gilman reagents generated from aryl (**B53**) or alkyl (**B54** and **B55**) bromides is accomplished to give the desired asymmetric α-diketones containing a solubilizing aliphatic group and protected benzaldehyde separated by no (**B56**), 3 (**B57**) or 12 (**B58**) methylene units (**Scheme B.8**).
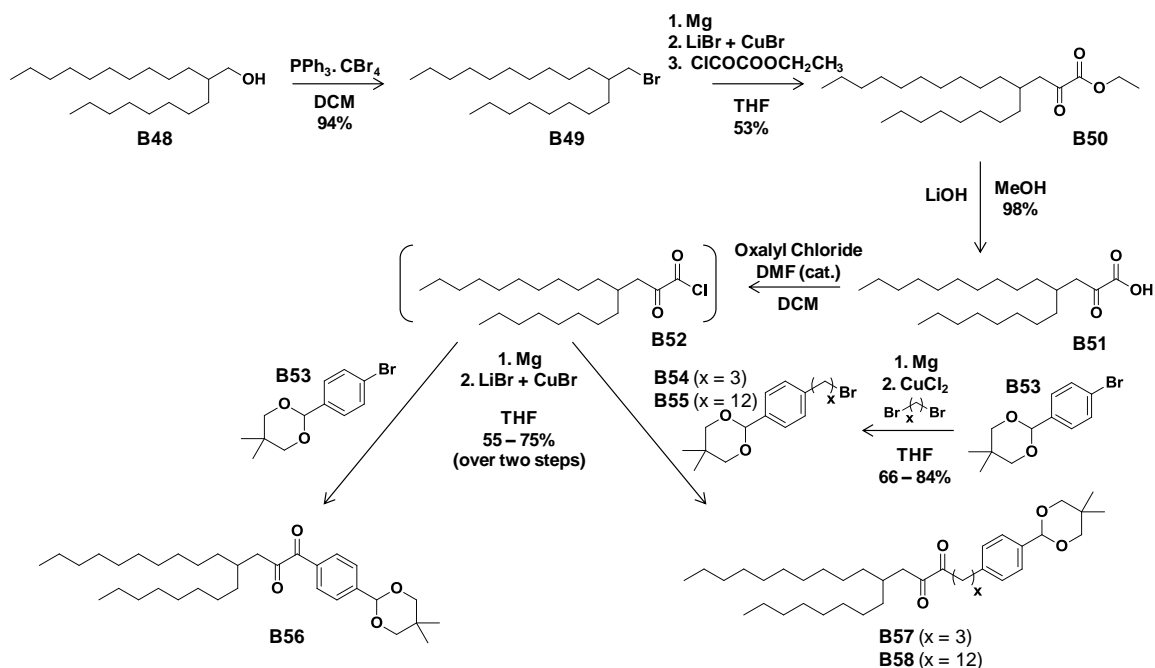
Scheme B.8 Synthesis of asymmetric α-diketones (**B56**, **B57** and **B58**) through a stepwise Gilman approach.

247

Nucleophilic addition of amines followed by dehydration is a common mechanism to form Schiff bases, or imines. Quinoxaline and its derivatives are prime examples of heterocyclic imines that are formed by the condensation of *ortho*-diamines and α-diketones. The target quinoxaline, **B63**, as shown in **Scheme B.9**, was synthesized starting from 1,2-diaminobenzene (**B59**). **B59** was reacted with thionyl chloride (SOCl₂) in the presence of triethylamine (TEA) to form benzothiadiazole (**72**), followed by bromination with bromine in HBr and CH₃COOH to yield dibromobenzothiadiazole (**B60**). Reduction of **B60** with NaBH₄ in ethanol reveals 3,6-dibromobenzene-1,2-diamine (**B61**). Imine formation proceeds smoothly between **B61** and the asymmetric α-diketone **B56**, yielding **B62**. The ketal of **B62** is then converted to the corresponding benzldehyde (**B63**) with trifluoroacetic acid (TFA). Like for the oligothiophene dyads, Stillle coupling of **B64** is utilized to incorporate thiophene on both sides of the functional quinoxaline (**B63**), to give a dithienoquinoxaline (**DTQ**) **B65**. Fullerene-C₆₀ is then covalently bound to **DTQ** using the Prato reaction with sarcosine, yielding **DTFQ** (**B66**).
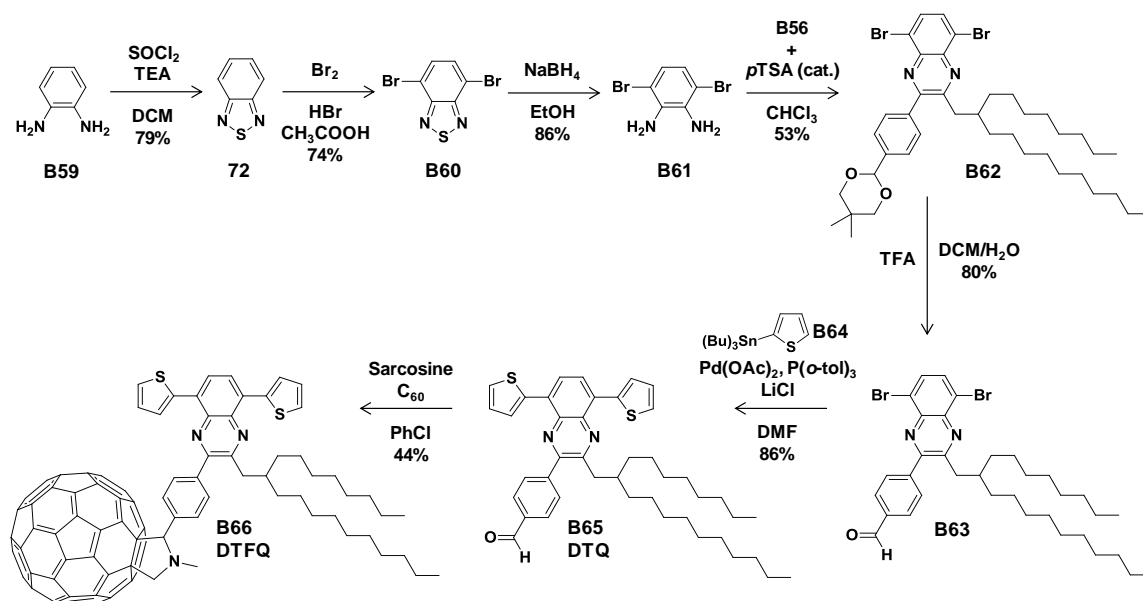
Scheme B.9 Synthesis of bis(thiophene)quinoxaline-fulleropyrrolidine dyad **DTFQ**, **B66**.

A second dyad was synthesized (**DTBTFQ**, **B72**), incorporating benzothiadiazole opposite to the quinoxaline to further reduce the E_g (**Scheme B.10**). The synthesis of **DTBTFQ** starts with a nitration of **B60** using nitric acid (HNO_3) in trifluoromethanesulfonic acid (triflic acid, CF_3SO_3H) to give **B67**, followed by a selective reduction of the nitro groups using iron in CH_3COOH to give the corresponding diamino compound **B68**. At this stage an analogous procedure to that used for **DTFQ** was followed; concurrently diamine **B68** condensation with α-diketone **B56** gave **B69**, **B69** benzaldehyde deprotection with TFA gave **B70**, Stille coupling between **B70** and **B64** gave dithieno-benzothiadiazolo-quinoxaline (**DTBTQ**, **B71**) and finally a Prato reaction using **DTBTQ**, sarcosine and fullerene-C_{60} gave the target compound dithieno-benzothiadiazolo-fulleroquinoxaline (**DTBTFQ**, **B72**).
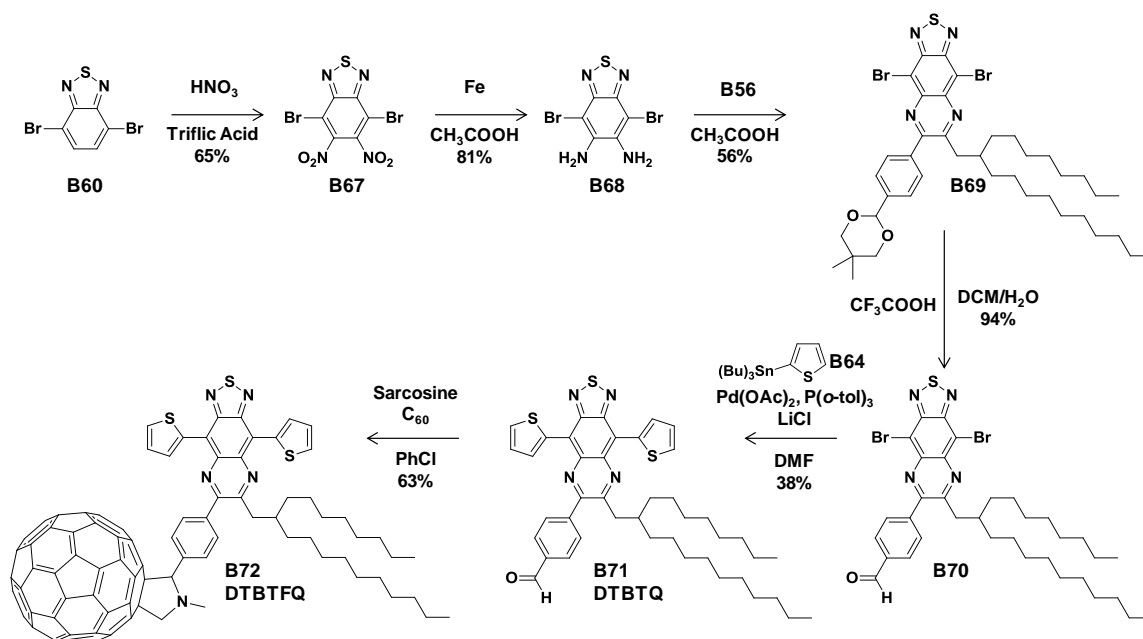
Scheme B.10 Synthesis of bis(thiophene)benzothiadiazoloquinoxaline-fulleropyrrolidine dyad **DTBTFQ**, **B72**.

The energy levels of **DTQ** and **DTBTQ** and the corresponding dyads **DTFQ** and **DTBTFQ** were measured using CV (**Figure B.8**). The voltammograms were obtained in

dichloromethane with 0.1 M tetrabutyl ammonium hexafluorophosphate (TBAPF$_6$) using a platinum working electrode, silver reference electrode and platinum auxiliary electrode. Ferrocene onset of oxidation ($E_{Fc/Fc+}$) was used as a reference for calibration. The onset of oxidation was used to determine the HOMO energy (E_{HOMO}) and the onset of reduction was used to determine the LUMO energy (E_{LUMO}) as shown in equations B.1 and B.2, given in the previous section.
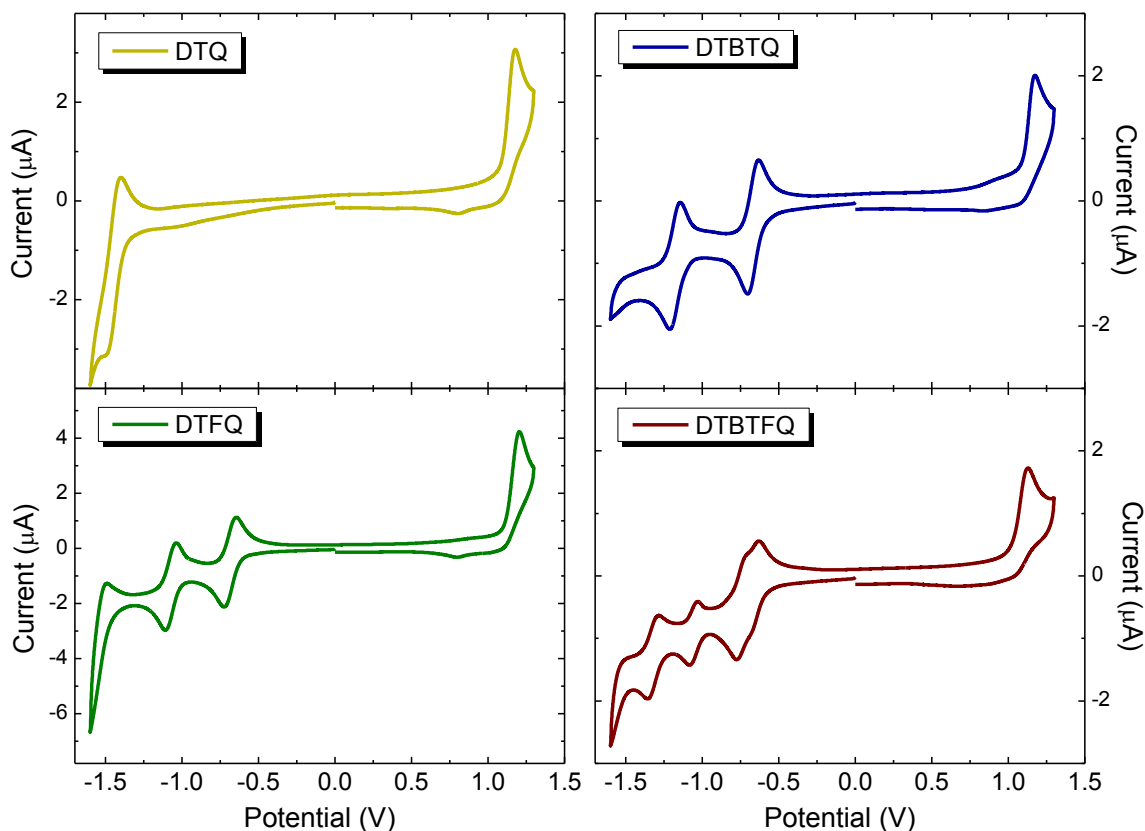
Figure B.8 Cyclic voltammograms of narrow energy gap dyads (**DTFQ** and **DTBTFQ**) and precursor benzaldehydes (**DTQ** and **DTBTQ**).

CV showed a substantially reduced E_g for **DTBTQ** (E_g = 1.61 eV) relative to **DTQ** (E_g = 2.34 eV), which was attributed to a substantially deeper LUMO for DBTQ (-3.92 vs -3.18 eV respectively). Additionally the bathochromic shift of absorption, as shown in **Figure B.9A**, confirms that **DTBTQ** has a narrower E_g than **DTQ**. The relative HOMO and LUMO levels for **DTQ**, **DTBTQ** and acceptor reference **B47** are plotted in

Figure B.9B. The similar LUMO energy levels for **DTBTQ** and **B47** suggest that electron transfer from **DTBTQ** to a fullerenopyrrolidine, as would be the case for **DTBTFQ**, would be difficult, due to a weak driving force. Simultaneously shifting the HOMO/LUMO energy levels of **DTBTQ** up may provide a material that can act as an effective one component photoactive layer in solar cells, capable of efficiently absorbing visible light and while being able to transfer an excited electron to a covalently bound fulleropyrrolidine.
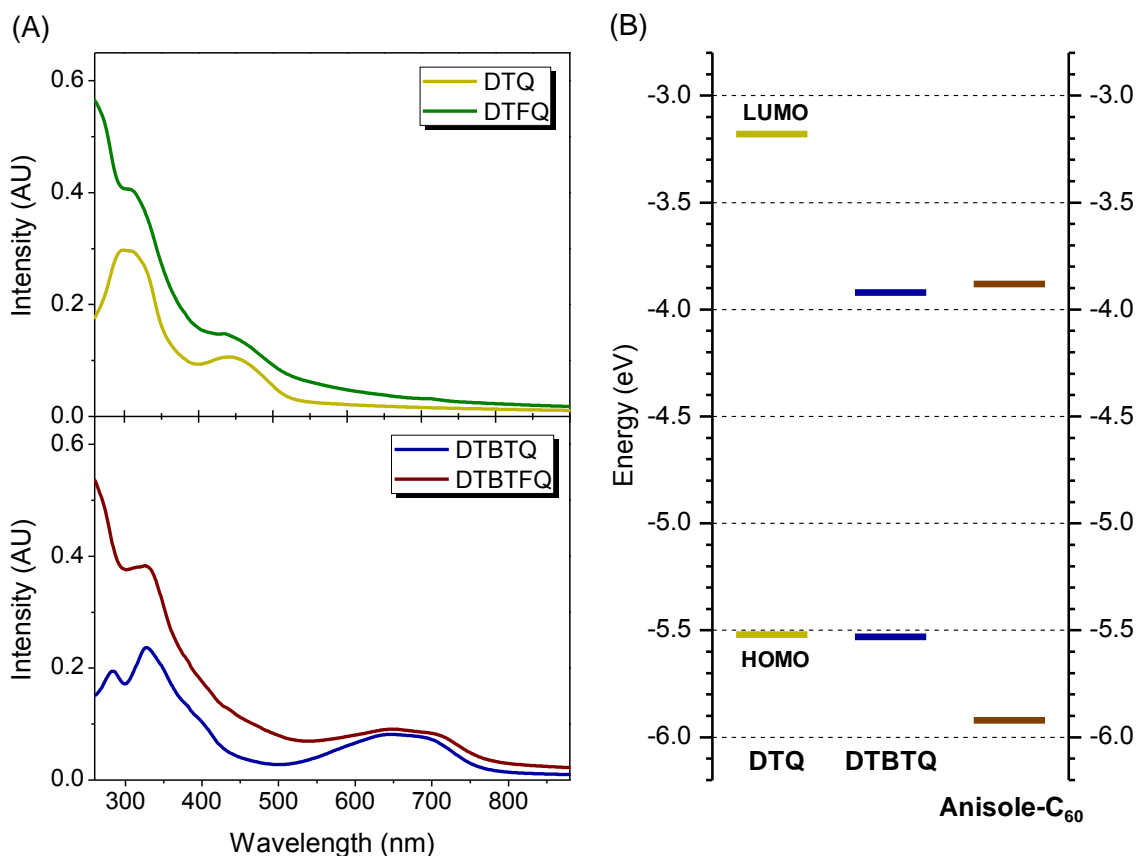
Figure B.9 Solid state UV-Vis absorption profiles (A) and energy level diagram (B) of narrow energy gap dyads. **Anisole-C$_{60}$** (**B47**) is given for reference.

BIBLIOGRAPHY

Andersson, M. Ekeblad, P. O. Hjertberg, T.; Wennerstrom, O. *Polym. Commun.* **1991**, *32*, 546–548.

Anuragudom, P.; El-daye, J.; Chinwangso, P.; Advincula, R. C.; Phanichphant, S.; Lee, T. R. *Polym. Int.* **2011**, *60* (4), 660-665.

Anuragudom, P.; Newaz, S. S.; Phanichphant, S.; Lee, T. R. *Macromolecules* **2006**, *39*, 3494-3499.

Arbuzov, A. E. *Chem. Zentr.* **1906**, *II*, 1639.

Arbuzov, A. E. *J. Russ. Phys. Chem. Soc.* **1906**, *38*, 687.

Asinger, F.; Scheuffler,B. *J. fuer Praktische Chemie (Leipzig)*, **1960** , *10*, 265-289.

Auragudom, P.; Tangonan, A. a.; Namboothiry, M. a. G.; Carroll, D. L.; Advincula, R. C.; Phanichphant, S.; Lee, T. R. *J. Polym. Res.* **2009**, *17* (3), 347-353.

Beaujuge, P. M.; Amb, C. M.; Reynolds, J. R. *Acc. Chem. Res.* **2010**, *43*, 1396-1407.

Beaujuge, P. M.; Ellinger, S.; Reynolds, J. R. *Nat. Mater.* **2008**, *7*, 795-799.

Betancur, R.; Romero-gomez, P.; Martinez-otero, A.; Elias, X.; Maymo, M.; Martorell, J. *Nat. Photonics* **2013**, *7*, 995-1000.

Blom, P. W. M.; Mihailetchi, V. D.; Koster, L. J. A.; Markov, D. E. *Adv. Mater.* **2007**, *19*, 1551–1566.

Boer, B. de; Hadipour, A. Mandoc, M. M. Woudenbergh, T. V.; Blom, P. W. M. *Adv. Mater.* **2005**, *17*, 621–625.

Boudreault, P.-L. T.; Najari, A.; Leclerc, M. *Chem. Mater.* **2011**, *23*, 456–469.

Brabec, C.J.; Shaheen, S.E.; Winder, C.; Sariciftci, N.S.; Denk, P. *Appl. Phys. Lett.* **2002**, 80, 1288–1290.

Braun, B. S.; Salaneck, W. R.; Fahlman, M. *Adv. Mater.* **2009**, *21*, 1450-1472.

Bröker, B.; Blum, R.-P.; Frisch, J.; Vollmer, A.; Hofmann, O. T.; Rieger, R.; Müllen, K.; Rabe, J. P.; Zojer, E.; Koch, N. *Appl. Phys. Lett.* **2008**, *93* (24), 243303.

Brown, H. R.; Russell, T. P. *Macromolecules* **1996**, *9297*, 8334-8342.

Buchmeiser, M. R. *Adv. Polym. Sci.* **2005**, *176*, 89-119.

Burroughes, J. H.; Bradley, D. D. C.; Brown, A. R.; Marks, R. N.; Mackay, K.; Friend, R. H.; Burns, P. L.; Holmes, A. B. *Nature* **1990**, *347*, 539-541.

Cacialli, F.; Daik, R.; Feast, W. J.; Friend, R. H.; Lartigau, C. *Opt. Mater.* **1999**, *12*, 315-319.

Cai, W.; Gong, X.; Cao, Y. *Sol. Energ. Mat. Sol. Cells* **2010**, *94*, 114–127.

Campbell, I.H.; Kress, J.D.; Martin, R.L.; Smith, D.L.; Barashkov, N.N.; Ferraris, J.P. *Appl. Phys. Lett.* **1997**, 71, 3528–3530.

Chapin, D. M.; Fuller, C. S.; Pearson, G. L. *J. Appl. Phys.* **1954**, *25*, 676.

Chen, C.-C.; Chang, W.-H.; Yoshimura, K.; Ohya, K.; You, J.; Gao, J.; Hong, Z.; Yang, Y. *Adv. Mater.* **2014**, *26*, 5670.

Chen, D.; Nakahara, A.; Wei, D.; Nordlund, D.; Russell, T. P. *Nano Lett.* **2011**, *11*, 561-567.

Chen, J.-D.; Cui, C.; Li, Y.-Q.; Zhou, L.; Ou, Q.-D.; Li, C.; Li, Y.; Tang, J.-X. *Adv. Mater.* **2015**, *27*, 1035.

Chen, X.; McRae, S.; Samanta, D.; Emrick, T. *Macromolecules* **2010**, *43*, 6261-6263.

Cho, N. H.; Kim, D. Y.; Kim, Y. C.; Lee, Y. J.; Kim, Y. C. *Adv. Mater.* **1997**, *9* (4), 326-328.

Chueh, C.; Chien, S.; Yip, H.; Salinas, J. F.; Li, C.; Chen, K.; Chen, F.; Chen, W.; Jen, A. K. *Adv. Energy Mater.* **2013**, *3*, 417-423.

Chueh, C.-C.; Li, C.-Z.; Jen, A. K.-Y. *Energy Environ. Sci.* **2015**, *8* (4), 1160-1189.

Coakley, K. M.; McGehee, M. D. *Chem. Mater.* **2004**, *16*, 4533–4542.

Coffin, R. C.; Peet, J.; Rogers, J.; Bazan, G. C. *Nat. Chem.* **2009**, *1*, 657-661.

Conjugated Polyelectrolytes: Fundamentals and Applications. Liu, B.; Bazan, G. C., Eds. Wiley-VCH. **2013**. pp 418.

Cowan, S. R.; Banerji, N.; Leong, W. L.; Heeger, A. J. *Adv. Funct. Mater.* **2012**, *22*, 1116-1128.

Crispin, X. Geskin, V. Crispin, A. Cornil, J. Lazzaroni, R. Salaneck, W. R.; Brédas, J.-L. *J. Am. Chem. Soc.* **2002**, *124*, 8131–8141.

Crowhurst, L.; Mawdsley, P. R.; Perez-Arlandis, J. M.; Salter, P. a.; Welton, T. *Phys. Chem. Chem. Phys.* 2003, *5*, 2790-2794.

Davey, A. P.; Drury, A.; Maier, S.; Byrne, H. J.; Blau, W. J. *Synt. Met.* **1999**, *103*, 2478-2479.

Deibel, C.; Dyakonov, V. *Rep. Prog. Phys.* **2010**, 73, 096401.

DiBenedetto, S.A.; Facchetti, A.; Ratner, M.A.; Marks, T. *Adv. Mater.* **2009**, *21*, 1407-1433.

Dou, L. You, J. Yang, J. Chen, C.-C. He, Y. Murase, S. Moriarty, T. Emery, K. Li, G.; Yang, Y. *Nat. Photonics* **2012**, *6*, 180-185.

Drury, A.; Maier, S.; Rüther, M.; Blau, W. J. *J. Mater. Chem.* **2003**, *13*, 485-490.

Duan, C.; Wang, L.; Zhang, K.; Guan, X.; Huang, F. *Adv. Mater.* **2011**, *23*, 1665-1669.

Duan, C.; Zhang, K.; Guan, X.; Zhong, C.; Xie, H.; Huang, F.; Chen, J.; Peng, J.; Cao, Y. *Chem. Sci.* **2013**, *4* (3), 1298-1307.

Duan, C.; Zhang, K.; Zhong, C.; Huang, F.; Cao, Y. *Chem. Soc. Rev.* **2013**, *42*, 9071-9104.

Duan, C.; Zhong, C.; Liu, C.; Huang, F.; Cao, Y. *Chem. Mater.* **2012**, *24*, 1682-1689.

Duarte, A.; Pu, K.-Y.; Liu, B.; Bazan, G. C. *Chem. Mater.*, **2011**, 23, 501-515.

Fang, J.; Wallikewitz, B. H.; Gao, F.; Tu, G.; Muller, C.; Pace, G.; Friend, R. H.; Huck, W. T. S. *J. Am. Chem. Soc.* **2011**, *133*, 683–685.

Feng, X.; Liu, M.; Pisula, W.; Takase, M.; Li, J.; Müllen, K. *Adv. Mater.* **2008**, *20* (14), 2684-2689.

Fernandez-Torre, D.; Kupiainen, O.; Pyykkoe, P.; Halonen, L. *Chem. Phys. Lett.* **2009**, 471, 239-243.

Gadisa, A.; Svensson, M.; Andersson, M.R.; Inganas O. *Appl. Phys. Lett.* **2004**, 84, 1609-1611.

Gao, Y. *Mater. Sci. Eng., R.* **2010**, *68*, 39-87.

Gendron, D.; Leclerc, M. *Energy Environ. Sci.* **2011**, *4*, 1225-1237.

Georgiev, G. S. Kamenska, E. B. Vassileva, E. D. Kamenova, I. P. Georgieva, V. T. Iliev, S. B.; Ivanov, I. A. *Biomacromolecules.* **2006**, *7*, 1329-1334.

Grätzel, M. *Acc. Chem. Res.* **2009**, *42*, 1788–1798.

Greenham, N. C.; Moratti, S. C.; Bradley, D. D. C.; Friend, R. H.; Holmes, A. B. *Nature* **1993**, *365*, 628-630.

Grimsdale, A. C.; Chan, K. L.; Martin, R. E.; Jokisz, P. G.; Holmes, A. B. *Chem. Rev.* **2009**, *109* (3), 897-1091.

Gu, C.; Chen, Y.; Zhang, Z.; Xue, S.; Sun, S.; Zhong, C.; Zhang, H.; Lv, Y.; Li, F.; Huang, F.; Ma, Y. *Adv. Energy Mater.* **2014**, *4*, 1301771.

Gunes, S.; Neugebauer, H.; Sariciftci, N. S. *Chem. Rev.* **2007**, *107*, 1324–1338.

Guo, F.; Zhu, X.; Forberich, K.; Krantz, J.; Stubhan, T.; Salinas, M.; Halik, M.; Spallek, S.; Butz, B.; Spiecker, E.; Ameri, T.; Li, N.; Kubis, P.; Guldi, D. M.; Matt, G. J.; Brabec, C. J. *Adv. Energy Mater.* **2013**, *3*, 1062-1067.

Guo, X.; Watson, M. D. *Org. Lett.* **2008**, *10*, 5333-5336.

Guo, X.; Zhang, M.; Ma, W.; Ye, L.; Zhang, S.; Liu, S.; Ade, H.; Huang, F.; Hou, J. *Adv. Mater.* **2014**, *26*, 4043-4049.

Haldorai, Y.; Zong, T.; Shim, J.-J. *Mater. Chem. Phys.* **2011**, *127*, 385-390.

Hallett, J. P.; Welton, T. *Chem. Rev.* **2011**, *111*, 3508-3576.

Hau, S. K.; Yip, H.; Acton, O.; Baek, S.; Jen, A. K. *J. Mater. Chem.* **2008**, *18*, 5113-5119.

Haugeneder, A.; Neges, M.; Kallinger, C.; Spirkl, W.; Lemmer, U.; Feldmann, J.; Scherf, U.; Harth, E.; Gügel, A.; Müllen, K. *Phys. Rev. B* **1999**, *59*, 15346–15351.

He, Z.; Wu, H.; Cao, Y. *Adv. Mater.* **2014**, *26* (7), 1006-1024.

He, Z.; Xiao, B.; Liu, F.; Wu, H.; Yang, Y.; Xiao, S.; Wang, C.; Russell, T. P.; Cao, Y. *Nat. Photonics* **2015**, *9* (3), 174-179.

He, Z.; Zhong, C.; Huang, X.; Wong, W.-Y.; Wu, H.; Chen, L.; Su, S.; and Cao, Y. *Adv. Mater.* **2011**, 23, 4636-4643.

He, Z.; Zhong, C.; Su, S.; Xu, M.; Wu, H.; Cao, Y. *Nat. Photonics* **2012**, *6*, 591-595.

Henson, Z. B.; Zhang, Y.; Nguyen, T.-Q.; Seo, J. H.; Bazan, G. C. *J. Am. Chem. Soc.* **2013**, *135*, 4163-4166.

Herrmann, W. A.; Kocher, C. *Angew. Chem. Int. Ed. Engl.* 1997, **36**, 2162-2187.

Hill, I.G.; Milliron, D.; Schwartz, J.; Kahn, A.; *Appl. Surf. Sci.*, **2000**, 166, 354-362.

Hiremath, U. S. *Tetrahedron Lett.* **2013**, *54* (26), 3419-3423.

Hou, L.; Huang, F.; Peng, J.; Wu, H.; Wen, S.; Mo, Y.; Cao, Y. *Thin Solid Films* **2006**, 515, 2632–2634.

Hoven, C. V.; Yang, R.; Garcia, A.; Crockett, V.; Heeger, A. J.; Bazan, G. C.; Nguyen, T.-Q. *Proc. Natl. Acad. Sci. U. S. A.* **2008**, *105*(35), 12730–12735.

Hu, Z.; Zhang, K.; Huang, F.; Cao, Y. *Chem. Commun.* **2015**, *51*, 5572-5585.

Huglin, M. B.; Radwan, M. A. *Makromol. Chem.* **1991**, *192*, 2433 -2445.

Hummelen, J. C.; Knight, B. W.; LePeq, F.; Wudl, F. *J. Org. Chem.* **1995**, *60*, 532-538.

Huo, L. Zhou, Y.; Li, Y. *Macromol. Rapid Commun.* **2009**, *30*, 925-931.

Hwang, J.; Wan A.; Kahn, A. *Mat. Sci. Eng. R* **2009**, 64, 1-31.

Hwang, Y.-J.; Earmme, T.; Courtright, B. a E.; Eberle, F. N.; Jenekhe, S. a. *J. Am. Chem. Soc.* **2015**, *137*, 4424-4434.

Ishii, B. H.; Sugiyama, K.; Ito, E.; Seki, K. *Adv. Mater.* **1999**, *11*(8), 605-625.

Jackson, N. E.; Savoie, B. M.; Marks, T. J.; Chen, L. X.; Ratner, M. a. *J. Phys. Chem. Lett.* **2015**, *6* (1), 77.

Jagadamma, L. K.; Al-Senani, M.; El-Labban, A.; Gereige, I.; Ngongang Ndjawa, G. O.; Faria, J. C. D.; Kim, T.; Zhao, K.; Cruciani, F.; Anjum, D. H.; McLachlan, M. a.; Beaujuge, P. M.; Amassian, A. *Adv. Energy Mater.* **2015**, 1500204.

Jiang, H.; Taranekar, P.; Reynolds, J. R.; Schanze, K. S. *Angew. Chem. Int. Ed.* **2009**, *48* (24), 4300-4316.

Jin, C.; Twamley, B.; Shreeve, J. M. *Organometallics* **2005**, 3020-3023.

Johnston-Hall, G.; Harjani, J. R.; Scammells, P. J.; Monteiro, M. J. *Macromolecules* **2009**, *42*, 1604-1609.

Jørgensen, M.; Norrman, K.; Krebs, F. C. *Sol. Energ. Mat. Sol. Cells* **2008**, *92*, 686-714.

Junkers, T.; Vandenbergh, J.; Adriaensens, P.; Lutsen, L.; Vanderzande, D. *Polym. Chem.* **2012**, *3* (2), 275-285.

Kahn, A.; Koch, N.; Gao, W. *J. Polym. Sci., Part B Polym. Phys.* **2003**, *41*, 2529.

Kallmann, H.; Pope, M. *J. Chem. Phys.* **1959**, *30*, 585–586 .

Karlsson, K. F. Asberg, P. Nilsson, K. P. R.; Inganas, O. *Chem. Mater.* **2005**, *17*, 4204-4211.

Kesters, J.; Ghoos, T.; Penxten, H.; Drijkoningen, J.; Vangerven, T.; Lyons, D. M.; Verreet, B.; Aernouts, T.; Lutsen, L.; Vanderzande, D.; Manca, J.; Maes, W. *Adv. Energy Mater.* **2013**, *3*, 1180-1185.

Kim J.Y.; Lee, K.; Coates, N.E.; Moses, D.; Nguyen, T.Q.; Dante, M.; Heeger, A.J. *Science* **2007**, 317, 222–225.

Kim, J.Y.; Kim, S.H.; Lee, H.-H.; Lee, K.; Ma, W.; gong, X.; Heeger, A.J. *Adv. Mater.* **2006**, 18, 572-576.

Kline, R. J.; McGehee, M. D. *J. Macromol. Sci., Polym. Rev.* **2006**, *46*, 27-45.

Koch, N. J. Phys.: Condens. Matter. **2008**, 184008.

Krebs, F. C. *Sol. Energ. Mat. Sol. Cells* **2009**, *93*, 465-475.

Krebs, F. C.; Gevorgyan, S. A.; Alstrup, J. *J. Mater. Chem.* **2009**, *19*, 5442-5451.

Kubisa, P. *Prog. Polym. Sci.* **2009**, *34*, 1333-1347.

Kularatne, R. S.; Taenzler, F. J.; Magurudeniya, H. D.; Du, J.; Murphy, J. W.; Sheina, E. E.; Gnade, B. E.; Biewer, M. C.; Stefan, M. C. *J. Mater. Chem. A* **2013**, *1* (48), 15535-15543.

Kumar, A.; Lakhwani, G.; Elmalem, E.; Huck, W. T. S.; Rao, A.; Greenham, N. C.; Friend, R. H. *Energy Environ. Sci.* **2014**, *7*, 2227-2231.

Kumar, A.; Pace, G.; Bakulin, A. a.; Fang, J.; Ho, P. K. H.; Huck, W. T. S.; Friend, R. H.; Greenham, N. C. *Energy Environ. Sci.* **2013**, *6* (5), 1589-1596.

Lai, Y.-Y.; Shih, P.-I.; Li, Y.-P.; Tsai, C.-E.; Wu, J.-S.; Cheng, Y.-J.; Hsu, C.-S. *ACS Appl. Mater. Interfaces* **2013**, *5*, 5122-5128.

Landau, L.D.; Lifshitz, E.M. Course of Theoretical Physics: Electrodynamics of continuous media; Nauka, Moscow, 1981.

Larsen, R. O.; Aksnes, G. *Phosphorus and Sulfur* **1983**, *15*, 219-228.

Larsen, R. O.; Aksnes, G. *Phosphorus and Sulfur* **1983**, *15*, 229.

Laughlin, B. J.; Smith, R. C. *Macromolecules* **2010**, *43* (8), 3744-3749.

Lee, E.; Hammer, B.; Kim, J.-K.; Page, Z.; Emrick, T.; Hayward, R.C. *J. Am. Chem. Soc.* **2011**, *133*, 10390-10393.

Lee, J. S.; Son, S. K.; Song, S.; Kim, H.; Lee, D. R.; Kim, K.; Ko, M. J.; Choi, D. H.; Kim, B.; Cho, J. H. *Chem. Mater.* **2012**, *24*, 1316-1323.

Lei, T.; Cao, Y.; Fan, Y.; Liu, C.-J.; Yuan, S.-C.; Pei, J. *J. Am. Chem. Soc.* **2011**, *133*, 6099-6101.

Li, C.; Chueh, C.; Ding, F.; Yip, H.; Liang, P.; Li, X.; Jen, A. K. *Adv. Mater.* **2013**, *25*, 4425-4430.

Li, C.; Chueh, C.; Yip, H.; Malley, K. M. O.; Chen, W.; Jen, A. K. *J. Mater. Chem.* **2012**, *22*, 8574-8578.

Li, C.-Z.; Chang, C.-Y.; Zang, Y.; Ju, H.-X.; Chueh, C.-C.; Liang, P.-W.; Cho, N.; Ginger, D. S.; Jen, A. K.-Y. *Adv. Mater.* **2014**, *26* (36), 6262-6267.

Li, C.-Z.; Yip, H.-L.; Jen, A. K.-Y. *J. Mater. Chem.* **2012**, *22* (10), 4161-4177.

Li, G.; Chu, C.W.; Shrotriya, V.; Huang, J.; Yang, Y. *Appl. Phys. Lett.* **2006**, 88, 253503.

Li, G.; Zhu, R.; Yang, Y. *Nat. Photonics.* **2012**, *6*, 153–161.

Li, H.; Tang, H.; Li, L.; Xu, W.; Zhao, X.; Yang, X. *J. Mater. Chem.* **2011**, *21*, 6563-6568.

Li, H.; Xu, Y.; Hoven, C. V; Li, C.; Seo, J. H.; Bazan, G. C. *J. Am. Chem. Soc.* **2009**, *131*, 8903-8912.

Li, L.; Yuan, C.; Dai, L.; Thayumanavan, S. *Macromolecules* **2014**, *47* (17), 5869-5876.

Li, S.; Lei, M.; Lv, M.; Watkins, S. E.; Tan, Z.; Zhu, J.; Hou, J.; Chen, X.; Li, Y. *Adv. Energy Mater.* **2013**, *3*, 1569-1574.

Li, X.; Zhang, W.; Wu, Y.; Min, C.; Fang, J. *J. Mater. Chem.* **2013**, *1*, 12413-12416.

Li, Y.; Sonar, P.; Murphy, L.; Hong, W. *Energy Environ. Sci.* **2013**, *6*, 1684-1710.

Li, Z.-K.; He, C.; Yang, M.; Xia, C.-Q.; Yu, X.-Q. *ARKIVOC* **2005**, *1*, 98-104.

Liang Y.Y.; Xu, Z.; Xia, J.B.; Tsai, S.T.; Wu, Y.; Li, G.; Ray, C.; Yu, L.P. *Adv. Mat.* **2010**, 22, E135-E138.

Liao, S.-H.; Jhuo, H.-J.; Yeh, P.-N.; Cheng, Y.-S.; Li, Y.-L.; Lee, Y.-H.; Sharma, S.; Chen, S.-A. *Sci. Rep.* **2014**, *4*, 6813.

Lim, D. C.; Seo, B. Y.; Nho, S.; Kim, D. H.; Hong, E. M.; Lee, J. Y.; Park, S.; Lee, C.; Kim, Y. D.; Cho, S. *Adv. Energy Mater.* **2015**, 1500393.

Lindell, L.; Burquel, A.; Jakobsson, F. L. E.; Lemaur, V.; Berggren, M.; Lazzaroni, R.; Cornil, J.; Salaneck, W. R.; Crispin, X. *Chem. Mater.* **2006**, *18* (18), 4246-4252.

Lindell, L.; Unge, M.; Osikowicz, W.; Stafström, S.; Salaneck, W. R.; Crispin, X.; de Jong, M. P. *Appl. Phys. Lett.* **2008**, *92* (16), 163302.

Liu, C.; Yi, C.; Wang, K.; Yang, Y.; Bhatta, R. S.; Tsige, M.; Xiao, S.; Gong, X. *ACS Appl. Mater. Interfaces* **2015**, *7* (8), 4928.

Liu, F.; Page, Z. A.; Duzhko, V. V.; Russell, T. P.; Emrick, T. *Adv. Mater.* **2013**, *25*, 6868-6873.

Liu, X.; Wen, W.; Bazan, G. C. *Adv. Mater.* **2012**, *24*, 4505-4510.

Liu, X.; Zhu, R.; Zhang, Y.; Liu, B.; Ramakrishna, S. *Chem. Commun*. **2008**, 3789–3791.

Liu, Y.; Chen, C.-C.; Hong, Z.; Gao, J.; Yang, Y. M.; Zhou, H.; Dou, L.; Li, G.; Yang, Y. *Sci. Rep.* **2013**, *3*, 3356.

Liu, Y.; Page, Z. A.; Russell, T. P.; Emrick, T. *Submitted*, **2015**.

Lowe, A. B.; McCormick, C. L. *Chem. Rev.* **2002**, *102* (11), 4177-4189.

Lu, J.; Yan, F.; Texter, J. *Prog. Polym. Sci.* **2009**, *34*, 431-448.

Luo, J.; Wu, H.; He, C.; Li, A.; Yang, W.; Cao, Y. *Appl. Phys. Lett*. **2009**, *95*(4), 043301.

Lyon, J. E. Cascio, A. J. Beerbom, M. M. Schlaf, R. Zhu, Y.; Jenekhe, S. A. *Appl. Phys. Lett.* **2006**, *88*, 222109.

Ma, H.; Yip, H.-L.; Huang, F.; and Jen, A. K.-Y. *Adv. Funct. Mater.* **2010**, 20, 1371-1388.

Ma, W.; Iyer, P. K.; Gong, X.; Liu, B.; Moses, D.; Bazan, G. C.; Heeger, A. J. *Adv. Mater.* **200**5, 17(3), 274–277.

Maggini, M. & Scorrano, G. Addition of Azomethine Ylides to C60: Synthesis, Characterization, and Functionalization of Fulleroene Pyrrolidines. *J. Am. Chem. Soc.* **115**, 9798–9799 (1993).

Margaretta, E.; Olmeda, C.; Yu, L. *J. Appl. Polym. Sci.* **2013**, *127*, 2453-2457.

Martínez-Otero, A., Elias, X., Betancur, R. & Martorell, J. High-Performance Polymer Solar Cells Using an Optically Enhanced Architecture. *Adv. Optical Mater.* **1**, 37–42 (2013).

Mary, P.; Bendejacq, D. D.; Labeau, M.; Dupuis, P. *J. Phys. Chem. B*. **2007**, *111*, 7767-7777.

Maschhoff, B.L.; Cowin, J.P. *J. Chem. Phys.* **1994**, 101, 8138 – 8151.

Mathews, C. J.; Smith, P. J.; Welton, T. *Chem. Commun.* **2000**, 1249-1250.

McLachlan, F.; Mathews, C. J.; Smith, P. J.; Welton, T. *Organometallics* **2003**, *22*, 5350-5357.

Mei, J.; Graham, K. R.; Stalder, R.; Reynolds, J. R. *Org. Lett.* **2010**, *12*, 660-663.

Mei, Q.; Li, C.; Gong, X.; Lu, H.; Jin, E.; Du, C.; Lu, Z.; Jiang, L.; Meng, X.; Wang, C.; Bo, Z. *ACS Appl. Mater. Interfaces* **2013**, *5*, 8076-8080.

Michaelis, A.; Kaehne, R. *Berichte* **1898**, *31*, 1048.

Mihailetchi, V. D.; Blom, P. W. M.; Hummelen, J. C.; Rispens, M. T. *J. Appl. Phys.* **2003**, *94*, 6849-6854.

Mihailetchi, V. D.; Koster, L. J. A.; Blom, P. W. M. *Appl. Phys. Lett.* **2004**, *85*, 970-972.

Mitchell, R. H.; Iyer, V. S. *Synlett* **1989**, No. 1, 55-57.

Mitsunobu, O.; Yamada, M. *Bull. Chem. Soc. Jpn.* **1967**, *40* (10), 2380-2382.

Mohd Yusoff, A. R. Bin; Kim, D.; Kim, H. P.; Shneider, F. K.; da Silva, W. J.; Jang, J. *Energy Environ. Sci.* **2015**, *8*, 303-316.

Mor, G. K.; Shankar, K.; Paulose, M.; Varghese, O. K.; Grimes, C. A. *Appl. Phys. Lett.* **2011**, *91*, 152111.

Mwaura, J. K.; Zhao, X.; Jiang, H.; Schanze, K. S.; Reynolds, J. R. *Chem. Mater.* **2006**, *18*(26), 6109-6111.

Nam, S.; Jang, J.; Cha, H.; Hwang, J.; An, T. K.; Park, S.; Park, C. E. *J. Mater. Chem.* **2012**, *22*, 5543-5549.

Nguyen, T. L.; Choi, H.; Ko, S.-J.; Uddin, M. a.; Walker, B.; Yum, S.; Jeong, J.-E.; Yun, M. H.; Shin, T. J.; Hwang, S.; Kim, J. Y.; Woo, H. Y. *Energy Environ. Sci.* **2014**, *7* (9), 3040-3051.

Nilsson, K. P. R.; Inganäs, O. *Nat. Mater.* **2003**, *2*, 419-424.

O'Malley, K. M.; Li, C.-Z.; Yip, H.-L.; and Jen, A. K.-Y. *Adv. Energy Mater.* **2012**, 2, 82-86.

Olivier-Bourbigou, H.; Magna, L.; Morvan, D. *Appl. Catal., A* **2010**, *373*, 1-56.

Organic Chemistry, 5th ed. Brown, W. H.; Foote, C. S.; Iverson, B. L.; Anslyn, E. V. Brooks/Cole Cengage Learning. **2009**. pp 495.

Osikowicz, W.; Jong, M. P.; Braun, S.; Tengstedt, C.; Fahlman, M.; Salaneck, W. R. *Appl. Phys. Lett.* **2006**, *88*, 193504.

Overman, L. E.; Peterson, E. a *Tetrahedron* **2003**, *59*, 6905-6919.

Page, Z. A.; Duzhko, V. V.; Emrick, T. *Macromolecules* **2013**, *46* (2), 344-351.

Page, Z. A.; Liu, F.; Russell, T. P.; Emrick, T. *Chem. Sci.* **2014**, *5*, 2368-2373.

Page, Z. A.; Liu, F.; Russell, T. P.; Emrick, T. *J. Polym. Sci., Part A Polym. Chem.* **2015**, *53* (2), 327-336.

Page, Z. A.; Liu, Y.; Duzhko, V. V.; Russell, T. P.; Emrick, T. *Science.* **2014**, *346*, 441-444.

Page, Z. A.; Liu, Y.; Puodziukynaite, E.; Russell, T. P.; Emrick, T. *In preparaiton*, **2015**.

Pang, Y.; Li, X.; Ding, H.; Shi, G.; Jin, L. *Electrochim. Acta* **2007**, *52*, 6172-6177.

Park, S. H.; Roy, A.; Beaupr e, S.; Cho, S.; Coates, N.; Moon, J. S.; Moses, D.; Leclerc, M.; Lee, K.; Heeger, A. J. *Nat. Photon.* **2009**, *3*, 297-302.

Peumans, P.; Yakimov, A.; Forrest, S.R. *J. Appl. Phys.* **2003**, 93, 3693-3723.

Pfeiffer, S.; Horhold, H. *Macromol. Chem. Phys.* **1999**, *200*, 1870-1878.

Pfeiffer, S.; Horhold, H.-H. *Synt. Met.* **1999**, *101*, 109-110.

Pilgram, K.; Zupan, M.; Skiles, R. *J. Heterocycl. Chem.* **1970**, *7*, 629-633.

Po, R.; Bianchi, G.; Carbonera, C.; Pellegrino, A. *Macromolecules* **2015**, *48*, 453.

Prato, M. & Maggini, M. Fulleropyrrolidines : A Family of Full-Fledged Fullerene Derivatives. *Acc. Chem. Res.* **31**, 519–526 (1998).

Principles of Fluorescence Spectroscopy, 3rd ed. Lakowicz, J.R. Springer, **2006**, pp 954.

Pringle, J. M.; Ngamna, O.; Lynam, C.; Wallace, G. G.; Forsyth, M.; MacFarlane, D. R. *Macromolecules* **2007**, *40*, 2702-2711.

Qi, B.; Zhang, Z.-G.; Wang, J. *Sci. Rep.* **2015**, *5*, 7803.

Reenen, S. van; Kouijzer, S.; Janssen, R. A. J.; Wienk, M. M.; Kemerink, M. *Adv. Mater. Interfaces* **2014**, *1*, 1400189.

Reichardt, C. *Green Chem.* 2005, **7**, 339-351.

Rider, B. D. A.; Worfolk, B. J.; Harris, K. D.; Lalany, A.; Shahbazi, K.; Fleischauer, M. D.; Brett, M. J.; Buriak, J. M. *Adv. Funct. Mater.* **2010**, *20*, 2404–2415.

Rodriguez, L.; Lu, N.; Yang, N.-L. *Synlett* **1990**, No. 4, 227-228.

Salaneck, W.R.; Loegdlund, M.; Fahlman, M.; Greczynski, G.; Kugler, Th. *Mat. Sci. Eng. R* **2001**, 34, 121-146.

Salzner, U.; Kose, M. E. *J. Phys. Chem. B.* **2002**, *106*, 9221-9226.

Scharber, M.C.; Muehlbacher, D.; Koppe, M.; Denk, P.; Waldauf, C.; Heeger, A.J.; and Brabec C.J. *Adv. Mat.* **2006**, 18, 789-794.

Schlaf, R.; Parkinson, B.A.; Lee, P.A.; Nebesny, K.W.; Jabbour, G.; Kippelen, B.; Peyghambarian, N.; Armstrong, N.R. *J. Appl. Phys.* **1998**, 84, 6729-6736.

Schlosser, M.; Jenny, T.; Guggisberg, Y. *Synlett* **1990**, 704.

Seo, J. H. Gutacker, A. Sun, Y. Wu, H. Huang, F. Cao, Y. Scherf, U. Heeger, A. J.; Bazan, G. C. *J. Am. Chem. Soc.* **2011**, *133*, 8416-8419.

Seo, J. H.; Gutacker, A.; Walker, B.; Cho, S.; Garcia, A.; Yang, R.; Nguyen, T.-Q.; Heeger, A. J.; Bazan, G. C. *J. Am. Chem. Soc.* **2009**, *131*, 18220-18221.

Seo, J. H.; Namdas, E. B.; Gutacker, A.; Heeger, A. J.; Bazan, G. C. *Adv. Funct. Mater.* **2011**, *21*, 3667-3672.

Seo, J. H.; Namdas, E. B.; Gutacker, A.; Heeger, A. J.; Bazan, G. C. *Appl. Phys. Lett.* **2010**, *97*(4), 043303.

Seo, J. H.; Nguyen, T.-Q. *J. Am. Chem. Soc.* **2008**, 130, 10042-10043.

Seo, J. H.; Yang, R.; Brzezinski, J. Z.; Walker, B.; Bazan, G. C.; Nguyen, T.-Q. *Adv. Mater.* **2009**, *21*(9), 1006-1011.

Sheldon, R. *Chem. Commun.* **2001**, 2399-2407.

Shi, C. Yao, Y. Yang, Y.; Pei, Q. *J. Am. Chem. Soc.* **2006**, *128*, 8980-8986.

Slinker, J. D.; DeFranco, J. A.; Jaquith, M. J.; Silveira, W. R.; Zhong, Y.-W.; Moran-Mirabal, J. M.; Craighead, H. G.; Abruña, H. D.; Marohn, J. A.; Malliaras, G. G. *Nat. Mater.* **2007**, *6*(11), 894–899.

Sonnenschein, L.; Seubert, A. *Tetrahedron Lett.* **2011**, *52*, 1101-1104.

Stas, S.; Sergeyev, S.; Geerts, Y. *Tetrahedron* **2010**, *66*, 1837-1845.

Steuerman, D. W.; Garcia, A.; Dante, M.; Yang, R.; Löfvander, J. P.; Nguyen, T.-Q. *Adv. Mater.* **2008**, *20*(3), 528-534.

Stokes, K. K. Heuze, K.; McCullough, R. D. *Macromolecules.* **2003**, *36*, 7114-7118.

Synthesis and Properties of Poly(arylene vinylene)s, chapter 4. In: *Handbook of Conducting Polymers*. 3rd ed. Skotheim, T. A., Reynolds, J. R., Eds.; Taylor & Francis Group, LLC, **2007**; pp 1–6.

Sze, S. M. & Ng, K. K. *Physics of Semiconductor Devices*. (John Wiley & Sons, Inc.: **2007**).

Tang C.W.; VanSlyke, S.A. *Appl. Phys. Lett.* **1987**, 51, 913-915.

Tang, C. W. *Appl. Phys. Lett.* **2012**, *183*, 5-8.

Tengstedt, C. Osikowicz, W. Salaneck, W. R. Parker, I. D. Hsu, C.-h; Parker, I. D. *Appl. Phys. Lett.* **2006**, *88*, 053502.

Theander, M.; Yartsev, A.; Zigmantas, D.; Sundstrom, V.; Mammo, W.; Andersson, M. R.; Inganas, O. *Phys. Rev. B* **2000**, *61*, 957-963.

Tress, W.; Petrich, A.; Hummert, M.; Hein, M.; Leo, K.; Riede, M. *Appl. Phys. Lett.* **2011**, *98*, 063301.

Usta, H.; Lu, G.; Facchetti, A.; Marks, T. J. *J. Am. Chem. Soc.* **2006**, *128*, 9034-9035.

Vandewal, K.; Tvingstedt, K.; Gadisa, A.; Inganas, O.; Manca, J.V. *Nat. Mater.* **2009**, 8, 904-909.

Vázquez, H.; Flores, F.; Kahn, A. *Org. Electron.* **2007**, *8* (2-3), 241-248.

Vygodskii, Y. S.; Lozinskaya, E. I.; Shaplov, A. S.; Lyssenko, K. A.; Antipin, M. Y.; Urman, Y. G. *Polymer* **2004**, *45*, 5031-5045.

Vygodskii, Y. S.; Shaplov, A. S.; Lozinskaya, E. I.; Filippov, O. a.; Shubina, E. S.; Bandari, R.; Buchmeiser, M. R. *Macromolecules* **2006**, *39*, 7821-7830.

Wagenpfahl, A.; Rauh, D.; Binder, M.; Deibel, C.; Dyakonov, V. *Phys. Rev. B* **2010**, *82*, 115306.

Wang, D.; Wang, J.; Moses, D.; Bazan, G. C.; Heeger, A. J. Langmuir **2001**, *17*, 1262-1266.

Wasserscheid, P.; Keim, W. *Angew. Chem. Int. Ed. Engl.* **2000**, *39*, 3772-3789.

Watanabe, Y. Mihara, T.; Koide, N. *Macromol. Chem. Phys.* **1998**, *199*, 977-983.

Wei, Q.; Nishizawa, T.; Tajima, K.; and Hashimoto, K. *Adv. Mater.* **2008**, 20, 2211-2216.

Weinberger, B. R.; Akhtar, M.; Gau, S. C. *Synth. Met.* **1982**, *4*, 187-197.

Weingärtner, H. *Angew. Chem. Int. Ed.* **2008**, *47*, 654-670.

White, M.S.; Olson, D.C.; Shaheen, S.E.; Kopidakis, N.; Ginley, D.S. *Appl. Phys. Lett.* **2006**, 89, 143517.

Woo, S.; Hyun Kim, W.; Kim, H.; Yi, Y.; Lyu, H.-K.; Kim, Y. *Adv. Energy Mater.* **2014**, *4*, 1301692.

Worfolk, B.J.; Hauger, T.C.; Harris, K.D.; Rider, D.A.; Fordyce, J.A.M.; Beaupre, S.; Leclerc, M.; and Buriak, J.M. *Adv. Energy Mater.* **2012**, 2, 361-368.

Wu, H.; Huang, F.; Mo, Y.; Yang, W.; Wang, D.; Peng, J.; and Cao, Y. *Adv. Mater.* **2004**, 16, 1826-1830.

Wu, X.-M.; Gu, Y.-B. *Lett. Org. Chem.* **2012**, *9*, 396-400.

Xia, R.; Leem, D.-S.; Kirchartz, T.; Spencer, S.; Murphy, C.; He, Z.; Wu, H.; Su, S.; Cao, Y.; Kim, J. S.; DeMello, J. C.; Bradley, D. D. C.; Nelson, J. *Adv. Energy Mater.* **2013**, *3* (6), 718-723.

Xin, B.; Zhang, Y.; Liu, L.; Wang, Y. *Synlett* **2005**, 3083-3086.

Yan, H.; Chen, Z.; Zheng, Y.; Newman, C.; Quinn, J. R.; Dötz, F.; Kastler, M.; Facchetti, A. *Nature* **2009**, *457*, 679-686.

Yan, N.; Yang, X.; Fei, Z.; Li, Y.; Kou, Y.; Dyson, P. J. *Organometallics* **2009**, *28*, 937-939.

Yang, X.; Chueh, C.; Li, C.; Yip, H.; Yin, P.; Chen, H.; Chen, W.; Jen, A. K. *Adv. Energy Mater.* **2013**, *3*, 666-673.

Yang, X.; Fei, Z.; Geldbach, T. J.; Phillips, A. D.; Hartinger, C. G.; Li, Y.; Dyson, P. J. *Organometallics* **2008**, *27*, 3971-3977.

Yang, Y.; Wudl, F. *Adv. Mater.* **2009**, *21*, 1401-1403.

Yao, K.; Salvador, M.; Chueh, C.; Xin, X.; Xu, Y.; Dane, W.; Hu, T.; Chen, Y.; Ginger, D. S.; Jen, A. K. *Adv. Energy Mater.* **2014**, *4*, 1400206.

Ye, L.; Zhang, S.; Zhao, W.; Yao, H.; Hou, J. *Chem. Mater.* **2014**, *26*, 3603-3605.

Yip, B. H.-lap; Hau, S. K. Baek, N. S. Ma, H.; Jen, A. K. *Adv. Mater.* **2008**, *20*, 2376-2382.

Yip, H.-L.; Jen, A. K.-Y. *Energy Environ. Sci.* **2012**, *5*, 5994-6011.

You, J.; Chen, C.-C.; Hong, Z.; Yoshimura, K.; Ohya, K.; Xu, R.; Ye, S.; Gao, J.; Li, G.; Yang, Y. *Adv. Mater.* **2013**, *25* (29), 3973-3978.

You, J.; Dou, L.; Yoshimura, K.; Kato, T.; Ohya, K.; Moriarty, T.; Emery, K.; Chen, C.-C.; Gao, J.; Li, G.; Yang, Y. *Nat. Commun.* **2013**, *4*, 1410-1446.

Yu, G.; Gao, J.; Hummelen, J. C.; Wudl, F.; Heeger, A. J. *Science* **1995**, *270*, 1789-1791.

Yu, G.; Zhao, D.; Wen, L.; Yang, S.; Chen, X. *AIChE J.* **2012**, *58*, 49-53.

Yuan, C.; Hou, L.; Shen, L.; Zhang, X. *J. Electrochem. Soc.* **2012**, *159*, A1323-A1328.

Zhang, K.; Zhong, C.; Liu, S.; Mu, C.; Li, Z.; Yan, H.; Huang, F.; Cao, Y. *ACS Appl. Mater. Interfaces* **2014**, *6*, 10429-10435.

Zhang, M.; Tsao, H. N.; Pisula, W.; Yang, C.; Mishra, A. K.; Müllen, K. *J. Am. Chem. Soc.* **2007**, *129*, 3472-3473

Zhang, M.; Wang, H.; Tang, C. W. *Appl. Phys. Lett.* **2011**, *99*, 213506.

Zhang, Q.; Kan, B.; Liu, F.; Long, G.; Wan, X.; Chen, X.; Zuo, Y.; Ni, W.; Zhang, H.; Li, M.; Hu, Z.; Huang, F.; Cao, Y.; Liang, Z.; Zhang, M.; Russell, T. P.; Chen, Y. *Nat. Photonics* **2014**, *9* (1), 35-41.

Zhang, S.; Sun, N.; He, X.; Lu, X.; Zhang, X. *J. Phys. Chem. Ref. Data* **2006**, *35*, 1475-1517.

Zhang, S.; Ye, L.; Zhao, W.; Yang, B.; Wang, Q.; Hou, J. *Sci. China. Chem.* **2015**, *58* (2), 248-256.

Zhang, W.; Wu, Y.; Bao, Q.; Gao, F.; Fang, J. *Adv. Energy Mater.* **2014**, *4*, 1400359.

Zhang, Z.; Li, H.; Qi, B.; Chi, D.; Jin, Z.; Qi, Z.; Hou, J.; Li, Y.; Wang, J. *J. Mater. Chem. A* **2013**, *1*, 9624-9629.

Zhang, Z.-G.; Qi, B.; Jin, Z.; Chi, D.; Qi, Z.; Li, Y.; Wang, J. *Energy Environ. Sci.* **2014**, *7*, 1966-1973.

Zheng, Z.; Zhang, S.; Zhang, M.; Zhao, K.; Ye, L.; Chen, Y.; Yang, B.; Hou, J. *Adv. Mater.* **2015**, *27* (7), 1189-1194.

Zhou, H.; Yang, L.; Stuart, A. C.; Price, S. C.; Liu, S.; You, W. *Angew. Chem. Int. Ed.* **2011**, *50* (13), 2995-2998.

Zhou, H.; Zhang, Y.; Mai, C.-K.; Collins, S. D.; Bazan, G. C.; Nguyen, T.-Q.; Heeger, A. J. *Adv. Mater.* **2015**, *27*, 1767-1773.

Zhou, H.; Zhang, Y.; Seifter, J.; Collins, S. D.; Luo, C.; Bazan, G. C.; Nguyen, T.-Q.; Heeger, A. J. *Adv. Mater.* **2013**, *25*, 1646-1652.

Zhou, Y.; Fuentes-Hernandez, C.; Shim, J.; Meyer, J.; Giordano, A. J.; Li, H.; Winget, P.; Papadopoulos, T.; Cheun, H.; Kim, J.; Fenoll, M.; Dindar, A.; Haske, W.; Najafabadi, E.; Khan, T. M.; Sojoudi, H.; Barlow, S.; Graham, S.; Brédas, J.-L.; Marder, S. R.; Kahn, A.; Kippelen, B. *Science* **2012**, *336*, 327-332.

Zhu, X.-Y.; Yang, Q.; Muntwiler, M. *Acc. Chem. Res.* **2009**, *42*, 1779-1787.

Zou, G.; Wang, Z.; Zhu, J.; Tang, J.; He, M. Y. *J. Mol. Catal. A: Chem.* **2003**, *206*, 193-198.